Atomistic Simulation of the Elasticity of Polymers

DISSERTATION

submitted to the

SWISS FEDERAL INSTITUTE OF TECHNOLOGY
ZÜRICH

for the degree of
Doctor of Natural Sciences

presented by

Marcel Zehnder
Dipl. Werkstoff-Ing. ETH
born June 16, 1966
citizen of Willisau-Land, LU

accepted on the recommendation of

Prof. Dr. Ulrich W. Suter, examiner
Dr. Andrei A. Gusev, co-examiner
Prof. Dr. Wilfred F. van Gunsteren, co-examiner

Zürich, 1997

I dedicate this work to the memory of my father

Hubert Zehnder (1938-1997)

Table of Contents

6 Appendices

Notation

a_i	acceleration vector **a**	m/s^2
a_{ij}	transformation matrix **A**	
a_{mn}	acceptance probability from m to n	
A	Helmholtz free energy	J/mol
A	general property	
a, b, c	cell edge lengths	m
a_i, b_i, c_i	cell edge vectors **a, b, c**	m
α_A	polarizability of atom species A	m^{-3}
α_{ij}	tensor of the thermal expansivity	K^{-1}
α_{mn}	attempt probability to go from m to n	
α, β, γ	cell edge angles	°
$A_{\alpha\beta}, B_{\alpha\beta}$	Lennard-Jones parameters between α and β	J/mol·m$^{6(12)}$
b	bond length	m
β	isothermal compressibility ($= K^{-1}$)	GPa^{-1}
$c_{0..5}$	components of the quintic spline	
c_{ab}	normalized correlation function	
C_{AB}	correlation function between A and B	
c_{ijkl}	small strain/stress elasticity tensor	GPa
C_{ij}	elasticity tensor in Voigt notation	GPa
C_{ijkl}	finite strain/stress elasticity tensor	GPa
C_v, C_p	isochoric, adiabatic heat capacity	J/(mol·K)
$C_{6..10}$	dispersion coefficients	
d_{ij}	stretching tensor **d**	
D	diffusion constant	cm^2/s
δ_{ij}	identity matrix **I**	
e_i	unit vector **e**	
ε	dielectric constant	
ε_i	principal values of ε_{ij}	
ε_0	permittivity of vacuum	As/Vm
ε_{ij}	symmetric small strain tensor **E**, ε	
$\varepsilon_{\alpha\beta}$	interaction energy between atom type α and β	J/mol
E	Young's modulus	GPa
E	energy	J/mol
f_i^α	force **f** on atom α	N
ϕ	torsion angle	°
ϕ_{ijk}	symmetrical tensor in the first pair of indices	

g_i	gravitational force vector	N
$g(x)$	gradient of the potential energy with respect to x	J/(mol·m)
g	metric tensor	m^2
$g_{\alpha\beta}$	pair-distribution function of α and β	
G	shear modulus	GPa
G^α	lattice function of atom α	
h	Planck's number	Js
$h(s)$	structure factor	
h_i	line search direction	m
h_{ij}	cell shape tensor h	m
H_{ij}	reference cell shape tensor H	m
H	Hamiltonian	J/mol
H	Hessian of the potential energy with respect to x	J/(mol·m^2)
H	displacement tensor	
η	shear viscosity	kg/(m·s)
η_i	finite strain tensor in Voigt notation	
η_{ij}	finite strain tensor	
I	identity matrix	
j_i^e	thermal flux	
j_i^{el}	electrical flux	Cm/s
J	determinant of J_{ij}	
J_{ij}	Jacobian matrix J	
k	Boltzmann factor	J/K
K	bulk (compression) modulus	GPa
K	kinetic energy	J/mol
κ	parameter of the Ewald summation	
I_i	invariants of the stress tensor	N/m^2
L	Lagrangian	J/mol
λ_T	thermal conductivity	W/(Km)
$\lambda_{n\times n}$	Eigenvalues of a $n{\times}n$ matrix	
λ, μ	Lamé constants	GPa
μ_i	dipole moment	Cm
μ_α	chemical potential of specie α	J/mol
M_i	number of systems in state i	
m_α	mass of atom α	kg
m_w	molecular mass	g/mol
m, n	exponents of the Lennard-Jones m-n potential	
m, n_i	possible states in MC move	

n_i	unit vector **n**	
n	*vector of integer numbers*	
$N_{(\alpha)}$	number of atoms (of type α)	
N_A	effective number of electrons of atom species A	
N_A	Avogadro's number	mol^{-1}
ν	Poisson's ratio	
p	pressure	N/m^2 (bar)
p_i^α	momentum of atom α	kg·m/s
p_i, q_i	arbitrary vectors	
$\mathbf{p}_i, \mathbf{q}_i$	conjugate momenta, coordinates of atom i	
P_i	origin of the coordinate system **x**	
P_{ij}	symmetric microscopic stress tensor	N/m^2
π_{mn}	transition probability	
$\mathbf{q}_i$	molecular conformation i	
q_i^*	selection probability of torsion angle i	
$q_i, q^{(i)}, Q$	partial charge on atom i, total charge	electron charge, C
Q	coupling mass between T and θ	
Q_{ThN}	canonical partition function	
$r_{(ij)}$	distance (between atom i and j)	m (Å)
r_i	arbitrary vector **r**	m
r_c, r_s	cutoff/spline radius	m (Å)
R	reduced minimum distance	
R	matrix or vector of random numbers	
ρ	density	kg/m^3
s	scaled coordinate of temperature coupling	
s_i	arbitrary scaled vector **s**	
s, S	length of vector x_i, X_i	m
s_{ijkl}	small stress/strain compliance tensor	GPa^{-1}
S_{ij}	compliance tensor in Voigt notation	GPa^{-1}
S_{ijkl}	finite stress/strain compliance tensor	GPa^{-1}
S	Entropy	J/(mol·K)
$S(r)$	quintic spline function with components $c_{0..5}$	
S_{AA}	spectral density function of A	
σ_e	electrical conductivity	Ω^{-1}m^{-1}
σ_i	finite stress tensor in Voigt notation	N/m^2
σ_{ij}	finite stress tensor σ	N/m^2
$\sigma_{\alpha\beta}$	collision distance between atom type α and β	m (Å)
t	time	s

t_i	thermodynamic tension tensor in Voigt notation	N/m^2
t_{ij}	thermodynamic tension tensor $\mathbf{t}$	N/m^2
T	temperature	K
T_i	torque	N/m
T_{ij}, T_{ijkl}	general tensor	
θ	bending angle	°
θ	conjugate scaled velocity	s^{-1}
Θ_{ij}	quadrupole moment	Cm^2
u_i	vector connecting two points before deformation	m
U	interaction energy	J/mol
v_i^α	velocity $\mathbf{v}$ of atom α	m/s
V	volume	m^3
w_i	Boltzmann weight i	
W	coupling mass between stress and cell shape change	kg
Ω	scaled momentum of pressure coupling	
ω	rotation angle	
Ω_{ij}	rotation tensor	
x_i, X_i	cartesian coordinate vectors, reference frame	m
$X(\theta)$	Rotation matrix (Euler angles)	
χ	out-of-plane parameter (Wilson definition)	°
χ_{ijk}	antisymmetric tensor in the last pair of indices	
ξ	thermodynamic friction	
Z	configuration integral	
$Z(\phi), Z(\psi)$	Rotation matrix (Euler angles)	

List of Acronyms

bcc	body-centered cubic
BMFT	Bundesministerium für Forschung und Technologie
BPA-PC	Bisphenol-A-Polycarbonate
fcc	face-centered cubic
FDT	Fluctuation Dissipation Theorem
GZS	Gusev-Zehnder-Suter
hcp	hexagonally close packed
MC	Monte Carlo
MD	Molecular Dynamics
MRS	Mechanical Relaxation Spectrum
MSI	Molecular Simulations, Incorp.

PA	Polyamide
PBC	Periodic Boundary Condition (= PCC)
PC	Polycarbonate
PCC	Periodic Continuation Condition (=PBC)
PE	Polyethylene (CH_3-$(CH_2)_n$-CH_3)
PR	Parrinello-Rahman

Abstract

In this work, the elastic constants of solids, in particular crystalline and amorphous polymers, are computed numerically.

The first part introduces in three chapters to the theory of elasticity, to atomistic modelling, and to the theory of fluctuations, laying the foundations for the second part, which presents the results of various computer simulations.

Starting from the stress and strain tensor, the properties of stiffness and compliance tensors are deployed in the first chapter. Special emphasis is put on symmetry operations and on coordinate transformations. In the chapter about atomistic modelling, the functional form and the computation of intra- and inter-molecular forcefield terms are covered as well as algorithms for the canonical sampling of the phase space. The focus of the third chapter is on methods that compute the complete tensor of the elastic constants from fluctuations of global parameters. At the moment, there are two such formula: The first is from Parrinello and Rahman and uses the fluctuations of the cell shape (i.e. the strain with respect to a reference shape) only, whereas the second was established in the course of this work and takes into consideration both the fluctuations of the strain and the correlation of stress and strain.

The generation of atomistic models of argon, polyethylene, polypropylene, cellulose, polyamide, and polycarbonate is described in the second part of this work. These models were propagated by MC and MD algorithms through phase space to compare the convergence behaviour of the two fluctuation approaches and to test their applicability to real polymeric materials. Exact results are delivered by fluctuation approaches only in the limit of an ergodic sampling of the phase space, i.e. for infinitely long simulations. The convergence behaviour of these algorithms is therefore of prime interest to get useful approximations in a reasonable time. It could be shown, that the new fluctuation formula converges at least as good as the well established Parrinello-Rahman formula. In some cases - low temperatures and small oscillations - the new stress-strain correlation method is even much faster. Comparison between the results of the two approaches allows for an estimation of the accuracy of the elastic constants.

There is a good agreement between calculated and experimental elastic constants both for amorphous and crystalline polymers. In contrast to other methods like the static minimum energy method, it was even possible to predict the influence of small guest molecules and of temperature changes on the elastic behaviour. Besides this, it is possible to use the huge amounts of data produced in molecular dynamics simulations to compute dynamic properties like relaxation spectra.

Zusammenfassung

Diese Arbeit befasst sich mit der numerischen Berechnung von elastischen Konstanten von Festkörpern, insbesondere von amorphen und kristallinen Polymeren. Im ersten Teil werden in drei Kapiteln die Elastizitätstheorie, die atomistische Modellierung und die Fluktuationsrechnung dargelegt, welche die Grundlage des zweiten Teils bilden, in welchem die Resultate diverser Computersimulationen präsentiert werden.

Ausgehend vom Spannungs- und Dehnungstensor werden zuerst die Eigenschaften des Elastizitäts- bzw. Nachgiebigkeitstensors in Bezug auf Symmetrieoperationen und Koordinatentransformationen behandelt. Im Abschnitt über atomistische Modellierung wird, nebst der funktionalen Form und Berechnung von intra- und intermolekularen Kraftfeldern, vor allem auf Algorithmen zur kanonischen Erfassung des Phasenraums eingegangen. Bei Fluktuationsrechnungen bilden Methoden, welche den vollständigen Elastizitätstensor aus den zeitlichen Schwankungen globaler Grössen berechnen, den Schwerpunkt. Zur Zeit existieren zwei solche Formalismen: der erste stammt von Parrinello und Rahman und benützt die Änderungen der Zelldehnung, während der zweite im Rahmen dieser Arbeit entwickelt wurde und sowohl Schwankungen der Dehnung als auch der aktuellen Spannung berücksichtigt.

Im zweiten Teil dieser Arbeit werden Festkörpermodelle von Argon, Polyethylen, Polypropylen, Cellulose, Polyamid und Polycarbonat erstellt und durch den Phasenraum propagiert, um einerseits das Konvergenzverhalten der Fluktuationsformeln zu vergleichen und um andererseits die Anwendbarkeit dieser Modelle auf reale Polymere zu testen. Fluktuationsformeln liefern exakte Resultate nur für den Grenzfall der ergodischen Abtastung des Phasenraums, d.h. für unendlich lange Simulationen. Es konnte gezeigt werden, dass die neuentwickelte Fluktuationsformel zumindest gleich gut und unter gewissen Bedingungen - tiefe Temperaturen und kleine Dehnungen - viel besser konvergiert. Der Vergleich der Resultate der beiden Fluktuationsmethoden erlaubt zudem eine Abschätzung des Ungenauigkeit der erhaltenen Elastizitätstensoren.

Im Allgemeinen wurde eine sehr gute Übereinstimmung zwischen berechneten und experimentellen elastischen Konstanten für kristalline und amorphe Polymere erzielt. Insbesondere sind die verwendeten Fluktuationsformeln in der Lage, den Einfluss von gelösten Stoffen und von Temperaturänderungen auf die elastischen Konstanten vorherzusagen. Bei diesen Simulationen fallen zudem grosse Mengen an Daten an, welche - mit Einschränkungen - für die Berechnung dynamischer Informationen, wie z. B. Relaxationsspektren, genutzt werden können.

Introduction

Only a few years after the establishment of the macromolecular character of polymers by Staudinger (1920)[Elias84], Meyer and Lothmar[Meyer36a] calculated the elastic modulus of isolated cellulose chains in 1936. They used spectroscopic data of low molar mass compounds to establish a forcefield of the cellulose backbone and computed the elastic constants from the spring constants of angles and valences. Basically the same *forcefield approach* was used twenty-five years later by Lyons[Lyons58a] and Treloar[Treloar60a] to estimate the elastic moduli of nylon, polyethylene terephthalate, and polyethylene chains. In 1966, Odajima and Maeda[Odajima66a] used Born's lattice dynamics theory to compute the full matrix of the elastic constants of polyethylene crystals. They included the intermolecular forces (at least the nearest neighbour interactions), which they found to contribute only 0.2 % in the case of polyethylene crystals, and the influence of temperature on the elastic constants in their model. Four years later, Wobser and Blasenbrey[Wobser70a] determined the elastic constants of PE single crystals using the theory of the dynamics of non-primitive lattices of Leibfried taking the first and second neighbour shell into consideration. In the following year, 1971, Shiro and Miyazawa[Shiro71a] developed a general method to transform the *potential energy matrix* (i.e. the forcefield) to the matrix of the elastic constants. Both intra- and intermolecular forces were included. With the same general matrix method, but reduced to the asymmetric unit cell, Tashiro *et al.*[Tashiro78a] perfected this methodology.

Another approach is the *static minimum energy method*, which uses the second derivative of the potential energy hypersurface with respect to strain to compute the elastic constants. There is no analytical computation of the forcefield Hessian, but a series of deformation and minimization steps are performed to discretize the energy surface. Two of the first applications for amorphous metals are described in the works of Maeda and Takeuchi[Maeda81a] in 1981 and Srolovitz *et al.*[Srolovitz83a] in 1983. Three years later, Theodorou and Suter[Theodorou86a] applied this method to polymeric systems with extended statistical mechanical considerations. Furthermore, they used a force approach - i.e. the first derivative of the stress with respect to the strain - to estimate the elastic constants.

Brown and Clarke[Brown91a] introduced in 1991 a phenomenological method, that estimates the elastic constants from the elongation of a simulation cell during a *molecular dynamics* simulation with a constantly increasing stress component. This method was applied to various polymers by Qian and

Ludovice[Ludovice93a].

All the methods presented above have certain disadvantages: The general matrix methods only work for ordered systems, whereas the static minimum energy approach completely neglects entropic effects, which makes its applicability to amorphous systems doubtful (see chapter 4.8.4.2). The molecular dynamics approach suffers from very high deformation rates and yields elastic constants which may considerably differ from experiment. It would therefore be desirable to have a method, that would take into account both entropic effects and the influence of small molecules on the elastic constants. Furthermore, the method should work both on crystalline and amorphous systems of any size and it should leave the microstructures close to their equilibrium conformations.

Already in 1969, Squire, Holt, and Hoover[Squire69a] introduced a method to compute the elastic constants from 'kinetic', 'Born', and *'fluctuation'* terms resulting from a Monte Carlo simulation. Parrinello and Rahman[ParrinelloRahman81a/82a] published in 1981 and 1982 their pioneering works about constant stress molecular dynamics and the computation of the matrix of the elastic constants from strain fluctuations. This laid the basis for a number of works, that compared the efficiency of fluctuation algorithms in MC and various MD-ensembles. Of importance are here the work of Sprik, Impey, and Klein[Sprik84a], Ray, Moody, and Rahman[Ray85a/86a], and the papers of Ray[Ray88a] and Fay and Ray[Fay92a]. Most calculations in these papers dealt with nearest-neighbour Lennard-Jones solids and with sodium.

In this work, the strain fluctuation method was applied for the first time to various polymeric systems to compute the full matrix of the elastic constants of crystals, glasses, and glasses with small diffusants. It turned out, that this fluctuation method was capable of reproducing the elastic constants of all these systems remarkably well, with one problem remaining: the convergence of the elastic constants with simulation time was slow, requiring long simulations. It is therefore most valuable to find a convergence criterion to optimize the duration of the long molecular dynamics runs. This criterion was found by establishing a new fluctuation formula that uses both the stress and the strain fluctuations of a model cell to compute its elastic constants. Comparison of the results of the strain and the stress-strain fluctuation method allowed to estimate the degree of convergence of a simulation.

The following work is organized in two major sections:

The first three chapters comprise the *theory section*, in which the relevant concepts of elasticity, molecular modelling and fluctuations are outlined. Since this section is quite detailed, it might serve as a tutorial introduction to the field covered by this thesis.

The fourth chapter with eight subchapters presents the *results* of molecular dynamics and Monte Carlo simulations of argon, polyethylene, polypropylene, cellulose, polyamides and polycarbonate. Some introductory remarks at the beginning explain the choice of the polymers by methodological and historical arguments.

Comments, conclusions and an outlook finish the main body and some appendices provide more detailed informations on certain topics.

1 Theory I - Elasticity of Anisotropic Solids

1.1 Stress Tensor

Forces acting upon a solid elastic body may be categorized as *body forces*, originating from gravitational or magnetic fields, or as *contact forces*, exerted by the surrounding matter.[Sands82,Wooster73,Malvern69] While body forces are effective on individual particles of the system (atoms, dipoles, etc) and therefore are proportional to the size, the contact forces act on the surface of the body and are dependent on its shape and the location of the contact points. Consider a volume element within the stressed body (Fig. 1.1). From the contact points forces are transmitted on the sides of the element by the material around it. These forces are proportional to the area of the surface of the element, and the force per actual unit area is called the *stress*.
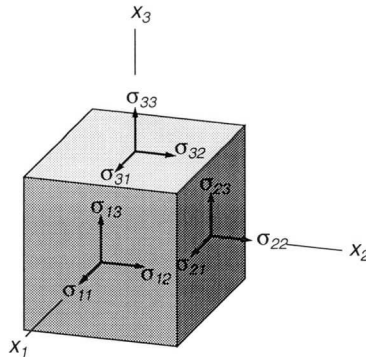
Figure 1.1: The stresses on the faces of a unit cube in a homogeneously stressed body

1.1.1 Homogeneous Stress

A stress can be called *homogeneous*, if the forces acting on the surface of an element of fixed shape and orientation are independent of the position of the element in the body[Nye85,Shuvalov88]. The volume element of Fig. 1.1 shows the stress acting on the three faces oriented towards the positive ends of the coordinate axes x_1, x_2 and x_3, with positive values given by the orientation of the vectors (tensile stress acting on the body is positive while compressive stress is negative). Since a homogeneous stress state is assumed, the stresses on the three opposite faces must be equal and opposite to those shown in the figure. This makes a total of nine different components of the stress.

If we further assume that the volume element is in static equilibrium, we

must have zero angular momentum around each coordinate axis. This is only fulfilled if

$$\sigma_{12} = \sigma_{21} \qquad \sigma_{12} = \sigma_{21} \qquad \sigma_{12} = \sigma_{21}$$

or (1-1)

$$\sigma_{ij} = \sigma_{ji} \, .$$

We thus can write the six independent components of the stress in a symmetric 3×3-matrix:

$$\sigma_{ij} = \begin{bmatrix} \sigma_{11} & \sigma_{12} & \sigma_{13} \\ \sigma_{12} & \sigma_{22} & \sigma_{23} \\ \sigma_{13} & \sigma_{23} & \sigma_{33} \end{bmatrix} \tag{1-2}$$

1.1.2 Inhomogeneous Stress

A stress-state is called *inhomogeneous*, if the stress varies from point to point. The actual stress at a given point is arrived at by taking the forces per area of a volume element and letting the size of the volume element tend to zero. The inhomogeneity of the stress can be expressed by it's gradient $\frac{\partial \sigma_{ij}}{\partial x_k}$.

The equations of motion of a small volume element in the presence of a (gravitational) body force g_i can be written as [Nye85]

$$\frac{\partial \sigma_{ij}}{\partial x_j} + \rho g_i = \rho \ddot{x}_i, \tag{1-3}$$

with ρ corresponding to the density of mass in the volume element. (Throughout the rest of this chapter, the summation convention is applied to indices occurring twice in a product).

Assuming statical equilibrium, all components of the acceleration $\ddot{x}_i$ must be zero, which leads to the *equations of equilibrium* of the theory of elasticity

$$\frac{\partial \sigma_{ij}}{\partial x_j} + \rho g_i = 0 \, . \tag{1-4}$$

In a small cube of size δ, the moment of inertia around an axis parallel to the edges through the center is $\frac{\delta^5}{24}$. Since the torque exerted by the shear-stresses on the surface of this cube and by an additional body-torque **G** is

$$T_k = (\sigma_{ij} - \sigma_{ji} + G_k)\delta^3 \qquad (k \neq i, j) \, , \tag{1-5}$$

the angular acceleration will be proportional to δ^{-2}, becoming infinite as δ tends to zero[KellyGroves70], unless

$$\sigma_{ij} - \sigma_{ji} + G_k = 0. \tag{1-6}$$

If body-torques are absent, the same relation as for homogeneous stresses (Eq. (1-1)) is obtained. With body-torques present, Hooke's law is still valid, if σ_{ij} is not the stress itself, but its symmetrical part $\frac{1}{2}(\sigma_{ij} + \sigma_{ji})$.[Nye85,Malvern69]

Actually, it is always possible[Landau86a] to find a transformation of the form

$$\sigma'_{ij} = \sigma_{ij} + \frac{\partial \chi_{ijk}}{\partial x_k}, \qquad \chi_{ijk} = -\chi_{ikj} \tag{1-7}$$

where χ_{ijk} is any tensor antisymmetric in the last pair of indices. If the antisymmetric part of σ_{ij} has the form

$$\sigma_{ij} - \sigma_{ji} = 2 \frac{\partial \phi_{ijk}}{\partial x_k}, \qquad \phi_{ijk} = \phi_{jik} \tag{1-8}$$

then an asymmetrical σ_{ij} can be *made symmetrical* by a transformation of this type (Eq. (1-7)). The symmetrical tensor is

$$\sigma'_{ij} = \frac{1}{2}(\sigma_{ij} + \sigma_{ji}) + \frac{\partial(\phi_{ikj} + \phi_{jki})}{\partial x_k} \tag{1-9}$$

with

$$\chi_{ijk} = \phi_{jki} + \phi_{ikj} - \phi_{ijk}. \tag{1-10}$$

1.1.3   Tensor Properties of the Stress Matrix

The nine components of a second-rank *tensor* **T** connect the components of two vectors **p** and **q** in a linear relationship

$$p_i = T_{ij}q_j \tag{1-11}$$

If the coordinate system is transformed, the elements of a tensor transform according to

$$T_{ij} = a_{ik}a_{jl}T_{kl}, \tag{1-12}$$

a_{ij} denoting the components of the transformation matrix **A** (Appendix A-1). Equation (1-12) thus represents a *definition of a* (second-rank) *tensor*.[Nye85,Goldstein80]

It can be shown[Nye85] that the stress matrix σ_{ij} indeed forms a second-rank tensor that connects the normal **n** of a small surface element δS with the force vector **p**δS acting through this surface element (Fig. 1.2).

If the area of the surface element becomes infinitesimally small, the local stress vector **p** is given by
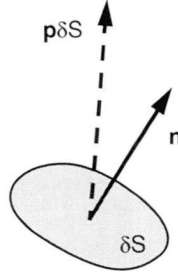
Figure 1.2: The force transmitted across a small surface element in a stressed body

$$p_i = \sigma_{ij} n_j. \tag{1-13}$$

This equation still holds when the stress is not homogenous, when body forces are acting, and when the body is not in statical equilibrium for these extra terms become negligible as the surface is made vanishingly small.

1.1.4 Eigenvalues of the Stress Tensor, Invariants

Since the stress tensor is symmetric (Eq. (1-1)), all its eigenvalues are real and the eigenvectors are orthogonal [Bronstein91]. It is thus possible to diagonalize the stress tensor by an appropriate transformation of the reference coordinate system using a transformation matrix a_{ij}

$$\sigma'_{kl} = a_{ik} a_{jl} \sigma_{ij} = \begin{bmatrix} \sigma_1 & 0 & 0 \\ 0 & \sigma_2 & 0 \\ 0 & 0 & \sigma_3 \end{bmatrix} \tag{1-14}$$

The unit vectors of the transformed coordinate system form an eigenspace, in which a volume element similar to that of Fig. 1.1 shows no shear stresses but only normal components.

Three invariants of the stress tensor are given by [Bhagavantam66]

$$I_1 = \sigma_1 + \sigma_2 + \sigma_3 = \sigma_{11} + \sigma_{22} + \sigma_{33}$$

$$I_2 = \sigma_2\sigma_3 + \sigma_3\sigma_1 + \sigma_1\sigma_2 = \begin{vmatrix} \sigma_{22} & \sigma_{23} \\ \sigma_{23} & \sigma_{33} \end{vmatrix} + \begin{vmatrix} \sigma_{11} & \sigma_{13} \\ \sigma_{13} & \sigma_{33} \end{vmatrix} + \begin{vmatrix} \sigma_{11} & \sigma_{12} \\ \sigma_{12} & \sigma_{22} \end{vmatrix}$$

$$I_3 = \sigma_1\sigma_2\sigma_3 = \begin{vmatrix} \sigma_{11} & \sigma_{12} & \sigma_{13} \\ \sigma_{12} & \sigma_{22} & \sigma_{23} \\ \sigma_{13} & \sigma_{23} & \sigma_{33} \end{vmatrix}$$

$$\tag{1-15}$$

1.2   Strain Tensor

1.2.1   Small or Linear-Elastic Strain Tensor

1.2.1.1   Small Strain and Rotation Tensor

A material subject to a stress reacts by deforming until the internal stresses generated by this deformation counterbalance the external stress. If the material relaxes to its initial shape after removal of the external stress, the deformation is called *elastic*; if a permanent change in shape remains, a *plastic* deformation has occurred. In the present work, only the elastic, thermodynamically reversible behavior of matter is being concerned.

The local small-scale deformation of a body can be described by looking at an arbitrary infinitesimal line vector *d***X** connecting two points *P* and *Q* in the undeformed state (Fig. 1.3).
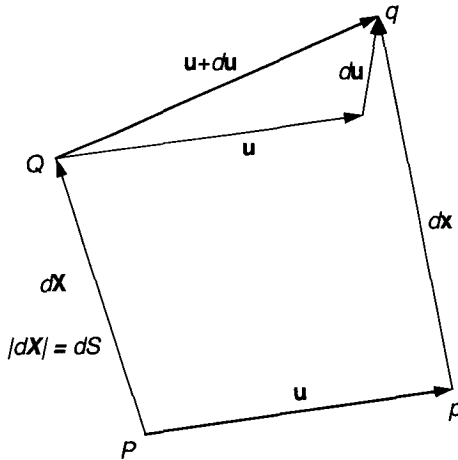
Figure 1.3:   Relative displacement *d***u** of *Q* relative to *P*.

Upon deformation, the two points move by **u** to *p* and by **u**+*d***u** to *q*, respectively. The unit relative displacement vector,

$$\frac{du_i}{dS} = \frac{\partial u_i}{\partial X_j}\frac{dX_j}{dS},$$

(1-16)

can be written briefly as

$$\frac{d\mathbf{u}}{dS} = \mathbf{J}_u\mathbf{n},$$

(1-17)

where $\mathbf{J}_U$ is the 3×3 *Jacobian matrix* or *displacement gradient matrix* and $\mathbf{n}$ the unit vector in the direction of $d\mathbf{X}$. The Jacobian matrix - the deformation process can be interpreted as a transformation from one coordinate system to another (Appendix A-6) - can be written as the sum of a symmetric matrix $\mathbf{E}$ and a skew-symmetric matrix Ω,

$$\mathbf{J}_U = \mathbf{E} + \Omega, \tag{1-18}$$

with

$$\mathbf{E} = \begin{bmatrix} \dfrac{\partial u_1}{\partial X_1} & \dfrac{1}{2}\left(\dfrac{\partial u_1}{\partial X_2} + \dfrac{\partial u_2}{\partial X_1}\right) & \dfrac{1}{2}\left(\dfrac{\partial u_1}{\partial X_3} + \dfrac{\partial u_3}{\partial X_1}\right) \\[3mm] \dfrac{1}{2}\left(\dfrac{\partial u_1}{\partial X_2} + \dfrac{\partial u_2}{\partial X_1}\right) & \dfrac{\partial u_2}{\partial X_2} & \dfrac{1}{2}\left(\dfrac{\partial u_2}{\partial X_3} + \dfrac{\partial u_3}{\partial X_2}\right) \\[3mm] \dfrac{1}{2}\left(\dfrac{\partial u_3}{\partial X_1} + \dfrac{\partial u_1}{\partial x_3}\right) & \dfrac{1}{2}\left(\dfrac{\partial u_3}{\partial X_2} + \dfrac{\partial u_2}{\partial X_3}\right) & \dfrac{\partial u_3}{\partial X_3} \end{bmatrix} \quad \varepsilon_{ij} = \dfrac{1}{2}\left(\dfrac{\partial u_i}{\partial X_j} + \dfrac{\partial u_j}{\partial X_i}\right) \tag{1-19}$$

and

$$\Omega = \begin{bmatrix} 0 & \dfrac{1}{2}\left(\dfrac{\partial u_1}{\partial X_2} - \dfrac{\partial u_2}{\partial X_1}\right) & \dfrac{1}{2}\left(\dfrac{\partial u_1}{\partial X_3} - \dfrac{\partial u_3}{\partial X_1}\right) \\[3mm] \dfrac{1}{2}\left(\dfrac{\partial u_1}{\partial X_2} - \dfrac{\partial u_2}{\partial X_1}\right) & 0 & \dfrac{1}{2}\left(\dfrac{\partial u_2}{\partial X_3} - \dfrac{\partial u_3}{\partial X_2}\right) \\[3mm] \dfrac{1}{2}\left(\dfrac{\partial u_3}{\partial X_1} - \dfrac{\partial u_1}{\partial X_3}\right) & \dfrac{1}{2}\left(\dfrac{\partial u_3}{\partial X_2} - \dfrac{\partial u_2}{\partial X_3}\right) & 0 \end{bmatrix} \quad \Omega_{ij} = \dfrac{1}{2}\left(\dfrac{\partial u_i}{\partial X_j} - \dfrac{\partial u_j}{\partial X_i}\right) \tag{1-20}$$

$\mathbf{E}$ represents the (symmetric) small-strain tensor with its components ε_{ij}. It can be shown[Malvern69] that Ω is a rotation tensor describing the rotation of a rigid body around an axis vector

$$\omega = \begin{bmatrix} -\Omega_{23} \\ -\Omega_{13} \\ -\Omega_{12} \end{bmatrix} \tag{1-21}$$

by an angle $|\omega|$.

1.2.1.2 Diagonalization, Dilatation Strain Quadric and Ellipsoid

Since strain, as defined by (1-19), is a symmetrical tensor it may be referred to its principal axes. The shear components then vanish,

$$\begin{bmatrix} \varepsilon_{11} & \varepsilon_{12} & \varepsilon_{13} \\ \varepsilon_{12} & \varepsilon_{22} & \varepsilon_{23} \\ \varepsilon_{13} & \varepsilon_{23} & \varepsilon_{33} \end{bmatrix} \rightarrow \begin{bmatrix} \varepsilon_1 & 0 & 0 \\ 0 & \varepsilon_2 & 0 \\ 0 & 0 & \varepsilon_3 \end{bmatrix}, \qquad (1\text{-}22)$$

leading to a simple definition of the *dilatation* Δ,

$$\Delta = (1+\varepsilon_1)(1+\varepsilon_2)(1+\varepsilon_3) - 1 = \varepsilon_1 + \varepsilon_2 + \varepsilon_3 = \text{tr}\mathbf{E}. \qquad (1\text{-}23)$$

The *principal axes of strain* only remain unchanged by deformation if the rotation tensor Ω is zero, otherwise they define three mutually perpendicular axes, which remain mutually perpendicular during the deformation.

It is possible to define a *strain quadric*

$$\varepsilon_{ij}x_i x_j = 1, \qquad (1\text{-}24)$$

which is identical with the quadric $J_{ij}x_i x_j = 1$.

The *strain ellipsoid*

$$\frac{{x_1'}^2}{(1+\varepsilon_1)^2} + \frac{{x_2'}^2}{(1+\varepsilon_2)^2} + \frac{{x_3'}^2}{(1+\varepsilon_3)^2} = 1, \qquad (1\text{-}25)$$

describes the shape of a sphere $(x_1^2 + x_2^2 + x_3^2 = 1)$ after the deformation.

The invariants of the strain matrix can be found analogous to Eq. (1-15).

1.2.2 Finite Strain Tensor

If a body is heavily (but still elastically) deformed, the linear relationship between change in shape and strain is no longer valid, as will be shown in this paragraph.[Landau86a]

Considering again the deformation shown in Fig. 1.3, the vector d**x**, connecting the two points P and Q, changes during the deformation to d**x** = d**X** + d**u**. The squared distance between the two points is $dS^2 = dX_i dX_i$ before and $ds^2 = dx_i dx_i = (dX_i + du_i)^2$ after the deformation. Substituting $du_i = (\partial u_i / \partial X_j) dX_j$, which is valid, if the strain is sufficiently homogeneous over the length scale given by d**X**, the length of the deformed connecting vector is

$$ds^2 = dS^2 + 2\frac{\partial u_i}{\partial X_j} dX_i dX_j + \frac{\partial u_i}{\partial X_j}\frac{\partial u_i}{\partial X_k} dX_j dX_k. \qquad (1\text{-}26)$$

The second term can be brought into an explicitly symmetrical form, because the summation is taken over both suffixes i and j:

$$2\frac{\partial u_i}{\partial X_j} dX_i dX_j \leftrightarrow \left(\frac{\partial u_i}{\partial X_j} + \frac{\partial u_j}{\partial X_i}\right) dX_i dX_j. \qquad (1\text{-}27)$$

In the third term, the indices i and k are interchanged and ds^2 takes the final form

$$ds^2 = dS^2 + 2\eta_{ij}dX_i dX_j,\tag{1-28}$$

where the *symmetric* tensor η_{ij} is defined as

$$\eta_{ij} = \frac{1}{2}\left(\frac{\partial u_i}{\partial X_j} + \frac{\partial u_j}{\partial X_i} + \frac{\partial u_k}{\partial X_i}\frac{\partial u_k}{\partial X_j}\right).\tag{1-29}$$

Comparing Eqs (1-19) and (1-29), one can clearly see that the small strain tensor is an approximation of the above equation neglecting the products of the derivatives. Equation (1-29) provides a correct[Malvern69] mathematical description of the strain that is valid for small and large deformations.

Assuming that P in Fig. 1.3 is located at $\mathbf{X}$ and p at $\mathbf{x}$, the displacement $\mathbf{u}$ is given by

$$u_i = x_i - X_i.\tag{1-30}$$

Combining Eq. (1-29) and Eq. (1-30), we find

$$\eta_{ij} = \frac{1}{2}\left(\frac{\partial x_k}{\partial X_i}\frac{\partial x_k}{\partial X_j} - \delta_{ij}\right),\tag{1-31}$$

which, using the definition of the Jacobian (Eq. (A-17)), can be written as

$$\eta_{ij} = \frac{1}{2}(J_{x,ki}J_{x,kj} - \delta_{ij}) \quad \text{or} \quad \eta = \frac{1}{2}\left(\mathbf{J}_x^{\mathsf{T}}\mathbf{J}_x - \mathbf{I}\right).\tag{1-32}$$

The two tensors $\mathbf{J}_x$ and $\mathbf{J}_u$ are related by

$$J_{u,ij} = \frac{\partial u_i}{\partial X_j} = \frac{\partial(x_i - X_i)}{\partial X_j} = \frac{\partial x_i}{\partial X_j} - \delta_{ij} = J_{x,ij} - \delta_{ij}.\tag{1-33}$$

1.2.3 Finite Strain Tensor from Cell Shape Tensors

1.2.3.1 Definition of the Cell Shape Tensor

The cell shape tensor $\mathbf{h}$ is simply constructed by taking the cell edge vectors $\mathbf{a}$, $\mathbf{b}$ and $\mathbf{c}$ (Fig. 1.4) as columns of a 3×3 matrix

$$\mathbf{h} = [\mathbf{a}, \mathbf{b}, \mathbf{c}] = \begin{bmatrix} a_1 & b_1 & c_1 \\ a_2 & b_2 & c_2 \\ a_3 & b_3 & c_3 \end{bmatrix}.\tag{1-34}$$

The cell shape tensor $\mathbf{h}$ is a scaling matrix that *transforms* all points in the cell into a cubic unit cell by

$$\mathbf{r}_\alpha = \mathbf{h}\mathbf{s}_\alpha \qquad \mathbf{s}_\alpha = \mathbf{h}^{-1}\mathbf{r}_\alpha.\tag{1-35}$$

1.2.3.2 Strain from Cell Shape Tensors

The strain (deformation) between a reference cell shape tensor **H** and an actual shape tensor **h** (Fig. 1.4) can be expressed by

$$\eta = \frac{1}{2}\left[\mathbf{H}^{T-1}\mathbf{h}^T\mathbf{h}\mathbf{H}^{-1} - \mathbf{I}\right], \tag{1-36}$$

with **I** representing the identity matrix ($I_{ij}=\delta_{ij}$, δ: Kronecker symbol). (The derivation of this formula is given in Appendix B-1.)
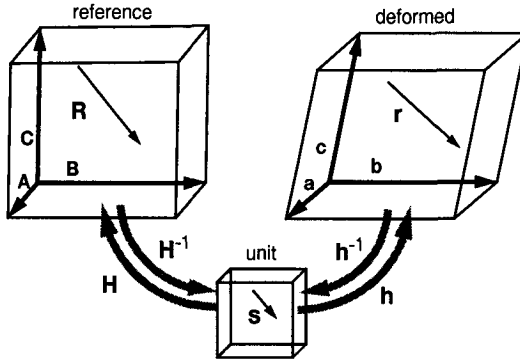
Figure 1.4:   Scaling matrices linking unit cell with reference and deformed cell

1.2.4 Finite Stress (Thermodynamic Tension)

1.2.4.1 Relation Between Actual Stress and Thermodynamic Tension

As stated in chapter 1.1.1, stress is defined as force per unit surface of the actual, deformed body. In contrast to this, strain is referred to the natural, unstressed state. For this reason the stress power necessary to deform a body with a certain deformation rate is not equal to the stress components times the differentials of the corresponding strain components. Quantities t_{ij}, called *thermodynamic tensions*, are defined such that the power to stretch a medium non-dissipatively equals the sum $t_{ij}\dot{\eta}_{ij}$ (per unit volume of undeformed body). This rate of change of the Helmholtz energy at constant temperature must equal the sum of the actual stress σ_{ij} times the actual deformation rate d_{ij}.[Thurston64]

$$\dot{U} - T\dot{S} = V_0 t_{st}\dot{\eta}_{st} = V\sigma_{ij}d_{ij}, \tag{1-37}$$

where U represents the internal energy, T the temperature, and S the entropy. V and V_0 denote the volume of the deformed and undeformed body, respectively and the *stretching tensor* d_{ij} is given by

$$d_{ij} = \frac{1}{2}\left(\frac{\partial v_i}{\partial x_j} + \frac{\partial v_j}{\partial x_i}\right) = \dot{\eta}_{st}\frac{\partial X_s}{\partial x_i}\frac{\partial X_t}{\partial x_j}.$$ (1-38)

The second equality can be rationalized by taking the time derivative of Eq. (1-31),

$$\dot{\eta}_{st} = \frac{1}{2}\left(\frac{\partial x_i}{\partial X_s}\frac{\partial v_i}{\partial x_j}\frac{\partial x_j}{\partial X_t} + \frac{\partial x_j}{\partial X_t}\frac{\partial v_j}{\partial x_i}\frac{\partial x_i}{\partial X_s}\right) = d_{ij}\frac{\partial x_i}{\partial X_s}\frac{\partial x_j}{\partial X_t}$$ (1-39)

Plugging (1-38) into (1-37) and using the relation between V and V_0 given by Eq. (A-20), the *thermodynamic tensions* and the actual stress are connected by

$$t_{st} = J\sigma_{ij}\frac{\partial X_s}{\partial x_i}\frac{\partial X_t}{\partial x_j} \quad \text{or} \quad \sigma_{ij} = \frac{1}{J}\frac{\partial x_i}{\partial X_s}\frac{\partial x_j}{\partial X_t}t_{st}.$$ (1-40)

This equation can be written in terms of the cell shape tensors $\mathbf{H}$ and $\mathbf{h}$[Ray84a]:

$$\mathbf{t} = J\mathbf{H}\mathbf{h}^{-1}\sigma\mathbf{h}^{T-1}\mathbf{H}^{T} \quad \text{or} \quad \sigma = \frac{1}{J}\mathbf{h}\mathbf{H}^{-1}\mathbf{t}\mathbf{H}^{T-1}\mathbf{h}^{T},$$ (1-41)

with the Jacobi determinant $J = \det(\mathbf{h}\mathbf{H}^{-1})$, and can also be found from comparison of Eqs. (1-32) and (1-36). (The derivation of these formulae can be found in Appendix B-2.) Since σ is a symmetric tensor, $\mathbf{t}$ must be symmetric too, as is shown in Appendix B-3.

1.2.4.2 Expressions for the Thermodynamic Tension

To find an expression for the t_{st}, the first equality of Eq. (1-37) is written down, considering that $A = U - TS$,[Thurston64]

$$\rho_0(\dot{A} - \dot{T}S) = t_{st}\dot{\eta}_{st}.$$ (1-42)

Assuming that the Helmholtz energy is a function of η_{st} and T, its total derivative can be written as

$$\dot{A} = \left(\frac{\partial A}{\partial \eta_{st}}\right)_T \dot{\eta}_{st} + \left(\frac{\partial A}{\partial T}\right)_{\eta_{st}} \dot{T}.$$ (1-43)

By substitution into (1-42), it is found that

$$\left(\rho_0\frac{\partial A}{\partial \eta_{st}} - t_{st}\right)\dot{\eta}_{st} + \rho_0\left(S + \frac{\partial A}{\partial T}\right)\dot{T} = 0,$$ (1-44)

whence

$$t_{st} = \rho_0\left(\frac{\partial A}{\partial \eta_{st}}\right)_T.$$ (1-45)

Another formula for the thermodynamic tensions was presented by Ray[Ray84a]:

$$t = J\mathbf{H}\mathbf{h}^{-1}\mathbf{P}\mathbf{h}^{T-1}\mathbf{H}^{T},$$ (1-46)

where **P** is the *symmetric microscopic stress tensor*

$$P_{ij} = V^{-1}\left[\sum_{\alpha}\frac{p_{\alpha i}p_{\alpha j}}{m_{\alpha}} - \sum_{\alpha < \beta}\frac{r_{\alpha\beta i}r_{\alpha\beta j}}{r_{\alpha\beta}}\frac{\partial U}{\partial r_{\alpha\beta}}\right],$$ (1-47)

with $\mathbf{p}_a$ denoting the momentum of atom a and $\mathbf{r}_{ab}$ representing the distance between atoms a and b. U is a potential energy, which depends on the interatomic distances only but is not necessarily pairwise additive.

From the comparison of Eq. (1-41) and Eq. (1-46), it is found that

$$\sigma = \mathbf{P},$$ (1-48)

which is equivalent to the virial theorem in the EhN-(constant energy, cell shape, and number of particles) ensemble and a $O\left(\frac{1}{N}\right)$ approximation of it in the HtN-(constant temperature, stress, and number of particles) ensemble[Ray84a].

1.3   Stiffness and Compliance Tensors

1.3.1   Definition of Stiffness and Compliance Tensor

As stated in chapter 1.2.1.1, a body subject to a stress deforms elastically until the internal forces generated by the emerging strain counterbalance the external stress. For sufficiently small stresses and strains, a linear (hookean) relationship between the two tensors can be observed. This is expressed by the following equations

$$\sigma_{ij} = c_{ijkl}\varepsilon_{kl} \qquad \text{or} \qquad \varepsilon_{ij} = s_{ijkl}\sigma_{kl},$$ (1-49)

where the c_{ijkl} are called the *stiffness* and the s_{ijkl} the *compliance* of the material (note that the symbols of these two quantities are the reverse of the corresponding initial letters). The above equation is an example of a *constitutive equation*, describing the macroscopic behavior of the material under consideration.

It can be shown[Nye85] that, since σ and ε both are second-rank tensors, c and s form fourth rank tensors, that transform like

$$T_{ijkl} = a_{im}a_{jn}a_{ko}a_{lp}T_{mnop},$$ (1-50)

with $a_{\alpha\beta}$ denoting the elements of the transformation matrix.

Dealing with relatively large stresses or strains, i.e. finite deformations, the stiffness and compliance tensors can be written as

$$t_{ij} = C_{ijkl}\eta_{kl} \quad \text{or} \quad \eta_{ij} = S_{ijkl}t_{kl} \tag{1-51}$$

The isothermal elastic constants (=stiffnesses C_{ijkl}) can be written for infinitesimally small stresses and strains in differential form as[Theodorou86a]

$$C_{ijkl}^T = \left(\frac{\partial t_{ij}}{\partial \eta_{kl}}\right) = \rho_0\left(\frac{\partial^2 A}{\partial \eta_{ij}\partial \eta_{kl}}\right)_T, \tag{1-52}$$

with the second equality given by (1-45). The elastic constants defined by the above equation are called second order because they involve the second derivatives of the energy. Third- and higher order elastic constants are defined in an analogous way to Eq. (1-52), but they are not of practical interest, since no experimental data is available.[CaginRay88a]

1.3.2 General Symmetry Relations

Since the stress (Eq. (1-1)) and the strain tensor (Eq. (1-29)) are symmetric, it follows from (1-51) that the indices in the first and the second pair of C_{ijkl} and S_{ijkl} can be exchanged

$$C_{ijkl} = C_{jikl} = C_{jilk} = C_{ijlk}. \tag{1-53}$$

Furthermore, the order of differentiation in Eq. (1-52) is immaterial and thus the first pair of indices can be interchanged with the second pair:

$$C_{ijkl} = C_{klij}. \tag{1-54}$$

Eqs (1-53) and (1-54) provide a total of 60 independent equations, which reduce the maximum number of independent elements of the elasticity (= stiffness) tensor to 21.

Similar considerations are also valid for the compliance tensor S_{ijkl}, which has 21 independent elements, too.

1.3.3 Voigt Notation

The symmetry relations discussed in the previous chapter can be used to represent the forth-rank stiffness and compliance tensors by two-dimensional matrices.[Nye85]

The symmetric stress and strain tensors are converted into column vectors by writing them with a single suffix running from 1 to 6:

$$\begin{bmatrix} \sigma_{11} & \sigma_{12} & \sigma_{13} \\ \sigma_{12} & \sigma_{22} & \sigma_{23} \\ \sigma_{13} & \sigma_{23} & \sigma_{33} \end{bmatrix} \leftrightarrow \begin{bmatrix} \sigma_1 & \sigma_6 & \sigma_5 \\ \sigma_6 & \sigma_2 & \sigma_4 \\ \sigma_5 & \sigma_4 & \sigma_3 \end{bmatrix} \quad \begin{bmatrix} \varepsilon_{11} & \varepsilon_{12} & \varepsilon_{13} \\ \varepsilon_{12} & \varepsilon_{22} & \varepsilon_{23} \\ \varepsilon_{13} & \varepsilon_{23} & \varepsilon_{33} \end{bmatrix} \leftrightarrow \begin{bmatrix} \varepsilon_1 & \frac{1}{2}\varepsilon_6 & \frac{1}{2}\varepsilon_5 \\ \frac{1}{2}\varepsilon_6 & \varepsilon_2 & \frac{1}{2}\varepsilon_4 \\ \frac{1}{2}\varepsilon_5 & \frac{1}{2}\varepsilon_4 & \varepsilon_3 \end{bmatrix}, \tag{1-55}$$

using the following rule to transform the 3×3-matrices to 6-dimensional vectors (compare Eq. (1-55)):

Table 1-1: Transformation rule of Voigt notation

Two-suffix notation	11	22	33	23,32	31,13	12,21
One-suffix notation	1	2	3	4	5	6

The factors of $\frac{1}{2}$ in the off-diagonal strains are introduced to allow direct comparison of the elements of the matrix of the elastic constants with those of the elasticity tensor. The same conversion also holds for the finite stress (t_{ij}, Eq. (1-40)) and strain tensor (η_{ij}, Eq. (1-29)).

It is now possible to re-write the stiffness and compliance tensors, C_{ijkl} and S_{ijkl} of Eq. (1-51), as 6×6-matrices connecting the Voigt-stresses and -strains:

$$t_m = C_{mn}\eta_n \qquad \text{or} \qquad \eta_m = S_{mn}t_n. \qquad (1\text{-}56)$$

At the same time factors of 2 and 4 are introduced as follows:

$$S_{ijkl} = S_{mn} \text{ when } m \text{ or } n \text{ are 1, 2 or 3}$$
$$2S_{ijkl} = S_{mn} \text{ when either } m \text{ or } n \text{ are 4, 5 or 6} \qquad (1\text{-}57)$$
$$4S_{ijkl} = S_{mn} \text{ when both } m \text{ and } n \text{ are 4, 5 or 6}$$

For the C_{ijkl} no factors of 2 and 4 are necessary, providing the simple relation

$$C_{ijkl} = C_{mn}, \qquad (1\text{-}58)$$

which explains the introduction of the factors of $\frac{1}{2}$ in (1-55).

Both C_{mn} and S_{mn} are symmetric matrices as follows from Eq. (1-54), leading to

$$C_{mn} = C_{nm} \qquad \text{or} \qquad S_{mn} = S_{nm}. \qquad (1\text{-}59)$$

We can now write the matrix of the elastic constants (and the compliance matrix) as follows:

$$C_{mn} = \begin{bmatrix} C_{11} & C_{12} & C_{13} & C_{14} & C_{15} & C_{16} \\ C_{12} & C_{22} & C_{23} & C_{24} & C_{25} & C_{26} \\ C_{13} & C_{23} & C_{33} & C_{34} & C_{35} & C_{36} \\ C_{14} & C_{24} & C_{34} & C_{44} & C_{45} & C_{46} \\ C_{15} & C_{25} & C_{35} & C_{45} & C_{55} & C_{56} \\ C_{16} & C_{26} & C_{36} & C_{46} & C_{56} & C_{66} \end{bmatrix} \quad S_{mn} = \begin{bmatrix} S_{11} & S_{12} & S_{13} & S_{14} & S_{15} & S_{16} \\ S_{12} & S_{22} & S_{23} & S_{24} & S_{25} & S_{26} \\ S_{13} & S_{23} & S_{33} & S_{34} & S_{35} & S_{36} \\ S_{14} & S_{24} & S_{34} & S_{44} & S_{45} & S_{46} \\ S_{15} & S_{25} & S_{35} & S_{45} & S_{55} & S_{56} \\ S_{16} & S_{26} & S_{36} & S_{46} & S_{56} & S_{66} \end{bmatrix} \quad (1\text{-}60)$$

These matrices contain the complete information about the elasticity of a

material and especially the matrix of the elastic constants is widely used in the following sections of this work. The two matrices are linked by the following relation,[Shuvalov88]

$$t_m = C_{mn}\eta_n = C_{mn}S_{no}t_o \quad \Rightarrow \quad C_{mn}S_{no} = \delta_{mo} \quad \Rightarrow \quad \begin{matrix} \mathbf{S} = \mathbf{C}^{-1} \\ \mathbf{C} = \mathbf{S}^{-1} \end{matrix}. \quad (1\text{-}61)$$

Although mathematical operations like inversion or multiplication with Voigt stress or strain vectors are quite straightforward, it has to be kept in mind that C_{mn} and S_{mn} do not represent tensors and that therefore the usual transformation law (Eq. (1-12)) is not valid. Instead of it, a more complicated transformation matrix described in Appendix A-2 has to be used.

1.3.4 Effect of Crystal Symmetry on the Matrix of the Elastic Constants

The relation between the symmetry of the physical properties of a crystal and its crystallographic symmetry is expressed by *Neumann's Principle*:[Nye85]

The symmetry elements of any physical property of a crystal must include the symmetry elements of the point group of the crystal.

Therefore, the elastic constants have the same or a higher symmetry than the crystal they are measured on. The elasticity and stiffness tensors are inherently centrosymmetric (i.e. invariant, if all three cartesian axes are inverted), as can be easily seen from Eq. (1-56),

$$t_m = C_{mn}\eta_n \quad \text{or} \quad \eta_m = S_{mn}t_n, \quad (1\text{-}56)$$

where a simultaneous change of the signs of the tensions t and the strains η is of no influence on the elastic constants.

If the crystal symmetry is higher than triclinic, the number of independent elastic constants is reduced from 21 to 13, 9, 7, 3 and 2 as the symmetry increases from monoclinic to cubic and isotropic.

There are several methods to introduce the crystal symmetry to the matrix of the elastic constants[Nye85,Bhagavantam66,Lovett89], among which the one outlined next is the most systematic:

Each of the symmetry elements of the point group of the crystal is expressed as a transformation matrix $\mathbf{A}$ (Eq. (A-3)), operating on the elasticity or stiffness tensor,

$$T_{ijkl} = a_{im}a_{jn}a_{ko}a_{lp}T_{mnop}. \quad (1\text{-}50)$$

Equating the old with the transformed moduli creates a set of equations describ-

ing the influence of the particular symmetry element on the elastic moduli. The combination of all the symmetry elements describes the point group and thus its influence on the elastic constants. In Table 1-2, the symmetry of the stiffness and compliance matrix as a function of the crystallographic crystal class is listed. A key to the notation can be found at the end of the table.

Table 1-2: Form of the C_{ij} and S_{ij} matrices
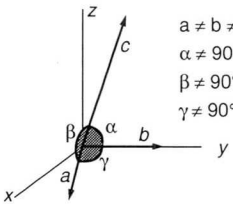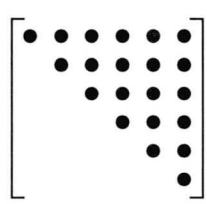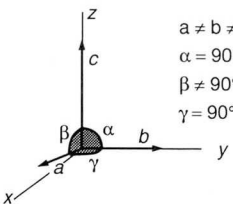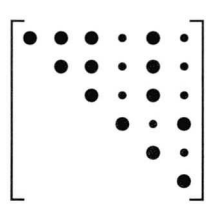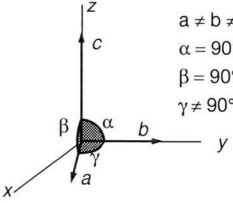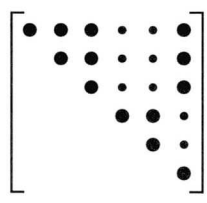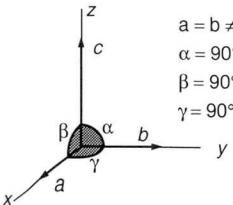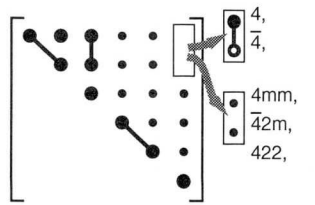
a) Triclinic

$a \neq b \neq c$
$\alpha \neq 90°$
$\beta \neq 90°$
$\gamma \neq 90°$

all classes: $1, \bar{1}$

b) Monoclinic

$a \neq b \neq c$
$\alpha = 90°$
$\beta \neq 90°$
$\gamma = 90°$

all classes: $2, m, 2/m$

Diad $\| x_2$

$a \neq b \neq c$
$\alpha = 90°$
$\beta = 90°$
$\gamma \neq 90°$

all classes: $2, m, 2/m$

Diad $\| x_3$

c) Tetragonal

$a = b \neq c$
$\alpha = 90°$
$\beta = 90°$
$\gamma = 90°$

$4,$
$\bar{4},$

$4mm,$
$\bar{4}2m,$
$422,$

Table 1-2: Form of the C_{ij} and S_{ij} matrices
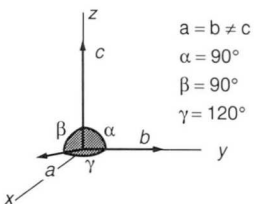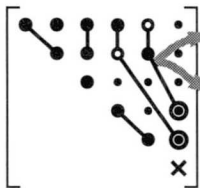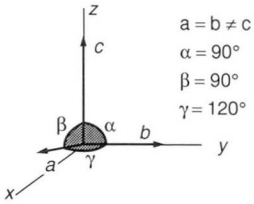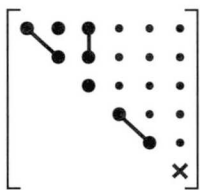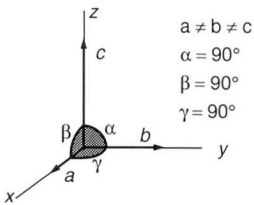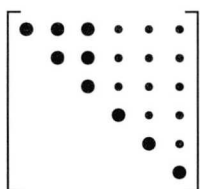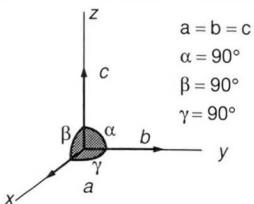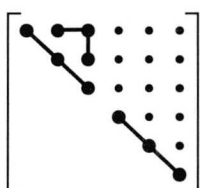
d) Trigonal

$a = b \neq c$
$\alpha = 90°$
$\beta = 90°$
$\gamma = 120°$

3,
3
= 0 for
32,
3m,

e) Hexagonal

$a = b \neq c$
$\alpha = 90°$
$\beta = 90°$
$\gamma = 120°$

all classes:
6, $\bar{6}$, 6/m,
622, 6mm
$\bar{6}$m2,
6/mmm

f) Orthorhombic

$a \neq b \neq c$
$\alpha = 90°$
$\beta = 90°$
$\gamma = 90°$

all classes:
222, mm2,
mmm

g) Cubic

$a = b = c$
$\alpha = 90°$
$\beta = 90°$
$\gamma = 90°$

all classes:
23, m3,
432, $\bar{4}$3m,
m3m

Table 1-2: Form of the C_{ij} and S_{ij} matrices

h) Isotropic	Key to notation
	• zero component ● non-zero component ●—● equal components ●—○ numerically equal, opposite in sign ◉ *S*: twice the numerical equal of ● ● *C*: numerically equal to heavy dot ✗ $2(S_{11} - S_{12})$, $\frac{1}{2}(C_{11} - C_{12})$

1.3.5 Mechanical Stability

The elastic constants are only defined if the material under consideration is in a state of equilibrium, i.e. if small changes in shape do not result in plastic deformation. This imposes two restrictions to the structure of the energy hyper-surface as a function of the applied strain: At zero strain, the first derivative of the strain energy is zero, i.e. no stresses act on the material and the second derivatives are positive. The second statement is equivalent to a mechanically stable system, where small deformations always increase the energy.[BornHuang54]

The elastic constants are proportional to the second derivative of the (free) energy with respect to strain and therefore, the matrix of the elastic constants must be positive definite, which is equivalent to the requirement that all eigenvalues should be positive[Gurtin72] or that all *principal minors* (Fig. 1.5) are positive[BornHuang54]. (The computation of the eigenvalues and eigenvectors of a 4th rank tensor is described in Appendix A-3.) This requirement imposes further restrictions to the elastic constants of the different crystal systems.

$$\begin{bmatrix} C_{11} & C_{12} & C_{13} & C_{14} & C_{15} & C_{16} \\ C_{12} & C_{22} & C_{23} & C_{24} & C_{25} & C_{26} \\ C_{13} & C_{23} & C_{33} & C_{34} & C_{35} & C_{36} \\ C_{14} & C_{24} & C_{34} & C_{44} & C_{45} & C_{46} \\ C_{15} & C_{25} & C_{35} & C_{45} & C_{55} & C_{56} \\ C_{16} & C_{26} & C_{36} & C_{46} & C_{56} & C_{66} \end{bmatrix}$$
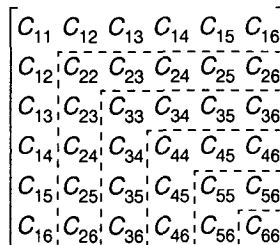
Figure 1.5: Principal minors of the matrix of the elastic constants

The analytic computation of the eigenvalues of the matrix of the elastic constants is straightforward only for the *cubic* system, where the matrix

$$\begin{bmatrix} C_{11} & C_{12} & C_{12} & 0 & 0 & 0 \\ C_{12} & C_{11} & C_{12} & 0 & 0 & 0 \\ C_{12} & C_{12} & C_{11} & 0 & 0 & 0 \\ 0 & 0 & 0 & C_{44} & 0 & 0 \\ 0 & 0 & 0 & 0 & C_{44} & 0 \\ 0 & 0 & 0 & 0 & 0 & C_{44} \end{bmatrix} \tag{1-62}$$

has the eigenvalues

$$C_{11} - C_{12} \qquad C_{11} - C_{12} \qquad C_{11} + 2C_{12} \qquad C_{44} \qquad C_{44} \qquad C_{44}. \tag{1-63}$$

The requirement that all Eigenvalues should be positive, is equivalent to the following conditions:

$$C_{44} > 0 \qquad C_{11} > |C_{12}| \qquad C_{11} + 2C_{12} > 0 \tag{1-64}$$

A similar treatment of the *hexagonal* and *trigonal* symmetry results in the following restrictions:

$$C_{44} > 0 \qquad C_{11} > |C_{12}| \qquad (C_{11} + C_{12}) C_{33} > 2C_{13}^2, \tag{1-65}$$

to which

$$C_{66} > 0 \tag{1-66}$$

is added for crystals of *tetragonal* symmetry.

For the *triclinic*, *monoclinic* and *orthorhombic* crystal classes, the eigenvalues are quite complicated, preventing the establishment of restrictions as compact as above. But numerically, the eigenvalues can be computed very efficiently from the matrix of the elastic constants, which allows a check of the mechanical stability of the system under consideration.

1.3.6 Voigt and Reuss Averages for Fibres and Powders

The elastic constants discussed so far are those of single crystals, but normally, matter is a conglomerate of crystallites of various size and orientation, embedded in a more or less amorphous matrix, which makes it very difficult to calculate the overall elastic behavior of a macroscopic body from the elasticity of its constituent domains. Two extreme approximations of the stress or strain field in a polycrystalline material are the Voigt and the Reuss limits:

- In the *Voigt* limit, it is assumed that all crystal elements are subject to the same *strain* and the elastic response of the material is obtained by taking the spatial average of the stiffness matrix.

- Equal *stress* is supposed to act on the crystallites in the *Reuss* limit and the overall compliance of the material is the spatial average of the individual compliances.

The spatial average of the stiffness or the compliance tensor equals the normalized integral over the distribution of orientation of the transformed tensor T'_{ijkl} given by

$$T'_{ijkl} = a_{im}a_{jn}a_{ko}a_{lp}T_{mnop} \qquad (1\text{-}50)$$

with a_{ij} describing the orientation of the crystalline element using the Euler angle formalism (Appendix A-7).

There are two spatial orientations of practical interest:

- The cylindrical symmetry, where one coordinate axis is oriented uniformly in one direction and one of the other two axes (as the only degree of freedom), is randomly distributed in the plane perpendicular to the direction of orientation. This corresponds ideally to the orientation distribution in a polymeric fibre.
- The powder symmetry, where all orientations are equally probable, which is a model for any unoriented polycrystal.

1.3.6.1 Fibre symmetry

The transformation matrix a_{ij} of a fiber oriented in the x_3-direction is

$$\mathbf{A}_\phi = \begin{bmatrix} \cos\phi & \sin\phi & 0 \\ -\sin\phi & \cos\phi & 0 \\ 0 & 0 & 1 \end{bmatrix} \qquad (A\text{-}21)$$

with ϕ denoting the angular position of the crystal. Writing the 3×3×3×3-tensor of the elastic constants in reading order (i.e. by row) as a column vector (denoted by { }) of 81 elements and multiplying the transformation matrices with the direct matrix product ($\otimes$) Eq. (1-50) can be written as[RutledgeSuter91a]

$$\{\mathbf{T}_\phi\} = (\mathbf{A}_\phi \otimes \mathbf{A}_\phi \otimes \mathbf{A}_\phi \otimes \mathbf{A}_\phi)\{\mathbf{T}\} = \mathbf{A}_\phi^{x4}\{\mathbf{T}\} \qquad (1\text{-}67)$$

$\mathbf{A}^{xn}$ being the self-direct product of degree n of the matrix $\mathbf{A}_\phi$. Then the cylindrical average over ϕ becomes

$$\langle\{\mathbf{T}_\phi\}\rangle = \frac{1}{2\pi}\int_0^{2\pi} \mathbf{A}_\phi^{x4}\{\mathbf{T}\}\,d\phi = \langle\mathbf{A}_\phi^{x4}\rangle\{\mathbf{T}\} . \qquad (1\text{-}68)$$

The result of the integration of the 4-fold product of the transformation matrix and

its subsequent multiplication with the stiffness tensor ($\mathbf{T} \equiv \mathbf{C}$) is shown below:

$$\langle \mathbf{C}_\phi \rangle = \begin{bmatrix} A & B & C & & \\ B & A & C & 0 & \\ C & C & D & & \\ & & & E & \\ 0 & & & & E \\ & & & & & F \end{bmatrix} \qquad \text{Voigt average} \qquad (1\text{-}69)$$

where

$$A = \frac{1}{8}(3C_{11} + 3C_{22} + 2C_{12} + 4C_{66})$$

$$B = \frac{1}{8}(C_{11} + C_{22} + 6C_{12} - 4C_{66})$$

$$C = \frac{1}{2}(C_{13} + C_{23})$$

$$D = C_{33} \qquad\qquad\qquad\qquad\qquad (1\text{-}70)$$

$$E = \frac{1}{2}(C_{44} + C_{55})$$

$$F = \frac{1}{8}(C_{11} + C_{22} - 2C_{12} + 4C_{66})$$

As a result of similar operations, the cylindrically averaged compliance matrix can be written as

$$\langle \mathbf{S}_\phi \rangle = \begin{bmatrix} A & B & C & & \\ B & A & C & 0 & \\ C & C & D & & \\ & & & E & \\ 0 & & & & E \\ & & & & & F \end{bmatrix} \qquad \text{Reuss average} \qquad (1\text{-}71)$$

where

$$A = \frac{1}{8}(3S_{11} + 3S_{22} + 2S_{12} + S_{66})$$

$$B = \frac{1}{8}(S_{11} + S_{22} + 6S_{12} - S_{66})$$

$$C = \frac{1}{2}(S_{13} + S_{23})$$

$$D = S_{33} \qquad\qquad\qquad\qquad\qquad\cdot \qquad (1\text{-}72)$$

$$E = \frac{1}{2}(S_{44} + S_{55})$$

$$F = \frac{1}{8}(S_{11} + S_{22} - 2S_{12} + S_{66})$$

1.3.6.2 Powder symmetry

To have estimates of the lower and upper bounds of polycrystalline materials, the transformation matrix

$$\mathbf{A}_{\phi\theta\psi} =$$

$$= \begin{bmatrix} \cos\psi\cos\phi - \cos\theta\sin\phi\sin\psi & \cos\psi\sin\phi - \cos\theta\cos\phi\sin\psi & \sin\psi\sin\theta \\ -\sin\psi\cos\phi - \cos\theta\sin\phi\cos\psi & -\sin\psi\sin\phi - \cos\theta\cos\phi\cos\psi & \cos\psi\sin\theta \\ \sin\theta\sin\phi & -\sin\theta\cos\phi & \cos\theta \end{bmatrix} \quad \text{(A-24)}$$

needs to be integrated over all possible orientations by

$$\langle \{\mathbf{T}_{\phi\theta\psi}\} \rangle = \frac{1}{2\pi} \int_0^{2\pi} \int_0^{\pi} \int_0^{2\pi} \mathbf{A}_{\phi\theta\psi}^{x4} \{\mathbf{T}\} \, d\psi \, d\theta \, d\phi = \langle \mathbf{A}_{\phi\theta\psi}^{x4} \rangle \{\mathbf{T}\} \, , \quad (1\text{-}73)$$

leading to an average matrix of the elastic constants (stiffnesses) of

$$\langle \mathbf{C}_{\phi\theta\psi} \rangle = \begin{bmatrix} A & B & B & & & \\ B & A & B & & 0 & \\ B & B & A & & & \\ & & & C & & \\ & 0 & & & C & \\ & & & & & C \end{bmatrix} \qquad \text{Voigt average} \qquad (1\text{-}74)$$

with the following elements

$$A = \frac{1}{15}(3C_{11} + 2C_{12} + 2C_{13} + 4C_{66} + 4C_{55} + 3C_{22} + 2C_{23} + 4C_{44} + 3C_{33})$$

$$B = \frac{1}{15}(C_{11} + 4C_{12} + 4C_{13} - 2C_{66} - 2C_{55} + C_{22} + 4C_{23} - 2C_{44} + C_{33})$$

$$C = \frac{1}{2}(A - B)$$

$$(1\text{-}75)$$

This corresponds exactly to the symmetry of an isotropic material (see Table 1-2), which will be discussed in the following chapter.

Averaging the stiffnesses, the Reuss average of the material is obtained as

$$\langle \mathbf{S}_{\phi\theta\psi} \rangle = \begin{bmatrix} A & B & B & & & \\ B & A & B & & 0 & \\ B & B & A & & & \\ & & & C & & \\ & 0 & & & C & \\ & & & & & C \end{bmatrix} \qquad \text{Reuss average} \qquad (1\text{-}76)$$

with the following elements

$$A = \tfrac{1}{15}(3S_{11} + 2S_{12} + 2S_{13} + S_{66} + S_{55} + 3S_{22} + 2S_{23} + S_{44} + 3C_{33})$$

$$B = \tfrac{1}{15}\left(S_{11} + 4S_{12} + 4S_{13} - \tfrac{1}{2}C_{66} - \tfrac{1}{2}C_{55} + C_{22} + 4C_{23} - \tfrac{1}{2}C_{44} + C_{33}\right). \quad (1\text{-}77)$$

$$C = 2(A - B)$$

1.3.7 Isotropic Materials: Lamé Constants, Elastic Constants

As shown in the previous chapter and in Table 1-2, the matrix of the elastic constants of an isotropic material can be written as[Sneddon58]

$$
\begin{bmatrix}
C_{11} & C_{12} & C_{12} & & & \\
C_{12} & C_{11} & C_{12} & & 0 & \\
C_{12} & C_{12} & C_{11} & & & \\
 & & & C_{44} & & \\
 & 0 & & & C_{44} & \\
 & & & & & C_{44}
\end{bmatrix}
\Leftrightarrow
\begin{bmatrix}
2\mu+\lambda & \lambda & \lambda & & & \\
\lambda & 2\mu+\lambda & \lambda & & 0 & \\
\lambda & \lambda & 2\mu+\lambda & & & \\
 & & & \mu & & \\
 & 0 & & & \mu & \\
 & & & & & \mu
\end{bmatrix}
\quad (1\text{-}78)
$$

with

$$\lambda = C_{12} \qquad\qquad 1^{st}\ \text{Lamé constant}$$

$$\mu = C_{44} = \tfrac{1}{2}(C_{11} - C_{12}) \qquad 2^{nd}\ \text{Lamé constant}$$

$$(1\text{-}79)$$

In order to be mechanically stable (chapter 1.3.5), μ and $(3\lambda+2\mu)$ must be positive.

Most engineering materials like metals, polymers, or ceramics behave macroscopically as isotropic elastic solids. Since in many cases only the elongation or the shear in relation to the acting normal or shear force is of interest, macroscopic elastic constants are often used for a more intuitive description of the behavior of elastic materials. The four most frequently used constants are[Sneddon58]

• *Young's modulus E* describes the elongation of a body in a direction in relation to the stress acting in the same direction:

$$E = \frac{\sigma_i}{\varepsilon_i} = \frac{(3\lambda + 2\mu)\mu}{\lambda + \mu} \qquad (i = 1, 2, \text{or } 3) \qquad (1\text{-}80)$$

• The *shear modulus G* is a measure of the shear deformation of a body in depends of the acting shear stress:

$$G = \frac{\sigma_i}{\varepsilon_i} = \mu \qquad (i = 4, 5, \text{or } 6) \qquad (1\text{-}81)$$

$$G = \frac{\sigma_i}{\varepsilon_i} = \mu \qquad (i = 4, 5, \text{ or } 6) \qquad (1\text{-}81)$$

- The *bulk modulus K* indicates the volume change ΔV of a material (with an initial volume of V) under a hydrostatic pressure Δp:

$$K = -V\frac{\Delta p}{\Delta V} = \lambda + \frac{2}{3}\mu \qquad (1\text{-}82)$$

- Finally, *Poisson's ratio* ν is defined as the ratio of the lateral contraction to the longitudinal extension of the cylinder:

$$\nu = -\frac{\varepsilon_j}{\varepsilon_{i \neq j}} = \frac{\lambda}{2(\lambda + \mu)} \qquad (i, j = 1, 2, \text{ or } 3) \qquad (1\text{-}83)$$

Taking the criteria for the mechanical stability ($\mu > 0$, $3\lambda + 2\mu > 0$), it follows that

$$-1 < \nu < \frac{1}{2}, \qquad (1\text{-}84)$$

where $\nu = \frac{1}{2}$ indicates a constant volume upon deformation and smaller values stand for material dilatation (for most materials, ν lies between 0.25 and 0.35).

Relations between these macroscopic constants and other physical quantities can be found in Ref. [vanKrevelen80].

2 Theory II - Atomistic Modeling

2.1 Representation of Potential Energy by a Force Field

2.1.1 Introduction

In a many-particle system - e.g. an atomistic model of a solid polymer - a considerable number of internal degrees of freedom exists, i.e. the system can adopt a huge number of conformations $\mathbf{q}_i$ with energies $E(\mathbf{q}_i)$. To compute a macroscopic property $\langle A \rangle$ of a system with a fixed number of particles, cell size and temperature (an ThN- or canonical ensemble, chapter 2.4.3), the individual conformations must be weighted with their Boltzmann factors

$$w(\mathbf{q}_i) = e^{\frac{-E(\mathbf{q}_i)}{kT}} \tag{2-1}$$

and averaged according to[McQuarrie76,Huang87]

$$\langle A \rangle = \frac{\sum_i w(\mathbf{q}_i) \cdot A(\mathbf{q}_i)}{\sum_i w(\mathbf{q}_i)} \tag{2-2}$$

($A(\mathbf{q}_i)$ is the value of the property of interest obtained from an conformation with energy $E(\mathbf{q}_i)$ and k is the Boltzmann constant).

It is therefore of prime interest to find an expression of the energy of a system as a function of the conformation of its constituents. The basic and most general way to find such an expression is an *ab initio* quantum mechanical computation of the energy of a molecular system. The calculation of the elastic constants of a polymer model typically involves hundreds and thousands of atoms and spans over several tenthousand to several hundredthousand simulation steps. This is just beyond the capabilities of present quantum mechanical methods, although first principle molecular dynamics has recently become quite powerful[Car95a].

In the Born-Oppenheimer approximation, the electronic degrees of freedom can be separated from the nuclear degrees of freedom. In an *ab-initio* quantum mechanical calculation, the electronic energy of a molecule is given first by the kinetic and potential energy of the electrons moving in the field of the nuclei, second by the electrostatic repulsion between all pairs of electrons, and third by the exchange interaction due to the correlation of parallel spins.[Leach96] All these

interactions together with the electrostatic interaction of the positive nuclei form a complex energy hypersurface depending on the positions of the nuclei.

In modern class-II force fields, this energy hypersurface and its derivatives are approximated by more or less complicated functions of the positions of the nuclei.[Hagler94a] The functional form of the different terms of these force fields is chosen such that the fit with the huge amount of quantum mechanically computed data is best with a reasonable number of parameters. This is in contrast to class-I force fields, where functional forms derived from classical models of the different molecular interactions are parametrized against a limited amount of experimental data (like crystallographic structures obtained by X-ray diffraction, IR-spectra, density measurements, etc.). Representatives of this class of force fields are CHARMM[Nilsson86a]and AMBER[WeinerKollman86a], whereas MM3[Allinger89a] and CFF93 belong to class-II.

2.1.2 The CFF93 Force Field

A good example of a class-II force field is the CFF93 force field, which is well described in the literature[HaglerMaple94a, HaglerHwang94a, HaglerMaple94b]. The MSI-Discover simulation package[MSIDiscover1] uses a close relative of this force field - PCFF91 - that was extended to work with polycarbonates and that was used for most of the simulations reported in the following chapters.

2.1.2.1 Methodology

The methodology of obtaining a class-II force field involves the following steps[HaglerSun94a]:

- The minimal energy configurations of a representative group of small molecules belonging to a particular class of compounds (e.g. alkanes, amides, etc.) are computed quantum mechanically using a HF/6-31G* basis set.
- After a normal mode analysis, the molecules are deformed by a random amount in the direction of the normal modes and *ab initio* calculations are performed on these structures to find the total energy, the first and the second derivatives of the energy, the dipole moments, and the derivatives of the dipole moments for each structure.
- Since the Hartree-Fock approximation excludes dispersion energies (chapter 2.1.3.2), the van-der-Waals parameters are determined empirically by fitting to crystal structures and sublimation energies. Because the charges from *ab initio* calculations with moderate basis sets usually do not reproduce the experimental electrostatic properties, the *ab initio* charges need to be scaled by a scaling factor obtained from crystal structures, too.

- The valence parameters (bond, angle, torsion, out-of-plane and cross terms) are calculated by fitting to the *ab initio* energy surface with both the charges and the van-der-Waals parameters held fixed. The resulting set of parameters is called the QMFF (quantum mechanical force field).

- Due to systematic deviations between experiment and quantum mechanical calculations, a small set of scaling factors (for bond, angle, torsion, out-of-plane and cross terms) is needed. In addition it is necessary to make minor adjustments to bond reference values, b_0, since these are calculated systematically too short in the HF approximation.

The functional form that allows a good fit to the quantum mechanical energy hypersurface while using a reasonable number of parameters is given in Fig. 2.1. The thirteen terms can be classified first into bonded (*a - k*) and non-bonded (*l, m*) interactions. The bonded interactions further split into diagonal (*a - d*) and cross terms (*e - k*).

2.1.2.2 Bonded Interactions

a) *Bond stretching*: The quartic polynomial approximates the morse potential function $(D_b[1-e^{-\alpha(b-b_0)}])$ well near the reference distance b_0[Leach96] and prevents bonds from breaking under large stress as can be observed for cubic polynomials. The anharmonicity in the potential is crucial for a good fit to the quantum mechanical energy hypersurface[HaglerMaple94a].

b) *Angle bending*: In contrast to the bond stretching potential, the anharmonic third and forth order terms of the bond angle θ seem to be of minor importance for the total energy and its first and second derivatives[HaglerMaple94a].

c) *Torsion potential*: The reference angle (0°) of the fourfold potential is given by the *trans* state of the torsion angle ϕ.

d) *Out-of-plane*: The Wilson definition of the out-of-plane angle is used to compute the energy of the deviation of the three bonds surrounding an sp^2-hybridized atom from planarity. The χ-value is the average of the angle between one bond and a plane defined by the two other bonds.

The following cross terms are essential for a good fit of the QMFF to the *ab-initio* energy surface and must not be omitted[Hagler94a]

e) *Bond-bond* cross term: The interaction energy between two bonds sharing a common atom (i.e. between the two bonds that form an angle). The number of these interactions equals the number of angles found in a molecular system.

f) *Angle-angle* cross term: The interaction energy between two angles sharing a common bond and a common central atom.

g) *Bond-angle* cross term: Two bond-angle interactions per angle contribute to
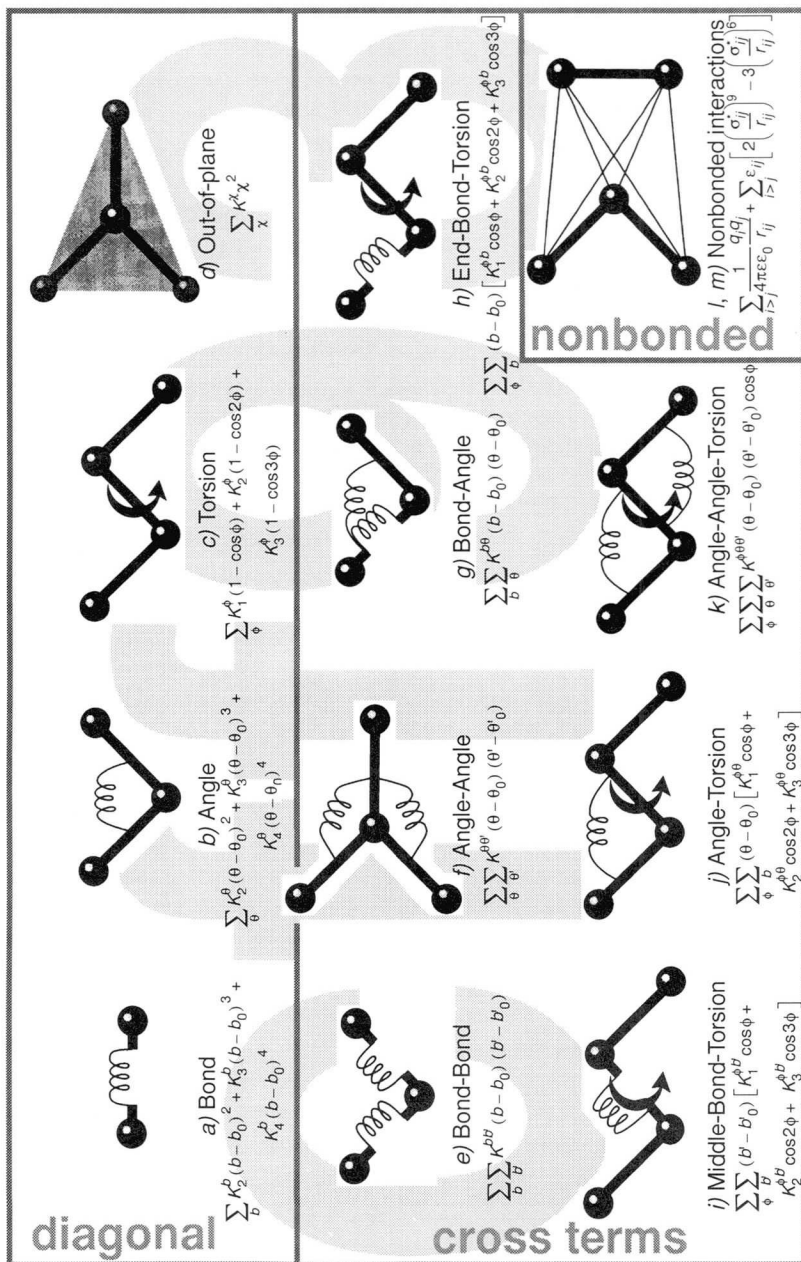
Figure 2.1: The terms of the cff93 force field

the cross term energy.

h) *End-bond-torsion* cross term: For each torsion angle, there are two end-bond-torsion cross terms and one

i) *Middle-bond-torsion* cross term.

j) *Angle-torsion* cross term: As with the bond-torsion interactions, there are two angle-torsion contributions and one

k) *Angle-angle-torsion* cross term per torsion angle.

2.1.2.3 Nonbonded Interactions

l) *Coulomb* interaction and

m) *van-der-Waals* interaction: These two interaction are computed between all pairs of nonbonded atoms. Two atoms are denoted nonbonded, if at least three bonds lie between them, i.e. there are nonbonded interactions between the first and last atom of a torsion angle. Since the nonbonded interactions are essential for the behavior of condensed systems, they will be discussed in greater detail below.

2.1.3 Nonbonded Interaction Potentials

2.1.3.1 General Remarks

The interaction energy of an assembly of molecules *i*, *j*, *k* ... can be written in form of a series of the sum of pairwise interaction terms, the sum of three-body terms, four-body terms and so on:

$$U(r, \Omega) = \sum_{i>j} U_{ij} + \sum_{i>j>k} U_{ijk} + \sum_{i>j>k>l} U_{ijkl} + \dots \quad (2\text{-}3)$$

In the first instance, it is assumed that only the pairwise interaction term is of significance for the energy of the nonbonded interactions. Corrections to this picture are however necessary and will be outlined later.

2.1.3.2 Quantum Mechanical Foundations

The functional form of the nonbonded interactions has been the subject of intense research since Boscovich formulated the first potential more than 200 years ago[Kaplan86]. In general, the interaction energy $U(r,\Omega)$ between neighboring molecules is a sum of the following terms[Stone96]:

$$U(r, \Omega) = U_{el}^{(1)} + U_{ex}^{(1)} + U_{ind}^{(2)} + U_{dis}^{(2)} + U_{ex-pol}^{(2)} + U^{(3..n)}, \quad (2\text{-}4)$$

with U_{el} being the *electrostatic* interaction, which is composed of attractive terms between the nuclei of one molecule and the electrons of the other molecule and repulsive terms between the nuclei and between the electrons on the two mole-

cules. U_{ex} is the so-called *exchange* energy, which has its origins in the Pauli principle limiting the electron density. These two contributions are first-order approximations (as indicated by the superscript index) of the Rayleigh-Schrödinger perturbation theory applied to the total Hamiltonian. This Hamilo-nian, the zeroth-order approximation, is obtained by a simple overlap of the molecular wave-functions Ψ^A and Ψ^B. The induction, U_{ind}, and the dispersion term, U_{dis}, are second-order approximations of the perturbation caused by the mutual influence of the electrons in one molecule on the electrons in the other molecule. The *induction* can be explained classically as the formation of a dipole in a non-polar molecule due to a charge or a permanent dipole on the other mol-ecule. The *dispersion* interaction has its origins in fluctuations of the electron density with time, which lead to the formation of momentary multipoles. These fluctuating multipoles induce charge separations in neighboring molecules and therefore interact with them in a analogous way to the mechanism of induction. Higher order approximations, symbolized by $U^{(3..n)}$, are not taken into consider-ation, and the second order approximation (polarization) of the exchange inter-action, U_{ex-pol}, is regarded both as being marginal in effect and difficult to handle theoretically[Kaplan86,Ratajczak80a,Murrell76].

All these terms depend of course on the distance r and the mutual orienta-tion Ω of the interacting molecules. The distance dependence of the various energy terms is of special interest and forms the topic of the next section.

2.1.3.3 Lennard-Jones Potential

If the molecules are very close to each other, their wave-functions overlap and the exchange interaction is the dominating term in the energy function. It is possible to show that this exchange term is proportional to $e^{-\alpha(R-1)}$,[Stone96] where α is a constant - typically between 12 and 15 - and $R = r/\sigma^*$, with σ^* being the minimum energy distance (see Fig. 2.2).

At larger distances, the dispersion energy is the dominant term in the van-der-Waals energy, since the induction energy is much smaller in general. Using the simple dipolar model of Drude[MaitlandRigby81], the most important contribution in a power expansion of the interaction energy,

$$U_{dis}(r) = C_6/r^6 + C_8/r^8 + C_{10}/r^{10} + \ldots., \qquad (2\text{-}5)$$

is the dispersion coefficient C_6, i.e. the electrostatic interactions decay with r^6 (Fig. 2.2). (The dispersion coefficients of higher order become more important, if quadrupoles, octupoles etc. are included in the Drude model.[Leach96]) The disper-sion coefficient C_6 can be approximated by the London formula,[Kaplan86]

$$C_6 \approx -\frac{3\,U_A U_B}{2\,(U_A + U_B)}\frac{\overline{\alpha}_A \overline{\alpha}_B}{(4\pi\varepsilon_0)^2},$$ (2-6)

with $\overline{\alpha}_A$ and $\overline{\alpha}_B$ standing for the average polarizabilities and U_A and U_B denoting the average excitation energies, which in turn can be approximated in the Slater-Kirkwood formula as[Stone96]

$$U_A \approx \left(\frac{N_A}{\alpha_A}\right)^{\frac{1}{2}}.$$ (2-7)

At very large distances above several hundred Å, the dispersion interaction is not proportional to r^{-6}, but to r^{-7}, because then the period of the charge fluctuations is comparable to the time required for the exchange of information by electromagnetic waves between the molecules (relativistic retardation effect)[Kaplan86].
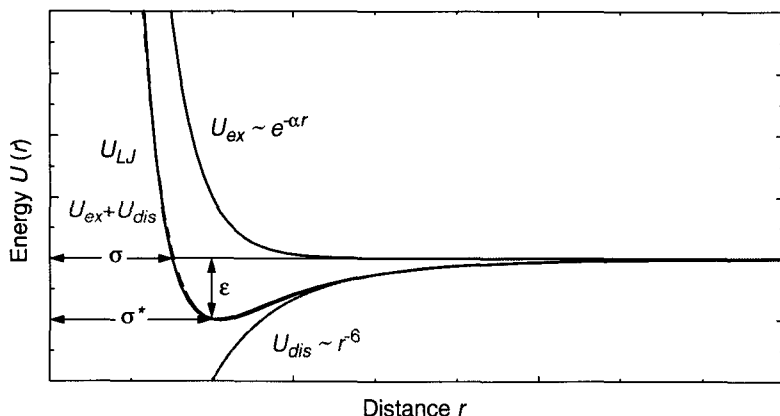
Figure 2.2:   Functional form of the exchange and dispersion energy as a function of the intermolecular distance r

The combination of repulsive exchange and attractive dispersion and induction terms is denoted U_{tot} in Fig. 2.2 and is approximated in many applications by a Lennard-Jones m-n-potential function,[AllenTildesley89]

$$U_{LJ}^{\alpha\beta} = 4\varepsilon_{\alpha\beta}\left[\left(\frac{\sigma_{\alpha\beta}}{r}\right)^m - \left(\frac{\sigma_{\alpha\beta}}{r}\right)^n\right],$$ (2-8)

where the indices α and β refer to the interacting atom types. Besides the above m-n form, exponential-6 potentials like the Hill and Buckingham

$$\left(U_B = \frac{\varepsilon}{\alpha - 6} \left[6 e^{-\alpha(x-1)} - \alpha x^{-6} \right] \right) \text{potential are also used.}$$

For the attractive second term of Eq. (2-8), the exponential n is almost always 6, according to the distance dependence of the dispersion and induction interaction, whereas the exponential rise of the exchange interaction is approximated with a large value of m, typically in the range of 9 - 12 (compare Fig. 2.2: the curve denoted by U_{LJ} is a 12-6-potential function, that approximates the quantum mechanical potential $U_{ex} + U_{dis}$ quite well). The *cff93* forcefield uses a 9-6 Lennard-Jones potential function to model the van-der-Waals interaction.

If the well depth ε and the radius of minimum energy σ^* (instead of the collision diameter σ) is used, Eq. (2-8) takes the form

$$U_{LJ}^{\alpha\beta} = \varepsilon_{\alpha\beta} \left[\frac{n}{m-n} \left(\frac{\sigma_{\alpha\beta}^*}{r} \right)^m - \frac{m}{m-n} \left(\frac{\sigma_{\alpha\beta}^*}{r} \right)^n \right] = \frac{A_{\alpha\beta}}{r^m} - \frac{B_{\alpha\beta}}{r^n}, \qquad (2\text{-}9)$$

which is also used in some force fields. A comparison between Eq. (2-8) and (2-9) immediately reveals that

$$A_{\alpha\beta} = 4\varepsilon_{\alpha\beta}\sigma_{\alpha\beta}^{12} \qquad B_{\alpha\beta} = 4\varepsilon_{\alpha\beta}\sigma_{\alpha\beta}^{6} \qquad (2\text{-}10)$$

and

$$\sigma_{\alpha\beta} = (A_{\alpha\beta}/B_{\alpha\beta})^{1/6} \qquad \varepsilon_{\alpha\beta} = B_{\alpha\beta}^{2}/4A_{\alpha\beta}. \qquad (2\text{-}11)$$

The two adjustable parameters σ and ε are obtained from experimental densities, molecular beam cross sections, etc[Murrell76]. For nonbonded interactions between two different types of atoms α and β, so called *mixing rules* have to be used. There are the commonly used Lorentz-Berthelot mixing rules,

$$\sigma_{\alpha\beta} = \frac{1}{2}(\sigma_{\alpha\alpha} + \sigma_{\beta\beta})$$
$$\varepsilon_{\alpha\beta} = \sqrt{\varepsilon_{\alpha\alpha}\varepsilon_{\beta\beta}} \qquad (2\text{-}12)$$

and the more recent rules form Hagler *et al.*[HaglerWaldman93a]

$$\sigma_{\alpha\beta} = \left(\frac{\sigma_{\alpha\alpha}^6 + \sigma_{\beta\beta}^6}{2} \right)^{\frac{1}{6}}$$
$$\varepsilon_{\alpha\beta} = 2(\varepsilon_{\alpha\alpha}\varepsilon_{\beta\beta})^{\frac{1}{2}} \left[\frac{\sigma_{\alpha\alpha}^3 \sigma_{\beta\beta}^3}{\sigma_{\alpha\alpha}^6 + \sigma_{\beta\beta}^6} \right] \qquad (2\text{-}13)$$

which seem to give consistently more accurate results.

2.1.3.4 Coulomb Interaction

Since electrons in molecules are not located at fixed points but distributed according to their wavefunctions over a (theoretically infinite) region in space, it is only possible to establish a probability density. However, the computation of nonbonded coulombic interactions between molecules based on quantum mechanical probability densities would be extremely time-consuming and difficult to perform. A number of methods to map this electron densities to a set of point charges or multipoles has been devised (Mulliken, Löwdin, Bader, etc.)[Leach96]. Alternatively, the electrostatic potential in the vicinity of a molecule can be determined and a set of charges can be calculated that fits this electrostatic potential best. There also exist approaches based on the electronegativity of the atoms.[Leach96] In the *cff93* force field, the charges are assigned incrementally bond per bond and located at the nuclear positions.[MSIDiscover1]

The result of such mapping is either a series of electronic moments - charges (monopoles), dipoles, quadrupoles, octupoles, and so on - that describe the molecule as a whole, the so-called *central multipole expansion*, or a set of point charges or distributed multipoles at various locations. If the point charges are placed at the positions of the nuclei, the calculation of the forces acting on the nuclei becomes particularly simple. On the other hand, it is not always possible to represent the complex electron density by a few point charges on the positions of the atoms.

An arbitrary distribution of charges q_i at positions $x_{i,j}$ can be grouped into the following quantities:

Table 2-1: Electronic moments of a distribution of charges q_i at positions $x_{i,j}$

Moment	Tensor rank	Formula
Total charge Q	0 (scalar)	$Q = \sum_i q_i$
Dipole μ	1 (vector)	$\mu_j = \sum_i q_i x_{i,j}$
Quadrupole Θ	2	$\Theta_{jk} = \sum_i q_i x_{i,j} x_{i,k}$
higher moments	n	$M_{j..n} = \sum_i q_i (x_{i,j}..x_{i,n})$

The classical electrostatic interaction between two scalar monopoles q_i and q_j, given by Coulomb's well-known formula,

$$U_{el} = \frac{1}{4\pi\varepsilon\varepsilon_0}\frac{q_i q_j}{r_{ij}},$$

(2-14)

depends as r^{-1} on the distance. The interaction energy between a monopole and a dipole drops as r^{-2}, whereas dipole-dipole interactions are proportional to r^{-3}. In general, the interaction energy between two electronic moments of rank m and n decreases as $r^{-(m+n+1)}$.[Leach96] In the case of the interaction between neutral molecules or neutral groups of atoms, where only dipoles and higher moments exist, the energy is proportional to r^{-3}, if the distance between the groups is larger than the size of the groups themselves.

2.1.3.5 Many-Body Effects

As mentioned in chapter 2.1.3.1, three-body and higher interaction terms are neglected. In most cases, the remarkable gain in computation time justifies this simplification. While the bonded interactions are proportional to N, the number of atoms in the system, the pairwise interactions are proportional to $N(N-1)/2$ operations and three-body terms to $N(N-1)(N-2)/6$.

There are, however, some cases where the three-body terms contribute significantly to the nonbonded energy or lead to completely different results. Examples comprise the well-known Ar-crystals, where the contribution of the Axilrod-Teller triple-dipole correction amounts to 10 - 20 % [Leach96, BellZucker76, Murrell76], and the modelling of ionic crystals of large halides and earth-alkaline metals, that leads to wrong structures if the polarization of the large halides due to Mg^{2+} or Cd^{2+} ions is neglected.[Stone96]

2.2 Modeling of Extended Dense Systems

With the force field derived in chapter 2.1, it is possible to model single molecules or assemblies of molecules *in vacuo*, but not extended solid or liquid matter. Even the smallest macroscopic bodies (grains or cells) contain $O(10^{10}\text{-}10^{20})$ atoms, which makes it impossible to simulate them as a whole. If only $O(10^2\text{-}10^3)$ atoms are used in a simulation - which is an appropriate number for current computers - most of them would be at or near the surface of the tiny body. The simulation of bulk properties would not be feasible this way. An elegant solution to this problem are the so-called *periodic continuation conditions* (PCC), also referred to as *periodic boundary conditions* (PBC).

2.2.1 Periodic Continuation Conditions

Periodic continuation conditions enable the modeling of bulk properties of solids or liquids with a relatively small number of atoms. Imagine a box with parallel walls (a parallelepiped) being replicated in all directions to give a periodic array. The walls of the box are pervious to the particles in it, so no physical boundaries are present. Particles leaving one side of the box, enter it at the opposite side immediately (compare Fig. 2.3), keeping the number of particles N
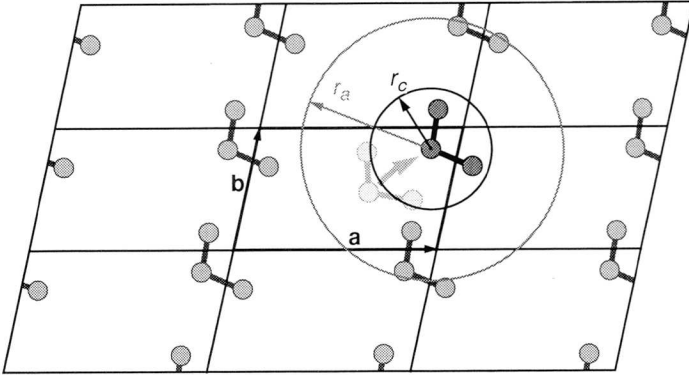
Figure 2.3: Periodic continuation conditions in two dimensions

constant. In principle, there exist 5 cell shapes, that fill space completely by translation from a central cell: the parallelepiped (and its special form, the cube), the hexagonal prism, the truncated octahedron, the rhombic dodecahedron and the 'elongated' dodecahedron.[Leach96] In this work, only the cube and the parallelepiped are used, because of the simple numeric implementation of these two conditions.[AllenTildesley89]

The use of PCCs invokes some problems: First, fluctuations with wavelengths greater than the dimensions of the box are not possible, the phonon spectrum is cut. Second, the radial distribution function $g_{\alpha\beta}(r)$ is not exactly isotropic.[Frenkel96]

The simulation cell is defined by n vectors, with n being the dimensionality of the simulation space (typically 3-dimensional), which form a $n \times n$ cell shape matrix $\mathbf{h}$ (chapter 1.2.3.1):

$$\mathbf{h} = [\mathbf{a}, \mathbf{b}, \mathbf{c}] = \begin{bmatrix} a_1 & b_1 & c_1 \\ a_2 & b_2 & c_2 \\ a_3 & b_3 & c_3 \end{bmatrix}. \qquad (1\text{-}34)$$

2.2.2 Long-range Interactions

The introduction of the PCC creates a virtually infinite, quasi-crystalline simulation system without boundaries. Since this would imply an infinite number of interactions between the atoms in the central cell and all their replicas, the nonbonded interactions can not be evaluated explicitly. Several methods are used to circumvent this problem: for van-der-Waals interactions, a cutoff plus a correction term is reasonable, while more sophisticated methods like Ewald summation or cell multipole expansion are needed for the Coulomb interactions.

2.2.2.1 Cutoffs

A cutoff truncates the computation of nonbonded interactions between a central atom and the other atoms of a system at a certain distance. If the cutoff-radius is larger than the smallest cell extension (r_a in Fig. 2.3), the central atom interacts with its replicas, causing unphysical finite-size effects. It is therefore useful to keep the radius of the interaction sphere smaller than half the smallest dimension of the box (r_c in Fig. 2.3). In this case, the *minimum image convention* is applied, stating that each atom 'sees' at most just one image of every other atom in the system.

Using a step function (like the Heavyside function) to define a cutoff causes problems because of the discontinuities in the potential function and its derivatives (i.e. the forces). So a switching function $S(r)$ (Fig. 2.4) smoothly switches
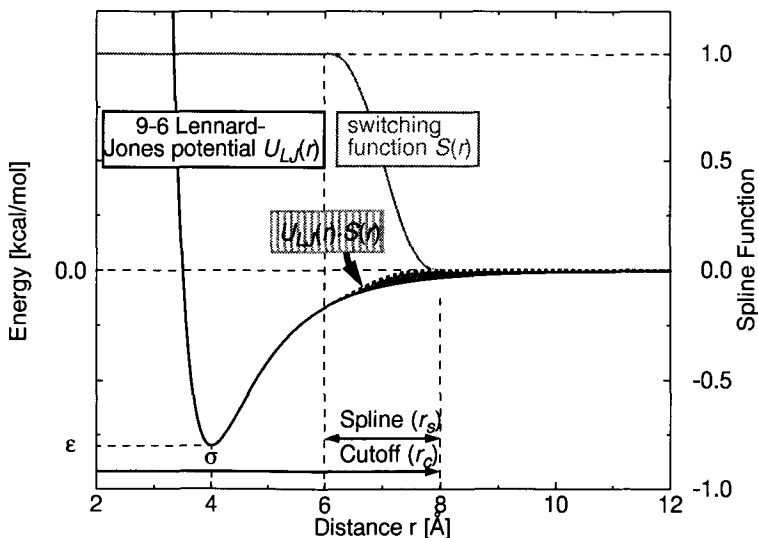
Figure 2.4:   Cutoff applied to a 9-6 Lennard-Jones potential (Cutoff = 8Å, Spline = 2Å)

the nonbonded interactions from their full values at $r_f = r_c - r_s$ to zero at r_c. The most common switching function is a quintic spline, defined by the conditions, that the first and second derivatives at r_f and r_c are zero and $S(r_f) = 1$ and $S(r_c) = 0$:

$$S(r) = c_0 + c_1 r + c_2 r^2 + c_3 r^3 + c_4 r^4 + c_5 r^5 \quad \text{with}$$

$$c_0 = r_c^3 \left(6r_c^2 - 15 r_c r_s + r_s^2 \right) / r_s^5$$

$$c_1 = -30 r_c^2 \left(r_c^2 - 2 r_c r_s + r_s^2 \right) / r_s^5$$

$$c_2 = 30 r_c \left(2 r_c^2 - 3 r_c r_s + r_s^2 \right) / r_s^5 \qquad (2\text{-}15)$$

$$c_3 = -10 \left(6 r_c^2 - 6 r_c r_s + r_s^2 \right) / r_s^5$$

$$c_4 = -15 \left(r_s - 2 r_c \right) / r_s^5$$

$$c_5 = -6 / r_s^5.$$

Even this smooth splining function causes considerable changes in the first and second derivatives of the interaction energy, which can lead to artifacts e.g. in the simulation of Ar-Crystals[a].

The cutting of the long-range interactions can be *atom-based* or *group-based*. If a cutoff is atom-based, the nonbonded interaction between two atoms is taken into account if the distance between the two atoms is smaller than the cutoff-distance. This check is made for every pair of atoms. Group-based algorithms perform the calculation of nonbonded interactions between two groups of atoms only if the two switching atoms are closer than the cutoff distance. If the groups of atoms are such, that the individual atomic charges sum up to zero, i.e. the group is neutral, the first term in the Coulombic energy potential is the dipole-dipole interaction, which is proportional to r^{-3} (chapter 2.1.3.4). Furthermore, the unphysical situation of having a net charge in the sphere of the cutoff is avoided by this procedure.

2.2.2.2 Tail Correction for Lennard-Jones Potentials

The attractive part of the Lennard-Jones interaction energy beyond a cutoff r_c is expressed by[Theodorou85a]

---

a. S. Santos, private communication (1996)

$$U_{tail} = \frac{1}{2} \sum_{\alpha=1}^{n} N_{\alpha} \sum_{\beta=1}^{n} \rho_{\beta} 4\pi \left[\int_{r_f}^{\infty} g_{\alpha\beta}(r) \, U_{LJ}^{\alpha\beta}(r) \, r^2 dr - \int_{r_f}^{r_c} g_{\alpha\beta}(r) \, U_{LJ}^{\alpha\beta}(r) \, S(r) \, r^2 dr \right]$$

(2-16)

where α and β run over all different forcefield-types of atoms, N_{α} denotes the number of atoms α and ρ_{β} the density of β atoms in the simulation cell. The volume element of the integration is a shell with a volume of $4\pi r^2 dr$ and $g_{\alpha\beta}$ is the pair distribution function of α and β (chapter 3.1.1).

Using a *m-n* Lennard-Jones interaction potential,

$$U_{LJ}^{\alpha\beta} = 4\varepsilon_{\alpha\beta} \left[\left(\frac{\sigma_{\alpha\beta}}{r} \right)^m - \left(\frac{\sigma_{\alpha\beta}}{r} \right)^n \right]$$

(2-8)

where $r = |r_{\beta} - r_{\alpha}|$, and the assumption, that $g_{\alpha\beta} \approx 1$ if $r > r_f$, the integration of the shaded area in Fig. 2.4 leads to

$$U_{tail} \approx \sum_{\alpha=1}^{n} N_{\alpha} \sum_{\beta=1}^{n} 8\pi\varepsilon \left[\frac{r_f^3}{3-n} \left(\frac{\sigma}{r_f} \right)^n - \frac{r_f^3}{3-m} \left(\frac{\sigma}{r_f} \right)^m - S(r_c, m) \left(\frac{\sigma}{r_c} \right)^m \right.$$
$$\left. + S(r_c, n) \left(\frac{\sigma}{r_c} \right)^n + S(r_f, m) \left(\frac{\sigma}{r_f} \right)^m - S(r_f, n) \left(\frac{\sigma}{r_f} \right)^n \right]$$

(2-17)

The integration at $r = \infty$ is zero only if $n,m > 3$ (this makes it impossible to use this method to estimate the long-range corrections for Coulombic interactions, which decay as $\frac{1}{r}$). The function $S(r,p)$ is defined by

$$S(r, p) = r^3 \left[\frac{c_0}{3-p} + \frac{c_1 r}{4-p} + \frac{c_2 r^2}{5-p} + \frac{c_3 r^3}{6-p} + \frac{c_4 r^4}{7-p} + \frac{c_5 r^5}{8-p} \right],$$

(2-18)

with the singular term ($\frac{c_n r^n}{n+3-p}$, with $n = p - 3$) replaced by $c_n r^3 \ln r$.

This energy expresses itself in forces that are all attractive, because at $r > r_{cutoff}$ the repulsive term is neglectable. To include this long-range effect, an external pressure is applied to the system, so that its energy contribution equals the tail correction energy:

$$p_{corr} V = U_{tail} \qquad p_{corr} = \frac{U_{tail}}{V}$$

(2-19)

The pressure p_{corr} is called the tail correction pressure. For dense polymeric systems and cutoffs of 8-9 Å, it is in the range of 500-2000 bar.

2.2.2.3 Tail Corrections for Coulombic Interactions

The long-range Coulombic interactions are far more difficult to deal with due to two reasons:

First, the Coulombic energy terms are farther-reaching than the van-der-Waals contributions; they decay as r^{-1} for monopole-monopole interactions and still as r^{-3} in the case of dipolar interactions, whereas the van-der-Waals energy drops as r^{-6}. The error introduced by cutting of the interactions at a relatively small distance of 8-10 Å is considerable.

Second, there are negative and positive interaction energies (attractive and repulsive forces) depending on the distribution of the monopoles or the mutual orientation of the dipoles. This prevents an integration of the neglected interactions as in Eq. (2-16) and leads to a quasi-random dependence of the coulombic energy from the cutoff distance (Fig. 2.5). This behavior is less pronounced for
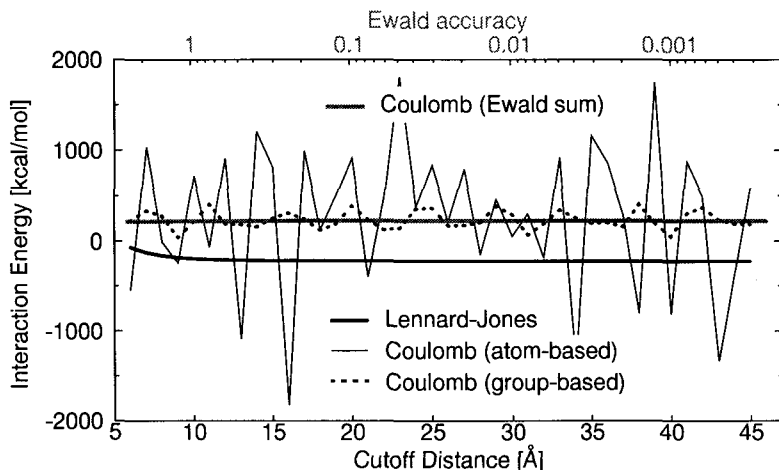
Figure 2.5: Dependence of the atom-based Lennard-Jones and Coulomb energies as a function of the cutoff distance. The Ewald sum as a function of the accuracy is plotted, too. (Cellulose-Iβ crystal, 16×16×21 Å size)

the group-based calculations than for the atom-based, but still too large to obtain reliable results for crystalline systems. Amorphous polymers with relatively small partial charges are not as problematic as the highly charged, dense polymer crystals of Cellulose, Nylon etc., which need special methods to deal with the long-range Coulombic interactions. One of the first of these methods, the Ewald summation, will be briefly discussed now:

For a cubic lattice (extension to general cell shapes is straightforward), with

N charges q_i in the simulation cell, the energy of the charge-charge interaction between all pairs of charges in the central cell and between the central cell and all surrounding cells is

$$U_{Coul} = \frac{1}{2} \sum_{|n| = 0}^{\infty} \sum_{i = 1}^{N} \sum_{j = 1}^{N} \frac{q_i q_j}{4\pi\varepsilon\varepsilon_0 |r_{ij} + n|} ; \qquad (2\text{-}20)$$

the position of a remote cell is given by the vector **n**. For **n**=0, the summation does not include terms, where $i=j$. The above sum is only *conditionally convergent*, i.e. the convergence rate is low and depends on the order of the summation of its terms.[Heyes81a]

The idea behind the Ewald summation is, that the sum in Eq. (2-20) is replaced by two sums with better convergence properties. One of the summations is carried out in real space, namely the summation of the original point charges plus a neutralizing charge distribution of equal magnitude and opposite sign (Fig. 2.6). The added charge distribution is compensated by the second
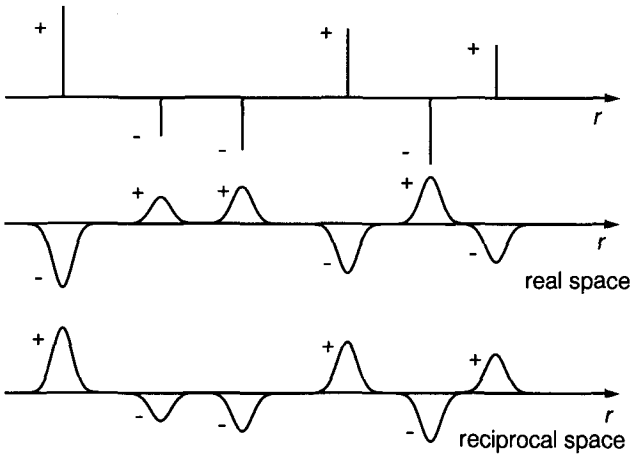
Figure 2.6: The point charges are surrounded by gaussian distributed charge clouds in real space, which are cancelled by charge clouds of opposite sign in the reciprocal space

summation, which adds up - in reciprocal space - a cancelling distribution of opposite sign. The distribution function is of minor importance, typically a Gaussian

$$\rho_i(\mathbf{r}) = \frac{q_i \kappa^3}{\pi^{3/2}} \exp\left(-\kappa^2 r^2\right)$$ (2-21)

A third term is necessary subtracting the self-interaction of each Gaussian in real space. The forth term finally takes into account that there is a medium with a permittivity ε beyond the cells taken into the summation. The final form of the Ewald summation looks as follows[Leeuw80,Leach96,Heyes81a].

$$U_{coul} = \frac{1}{2} \sum_{i=1}^{N} \sum_{j=1}^{N} \left\{ \begin{array}{l} \displaystyle\sum_{|\mathbf{n}|=0}^{\infty} \frac{q_i q_j}{4\pi\varepsilon_0} \frac{\text{erfc}\left(\kappa|\mathbf{r}_{ij}+\mathbf{n}|\right)}{|\mathbf{r}_{ij}+\mathbf{n}|} \\[2ex] + \displaystyle\sum_{k\neq 0} \frac{1}{\pi L^3} \frac{q_i q_j}{4\pi\varepsilon_0} \frac{4\pi^2}{k^2} \exp\left(\frac{-k^2}{4\kappa^2}\right) \cos\left(\mathbf{k}\cdot\mathbf{r}_{ij}\right) \\[2ex] - \frac{\kappa}{\sqrt{\pi}} \displaystyle\sum_{k=1}^{N} \frac{q_k^2}{4\pi\varepsilon_0} \\[2ex] + \frac{2\pi}{3L^3} \left| \displaystyle\sum_{k=1}^{N} \frac{q_k}{4\pi\varepsilon\varepsilon_0} r_k \right|^2 \end{array} \right.$$ (2-22)

The parameter κ of the convergence function $\text{erfc}(r,\kappa) = 1 - \text{erf}(r,\kappa) = 2/\sqrt{\pi} \int_x^\infty \exp\left(-t^2\right) dt$ and the Gaussian determines the number of terms in the real and reciprocal space summation: The smaller κ, the faster the reciprocal space calculations converges, whereas a large κ improves the convergence of the real space calculations. Optimization of κ is therefore necessary to minimize computation times[Karasawa89a]

For large systems, the Ewald summation is quite slow, since it scales as N^2. The *cell multipole expansion* exhibits a linear dependence on N and is therefore well suited for large systems with considerable partial charges. The idea of the method is to divide the central simulation cell into small cubic subcells of a few atoms and to compute the monopole, dipole and higher electric moments (Fig. 2.7). The interaction between the central cell and surrounding subcells is taken pairwise, if the distance between the central cell and the subcells is larger than the size of the subcells. For larger distances, the subcells are grouped into larger entities and their moments are added. With increasing distance, the influence of the larger cells becomes smaller and thus the error is kept at a more or less constant level.

Another way of taking the far reaching Coulomb terms into account is given by the *reaction field* method, where a sphere of the size of the cutoff radius is constructed around a dipole μ_i containing N atoms with a total dipole moment of
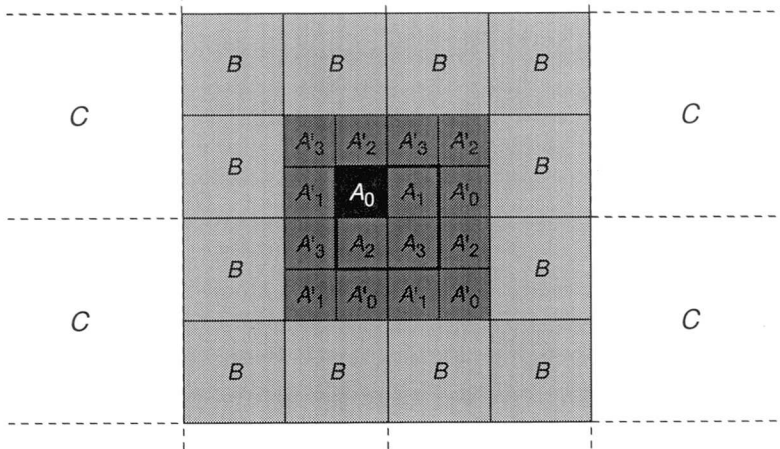
Figure 2.7:   Definition of hierarchical cells and division of the central cell A into smaller subcells
The cell B is made up from A_3, A_2, A_1 and A_0.

μ_j. This dipole induces an charge distribution in a surrounding dielectric ε_s, which in turn generates a reaction field $\mathbf{E}_i$. The interaction energy is thus $\mathbf{E}_i \mu_i$ with

$$\mathbf{E}_i = \frac{2\,(\varepsilon_s - 1)}{\varepsilon_s + 1} \left(\frac{1}{r_c^3}\right) \sum_{r_{ij} \leq r_c}^{N} \mu_i. \tag{2-23}$$

2.2.3   Introduction of Strain and Stress

The concept of a cell with PCCs allows the implementation of strains and stresses, which have already been discussed in chapter 1.

The finite strain of a cell $\mathbf{h}$ with respect to a reference cell $\mathbf{H}$ is given by

$$\eta = \frac{1}{2}\left[\mathbf{H}^{T-1}\mathbf{h}^T\mathbf{h}\mathbf{H}^{-1} - \mathbf{I}\right]. \tag{1-36}$$

and the finite stress by

$$\mathbf{t} = J\mathbf{H}\mathbf{h}^{-1}\tilde{\mathbf{P}}\mathbf{h}^{T-1}\mathbf{H}^T. \tag{1-46}$$

2.3   Energy Minimization Methods

2.3.1   Introduction

Once an energy representation of an atomistic system with N atoms is established, the total potential energy U, its gradient $\mathbf{g}$, and its second derivative $\mathbf{H}$ (the Hessian) as a function of the atomic coordinates $\mathbf{x}$ can be specified as

$$U = U(\mathbf{x}), \qquad \boldsymbol{g} = \nabla U_i = \frac{\partial U}{\partial x_i} \qquad \text{and} \qquad \boldsymbol{H} = \nabla^2 U_{ij} = \frac{\partial^2 U}{\partial x_i \partial x_j}. \qquad (2\text{-}24)$$

$U(\mathbf{x})$ forms a complicated hypersurface in $3N - 5$ dimensions, with maxima $(\boldsymbol{g}(\mathbf{x}_M){\approx}0,\ \boldsymbol{H}(\mathbf{x}_M){<}0)$, minima $(\boldsymbol{g}(\mathbf{x}_m){\approx}0,\ \boldsymbol{H}(\mathbf{x}_m){>}0)$ and saddle-points $(\boldsymbol{g}(\mathbf{x}_s){\approx}0,\ H_{ij}(\mathbf{x}_s){>}0,$ and $H_{kl}(\mathbf{x}_s){<}0)$. The minima are of special interest, because the system is most probably located at low energy conformations (Eq. (2-1)). This section therefore deals with numerical methods that minimize a high-energy structure. Except for the simulated annealing, all these methods just find the nearest local minimum, regardless how high its energy might be.
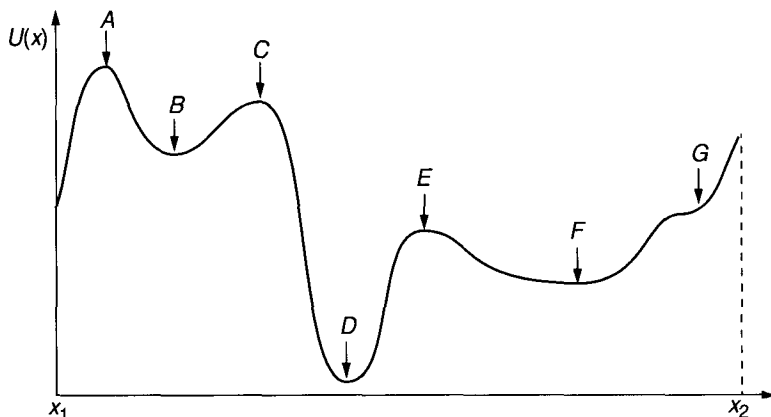
Figure 2.8: Extrema of a function of an arbitrary coordinate in an interval $[x_1, x_2]$. The minima B, D, and F consist of the local minima B and F and the global minimum D. A, C, and E are maxima with A being the global maximum and G is a saddle-point.

If, for example, the starting point of the minimization of the simple function in Fig. 2.8 lies between A and C, the high-energy, local minimum B will be the result of the numerical evaluation. Since this local minimum contributes nearly nothing to the average of Eq. (2-2), it would be of interest not only to find local minima but to specify the global minimum. Except for the smallest systems of a few atoms, the high dimensionality of the conformation space prohibits the necessary systematic search.

The minimization methods can be categorized by the order of the derivatives involved in the computation. There are simple methods that need only function evaluations, so-called zeroth-order algorithms, whereas more efficient ones require the computation of gradients (first-order) and the fastest, yet least robust ones demand the matrix of the second derivatives, the Hessian. In the last para-

graph (2.3.5) the method of simulated annealing is discussed, which tries to find the global minimum instead of a local one.

In general, all the methods summarized below do not find an exact minimum, but approach it more or less. From a numerical point of view, convergence is achieved, if the change in energy between successive steps is smaller than ε (the computer's floating point precision). This limits the exactness of the position of the atoms to about $\sqrt{\varepsilon}$.[Pressetal92]

2.3.2 Zeroth-order Algorithms

Zeroth-order algorithms rely only on direct function evaluations without the use of gradients or derivatives of higher order. They are therefore quite simple to program and efficient in memory usage. The most simple line search algorithm finds a minimum in a one-dimensional curve by bracketing and is used by first-order methods too. The more advanced simplex routine is able to find a local minimum in an M-dimensional conformation space, but will not be discussed here.

2.3.2.1 Line-search Algorithm

Consider a function of one variable and three initial points x_1, x_2 and x_3 given by Fig. 2.9. This function might well be a one-dimensional cross-section through a multidimensional hypersurface.
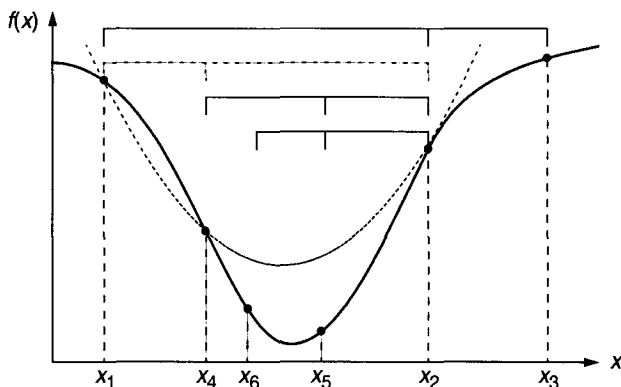
Figure 2.9: Bracketing the minimum of a one-dimensional function $f(x)$

Since the function value $f(x_2)$ is smaller than the neighboring $f(x_1)$ and $f(x_3)$, the minimum must be between x_1 and x_3. The bracketing algorithm now chooses a new point x_4 in this interval on one or the other side of x_2. If this new point is

smaller than x_2, the new interval lies between x_1 and x_2 (in the above figure). The same procedure is repeated at x_5 and x_6. If the function value at the new point is higher than the central value, the border of the interval is shifted to this new position, otherwise the new point becomes the central point and the border is moved to the former central point.[Pressetal92]

The optimal bracketing interval

$$\frac{x_3 - x_2}{x_3 - x_1} = \frac{x_4 - x_1}{x_2 - x_1} = ... = \frac{3 - \sqrt{5}}{2} \approx 0.38197 \qquad (2\text{-}25)$$

is the *golden section*.[Pressetal92] In case of an approximately harmonic function, the minimum can be found quite efficiently by fitting a parabola through the three bracketing points and placing the new trial point at the minimum of the parabola (Fig. 2.9). The exactness of the line search algorithm can be tuned by restrictions on the width of the bracketing interval or by using the fact that at the minimum, the local gradient g_{i+1} is normal to the line search direction h_i. Thus,

$$\left| g_{i+1} \cdot h_i \right| \leq -\sigma g_i \cdot h_i \qquad (2\text{-}26)$$

allows to control the precision of finding the minimum by varying σ: $\sigma=0$ enforces an exact search for the algorithm, whereas $\sigma>0$ produces a weak line search.[Harley86]

2.3.3 First-order Algorithms

These algorithms are widely used in atomistic simulations, because they combine robustness with efficiency and thus normally lead to well converged structures. The most straightforward method is the

2.3.3.1 Steepest Descent Method,

where the local gradient $\nabla U(\mathbf{x})$ is taken as the direction, in which a line search (section 2.3.2.1) is performed. The minimum of this one-dimensional cross-section is the new starting point $\mathbf{x}_n$ of the next iteration. At $\mathbf{x}_n$, the gradient $\nabla U(\mathbf{x}_n)$ is orthogonal to the initial gradient. This behavior can lead to slow convergence, if the potential energy surface forms a long narrow valley, in which the algorithm performs a zig-zag (Fig. 2.10).[MSIDiscover1]

At every step, part of the information obtained in the previous minimization is lost again due to an overcorrection of errors. This can be prevented by the

2.3.3.2 Conjugate Gradient Minimization

Here, the directions h_i and h_{i+1} of two successive line minimizations are not

Figure 2.10: Undesirable behavior of the steepest descent algorithm

orthogonal but form a conjugate set, with mutually orthogonal local gradients g_i. This is achieved by taking h_{i+1} as

$$h_{i+1} = g_{i+1} + \gamma_i h_i \qquad (2\text{-}27)$$

with

$$\gamma_i = \frac{g_{i+1} \cdot g_{i+1}}{g_i \cdot g_i} \qquad \text{(Polak-Ribiere)} \qquad (2\text{-}28)$$

or

$$\gamma_i = \frac{(g_{i+1} - g_i) \cdot g_{i+1}}{g_i \cdot g_i} \qquad \text{(Fletcher-Reeves)}. \qquad (2\text{-}29)$$

With the above set of line search directions h_i, the nearest local minimum of an energy function in M dimensions is reached exactly in M steps, if the function $U(x)$ has a quadratic form like

$$U(x) = U(P) + g(P) \cdot x + \frac{1}{2} x \cdot H(P) \cdot x, \qquad (2\text{-}30)$$

with P being at the origin of the coordinate system x. If the energy function is not exactly quadratic, repeated cycles of M line minimizations are necessary, but the convergence to the minimum is quadratic.

2.3.4 Second-order Algorithms

2.3.4.1 The Newton-Raphson Method

Taking Eq. (2-30), the gradient of $U(x)$ at x can be expressed as

$$g(x) = H(P) \cdot x - g(P). \qquad (2\text{-}31)$$

Using the fact, that at a local minimum the gradient $g(x_m)$ is zero, solving the equation

$$H(P) \cdot x_m = g(P) \qquad \Leftrightarrow \qquad x_m = H^{-1}(P) \cdot g(P) \qquad (2\text{-}32)$$

would lead immediately to the minimum of a quadratic energy function. For

anharmonic potentials, a number of iterations would be necessary, but convergence would be achieved quadratically.[Harley86]

However, this method has a number of drawbacks, which prevent a unmodified implementation. The second derivatives are sometimes difficult to compute and the full Hessian requires $O(M^2)$ memory, which can be prohibitive for large ($M{\approx}3N$ >1000) systems. Furthermore, the minimization can become unstable, if the forces (gradients) are large and the curvature (second derivative) is small, as is the case on the steep repulsive wall of a van-der-Waals potential. In this situation, a large step is computed, that may overshoots the minimum, leading to a divergent behavior.[MSIDiscover1]

However, if the gradients are already small and the system is of moderate size, the above Newton-Raphson method leads to a rapid convergence to an extremely precise minimum, as is needed for a vibrational normal mode analysis.

2.3.4.2 Quasi Newton-Raphson

The idea behind the quasi-Newton methods is it, to use an approximation **A** of the Hessian **H**. This approximation is by construction positive definite and symmetric, which is necessary if the solution of Eq. (2-32) should be descendent. Close to the minimum, **A** approaches the true Hessian **H**, and the fast convergence of the Newton-Raphson algorithm can be used.

Since the derivation of the matrix **A** is not straightforward, only the final result will be given here, details can be found in [Harley86]. With

$$\Delta \mathbf{x} = \mathbf{x}_{i+1} - \mathbf{x}_i \qquad \text{and} \qquad \Delta \boldsymbol{g} = \boldsymbol{g}_{i+1} - \boldsymbol{g}_i \qquad (2\text{-}33)$$

as the changes in coordinates and gradients between successive steps, the approximate matrix $\mathbf{A}_{i+1}$ is given in the DFP (Davidson, Fletcher, and Powell)-method by[Acton90]

$$\mathbf{A}_{i+1} = \mathbf{A}_i + \frac{\Delta \mathbf{x} \cdot \Delta \mathbf{x}^T}{\Delta \mathbf{x}^T \cdot \Delta \boldsymbol{g}} - \frac{\mathbf{A}_i \cdot \Delta \boldsymbol{g} \cdot \Delta \boldsymbol{g}^T \mathbf{A}_i}{\Delta \boldsymbol{g}^T \cdot \mathbf{A}_i \cdot \Delta \boldsymbol{g}}, \qquad (2\text{-}34)$$

and in the BFGS (Broyden, Fletcher, Goldfarb, and Shanno)-method by

$$\mathbf{A}_{i+1} = \mathbf{A}_i + \left(1 + \frac{\Delta \boldsymbol{g}^T \cdot \mathbf{A}_i \cdot \Delta \boldsymbol{g}}{\Delta \mathbf{x}^T \cdot \Delta \boldsymbol{g}}\right)\frac{\Delta \mathbf{x} \cdot \Delta \mathbf{x}^T}{\Delta \mathbf{x}^T \cdot \Delta \boldsymbol{g}} - \frac{\mathbf{A}_i \cdot \Delta \boldsymbol{g} \cdot \Delta \boldsymbol{g}^T \mathbf{A}_i}{\Delta \boldsymbol{g}^T \cdot \mathbf{A}_i \cdot \Delta \boldsymbol{g}}. \qquad (2\text{-}35)$$

In general, all minimization routines must be somehow terminated, because the

exact minimum can only be approximated with machine precision at best. It is either possible to monitor the energy decrease or the change in coordinates from one iteration to the next or to calculate the root-mean-square gradient,

$$RMS = \sqrt{\frac{g^T g}{3N}},$$ (2-36)

and to stop the computation if either of these values drops below a certain limit.

2.3.5 Simulated Annealing

All methods mentioned so far are only capable of finding the nearest local minimum. Except for molecular crystals, that have a limited number of local minima and eventually one deep global minimum, the high dimensionality of the conformation space especially of polymers makes it very improbable that the nearest local minimum is a global minimum or even just a 'good' minimum.

It is therefore necessary to search the conformation space for probable structures, i.e. structures of reasonably low energy. As the Boltzmann weight of a conformation depends exponentially on its energy E_i,

$$w_i = e^{\frac{-E_i}{kT}}$$ (2-1)

typically only a few of the many possible conformations are important for the ensemble average. But the energy of a minimum alone does not tell the whole truth: Comparing minimum D and F of Fig. 2.8 on p. 45, it is not *a priori* clear, which one has a larger weight, because the integral

$$w^{site} = \int\limits_{site} e^{\frac{-E(x)}{kT}} dx^M$$ (2-37)

may be larger for the interval E to x_2 (minimum F) than for the interval C to E (minimum D). It is therefore of interest to find the most probable conformations, not just the deepest minima. The necessary sampling of the conformation space is the topic of chapter 2.5, and just the principle idea of the so-called *simulated annealing* will be outlined here.[Otten89]

Annealing in metallurgy consists in a slow cooling down of a material from above melting temperature to low temperatures in order to equilibrate it. After annealing, the material is in a state of low internal energy. This process is simulated on the computer by starting a sampling procedure (Monte Carlo, Molecular Dynamics etc.) at a high temperature, where the conformation space is sampled

efficiently because the saddle-points between local minima are lower than the energy of the assembly. The temperature of the sampling procedure is gradually lowered, restricting the available conformation space to smaller and smaller volume. If the cooling process is sufficiently slow, the structure is able to reach a well equilibrated (= minimized at 0 K) state. This procedure can be used in a variety of problems, that are not tractable with other methods, the most famous of them being the travelling salesman (connection of randomly placed cities by a route of minimal length).[Harley86,Pressetal92]

2.4 Ensembles

The following section provides a short introduction to statistical mechanics, basically introducing the terminology and the concepts of relevance. More detailed descriptions can be found in standard textbooks like [McQuarrie76, Friedman85]

2.4.1 Introduction

In the computation of macroscopic properties from atomistic simulations – the domain of statistical mechanics – the concept of *phase space* is of prime importance. For a molecule of N atoms with a Lagrangian L (Eq. (2-62)), the classical phase space $\Gamma(\mathbf{q},\mathbf{p})$ contains $6N$ dimensions, $3N$ for the coordinates $\mathbf{q}_i$ and $3N$ for the conjugate momenta $\mathbf{p}_i = \partial L/\partial \dot{\mathbf{q}}_i$.[AllenTildesley89] The state of a molecule at a time t is completely described by these $6N$ *generalized coordinates*, which define a point $\Gamma(t)$ in the phase space. In the course of time, this point moves through phase space on a trajectory $\Gamma(t)$, governed by the *equations of motion*. These equations are different for the different *ensembles* that exist and link the macroscopic parameters of the system as a whole with the regions of the phase space accessible to the molecule. An ensemble is a set of points in phase space that obey certain restrictions, e.g. the volume of the unit cell is the same or the kinetic energy follows a Boltzmann distribution. Relevant ensembles will be shortly introduced in section 2.4.3.

The above description was based on classical mechanics, where the phase space is continuous. The atomistic systems described here obey, in principle, the laws of quantum mechanics and thus the phase space is not continuous, but is made up of a countably infinite set of quantum states. In the following discussion it is assumed that the classical and the quantum mechanical representation can be both used interchangeably.

2.4.2   The Ergodic Hypothesis and the Liouville Theorem

The ergodic hypothesis is of central importance for the molecular dynamics and Monte Carlo sampling methods (chapter 2.5). It states that the set of ensemble points in phase space compliant with the restrictions posed by the different ensembles can be obtained by following the trajectory of one initial point. It is now possible to replace the ensemble average of Eq. (2-40) by a time average. An exact average, however, is only obtained for infinitely long trajectories that sample all relevant parts of the phase space. This is not *a priori* given and can not be proved rigorously: The phase space is maybe such that trajectories form closed loops or remain trapped for a very long time in a region surrounded by narrow saddle points.[AllenTildesley89]

The points in phase space belonging to an ensemble have a density $\rho(\mathbf{q},\mathbf{p},t)$ in the phase space volume $d\mathbf{q}\,d\mathbf{p}$ around $\mathbf{q},\mathbf{p}$. The Liouville equation[McQuarrie76],

$$\frac{\partial \rho}{\partial t} + \sum_{j=1}^{3N}\left(\frac{\partial \rho}{\partial p_j}\right)\dot{p}_j + \sum_{j=1}^{3N}\left(\frac{\partial \rho}{\partial q_j}\right)\dot{q}_j = 0\,, \tag{2-38}$$

which is equivalent to

$$\frac{d\rho}{dt} = 0\,, \tag{2-39}$$

conserves the density of these phase space points as they move along their trajectories. This is equivalent to the statement, that the size (but not necessarily the shape) of the volume element $d\mathbf{q}\,d\mathbf{p}$ in phase space remains constant.

2.4.3   Relevant Ensembles

2.4.3.1   Microcanonical (*Eh*N-)Ensemble[a]

This ensemble is equivalent to a container with solid, thermally insulating walls (e.g. a dewar), because the number of particles N, the shape of the simulation cell **h** and the energy E are kept fixed during the simulation. The temperature, on the other hand, is allowed to fluctuate during the simulation around a constant mean value, because only the sum of the potential and the kinetic energy remains constant. This ensemble is actually the microcanonical ensemble, which is commonly denoted as *NVE*-ensemble, neglecting the difference between constant shape and constant volume.[Ray84a]

---

a. Throughout this work, the notation found in Ref. [GrabenRay93] and [Ray88a] was used

2.4.3.2 Canonical (*ThN*-)Ensemble

If an experiment is performed in a container with heat conducting walls and the container is immersed in a bath of constant temperature *T*, the phase space points are distributed according to the canonical ensemble. Commonly, this ensemble is denoted *TVN*-ensemble (see the remark in the previous paragraph).

2.4.3.3 Constant Stress-Constant Temperature (*TtN*-)Ensemble

A solid body at a constant external thermodynamic tension **t** (quite often $t_{ext}=0$) and constant temperature *T* belongs to the *TtN*-ensemble. Since this is a common state of solids, most of the simulations of this work were carried out in this ensemble.

2.4.3.4 Other ensembles

In total, there exist eight commonly used ensembles, which are depicted in
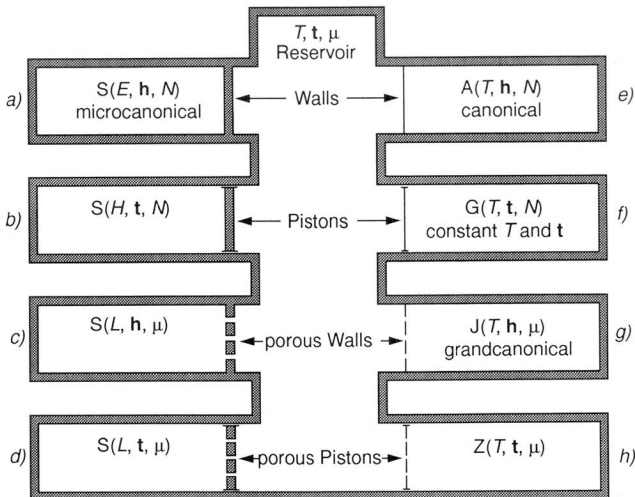
Figure 2.11: Eight thermodynamic ensembles, that are in contact with a temperature, pressure and chemical potential reservoir. Ensembles on the left are adiabatically insulated, those on the right are in thermal contact with the reservoir

Fig. 2.11 [GrabenRay93]. For all these ensembles, sampling methods have been devised. The microcanonical, canonical, and constant temperature - constant stress ensemble have already been introduced. Of importance in simulations is furthermore the grandcanonical ensemble, which allows changes in the number of particles to keep the chemical potential constant.[Panagiatopoulos87]

2.4.4   The Partition Function

The relationship between an arbitrary microscopic property A, which can be expressed as a function of the generalized coordinates $A(\Gamma)$, and its macroscopic observable A_{obs} is given simply by

$$A_{obs} = \langle A(\Gamma) \rangle_{ens},\qquad(2\text{-}40)$$

where $\langle\ \rangle_{ens}$ denotes the ensemble average of $A(\Gamma)$. This ensemble average as well as the observable property are different for the different ensembles. Using the principle of a priori equal probabilities[McQuarrie76], the average for the canonical ensemble is given by (Eqs (2-1) and (2-2))

$$\langle A \rangle_{ThN} = \frac{\sum_{\Gamma} A(\Gamma) e^{-\frac{H(\Gamma)}{kT}}}{\sum_{\Gamma} e^{-\frac{H(\Gamma)}{kT}}},\qquad(2\text{-}41)$$

with a denominator

$$Q_{ThN} = \sum_{\Gamma} e^{-\frac{H(\Gamma)}{kT}} \approx \frac{1}{N!}\frac{1}{h^{3N}}\int e^{-\frac{H(\mathbf{q},\,\mathbf{p})}{kT}}\,d\mathbf{q}\,d\mathbf{p}\qquad(2\text{-}42)$$

called the *(canonical) partition function.* The second approximate equality is the classical description of the partition function in the continuous phase space. The leading quantum correction $Q_{\text{quantum mechanical}} - Q_{\text{classical}}$ is small for high temperatures and weak interactions.[Friedman85]

Since, for a system obeying classical statistics, the Hamiltonian H (in cartesian coordinates) can always be written as the sum of kinetic ($\mathbf{p}$-dependent) and potential ($\mathbf{q}$-dependent) contributions, the partition function factorizes into a product of kinetic (ideal gas) and potential (excess) parts[AllenTildesley89]:

$$Q_{ThN} = \frac{1}{N!}\frac{1}{h^{3N}}\int e^{-\frac{K(\mathbf{p})}{kT}}\,d\mathbf{p}\int e^{-\frac{U(\mathbf{q})}{kT}}\,d\mathbf{q} = Q^{id}_{ThN}Q^{ex}_{ThN}.\qquad(2\text{-}43)$$

Instead of the excess partition function Q^{ex}_{ThN}, often, the *configuration integral*

$$Z = V^{N}Q^{ex}_{ThN} = \int e^{-\frac{U(\mathbf{q})}{kT}}\,d\mathbf{q}\qquad(2\text{-}44)$$

is computed in a configuration-space MC simulation and the ideal gas properties are added onto the results afterwards.

In the microcanonical ensemble, the energy is constant and each point has therefore equal weight. The partition function is simply the number of micro-scopic instances of the property A, provided the energy $E(\Gamma)$ of the microstate is exactly E:

$$Q_{EhN} = \sum_{\Gamma} \delta(E(\Gamma) - E) \approx \frac{1}{N!}\frac{1}{h^{3N}}\int \delta(E(\mathbf{q},\mathbf{p}) - E)\, d\mathbf{q}\, d\mathbf{p}. \qquad (2\text{-}45)$$

The partition functions of the isothermal-isobaric ensem-ble,[AllenTildesley89]

$$Q_{ThN} = \sum_{\Gamma}\sum_{h} e^{-\frac{tr(t\eta)}{kT}} e^{-\frac{E(\Gamma)}{kT}} \approx \frac{1}{N!}\frac{1}{h^{3N}}\frac{1}{\|h_0\|}\int e^{-\frac{tr(t\eta)}{kT}}\, d h\int e^{-\frac{E(\mathbf{q},\mathbf{p})}{kT}}\, d\mathbf{q}\, d\mathbf{p} \qquad (2\text{-}46)$$

and the grand-canonical ensemble,

$$Q_{Th\mu} = \sum_{\Gamma}\sum_{N} e^{\frac{\mu N}{kT}} e^{-\frac{E(\Gamma)}{kT}} \approx \sum_{N} \frac{1}{N!}\frac{1}{h^{3N}} e^{\frac{\mu N}{kT}}\int e^{-\frac{E(\mathbf{q},\mathbf{p})}{kT}}\, d\mathbf{q}\, d\mathbf{p}, \qquad (2\text{-}47)$$

can be obtained from the canonical partition function Q_{ThN} directly with the aid of Legendre transformations.[GrabenRay93]

The partition function and its temperature derivative are of interest, because all macroscopic thermodynamic properties can be derived from it, as the following equations show for the canonical ensemble: [ReedGubbins73]

$$U = kT^2\left(\frac{\partial \ln Q}{\partial T}\right)_{V, N_\alpha} \qquad\qquad \text{a)}$$

$$p = kT\left(\frac{\partial \ln Q}{\partial V}\right)_{T, N_\alpha} \qquad\qquad \text{b)}$$

$$H = kT^2\left(\frac{\partial \ln Q}{\partial T}\right)_{V, N_\alpha} + kTV\left(\frac{\partial \ln Q}{\partial V}\right)_{T, N_\alpha} \qquad \text{c)}$$

$$C_v = \left(\frac{\partial U}{\partial T}\right)_{V, N_\alpha} \qquad\qquad \text{d)}$$

$$C_p = \left(\frac{\partial H}{\partial T}\right)_{p, N_\alpha} \qquad\qquad \text{e)} \qquad\qquad (2\text{-}48)$$

$$S = k\ln Q \qquad\qquad \text{f)}$$

$$A = -kT\ln Q \qquad\qquad \text{g)}$$

$$G = -kT\ln Q + kTV\left(\frac{\partial \ln Q}{\partial V}\right)_{T, N_\alpha} \qquad \text{h)}$$

$$\mu_\alpha = -kT\left(\frac{\partial \ln Q}{\partial N_\alpha}\right)_{T, V, N_{\beta\neq\alpha}} \qquad\qquad \text{i)}$$

Similar relations exist for the other ensembles. Except for the smallest systems, it is, however, not possible to evaluate the partition function analytically or numerically, because the high dimensionality ($O(10^2$-$10^4)$) of typical simulations prevents a systematic sampling of the phase space. It is therefore necessary to use specialized sampling methods (chapter 2.5)

2.4.5 Equipartition of the Hamiltonian

For any two degrees of freedom x_i, x_j of a system with a Hamiltonian H, it can be shown [Pathria72] that

$$\left\langle x_i \frac{\partial H}{\partial x_j} \right\rangle = \delta_{ij} kT. \tag{2-49}$$

If H (the sum of the kinetic and potential energy) is of a quadratic form[McQuarrie76]

$$H(p_1, p_2, ..., q_s) = \sum_{i=1}^{m} a_i p_i^2 + \sum_{j=1}^{n} b_j q_j^2 + H(p_{m+1}, ..., p_s, q_{n+1}, ..., q_s), \tag{2-50}$$

each of the harmonic degrees of freedom contributes $\frac{1}{2}kT$ to the average energy of the system. The theorem is also valid if the 'constants' a_i and b_j are functions of the coordinates and momenta $p_{m+1},...,p_s,q_{n+1},...,q_s$ not involved in the quadratic terms.

2.5 Sampling Methods

The sampling procedure stands in the center of every atomistic simulation. Specification of the force field, the simulation cell, and the ensemble (i.e. the macroscopic variables that are constant) allows the computation of the energy and, if necessary, of the forces acting on the atoms in the simulation. Using one of the subsequently described methods, the phase space of the system can be explored and thermodynamical and mechanical properties can be calculated afterwards from microscopic configurations.

Basically, there are two different methods to sample the phase space. The more intuitive way is maybe molecular dynamics (MD), which solves the equations of motion compliant with the ensemble being used and tries thus to mimic nature. A more abstract, but equivalent, way is to generate conformations in a more or less random fashion and to select those that fit into the chosen ensemble. Due to the randomness in the generation process, this method is termed Monte Carlo.[Metropolis49]

2.5.1 Monte Carlo

As pointed out in chapter 2.4.4, the classical partition function in cartesian coordinates can be split into a term depending on the momenta, which is known from kinetic gas theory, and a term that depends solely on the coordinates **q** - the configurational integral - the approximate computation of which is the task of the MC algorithm.

2.5.1.1 Simple sampling

The most straightforward way to integrate (2-44) would be the use of a equispaced grid spanning the whole configuration space. Since the total number of points equals p^{3N}, p giving the number of grid points in one dimension and N the number of atoms, this method is impractical except for the smallest molecules. Furthermore, virtually all grid points would lay in areas of the phase space where the interaction energy is so high that the Boltzmann factor almost vanishes.

The same inefficiency can be observed, if the points in phase space are chosen at random rather than on a grid. In dense atomic systems, a fraction of only about 10^{-260} of all points makes significant contributions to the conformational integral.[Frenkel96]

It would be much better to chose the phase space points with a probability corresponding to their Boltzmann factor and to weight them evenly instead of selecting them with equal probability and to weight them afterwards. This is the fundamental concept of *importance sampling*.

2.5.1.2 Importance sampling

Given a distribution ρ of N states (Fig. 2.12) with a set of transitions π
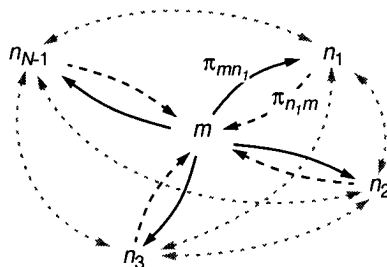
Figure 2.12: Transition probabilities between N (= 5) different states

between all possible states. In particular, π_{mn_i} denotes the transition probability

to go from state m to state n_i and $\pi_{n_i m}$ the probability of going from n_i to m. The transition probabilities form a $N \times N$ matrix whose rows add to one. The number density of state i is given by

$$\rho_i = \frac{M_i}{M},\qquad\qquad (2\text{-}51)$$

where M_i is the number of systems that are in state (configuration) i out of an ensemble of $M \gg N$ configurations. In thermodynamic equilibrium, the number densities are distributed according to their Boltzmann factors:

$$\rho_i \propto e^{-\frac{H(\mathbf{q}_i)}{kT}}.\qquad\qquad (2\text{-}52)$$

Starting with a given density ρ_{old}, the new number densities ρ_{new} can be evaluated by matrix multiplication as

$$\rho_{new} = \rho_{old}\pi.\qquad\qquad (2\text{-}53)$$

It is required that the limiting distribution resulting from repetition of (2-53) equals the one given by (2-52). This is fulfilled, if the sum of all transitions from, say, state m to the other states n_i (solid lines in Fig. 2.12) equals the transitions from these states to m (dashed lines in Fig. 2.12),

$$\sum_i \rho_m \pi_{mn_i} = \sum_i \rho_{n_i} \pi_{n_i m}.\qquad\qquad (2\text{-}54)$$

In normal simulations, this sufficient condition is replaced by the unnecessarily strong requirement of *detailed balance* of all possible transitions,

$$\rho_m \pi_{mn_i} = \rho_{n_i} \pi_{n_i m}.\qquad\qquad (2\text{-}55)$$

The transition probability π_{mn} is the product of a probability α_{mn} to attempt to change the configuration from m to n and a probability a_{mn} to accept this move,

$$\pi_{mn} = \alpha_{mn} \cdot a_{mn}.\qquad\qquad (2\text{-}56)$$

Assuming a symmetric underlying matrix α, the acceptance probability[Metropolis53]

$$\begin{aligned} a_{mn} &= 1 & \rho_n \geq \rho_m \\ a_{mn} &= \frac{\rho_n}{\rho_m} & \rho_n < \rho_m \end{aligned},\qquad\qquad (2\text{-}57)$$

is able to generate with a Markov[a] chain a set of canonically distributed configu-

rations.[Binder92b] Although there are other solutions to Eq. (2-55),[AllenTildesley89] Eq. (2-57) - known as the asymmetrical Metropolis solution - is the most common one. Averages obtained from transition matrices such as (2-57) differ from the true canonical average by a term $O(n_{steps}^{-1/2})$.

The asymmetrical Metropolis solution shown above is equivalent to accepting a trial move with a probability of $\exp\left(\frac{-\Delta H}{kT}\right)$. In a practical simulation, a random number η is drawn from the interval $(0,1)$ and the move is accepted if

$$\eta \leq e^{-\frac{\Delta H_{mn}}{kT}}. \tag{2-58}$$

It is of great importance to use reliable random number generators not only for the acceptance step, but also for all different kinds of moves presented in the next section. A short discussion of the random number generators used in this work is therefore given in Appendix C.

For ensembles other than the canonical, the same acceptance probability can be used as above, but the Hamiltonian in the evaluation of the number densities is different. In the TtN ensemble, for example, the configurational Hamiltonian is[AllenTildesley89]

$$H_{TtN} = U(\mathbf{q}) + V_0 \text{tr}(\mathbf{t}\eta) + kTN\ln V, \tag{2-59}$$

the last term correcting for the fact that different volumes are sampled and thus the kinetic configurational part is different for each point contributing to the ensemble. Alternatively, the momenta can be included explicitly.[Lill92a]

2.5.1.3 Umbrella Sampling

Figure 2.13 shows the distribution of the cell edge length in the c-direction during the last 500 ps of a 1 ns $T\sigma N$-simulation of a PP crystal (chapter 4.3). The quantity of interest is the width of the cell edge length distribution, since it is proportional to the compliance in this direction. In contrast to the mean value, the width converges rather slowly, because it is more dependent on the tails of the distribution. The tails of the distribution, however, are only rarely sampled by the MD algorithm, which weights the individual conformations according to their Boltzmann weights. Normally, MC samples the phase space in the same manner, but it needn't necessarily do so. A number of schemes have been devised to

---

a. (A Markov chain is a sequence of trial moves that satisfies two conditions:
  - The outcome of each trial belongs to a finite set of outcomes $\{m,n_1,...,n_{N-1}\}$, called the state space
  - The outcome of each trial depends only on the outcome of the trial that immediately precedes it.)
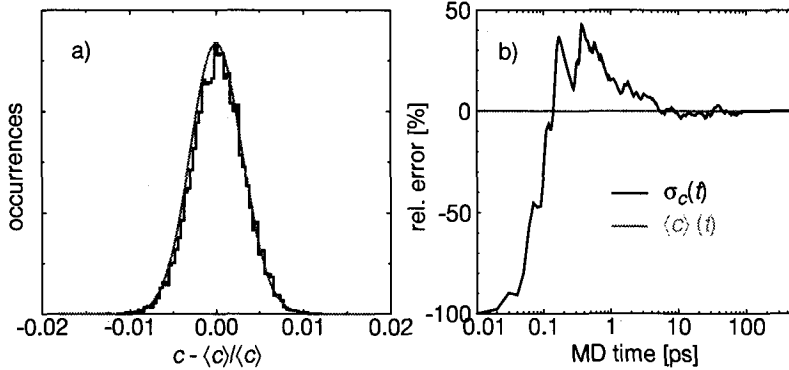
Figure 2.13: a) Distribution of the cell edge vector c during the last 500 ps of a 1 ns $T\sigma N$-MD run of a PP crystal at 300 K (black line) and fitted gaussian distribution (gray); b) relative error of the mean (grey line) and the standard deviation (black) as a function of time

introduce a bias - that needs to be removed in the averaging process - which enhances the probability of accepting configurations at the tails.[AllenTildesley89] The one-half umbrella sampling algorithm used in this work originates from Lee and Scott[Lee80a] and accepts a new MC conformation if

$$\eta \le W(\Delta U_{mn}) \, e^{-\frac{\Delta U_{mn}}{kT}} , \qquad (2\text{-}60)$$

where h is a random number in the interval [0,1] and $W(\Delta U_{mn}) = e^{-\frac{\Delta U_{mn}}{2kT}}$. The correct averages are computed from the weighted ones by

$$\langle A \rangle_0 = \frac{\langle A/W \rangle_W}{\langle 1/W \rangle_W} . \qquad (2\text{-}61)$$

2.5.1.4 Monte Carlo Moves

Up to now the structure of the underlying matrix α, the probability of attempting a move, has not been specified, except that it should be symmetric. It is the great advantage (and difficulty) of the Monte Carlo method that this matrix can be chosen with great freedom, allowing all kinds of moves in a variety of ensembles.

In principle, the moves performed by α should be ergodic, i.e. any state n should be reachable from any state m by an (infinite) number of steps. In practice, the choice of α is a compromise between the necessity to sample a representative part of the configurational space with a finite number of steps and the desire to obtain a statistically sufficient number of configurations. The first argu-

ment requires large moves, that quickly decorrelate the structure and the second one demands a certain fraction of accepted moves. Typically, the stepwidth is chosen such that an acceptance ratio of about 50% is obtained. There is evidence, however, that lower acceptance ratios often lead to better performance.[Frenkel96,Leontidis94a,AllenTildesley89]

It is beyond the scope of this work to discuss the nearly numberless types of moves that have been created for all kinds of problems. A good overview can be found in [Widmann96a,Leontidis94a,Binder92a] and references therein. In the simulation of dense polymeric systems, the simple scheme of randomly changing any degree of freedom leads only to a slow sampling of the phase space. A number of other techniques have therefore been developed[Leontidis94a], some of which are mentioned now, neglecting coarse-grained lattice models, which operate on other time- and length-scales.

As already mentioned, the *simple random change* of one (local move) or all degrees of freedom simultaneously (global move) exhibits poor efficiency in equilibrating dense polymer structures. For systems of individual atoms or small molecules, local moves make better use of computational effort than global updates of the coordinates. In the case of dense polymers, the situation is reversed. Due to the dense packing and entanglement of the chains, global changes of the configuration seem to be more efficient in finding a way through bottlenecks in phase space.[Forrest94a]

The *reptation* of chain molecules by one or several repeat units yields a good equilibration for chains of relatively short length. If the molecules are longer or contain bulky side groups, cage effects reduce the acceptance ratio unacceptably or lead to a stationary vibration of the chain due to forth and back moves.

A similar algorithm is *Continuum-Configurational-Bias Monte Carlo* (CBMC), in which a polymer chain is cut at a randomly chosen segment and rebuilt in a step-wise fashion. At each step, the Boltzmann weight of a number of torsion angles is computed and one of the angles chosen proportional to its weight. This bias has to be removed at the end of the regrowth process by comparing the statistical weight of the old and the new changed part of the chain.

The *Concerted-Rotation* method tries to move four segments in the middle part of the chain by changing a torsion angle while holding all other segments constant. This requires to solve a set of constraint equations numerically and to compute the Jacobian of the transition from the torsion angle space to the space of the constraint equations in order to achieve detailed balance.

A similar algorithm is used by the *Variable-Connectivity* method to create bridges between different molecules. Therefore, a distribution of chain lengths is

generated and the simulation samples the semigrand ($NnPT\mu^*$) ensemble.[Pant95a]

A new, yet unpublished idea is the *Parallel-Rotation*, in which a driver angle and three dependent torsion angles are used to shift the remaining part of the polymer chain parallel to itself.[a]

All the above methods, however, change the polymer matrix only locally. As already stated, it would be advantageous to update the degrees of freedom globally. Hybrid Monte Carlo methods use short MD runs to create new configurations and apply a Metropolis criterion to accept or reject them. Before presenting shortly this approach, the MD method will be introduced.

2.5.2 Molecular Dynamics

2.5.2.1 Equations of Motion

The Lagrangian L of a system of N particles is its kinetic minus its potential energy[Landau86b]

$$L = K(\dot{\mathbf{q}}) - U(\mathbf{q}) , \tag{2-62}$$

where $\mathbf{q}$ and $\dot{\mathbf{q}}$ are the $n = 3N$ generalized coordinates and n generalized velocities.

Applying the *principle of least action*, the *equations of motion* are obtained as

$$\frac{d}{dt}\left(\frac{\partial L}{\partial \dot{q}_i}\right) - \frac{\partial L}{\partial q_i} = 0 \qquad i = 1, 2, ..., n . \tag{2-63}$$

Integration of these equations allows to propagate the system through the phase space.

Depending on the ensemble (i.e. fixed macroscopic variables) the Lagrangian has a different form. Two examples, the microcanonical (EhN) and the isothermal-isotension (TtN)-ensemble, are given. The microcanonical ensemble is the natural ensemble of MD (as the canonical is for MC), while the TtN-ensemble is the one, in which most of the simulations presented in this work were carried out.

The Lagrangian of the *microcanonical ensemble* is just

$$L_{NhE} = \frac{1}{2}\sum_{i,k} a_{ik}(\mathbf{q})\,\dot{q}_i\dot{q}_k - U(\mathbf{q}) = \sum_{\alpha}^{N}\frac{p_{\alpha}^2}{2m_{\alpha}} - U(\mathbf{r}) . \tag{2-64}$$

---

a. S. Santos, private communication (1996)

The first equality is valid for arbitrary generalized coordinates and velocities, the second only for cartesian coordinates, a_{ik} is a function of the coordinates $\mathbf{q}$ only and m_α and p_α are the mass and the momentum of atom α, respectively. Deriving the equations of motion from the second equality, one obtains

$$\frac{1}{m_\alpha}\frac{dp_\alpha}{dt} = -\frac{\partial U}{\partial \mathbf{r}_\alpha} \qquad \Leftrightarrow \qquad m_i\ddot{r}_i = F_i, \qquad (2\text{-}65)$$

exactly Newton's equations of motion.

In case of the TtN-ensemble, the Lagrangian in cartesian coordinates is much more complicated:[Lill93a]

$$\tilde{L}_{TtN} = \sum_\alpha^N \frac{{\pi'}^{(\alpha)^T}\mathbf{g}^{-1}{\pi'}^{(\alpha)}}{2m^{(\alpha)}s^2} - U(\mathbf{r}) + \frac{\mathrm{Tr}\left(\Omega'^T\Omega'\right)}{2Ws^2} - V_0\mathrm{Tr}\,(t\eta) + \frac{\theta^2}{2Q} - nkT\ln s, (2\text{-}66)$$

where the first term expresses the kinetic energy of the particles as a function of their scaled, virtual momenta ${\pi'}^{(\alpha)} = \mathbf{h}^T\mathbf{p}^{(\alpha)}/s$ and the metric tensor $\mathbf{g}$ (Eq. (A-14)). $U(\mathbf{r})$ is the potential energy, that depends only on the interparticle distances. The kinetic energy of the simulation cell is given by the third term. Ω' is the virtual momentum (Ω/s) and the parameter W has the dimension of mass and governs the coupling between the net pressure and the rate, with which the cell changes its shape. The fourth term is the potential energy of the elastically deformed cell, with the thermodynamic tension $\mathbf{t}$ given by Eq. (1-41) and the strain η by Eq. (1-36). The volume V_0 is given by $V_0 = |\mathbf{H}|$, the determinant of the reference cell shape $\mathbf{H}$. The third and fourth term together form an additional degree of freedom, originally introduced by Parrinello and Rahman.[ParrinelloRahman81a] The fifth and sixth term are the kinetic and potential energy of a similar additional degree of freedom with coordinate s and mass Q and a conjugate momentum θ originating from the Nosé-Hoover thermostat.[Nose84a,Nose84b,Nose91a] (Note the difference between the coordinate s of the Nosé-Hoover thermostat and the scaled coordinates $\mathbf{s}_\alpha$.)The quantity n denotes the number of degrees of freedom ($3N+3$). The Lagrangian is tilded, because a term $m^{(\alpha)}\dot{\mathbf{h}}\mathbf{s}^{(\alpha)}$, which is considered to be small, was neglected in the expression of the particle momentum in a fluctuating cell.[Ray84a]

The equations of motion are obtained as described above; transforming them to physical time introduces a thermodynamic friction ξ[Hoover85a] into the atomic and lattice dynamics:[Lill93a]

$$\dot{s} = \xi s \tag{a}$$

$$\dot{\xi} = \frac{1}{Q}\left[\sum_{\alpha}^{N} \frac{\pi_i^{(\alpha)} \mathbf{g}_{ij}^{-1} \pi_j^{(\alpha)}}{m_\alpha} + \frac{\Omega_{ij}\Omega_{ij}}{W} - nkT\right] \tag{b}$$

$$\dot{\mathbf{s}}_i^{(\alpha)} = \frac{\mathbf{g}_{ij}^{-1} \pi_j^{(\alpha)}}{m_\alpha} \tag{c}$$

$$\dot{\pi}_i^{(\alpha)} = \sum_{\alpha}^{N;\alpha \neq \beta} \left[-\frac{1}{r_{\beta\alpha}}\frac{\partial U}{\partial r_{\beta\alpha}}\right]\mathbf{g}_{ij}(\mathbf{s}_\beta - \mathbf{s}_\alpha)_j - \xi\pi_i^{(\alpha)} \tag{d}$$

$$\mathbf{J}_{ij} = \frac{\Omega_{ij}}{W} \tag{e}$$

$$\dot{\Omega}_{ij} = (\mathbf{P} - \Pi)_{ik}|\mathbf{h}|\mathbf{J}_{jk}^{-1} - \xi\Omega_{ij} \tag{f}$$

$$\Omega_{ij}^s = \frac{1}{2}\left[\Omega_{ip}\mathbf{J}_{pk}^{-1} + \Omega_{kp}\mathbf{J}_{pi}^{-1}\right]\mathbf{J}_{kj} \tag{g}$$

$$\Pi_{ij} = -\frac{1}{|\mathbf{J}|}\left[\delta_{ij}(\mathbf{t}_{kp}\eta_{kp}) + \mathbf{J}_{ki}^{-1}\mathbf{t}_{kp}\mathbf{J}_{jp}\right] = -\left[\delta_{ij}(\sigma_{kp}\mu_{kp}) + \mathbf{J}_{ki}^{-1}\mathbf{J}_{kp}^{-1}\sigma_{pj}\right] \tag{h}$$

(2-67)

The internal virial pressure **P** is defined by Eq. (1-47), Π is the effective external pressure, and σ the stress imposed on the system. The strain μ is defined as $\mu_{ij} = \frac{1}{2}\left(\delta_{ij} - \mathbf{J}_{ki}^{-1}\mathbf{J}_{kj}^{-1}\right)$.

Bulgac and Kosnezov[Bulgac90a] found that it is sufficient to control the ratio of two quantities to achieve a constant temperature condition and the canonical distribution. Since any pair of quantities, the ratio of whose canonical ensemble averages is kT, could be chosen, the Lagrangian of Eq. (2-66) is only one of many possible representations of a TtN-ensemble.

2.5.2.2 Manostats

Equation (2-67-f) describes the relation between the change in the cell momentum and the difference between the internal stress **P** and the external stress Π, which is defined by Eq. (2-67-h). To prevent an unphysical rotation of the cell, its momentum tensor is symmetrized by Eq. (2-67-g).

The Parrinello-Rahman algorithm produces a canonical distribution if the step-width of the integration is infinitely small. However, at finite step-sizes the average of the actual stress during a simulation is always lower than the target stress, as can be seen in Table 2-2. This deviations become very large with increasing time-step, making simulations of fully flexible polymeric systems with a stepwidth larger than about 0.5 fs questionable.

The above equations of motion let the cell change its volume and shape without restrictions. For structures far from mechanical equilibrium, this can lead

Table 2-2: Average stress components of a simulation using a Parrinello-Rahman manostat at $T = 300$ K (PA-12 structure of 1038 atoms with a tail correction pressure of 1110 bars, equilibrated by 1 ns of 7tN-MD, averages from 50 ps of 7tN-MD with new velocities). At a stepsize of 2 fs, the simulation became unstable and crashed.

Δt [fs]	σ_{xx}	σ_{yy}	σ_{zz}	σ_{yz}	σ_{xz}	σ_{xy}
0.1	-1107	-1088	-1100	1.6	-9.5	6.0
0.2	-1090	-1100	-1092	0.4	3.8	10.0
0.5	-1021	-1003	-1003	2.0	4.0	0.8
1.0	-739	-713	-696	-10.2	-1.3	2.0
1.5	-336	-322	-263	16.7	3.3	27.8
2.0	2.7	6.4	104.3	68.5	36.0	61.7

to large distortions in the cell shape, which prevent further use in simulations. In the initial stage of simulation, it is therefore often desirable to use a constant-pressure algorithm[Andersen80a] that changes only the size of a model box, while leaving the shape orthogonal. Constant pressure algorithms using uniform cell dilation and flexible cells with isotropic external tension are discussed in Ref. [Martyna94a].

A more direct coupling between the internal stress **P** and the particle coordinates r_i and the cell shape tensor **h** was suggested by Berendsen.[Berendsen84a] In his weak-coupling scheme, r_i and **h** are scaled according to

$$\begin{aligned} \mathbf{r}'_i &= \mu \mathbf{r}_i \\ \mathbf{h}' &= \mu \mathbf{h} \end{aligned} \qquad (2\text{-}68)$$

where the scaling tensor μ is proportional to the difference between the internal stress tensor and the externally imposed stress $\mathbf{P}_0$:

$$\mu = \mathbf{I} - \frac{\beta \Delta t}{3\tau_p}(\mathbf{P}_0 - \mathbf{P}) \qquad (2\text{-}69)$$

(β is the isothermal compressibility, Δt the time-step, and τ_p a parameter).

2.5.2.3 Thermostats

Omitting the kinetic energy of the cell in Eq. (2-67-b), the change of the thermodynamic friction coefficient is proportional to the difference between the actual and the target kinetic energy,

$$\dot{\xi} = \frac{1}{Q}\left[\sum_{\alpha}^{N}\frac{\pi_i^{(\alpha)}\,\mathbf{g}_{ij}^{-1}\,\pi_j^{(\alpha)}}{m_\alpha} - nkT\right] = \frac{1}{Q}[K - nkT].\qquad(2\text{-}70)$$

If the temperature is too high, the thermodynamic friction ξ increases and the momenta of the particles are reduced by the last term of Eq. (2-67-d).

As observed with the Parrinello-Rahman algorithm, the average temperature of a Nosé-Hoover thermostat depends heavily on the time step used for the MD integration. As Fig. 2.14 shows, the actual temperature approaches the tar-
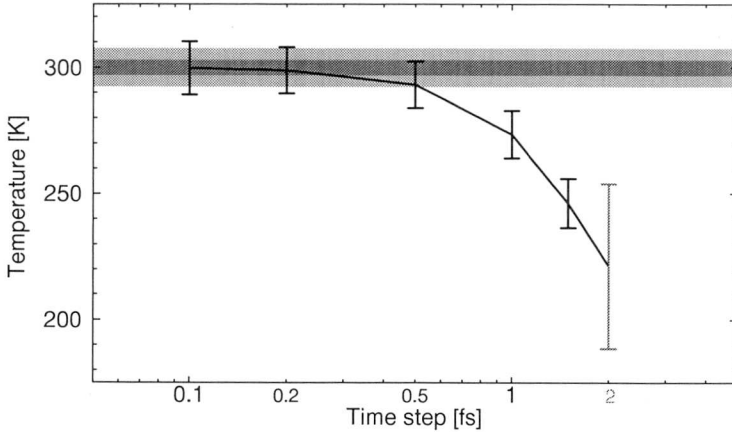
Figure 2.14: Average temperature of a simulation using a Nosé-Hoover thermostat at $T = 300$ K (PA-12 structure of 1038 atoms, equilibrated by 1 ns of $7tN$-MD, averages from 50 ps of $7tN$-MD with new velocities; the bar indicates the correct mean and standard deviation). At a stepsize of 2 fs, the simulation became unstable and crashed.

get temperature as the integration step gets smaller and the width of the fluctuations becomes[Nose91a]

$$\langle\delta T^2\rangle = \frac{2}{3N}\langle T\rangle^2,\qquad(2\text{-}71)$$

which is, for the above example, about 7.6 K. As a compromise between speed and accurate temperature and pressure control, a stepsize of 0.5 fs was used in all simulations that used one of the two extended control mechanisms. The coupling parameter Q is suggested to be proportional to $3NkT\cdot(T_0)^2$, where T_0 represents a characteristic time of the system. The proportionality factor has been set empirically to $1.41\cdot10^{-7}/(T_0)^2$, with T_0 set to 1.[MSIDiscover1]

In *Berendsen's thermostat*[Berendsen84a], an expression quite similar to Eq. (2-70) is used, but instead of $\dot{\xi}$, it is ξ directly, which is controlled:[Nose91a]

$$\xi = \frac{1}{Q}\left[\sum_\alpha^N \frac{\pi_i^{(\alpha)} g_{ij}^{-1} \pi_j^{(\alpha)}}{m_\alpha} - nkT\right] = \frac{1}{Q}[K - nkT] \quad . \tag{2-72}$$

In contrast to the Nosé-Hoover thermostat, the above equation is not capable of generating a canonical ensemble.[Hoover85a,Evans85a]

The first and most straightforward temperature control method is the *velocity scaling* algorithm of Woodcock[Woodcock71a], where the velocities are simply scaled after each integration step by a factor λ, which is given by

$$\lambda = \sqrt{\frac{T}{T_{act}}} \tag{2-73}$$

(T is the target simulation temperature and T_{act} is the actual temperature, obtained from the kinetic energy).

A further possibility to control the temperature consists in *stochastic collisions* of imaginary particles with individual atoms, that redistribute the kinetic energies.[Andersen80a] Both the velocity scaling and the stochastic collision method do not fulfil the requirement stated at the end of chapter 2.5.2.1 and are therefore not canonical.

2.5.2.4 Integrators

The above equations of motion (Eqs (2-65) or (2-67)) define a *trajectory* of the system in phase space. Except for the simplest cases (e.g. two interacting bodies), the trajectory can not be computed analytically but must be obtained numerically using a *finite difference* method.

All methods of this kind start at a given time t, at which the locations $r(t)$, the velocities $v(t)$ and - via the evaluation of the forces $f(t)$ - the accelerations $a(t)$ of all particles are known. The *integrator* propagates the system by a small timestep Δt of $O(10^{-15}s)$ to a new time $t + \Delta t$ and so on.

For an integrator to be useful in MD, it should be:

- fast (only one force evaluation per timestep)
- small (minimal consumption of computer memory)
- robust (good energy conservation even at large Δt)
- time reversible and canonical.

A necessary condition to achieve canonicity is the conservation of the phase space volume in the course of the MD simulation according to the Liouville theo-

rem (chapter 2.4.2). A more detailed discussion about this topic can be found in Appendix D, where it becomes manifest that - for MD simulations - the velocity Verlet algorithm is a better choice than the complicated and slow predictor-corrector algorithms, especially the ABM4 method. Since the velocity Verlet algorithm was used for all MD simulations in this work, it will be briefly derived from its ancestor, the *Verlet* integrator.[Frenkel96]

A Taylor expansion of the coordinates at $t + \Delta t$ and $t - \Delta t$ yields

$$\mathbf{r}(t+\Delta t) = \mathbf{r}(t) + \mathbf{v}(t)\Delta t + \frac{1}{2}\mathbf{a}(t)\Delta t^2 + \frac{1}{3!}\frac{d^3\mathbf{r}}{dt^3}\Delta t^3 + O\left(\Delta t^4\right)$$

$$\mathbf{r}(t-\Delta t) = \mathbf{r}(t) - \mathbf{v}(t)\Delta t + \frac{1}{2}\mathbf{a}(t)\Delta t^2 - \frac{1}{3!}\frac{d^3\mathbf{r}}{dt^3}\Delta t^3 + O\left(\Delta t^4\right),$$

(2-74)

which sum up as

$$\mathbf{r}(t+\Delta t) = 2\mathbf{r}(t) - \mathbf{r}(t-\Delta t) + \mathbf{a}(t)\Delta t^2 + O\left(\Delta t^4\right).$$ (2-75)

Neglecting the last term in Eq. (2-75), one obtains the Verlet integrator. Remarkably, the new positions can be estimated with an accuracy of Δt^4, without knowledge of the velocities. But in many cases, the velocities are needed to define an actual temperature. A first variant of the Verlet algorithm that includes the velocities is the so-called *Leapfrog* scheme,[Berk70a] which got its name from the fact that the velocities and positions are leaping over each other, separated by $\frac{\Delta t}{2}$:

$$\mathbf{r}(t+\Delta t) = \mathbf{r}(t) + \mathbf{v}\left(t+\frac{\Delta t}{2}\right)\Delta t$$

$$\mathbf{v}\left(t+\frac{\Delta t}{2}\right) = \mathbf{v}\left(t-\frac{\Delta t}{2}\right) + \mathbf{a}(t)\Delta t$$

(2-76)

This asynchronicity prevents direct modifications of the velocities, as required by a thermostat. Therefore, an algorithm of the Verlet type was developed, which evaluates the positions and velocities at the same time - the *velocity Verlet* algorithm,[Swope82a]

$$\mathbf{r}(t+\Delta t) = \mathbf{r}(t) + \mathbf{v}(t)\Delta t + \frac{1}{2}\mathbf{a}(t)\Delta t^2$$

$$\mathbf{v}(t+\Delta t) = \mathbf{v}(t) + \frac{1}{2}[\mathbf{a}(t) + \mathbf{a}(t+\Delta t)]\Delta t$$

(2-77)

As a last remark about integrators, it should be noted that it is not important that an algorithm is able to follow the 'true' trajectory extremely well. This is due to the fact that even an extremely small difference in the initial conditions of two

otherwise identical simulations will lead to completely uncorrelated trajectories after a few hundred or thousand steps. This effect is called the *Lyapunov instability* and can be quantified as

$$|\Delta \mathbf{r}(t)| = \varepsilon \cdot \exp(\lambda t) \tag{2-78}$$

with λ being the largest Lyapunov exponent.

Figure 2.15 shows the effects of this 'chaotic' behaviour on a 'real' example. A DISCOVER simulation was performed and in the course of the simulation, a '.xdyn' file was created. A second simulation was now started, using the data of the '.xdyn' file and the potential and the kinetic energy of the continued and the restarted run were compared. The only difference between the two simulations was the precision of the initial data: The continued run was using the 64 bit
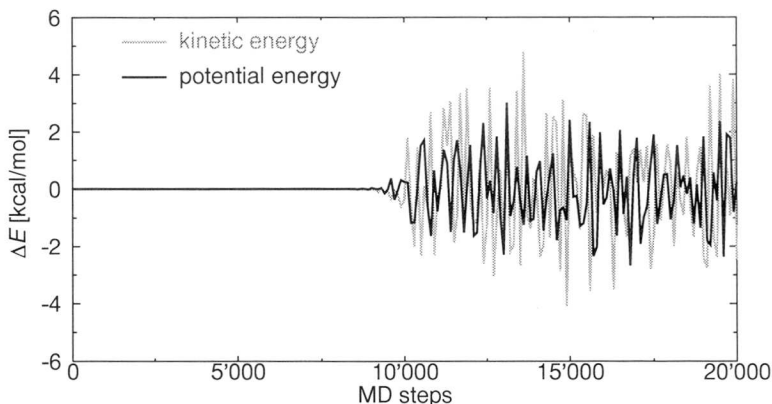
Figure 2.15: Difference between the kinetic and potential energies of a restarted and a continued DISCOVER run (Ar-nearest-neighbour crystal, 108 atoms, T^*=0.3, Δt = 6.024 fs)

data format, with which numbers are stored in the memory, while the '.xdyn' file was written with a smaller (although unknown) precision to the disk. The effects of this small difference are well visible: After approximately 10'000 MD steps, the small initial difference has increased so much that the trajectories became completely uncorrelated. The fluctuation of the difference becomes twice as large as the fluctuations of the individual values.

2.5.3 Hybrid Monte Carlo (HMC)

One of the main disadvantages of Molecular Dynamics simulations is that the stepsize of the integration has to be quite small in order to achieve a reason-

able conservation of quantities of interest such as energy and temperature. Furthermore, constant-temperature MD methods are only canonical in the limit of infinitely small time steps.

In contrast to this, Monte Carlo methods are numerically stable and canonical, but suffer from the fact that it would be often necessary to use collective instead of isolated moves to pass certain barriers in the equilibration of structures. Random global moves, however, normally lead to very low acceptance ratios.[Mehlig87a]

A solution to this dilemma is the use of Hybrid Monte Carlo (HMC)[Duane87a], which combines the advantages of both MD and MC. The framework of this method is a standard Monte Carlo algorithm (chapter 2.5.1), in which the change of the coordinates is performed by a relatively short MD simulation. In contrast to 'normal' MC, the Hamiltonians (potential plus kinetic energy) and not the potential energies of the initial and final structure are compared and the new configuration is accepted according to the criterion stated in Eq. (2-57). Detailed balance can only be maintained, if the integration algorithm is both *time reversible* and *area preserving*.[Forrest94a] Since the numerical instability of longer time steps always leads to an increase ΔH in the energy, the acceptance ratio, which is proportional to

$$p_{acc} \propto e^{-\frac{\Delta H}{kT}} \qquad (2\text{-}79)$$

always drops. These two tendencies - better decorrelation and lower acceptance ratio with larger time steps - must be balanced for optimum performance.

Among the technical details of interest is the fact that the velocities are randomized at the beginning of each MD run, whether or not its precessor has been accepted (otherwise detailed balance cannot be satisfied)[Forrest94a].

In contrast to this, another Hybrid-MC scheme, the stochastic dynamics - Monte Carlo (SD-MC) algorithm[Guarnieri94a] leaves the velocities unaffected by the acceptance or rejection of the MC step. The algorithm seems to be capable of sampling the phase space efficiently, but without proof of canonicity.

3 Theory III: Correlations and Fluctuations

3.1 Correlation Functions in Space and Time

Correlation functions are of outstanding importance in atomistic modeling since they provide the necessary link between quantities computed by the simulation (e.g. velocity and location of the atoms) and experimentally observable properties (diffusion coefficient, electrical conductivity, etc.). In this subchapter, the correlation functions in space and time will be introduced, some of their properties investigated, and a few applications mentioned.

3.1.1 The Radial Distribution Function

A 'lattice' function $G^\alpha(\mathbf{r})$ is introduced, which describes the probability of finding an atom of kind α at the position $\mathbf{r}$. The analytical form of G depends on the atomistic system being investigated. A structure at very low temperature or an individual frame of an MC or MD simulation produces a sum of delta functions:

$$G^\alpha(\mathbf{r'}) = \sum_{i=1}^{N^\alpha} \delta\left(\mathbf{r'} - \mathbf{r}^{(i)}\right), \tag{3-1}$$

with N^α being the number and $\mathbf{r}^{(i)}$ the position of the atoms of kind α. If structures at higher temperatures or a large number of simulation frames are considered, the distribution of the individual atomic positions is gaussian - provided, the underlying interaction potential is harmonic:

$$G^\alpha(\mathbf{r'}) = \sum_{i=1}^{N^\alpha} \frac{1}{\sqrt{2\pi}\sigma} e^{-\frac{[\mathbf{r'} - \mathbf{r}^{(i)}]^2}{2\sigma^2}} \tag{3-2}$$

Other 'lattice' functions than (3-1) and (3-2) are possible, but their normalization constant is always

$$\int_{R^3} G^\alpha(\mathbf{r'}) \, d\mathbf{r'} = N^\alpha. \tag{3-3}$$

Using the 'lattice' functions, the pair distribution function $g_{\alpha\beta}(\mathbf{r})$ can be defined as

$$g_{\alpha\beta}(\mathbf{r}) = \frac{1}{N^\alpha N^\beta} \int_{R^3} G^\alpha(\mathbf{r'} - \mathbf{r}) \, G^\beta(\mathbf{r'}) \, d\mathbf{r'}, \tag{3-4}$$

which, integrated over all $\mathbf{r}$ of equal length, results in the *radial distribution function*

$$g_{\alpha\beta}(r) = \frac{1}{4\pi} \int_0^\pi d\vartheta \int_{-\pi}^\pi \sin\vartheta \, d\varphi \, g_{\alpha\beta}(\mathbf{r}) \quad , \tag{3-5}$$

with $\mathbf{r}=f(r,\vartheta,\varphi)$.

Using the convolution theorem[Pressetal92], (3-4) can be expressed by the Fourier transforms (Eq. (3-15)) of G^α and G^β as

$$g_{\alpha\beta}(\omega) = G^\alpha(\omega) \, G^\beta(\omega) . \tag{3-6}$$

An example of calculated radial distribution functions is given in Fig. 3.1, where
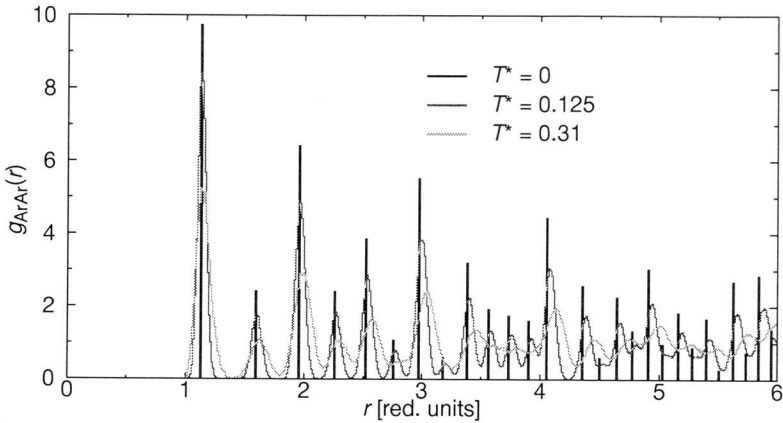
Figure 3.1:   Radial distribution function of an nearest-neighbour Lennard-Jones crystal at three different reduced temperatures (2048 atoms with variable-shape MC after $3{\cdot}10^6$ global updates)

the distributions in a nearest-neighbour Lennard-Jones crystal (which is quite similar to an argon crystal) at a reduced temperature T^* of 0, 0.125, and 0.31 are compared (the melting point of the crystal is at about $T^* \approx 0.5$). The broadening and shift of the peaks to higher values with increasing temperature can be well observed.

The radial distribution function is of central importance in the theory of disordered systems for two reasons:[Hansen86,McQuarrie76]

First, the radial distribution function can be measured experimentally both by X-ray diffraction and by neutron scattering methods. The structure factor

$$h(s) = \rho \int_{-\infty}^{\infty} [g(r) - 1] e^{is \cdot r} dr, \qquad (3\text{-}7)$$

the Fourier transform of $g(r) - 1$, can be evaluated directly with radiation-scattering experiments.

Second, thermodynamical quantities such as the potential energy U, the pressure p, and the chemical potential μ can be calculated, once the radial distribution function is known.

3.1.2 The Time-Autocorrelation Function

In Molecular Dynamics as well as in Monte Carlo simulations, successive conformations are normally highly correlated (i.e. differ only little). A convenient measure of the fading of the correlation of a dynamical variable $A(t)$ (e.g. the velocity $v_i(t)$ or the position $r_i(t)$ of a particle) is the *time-autocorrelation function*[Hansen86]

$$C_{AA}(\tau) \approx \frac{1}{t_{max}} \int_0^{t_{max}} A(t+\tau) A(t) \, dt \approx \frac{1}{n_{max}} \sum_{i=1}^{n_{max}} A_{i+\tau/\Delta t} A_i = \langle A(\tau) A \rangle. \qquad (3\text{-}8)$$

The first equality is valid for continuous values of $A(t)$ whereas the second equality defines the autocorrelation function of A at discrete values of t; assuming constant time intervals Δt between successive samples; A_k is defined as $A(k \cdot \Delta t)$. The third equality is only valid, if the process that governs the time evolution of $A(t)$ is ergodic[McQuarrie76], because the angular brackets denote an ensemble average. In the subsequent derivations, however, this notation will be used both for time and ensemble averages.

If $A(t)$ fluctuates around a non-zero mean value $\langle A \rangle$, only its deviations from this mean value are of interest, giving

$$a(t) \equiv A(t) - \langle A \rangle. \qquad (3\text{-}9)$$

The correlation function of this quantity can be normalized by dividing it by $C_{aa}(0)$,

$$c_{aa}(\tau) = \frac{\langle a(\tau) a \rangle}{\langle a(0) a \rangle} = \frac{\langle a(\tau) a \rangle}{\langle a^2 \rangle}. \qquad (3\text{-}10)$$

The normalized correlation function c_{aa} has the following important properties:[Leach96,McQuarrie76]

$$c_{aa}(0) = \frac{\langle a(0)\, a\rangle}{\langle a(0)\, a\rangle} = 1$$

$$c_{aa}(t) \in [\,(-c)_{aa}(0), c_{aa}(0)\,] \,,\qquad (3\text{-}11)$$

$$c_{aa}(\infty) = \langle a\rangle\langle a\rangle = 0$$

with the second equation following from Schwarz's inequality and the third from the definition of $a(t)$ (Eq. (3-9)). The time-autocorrelation function is thus a measure how long it lasts until the system has lost its 'memory' of the previous conformations or states. A value of 1 indicates complete correlation with the state of reference, whereas 0 indicates complete loss of all information about the initial state.

A typical autocorrelation function looks similar to the one given in Fig. 3.2.
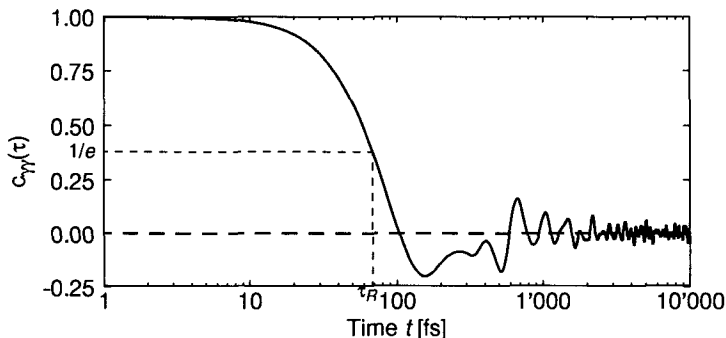
Figure 3.2:   Autocorrelation function of the γ-angle of Cellulose at 325 K (TtN-MD simulation with Ewald summation of the coulombic interactions, data from 0 to 132 ps)

At short times (< 10 fs), there is hardly any change in the quantity of interest (the γ angle of the cell shape), whereas, at about 100 fs, a quick decorrelation starts, corresponding to a fluctuation of the cell with a period of about 350 fs. This period is reflected too in the oscillations at long times and is linked to the cell mass W of the constant-pressure MD algorithm (Eq. (2-66)). At very long times, these oscillations become smaller and smaller because the fluctuations of the cell are not monochromatic. The relaxation time τ_R, i.e. the time where $c_{\gamma\gamma}(t)$ has dropped to $\frac{1}{e}$, is about 70 fs in the above example.

3.1.3   The Time-Crosscorrelation Function

The temporal dependence between two different variables $A(t)$ and $B(t)$ is expressed by the crosscorrelation function

$$C_{AB}(t) = \frac{1}{t_{max}} \int_0^{t_{max}} A(t+\tau) B(t) \, dt \approx \frac{1}{n_{max}} \sum_{i=1}^{n_{max}} A_{i+\tau/\Delta t} B_i \equiv \langle A(\tau) B \rangle, \quad (3\text{-}12)$$

which can be normalized by subtracting the mean values from the variables $A(t)$ and $B(t)$ and dividing the correlation function by $\langle a(0)b \rangle$:

$$c_{AB}(\tau) = \frac{\langle a(\tau) b \rangle}{\langle a(0) b \rangle}, \quad (3\text{-}13)$$

with $a(t) = A(t) - \langle A \rangle$ and $b(t) = B(t) - \langle B \rangle$. Again $c_{AB}(\tau)$ is proportional to the probability of $a(t+\tau)$ evolving parallel with $b(t)$.

According to Eqs. (3-8) and (3-12), the correlation functions are functions of the time difference τ only and are thus said to be *stationary*. Therefore, the relations

$$\langle \dot{A}(\tau) B \rangle = -\langle A(\tau) \dot{B} \rangle,$$

$$\langle \dot{A} A \rangle = 0 \quad (3\text{-}14)$$

$$\langle \ddot{A}(\tau) B \rangle = -\langle \dot{A}(\tau) \dot{B} \rangle$$

are valid.[Hansen86]

3.1.4 The Wiener-Khinchin Theorem

If $A(\omega)$ denotes the Fourier-transform of the familiar dynamic variable $A(t)$,

$$A(\omega) = \lim_{T \to \infty} \int_{-T}^{T} A(t) \, e^{i\omega t} dt, \quad (3\text{-}15)$$

the spectral density function of $A(t)$ is defined as

$$S_{AA}(\omega) = \lim_{T \to \infty} \frac{1}{2T} A(\omega) A^*(\omega), \quad (3\text{-}16)$$

where $A^*(\omega)$ stands for the complex conjugate of $A(\omega)$.

The Wiener-Khinchin theorem now connects the spectral density and the time-correlation function of $A(t)$ by stating that[Reichl80a]

$$S_{AA}(\omega) = \int_{-\infty}^{\infty} e^{i\omega\tau} \langle A(\tau) A \rangle \, d\tau = \int_{-\infty}^{\infty} e^{i\omega\tau} C_{AA}(\tau) \, d\tau. \quad (3\text{-}17)$$

This is equivalent to the more general 'Correlation Theorem'[Pressetal92]

$$C_{AB}(\tau) = A(\omega) B^*(\omega), \quad (3\text{-}18)$$

which allows to compute the correlation function by multiplication of the Fourier transform of the fluctuating variable(s).

3.1.5 Kubo-Green Formula

The well-known Einstein formula for the self-diffusion coefficient AllenTildesley89

$$D = \lim_{t \to \infty} \frac{1}{6t} \langle [\mathbf{r}^{(i)}(t) - \mathbf{r}^{(i)}(0)]^2 \rangle \qquad (3\text{-}19)$$

can be generalized to the following form:Hansen86

$$K = \langle \Delta A(t) \rangle = \frac{1}{kTV} \lim_{t \to \infty} \frac{1}{2t} \langle [A(t) - A(0)]^2 \rangle . \qquad (3\text{-}20)$$

This equation is equivalent to

$$K = \langle \Delta A(t) \rangle = \lambda \int_t^\infty \chi_{AB}(\tau) \, d\tau \qquad (3\text{-}21)$$

with λ being the constant external perturbation and χ_{AB} the 'after effect' function

$$\chi_{AB}(t) = \begin{array}{ll} -\dfrac{1}{kT} \langle B(0) \dot{A}(t) \rangle & \text{for } t > 0 \\[6pt] 0 & \text{for } t \le 0 \end{array} . \qquad (3\text{-}22)$$

(3-22) is the so-called *Green-Kubo relation* between a transport coefficient and an integral over a time-correlation function. There exists a number of such relations, some of which are given in the next equations:Frenkel96a

$$D = \int_0^\infty \langle \mathbf{v}^{(i)}(\tau) \cdot \mathbf{v}^{(i)}(0) \rangle \, d\tau$$

$$\eta = \frac{1}{kTV} \int_0^\infty \langle \sigma_{ik}(\tau) \sigma_{ik}(0) \rangle \, d\tau \qquad \sigma_{ik} = \sum_{\alpha=1}^N \left[m^\alpha v_i^\alpha v_k^\alpha + \frac{1}{2} \sum_{\beta \ne \alpha} r_i^{\alpha\beta} f_k \{ r^{\alpha\beta} \} \right]$$

$$\lambda_T = \frac{1}{kT^2 V} \int_0^\infty \langle j_i^e(\tau) j_i^e(0) \rangle \, d\tau \qquad j_i^e = \frac{d}{dt} \sum_{\alpha=1}^N r_i^\alpha \frac{1}{2} \left[m^\alpha v_\alpha^2 + \sum_{\beta \ne \alpha} U\{ r^{\alpha\beta} \} \right]$$

$$\sigma_e = \frac{1}{kTV} \int_0^\infty \langle j_i^{el}(\tau) j_i^{el}(0) \rangle \, d\tau \qquad j_i^{el} = \sum_{\alpha=1}^N q^\alpha v_i^\alpha .$$

$$(3\text{-}23)$$

As stated in the remarks of Eq. (3-8), the angular brackets actually denote

ensemble averages. The notation of the variables is given at the beginning of this work. Assuming ergodicity to hold, the ensemble averages can be replaced by time averages (chapter 2.4.2). For Eqs. (3-23) to be exactly valid, it would actually be necessary to simulate for an infinite amount of time. Since this is not possible in practical computer simulations, all quantities calculated from the above equations are just finite-time approximations of the 'real' values. It is therefore necessary to check whether or not the simulation has been long enough for the results to converge.

3.2 The Fluctuation-Dissipation Theorem and the Elastic Constants

3.2.1 The Fluctuation-Dissipation Theorem

The famous *fluctuation-dissipation theorem*[Landau86c],

$$\langle x^2 \rangle = \frac{h}{2\pi^2} \int_0^\infty \alpha''(\omega) \coth\frac{h\omega}{4\pi kT} d\omega, \tag{3-24}$$

connects the imaginary part of the *generalized susceptibility* $\alpha(\omega)$ to the mean square of the fluctuations of a general physical quantity x. The generalized susceptibility is the Fourier-transform of the proportionality $\hat{\alpha}$ of the *linear* response $\bar{x}(t)$ of a physical quantity $x(t)$ to an external perturbation force $f(t)$:

$$\bar{x}(t) = \hat{\alpha} f(t). \tag{3-25}$$

The perturbation force $f(t)$ and the physical property $x(t)$ can be any pair of conjugate quantities (e.g. electrical field and dipole moment); in the case of the elastic properties, $f(t)$ is a mechanical force (or stress) acting on a solid body that invokes a deformation (or strain) response $x(t)$. The proportionality factor $\hat{\alpha}$ between these two quantities is the familiar elastic compliance (Eq. (1-56)).

In the limit of high temperatures $kT \gg h\omega/2\pi$ - the classical case - the fluctuation-dissipation theorem (FDT) can be simplified to[Landau86c]

$$\langle x^2 \rangle = kT\alpha(0) \tag{3-26}$$

The first formulation (3-24) of the FDT allows to obtain informations about the underlying atomistic processes from macroscopic measurement of the imaginary part of the general susceptibility. By reformulating the FDT, it is also possible to compute a general susceptibility from the fluctuations of the corresponding physical quantity. The following equation for the generalized susceptibility is due

to Kubo[Kubo66a]

$$\alpha(\omega) = \frac{i2\pi}{h} \int_0^\infty e^{i\omega t} \langle \hat{x}(t) \, (\hat{x}(0) - \hat{x}(0) \, (\hat{x}(t))) \rangle \, dt, \tag{3-27}$$

In the classical limit, this formula is equivalent to Eqs. (3-23) (and of course Eq. (3-26)).

3.2.2 The Fluctuation Equations of the Elastic Constants

The *strain-strain fluctuation formula* of the elastic constants,

$$\langle \eta_{ik}\eta_{lm} \rangle = \frac{kT}{\langle V \rangle} S_{iklm} \tag{3-28}$$

can be directly derived from (3-26). Using the stiffnesses instead of the compliances leads to the familiar form of the equation[ParrinelloRahman82a]:

$$C_{iklm} = \frac{kT}{\langle V \rangle} \langle \eta_{ik}\eta_{lm} \rangle^{-1}. \tag{3-29}$$

The *stress-strain fluctuation formula* of the elastic constants is obtained in the following way[Gusev96a]:

In the absence of external stresses, the Hamiltonian H of a N-particle system can be written as

$$H = \sum_\alpha \frac{p_\alpha^2}{2m_\alpha} + U(r_{\alpha\beta}) , \tag{3-30}$$

where $\mathbf{p}_\alpha$ and m_α are the momentum and mass of particle α and $U(r_{\alpha\beta})$ is the potential energy, which depends only on the distances $r_{\alpha\beta}$ between the particles. Considering six independent components of the strain tensor η_{ik} (Eq. (1-36)) as 'generalized coordinates' (degrees of freedom) the follwing identity holds:

$$\left\langle \eta_{ik}\frac{\partial H}{\partial \eta_{lm}} \right\rangle = kT\delta_{ii}\delta_{lm}. \tag{3-31}$$

Equations (3-31) and (2-49) are examples of the general form $\langle A\partial H/\partial q \rangle = kT\langle \partial A/\partial q \rangle$ that holds[Münster69,Pathria72] for any generalized coordinate q and function A in the canonical ensemble and is valid to $O(N^{-1})$ in any other ensemble.

To calculate the derivatives of the Hamiltonian with respect to the strain components, Eq. (1-28) takes the form

$$r^2 = R^2 + 2\eta_{ik}X_iX_k, \tag{3-32}$$

which is acutally the definition of the strain tensor for homogeneous deformations. Differentiating both sides of (3-32) with respect to η_{ik} and noting that $X_i = H_{ij}h_{jk}x_k$ (Eq. (B-1)), we obtain from (3-30) - (3-32)

$$\langle \eta_{ik} \sum_{\alpha > \beta} \frac{\partial U}{\partial r_{\alpha\beta}} \frac{H_{lp}h_{pq}^{-1}(x_{\alpha\beta})_q H_{mt}h_{ts}^{-1}(x_{\alpha\beta})_s}{r_{\alpha\beta}} \rangle = \frac{1}{2}kT(\delta_{il}\delta_{km} + \delta_{im}\delta_{kl}). \tag{3-33}$$

The kinetic term of the Hamiltonian was left out in the above equation, because it does not contribute, since $\langle \eta_{ik} \rangle = 0$. From Eqs (3-29) and (3-33) a new fluctuation formula for the elastic constants follows:

$$C_{iklm} = \frac{1}{\langle V \rangle} \langle \eta_{ik} \sum_{\alpha > \beta} \frac{\partial U}{\partial r_{\alpha\beta}} \frac{H_{np}h_{pq}^{-1}(x_{\alpha\beta})_q H_{jt}h_{ts}^{-1}(x_{\alpha\beta})_s}{r_{\alpha\beta}} \rangle \langle \eta_{nj}\eta_{lm} \rangle^{-1}. \tag{3-34}$$

According to Eqs (1-46) and (1-47), the summation term is equivalent to the thermodynamic tension **t**. This results in the following notation of the fluctuation formula for finite stress and strain:

$$C_{iklm} = \langle \eta_{ik}t_{nj} \rangle \langle \eta_{nj}\eta_{lm} \rangle^{-1}. \tag{3-35}$$

If the difference between the instantaneous scaling matrix **h** and the average scaling matrix **H** is small (e.g. at low temperatures), the linear stress tensor σ can be used instead:

$$C_{iklm} = \langle \eta_{ik}\sigma_{nj} \rangle \langle \eta_{nj}\eta_{lm} \rangle^{-1}. \tag{3-36}$$

In the limit of thermodynamic equilibrium, both fluctuation approaches yield the same result, leading to the following convergence criterion:

$$\langle \eta_{ik}t_{lm} \rangle = \frac{1}{2}\frac{kT}{\langle V \rangle} \langle \delta_{il}\delta_{km} + \delta_{im}\delta_{kl} \rangle, \tag{3-37}$$

which is equivalent to (3-33).If linear stresses are assumed, the convergence criterion can be written as

$$\langle \eta_{ik}\sigma_{lm} \rangle = \frac{1}{2}\frac{kT}{\langle V \rangle} \langle \delta_{il}\delta_{km} + \delta_{im}\delta_{kl} \rangle. \tag{3-38}$$

Equation (3-37) shows, that formally the constant term $kT/\langle V \rangle$ of Eq.(3-29) is replaced by the fluctuating components of the stress-strain correlation. Unless the instantaneous stresses and strains are correlated, this would not improve the

convergence of the elastic constants calculation. But they indeed are correlated, as is most obvious in the limit of low temperature, where the entropic contributions are negligible and the instantaneous stresses are unambigously determined by the instantaneous strains via Hooke's law

$$\sigma_{ij} = c_{ijkl}\varepsilon_{kl}.$$ (1-49)

As discussed in Ref. [Gusev96a], this correlation between the instantaneous stresses and strains allows for an evaluation of the elastic constants by using (3-35) or (3-36) without fully converged second moments $\langle \eta_{nj}\eta_{im} \rangle$ of the strain fluctuations, as explicitly required by (3-29).

3.2.3   Size Dependence of the Elastic Thermal Fluctuations

The amplitude of the thermal fluctuations of a body with Young's modulus E is increasing with decreasing sample dimension l approximately like

$$\sqrt{\langle \delta l^2 \rangle} = \sqrt{\frac{kT}{El}}.$$ (3-39)

This can be rationalized by considering l as a degree of freedom of the system as a whole and assigning an average energy of $\frac{1}{2}kT$ to it. The average elastic energy of a cubic cell due to the fluctuation of the cell size l matches this value in thermodynamic equilibrium, as is expressed by

$$\left\langle \frac{1}{2}lE\delta l^2 \right\rangle = \frac{1}{2}kT.$$ (3-40)

Figure 3.3 gives an example of the absolute value of the thermal fluctuations of a
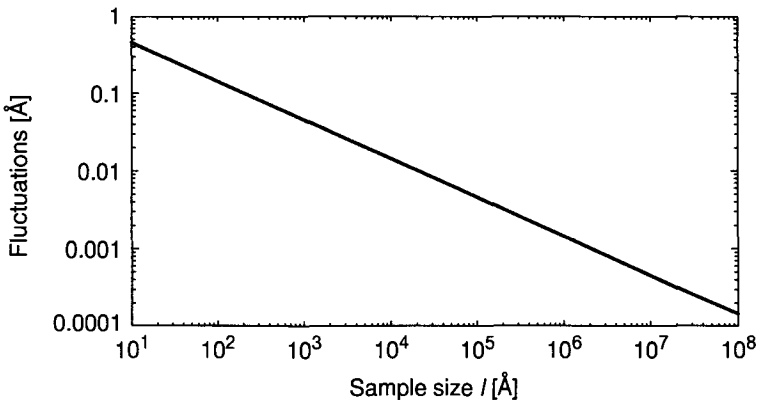
Figure 3.3:   Root mean squared fluctuations of a body with a Young modulus of 3 GPa as a function of its size l.

cubic body with a Young modulus of $E = 3$ GPa. It is clearly visible that, at macroscopic dimensions of centimeters (10^8 Å), the fluctuations are vanishingly small. At very small dimensions of 10 - 30 Å typically present in simulations, the fluctuations are in the range of a few percent of the cell dimension l. This considerable absolute value guarantees an accurate numerical registration of the effect, i.e. a good signal/noise ratio. On the other hand, dynamical instabilities occur if the cell size is very small or Young's modulus very low. It furthermore often requires the use of finite instead of linear stresses and strains.

4 Results

This section contains the description of the various atomistic model systems that were simulated in the course of this Ph. D. thesis and of the results obtained from these simulations.

Chronologically, the first polymer that was investigated was polycarbonate (BPA-PC) in its glassy state. In order to have a more simple system and to avoid the imponderabilities of generating amorphous structures, a monocrystal of polyethylene was the next system of interest. Polypropylene followed, because it allowed to get insights into the elasticity of helical chains. The final step in the direction of more simple and computationally well tractable systems was reached by simulating a crystal of nearest-neighbour Lennard-Jones particles. This system allowed to compare the different fluctuation formulae and to have a close look at the influence of the temperature on the elastic constants. Due to the experience gained in this system, it became possible to aim for more complicated structures: crystalline polyamide-6 and Cellulose-Iβ were modeled at various temperatures. The whole work ended with an extensive simulation of amorphous polyamide-6 and -12 in dry and water-saturated state at different temperatures to quantify the influence of these parameters on the mechanical behaviour.

The model systems, however, will be presented starting from the most simple and best understood going to more and more complicated problems:

- Lennard-Jones solid - nearest neighbours
- Polyethylene - planar zig-zag chains
- Polypropylene - helical chains
- Cellulose-Iβ - chains with hydrogen bonds
- Polyamide-6 - chains with hydrogen bonds
- Polyamide-6 - amorphous, with and without water
- Polyamide-12 - amorphous, with and without water
- Polycarbonate - amorphous

For each system, a short description about the structure and its generation process is given, followed by details about the simulation procedure. Problems encountered during the simulation and the results obtained from the trajectories are discussed. Finally a comparison with other numerical approaches and with experimental values (if available) is made and conclusions are drawn.

4.1 Lennard-Jones Solid - Nearest-Neighbours

4.1.1 Introduction

Crystals of the rare gases Ne, Ar, Kr, and Xe have been studied particularly well[Horton76] due to their extremely simple structure: they consist of individual atoms which form an fcc (face-centered cubic) lattice. This lattice is held together only by van-der-Waals forces (dispersion and exchange terms); Coulombic or bonded interactions as well as induction terms are completely missing. Nevertheless, theoretical and experimental determination of the precise form of the interaction potential is by no means trivial. One of the best approximations is the so-called Barker-Fisher-Watts (BFW) potential[Barker76]

$$U(r) = \varepsilon \left[e^{\alpha(1-R)} \sum_{i=1}^{5} A_i (R-1)^i - \frac{C_6}{\left[R^6 + \delta\right]} - \frac{C_8}{\left[R^8 + \delta\right]} - \frac{C_{10}}{\left[R^{10} + \delta\right]} \right] .^a \quad (4\text{-}1)$$

As already mentioned in chapter 2.1.3.5, many-body interactions contribute substantially to the total energy, making it necessary to include at least the triple-dipole contribution to obtain reliable results.[Barker76] It is also worth noting that all calculations predict an extremely small energy difference between the hexagonally close packed (hcp) and the fcc lattice. This difference is a fraction of a percent of the crystal potential energy and by far not enough to explain the fact that the above mentioned rare gases crystallize in the fcc structure.[BellZucker76]

Since the above potential is quite complicated, the more simple 12-6 Lennard-Jones function of Eq. (2-8) is used for model calculations. This so-called Lennard-Jones solid (which - by reasons stated above - is not identical to a solid rare gas) is a widely used model system. In many simulations, the simplicity of this model is further increased by neglecting all but the nearest-neighbour interactions. The result is the *Nearest-neighbour Lennard-Jones* solid, a well-investigated reference system against which new sampling methods can be tested.[Rahman64a,Verlet67a,Sprik84a,Rutledge94b]

The intention of the following work was to study the convergence behaviour of different fluctuation approaches, in particular the Parrinello-Rahman strain-strain correlation formula (Eq. (3-36)) and the new stress-strain correlation formula (Eq. (3-34)). Another objective was it to establish the influence of the simulation box size and the temperature on the convergence rate and the 'final'

---

a. $R = r/\sigma^*$ (chapter 2.1.3.3), $\sigma^* = 3.7612$ Å, $\varepsilon/k = 142.095$ K, $R_0 = 3.3605$ Å, $A_0 = 0.27783$, $A_1 = -4.50431$, $A_2 = -8.331215$, $A_3 = -25.2696$, $A_4 = -102.0195$, $A_5 = -113.25$, $C_6 = 1.10727$, $C_8 = 0.16971325$, $C_{10} = 0.013611$, $\alpha = 12.5$, and $\delta = 0.01$

results. Therefore, Monte Carlo and molecular dynamics simulations of a variety of systems from 32 to 2048 and even 23328 atoms were performed at different temperatures. This was possible because the extreme simplicity of the interaction function (Eq. (E-2)) allowed to write highly efficient code (an example: one global-update MC step of a 108-atom system took 1.3 milliseconds on a workstation).

The results of these simulations will be examined in detail in order to introduce the methodology for the subsequent polymeric systems.

4.1.2 Description and Cell Generation

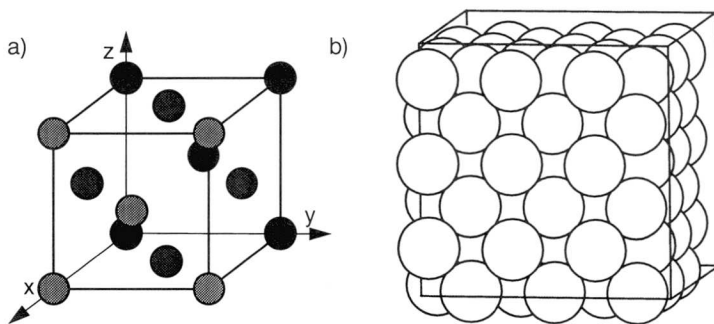With an fcc unit cell of 4 atoms (Fig. 4.1 a)) and a cubic overall shape the

Figure 4.1: a) Unit cell of the fcc Nearest-neighbour Lennard-Jones solid, b) simulation assembly of 108 atoms (n = 3) subject to PCC

simulation system contains n^3*4 atoms (n being integer). In the literature, all possible systems from 32 $(n = 2)$[Squire69a] to 864 $(n = 6)$[Lebowitz67a] particles have been described and used. Due to the cubic symmetry, there are only three independent elastic constants, C_{11}, C_{12}, and C_{44}, as indicated in Table 1-2 on page 18. Many of the results in the following sections are thus given as an average over the symmetry-equivalent components of the matrix of the elastic constants. The standard deviation serves as an indication of the precision of the calculation, as do the elements that should be zero.

The generation of cubic simulation boxes of arbitrary size was done by a small program (makecar.f), which calculated the size of the box, the positions of the individual atoms, and the list of nearest-neighbour interactions from the number of unit cells per dimension, n. It was not necessary to specify the Lennard-Jones parameter σ because reduced units were used (Appendix E). To convert

from reduced to SI units, σ = 3.805 Å and ε = 119.8 k[Sprik84a] have been used.

To speed up equilibration, it is favourable to multiply the **h** matrix describing the box shape with an empirical, temperature-dependent constant which accounts for the thermal expansion of the simulation box. Typical values of this constant lie between 1.1 and 1.2[Cowley83a]. The file created by the above program, and used as the input of the subsequent MC simulation, had a structure that is given in Table 4-1.

Table 4-1: The data file of the nearest-neighbour Lennard-Jones solid

a_1 b_1 c_1	
a_1 b_1 c_1 a_2 b_2 c_2 a_3 b_3 c_3	**h**-matrix [**a,b,c**]
s_{11} s_{12} s_{13} s_{21} s_{22} s_{23}	scaled coordinates of the $4n^3$ atoms
at_i at_k	list of $6 \cdot 4n^3$ pairs of nearest neighbours

4.1.3 Simulation Procedure

4.1.3.1 Monte Carlo Simulations

A simple global-update Monte Carlo move was used to simulate a TtN-ensemble: In one move both the cell shape matrix **h** and the coordinates $\mathbf{x}^{(\alpha)}$ of all atoms were changed randomly. The cell shape matrix was altered symmetrically by

$$\mathbf{h}_{new} = \mathbf{h}_{old} + \Delta h_{max}(2\mathbf{R} - 1) \qquad R_{ik} = R_{ki} \qquad (4\text{-}2)$$

to prevent rotations of the cell as a whole. The positions of all atoms were changed by

$$\mathbf{x}_{new}^{(\alpha)} = \mathbf{x}_{old}^{(\alpha)} + \Delta x_{max}(2\mathbf{R} - 1) \qquad (4\text{-}3)$$

with **R** denoting a symmetric 3×3 matrix (Eq. (4-2)) or a vector (Eq. (4-3)) of random numbers between 0 and 1 and **1** being a matrix or a vector full of 1's. All random numbers were generated by the Lagged Fibonacci algorithm described in Appendix C-2.

The maximum possible change of the cell parameters and of the coordinates, Δh_{max} and Δx_{max}, were set to the same proportion by

$$\Delta x_{max} = \frac{\Delta h_{max}}{N^{1/3}}, \qquad (4\text{-}4)$$

with N being the number of atoms. Δh_{max} was not a true degree of freedom since it was adapted during the simulation to yield a certain acceptance ratio. An auto-adjustment procedure was introduced that modified these values to keep the acceptance ratio p_{acc} between p_{acc_min} and p_{acc_max}. If the actual acceptance ratio - computed over at least 100 steps - was smaller than p_{acc_min}, Δh_{max} was reduced by 10% (multiplied with 0.9). If it exceeded p_{acc_max}, Δh_{max} was multiplied with 1.1 instead. Stationary values of Δh_{max} were reached after $2 \cdot 10^4$ - $4 \cdot 10^5$ MC steps. Typically, this initial period with varying Δh_{max} comprised less than a percent of the total simulation and its influence on the final result should therefore be negligible. However, in some cases a faster convergence would have been achieved by starting with a better guess of Δh_{max}.

After a random change of the cell shape and atom coordinates, E_{new}, the sum of the interaction energies between the nearest neighbours was calculated. A move was accepted if

$$\min\left(1, \left(\frac{V_{new}}{V_{old}} \right)^N \cdot \exp\left(-\frac{E_{new} - E_{old}}{kT} \right) \right) \qquad (4\text{-}5)$$

was larger than a random number between 0 and 1. In this case, the new configuration replaced the old one and was added to the ensemble average. Otherwise, the old configuration contributed again to the ensemble average. The ensemble sampled in this way was the TtN-ensemble and the elastic constants are the isothermal ones.

Tables 4-2 and 4-3 show the simulations that were performed using the TtN-MC algorithm. The linear form of the stress-strain correlation function (Eq. (4-16)) was used to compute the elastic constants in Table 4-2. In Table 4-3, the finite-stress-strain correlations were computed by Eq. (4-20). In each cell, the number of equilibration steps is indicated in the upper left and the number of sampling steps in the lower right half.The last row in the first table lists the CPU time per MC step on a workstation (SGI Crimson). Since only nearest-neighbour interactions were considered, the computation time scales linearly with N. There is no significant difference in the computation time if finite stresses were assumed.

Besides these simulations, the influence of the acceptance probability on the convergence of the elastic constants was investigated by a series of three runs with 32 atoms at $T^* = 0.3$, each of 10^6 steps. The maximum possible

Table 4-2: πN-MC simulations of nearest-neighbour Lennard-Jones solid of various size at a range of temperatures, *linear* stresses were assumed in all calculations

N / T^*	32	108	256	2048	23328
0.125	10^6 / 10^8	10^8 / 10^8	10^6 / 10^7	$2 \cdot 10^6$ / $4 \cdot 10^8$	-
0.225	-	10^8 / 10^8	-	-	-
0.3	-	10^8 / 10^8	-	-	-
0.31	10^6 / 10^8	-	$2 \cdot 10^6$ / 10^7	$2 \cdot 10^6$ / $4.4 \cdot 10^6$	- / 10^6
0.5	10^6 / 10^8	-	10^6 / 10^7	10^6 / $4.4 \cdot 10^6$	-
t_{CPU} [s]	0.0013	0.0043	0.0095	0.1180	0.8946

Table 4-3: πN-MC simulations of nearest-neighbour Lennard-Jones solid of various size at a range of temperatures, in all calculations, *finite* stresses were taken into account

N / T^*	32	108	256	2048
0.01	-	10^7 / 10^7	-	-
0.02	-	$1.5 \cdot 10^7$ / $1.5 \cdot 10^7$	-	-
0.05	-	$1.5 \cdot 10^7$ / $1.5 \cdot 10^7$	-	-
0.125	- / 10^8	$2 \cdot 10^8$ / 10^8		
0.225	-	$2 \cdot 10^8$ / 10^8	-	-
0.3	- / 10^8	$2 \cdot 10^8$ / 10^8	- / 10^7	$2 \cdot 10^6$ / $2 \cdot 10^6$
0.5	- / 10^8	- / 10^8	- / 10^7	$2 \cdot 10^6$ / $2 \cdot 10^6$

change of the cell parameters, Δh_{max}, was set such, that the acceptance probabilities were 5 - 10%, 45 - 50%, and 90 - 95%, respectively.

4.1.3.2 Molecular Dynamics Simulations

To check the results of the MC algorithm and to get an idea of its efficiency, some MD simulations were performed. For this purpose, argon structures of 108 atoms were built with InsightII and minimized with Discover94. The forcefield used for the minimization and the subsequent MD simulations contained only a 12-6 Lennard-Jones interaction term with $\sigma = 3.805$ Å and $\varepsilon/k = 119.8$ K (the

value of σ was taken from ref. [Sprik84a] and is somewhat too large). Runs in the $T\sigma N$-ensemble were made with a stepsize of $\Delta t^* = 0.0025$ (6.024 fs), approximately half the typical value found in the literature, which ranges from 8.6 fs[Sprik84a] to 12.05 fs[Ray85a,Ray88a]. This small value was chosen because the Nosé-Hoover thermostat used for the temperature control requires relatively small timesteps (chapter 2.5.2.3).

Consecutive simulations of several 10^4 steps wrote the cell size and the stresses to a table file from where these values were read by essentially the same program which computed the elastic constants of the MC runs. A description of this program will be given in chapter 4.1.4. Because it would have been too complicated to access the forces acting on the individual atoms, the stress-strain correlation term in the Gusev-Zehnder-Suter formula was only calculated assuming linear (Eq. (3-36)) and not finite (3-35) stresses. So the results were just compared with MC calculations using linear stresses, too.

All MD and the MC simulations mentioned in this chapter were performed on a 108-atom Lennard-Jones crystal at a reduced temperature $T^* = 0.3$ and consisted of 10^7 steps. To circumvent the inability of the Discover MD-software to compute just nearest-neighbour interactions (as described in chapter 4.1.3.3), a set of runs with cutoffs of 5.35 Å without splines and 5.2 Å with various spline widths was used for both the MD and the MC simulations. The following table gives an overview of all simulations performed:

Table 4-4: Simulations with $N = 108$ and $T^* = 0.3$ (36 K), MC and MD runs (for comparison)

	cutoff [Å]	spline [Å]	runs
MC	5.35	-	1
	5.4	0.4	2
MD	5.4	0.4	2
	5.8	1.2	1

4.1.3.3 Hybrid Monte Carlo

As a third independent sampling method, Hybrid Monte Carlo runs were done with Discover 94 for the structures of 108 and 500 atoms. Two different ensembles were sampled hereby: the canonical ThN- and the isothermal-isostress $T\sigma N$-ensemble. In both cases, an input-script for Discover 94 generated the necessary random numbers (Appendix C-1), extracted the energies from output files, and controlled the writing of conformations and cell stresses. How-

ever, various technical problems and limitations of Discover 94 prevented the use of this method for calculating elastic constants.

One of the first problems arouse with the cutoffs: For MD and HMC simulations, the interactions between nearest-neighbour interactions were replaced by those within a cutoff of 5.35 Å. This value was found by plotting a histogram of the interparticle distances at the desired simulation temperature of $T^* = 0.3$. As Fig. 3.1 reveals and as was confirmed by subsequent simulations, the first and second neighbour shells are so close that atoms from one or the other shell occasionally cross the sharp cutoff and change the energy by -0.1232 kcal/mole abruptly (Fig. 4.2 a)). No way was found to influence the update rate of the neighbour list in order to alter this unphysical behaviour. Hybrid-MC simulations of the nearest-neighbour Lennard-Jones solid were therefore not possible because a jump of 0.12 kcal/mole is equal to a reduction of the acceptance down to 18%.
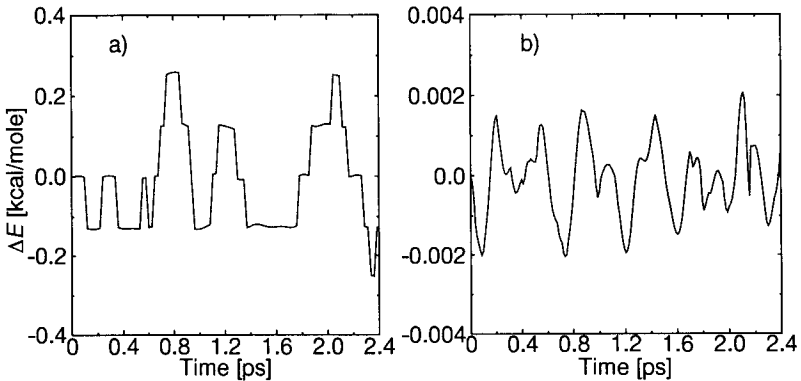

Figure 4.2: Potential energy during an EhN-MD simulation of a Lennard-Jones solid (500 atoms, $T^* = 0.3$, $\Delta t^* = 0.005$) with a) a sharp cutoff at 5.35 Å and b) a splined cutoff between 5.0 and 5.4 Å

The above jumps in the potential energy could be made much smaller by the introduction of a spline between 5.0 and 5.4 Å. As can be seen in Fig. 4.2 b), the fluctuations in the potential energy become approximately two orders of magnitude smaller and are less abrupt. These small fluctuations are hardly influencing the HMC algorithm anymore (influence on the acceptance rate is less than 3 %). But by introducing this spline of 0.4 Å width, one is no longer able to simulate a nearest-neighbour Lennard-Jones solid which has a strong impact on the elastic constants (chapter 4.1.5.5).

To sample conformations in the TtN-ensemble, a hybrid scheme was

devised that consists of two parts: In one part, the cell is deformed by a random amount according to Eq. (4-2) without change of the atom coordinates; in the other part, a short *EhN*-MD run is performed. In order to achieve detailed balance (microreversibility), the sequence of the two parts must not always be the same. It is possible to use a 50-50 mixture of moves that perform first a deformation and afterwards a MD simulation and moves that do the opposite. The other - equal - solution consists of a mixture of pure deformation and pure Hybrid-MC processes:
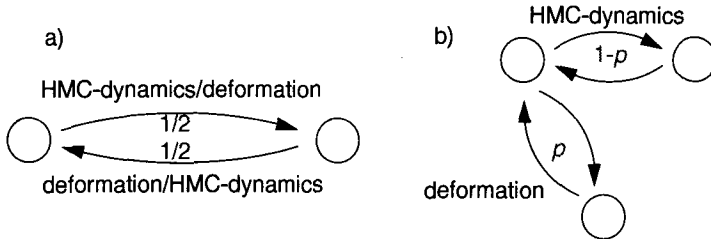
a)
HMC-dynamics/deformation

b)
HMC-dynamics

deformation/HMC-dynamics   deformation

Figure 4.3: *ThN*-HMC schemes: a) equal probability of dynamics/deformation and deformation/ dynamics moves; b) adjustable proportion of deformation and dynamics

In Discover 94, however, the velocities can not be scaled simultaneously with the change of the cell shape matrix, so that the dynamics/deformation move can not be programmed straightforwardly.

To avoid these problems, variable shape (*EσN*)-MD simulation runs with relatively large timesteps (90.36 fs with a Nosé-Hoover thermostat) were used to sample the phase space on the limit of stability of MD. The acceptance criterion was modified by an 'umbrella' sampling technique described in chapter 2.5.1.3. The test system was again a 108-atom nearest-neighbour Lennard-Jones solid at $T^* = 0.3$.

Again for comparison, the same system was used in a self-made MC code,

Table 4-5: Simulations with $N = 108$ and $T^* = 0.3$, nearest-neighbour interactions only

	MD steps	global steps	runs
Deformation only	-	$8 \cdot 10^7$	1
Deformation + MD	100	10^7	1
MD + Deformation	100	10^7	1

which was extended to follow a short *EhN*-MD trajectory with a velocity-Verlet integrator (Appendix E). Using this code, the calculations listed in Table 4-5 were

carried out, and the different number of steps in the runs with and without MD reflects the different timings to do one global step.

4.1.4 Evaluation of the Elastic Constants

In order to calculate the elastic constants with the Parrinello-Rahman formula,

$$C_{iklm} = \frac{kT}{\langle V \rangle} \langle \eta_{ik}\eta_{lm} \rangle^{-1}, \tag{3-29}$$

or with the Gusev-Zehnder-Suter approach,

$$C_{iklm} = \langle \eta_{ik}t_{nj} \rangle \langle \eta_{nj}\eta_{lm} \rangle^{-1}, \tag{3-35}$$

it is necessary to evaluate the averages of the strain-strain and of the stress-strain correlation matrices, $\langle \eta_{ik}\eta_{im} \rangle$ and $\langle \eta_{ik}t_{nj} \rangle$. But both the definition of the finite strain,

$$\eta = \frac{1}{2}\left[\mathbf{H}^{T^{-1}}\mathbf{h}^T\mathbf{h}\mathbf{H}^{-1} - \mathbf{I} \right], \tag{1-36}$$

and the finite stress,

$$\mathbf{t} = J\mathbf{H}\mathbf{h}^{-1}\sigma\mathbf{h}^{T^{-1}}\mathbf{H}^T, \tag{1-46}$$

contain the reference cell shape $\mathbf{H}$, which is not known *a priori*, but can be set equal to the average cell shape $\langle \mathbf{h} \rangle$[ParrinelloRahman81a]. For the average cell shape in a TtN-simulation is the cell shape formed by the average stress, and the net stress in all simulations was set to zero bar, this average cell shape should represent an equilibrium (i.e. strain-free) cell.

If the cell shape $\mathbf{h}(t)$ and the actual stress $\sigma(t)$ are known as a function of time - MD simulation time or sequence of MC frames - the elastic constants can be expressed as a function of t, too. The easiest and most straightforward way to do this is to store the cell parameters and the stress of all relevant frames and to obtain first the average cell shape and the average stress and to use these values in Eqs. (1-36) and (1-46) to compute the actual strain and stress, which themselves are needed to obtain the strain-strain and the stress-strain correlation matrices.

Although the correlation between successive frames makes it necessary to save, say, only every 10th frame, long simulations easily produce 10^7 (MD) or 10^8(MC) frames. Even if the 64-bit binary representation is used, the storage of the 6 cell parameters and the 6 stress values consumes 100 to 1000 MBytes of

data per run. It is therefore necessary to find an algorithm, which computes the double averages of **h** and σ 'on the fly':

The strain of a cell matrix **h** with respect to the average cell $\langle \mathbf{h} \rangle$ is expressed as

$$\eta = \frac{1}{2}\left[\langle \mathbf{h}^T \rangle^{-1} \mathbf{h}^T \mathbf{h} \langle \mathbf{h} \rangle^{-1} - \mathbf{I}\right] = \frac{1}{2}[H - \mathbf{I}] \tag{4-6}$$

(Note the difference between **H**, the reference cell shape, now replaced by $\langle \mathbf{h} \rangle$, and H, given by the above equation.) The strain-strain correlation can be expanded now as

$$\langle \eta_{ij} \cdot \eta_{kl} \rangle = -\frac{1}{4}[\delta_{ij} \cdot \delta_{kl} - \delta_{ij} \cdot \langle H_{kl} \rangle - \delta_{kl} \cdot \langle H_{ij} \rangle - \langle H_{ij} \cdot H_{kl} \rangle] \tag{4-7}$$

The important quantities to keep account of are $\langle H_{ij} \rangle$ and $\langle H_{ik}H_{jl} \rangle$. These quantities can be expressed as functions of the $\langle \mathbf{h} \rangle$ and **h** matrices that describe the average and the actual shape of the simulation cell. Using matrix multiplication algebra, the individual elements of the H matrix can be written as:

$$H_{ij} = \sum_{k=1}^{3} \langle h^T \rangle_{ik}^{-1} \left[\sum_{l=1}^{3}\left[\sum_{m=1}^{3} h_{mk}h_{ml}\right]\langle h \rangle_{lj}^{-1}\right] \tag{4-8}$$

Due to the interchangeability of inversion and transposition and the fact that $h_{ik}^T = h_{ki}$, it is possible to write H_{ij} in the form

$$H_{ij} = \sum_{k=1}^{3} \langle h \rangle_{ki}^{-1} \sum_{l=1}^{3} \langle h \rangle_{lj}^{-1} \sum_{m=1}^{3} h_{mk}h_{ml} \tag{4-9}$$

The following rules,

$$\left\langle \sum_{\alpha} x_{\alpha} \right\rangle = \frac{1}{t}\sum_{t}\sum_{\alpha} x_{\alpha}^t = \frac{1}{t}\sum_{\alpha}\sum_{t} x_{\alpha}^t = \sum_{\alpha}\frac{1}{t}\sum_{t} x_{\alpha}^t = \sum_{\alpha}\langle x_{\alpha} \rangle, \tag{4-10}$$

and

$$\left\langle \sum_{\alpha}\sum_{\beta}\sum_{\gamma} \langle x_{\alpha\beta} \rangle x_{\alpha\gamma}x_{\beta\gamma} \right\rangle = \frac{1}{t}\sum_{t}\sum_{\alpha}\sum_{\beta}\sum_{\gamma} \langle x_{\alpha\beta} \rangle x_{\alpha\gamma}x_{\beta\gamma} =$$

$$\frac{1}{t}\sum_{t}\sum_{\alpha}\sum_{\beta} \langle x_{\alpha\beta} \rangle \sum_{\gamma} x_{\alpha\gamma}x_{\beta\gamma} = \sum_{\alpha}\sum_{\beta} \langle x_{\alpha\beta} \rangle \frac{1}{t}\sum_{t}\sum_{\gamma} x_{\alpha\gamma}x_{\beta\gamma} = \tag{4-11}$$

$$\sum_{\alpha}\sum_{\beta} \langle x_{\alpha\beta} \rangle \sum_{\gamma}\frac{1}{t}\sum_{t} x_{\alpha\gamma}x_{\beta\gamma} = \sum_{\alpha}\sum_{\beta} \langle x_{\alpha\beta} \rangle \sum_{\gamma} \langle x_{\alpha\gamma}x_{\beta\gamma} \rangle$$

allow to obtain the average of Eq. (4-9) as

$$\langle H_{ij}\rangle = \sum_{k=1}^{3}\sum_{l=1}^{3}\langle h\rangle_{ki}^{-1}\langle h\rangle_{lj}^{-1}\sum_{m=1}^{3}\langle h_{mk}h_{ml}\rangle. \qquad (4\text{-}12)$$

The right side of Eq. (4-12) contains $3\cdot9=27$ elements over which the averages have to be summed. The last term of Eq. (4-7), $\langle H_{ij}H_{kl}\rangle$, is much more complicated: no less than 738 terms have to be watched:

$$\langle H_{ij}\cdot H_{kl}\rangle = \sum_{m=1}^{3}\sum_{n=1}^{3}\sum_{o=1}^{3}\sum_{p=1}^{3}\langle h\rangle_{mi}^{-1}\langle h\rangle_{nj}^{-1}\langle h\rangle_{ok}^{-1}\langle h\rangle_{pl}^{-1}$$
$$\sum_{q=1}^{3}\sum_{r=1}^{3}\langle h_{qm}h_{qn}h_{ro}h_{rp}\rangle \qquad (4\text{-}13)$$

Inserting the above terms into Eq. (4-7), the average of the product of the strains is expressed in quite a lengthy expression:

$$\langle \eta\cdot\eta\rangle_{ijkl} = \frac{1}{4}\delta_{ij}\cdot\delta_{kl} - \frac{1}{4}\delta_{ij}\cdot\sum_{m=1}^{3}\sum_{n=1}^{3}\langle h\rangle_{mk}^{-1}\langle h\rangle_{nl}^{-1}\langle\sum_{o=1}^{3}h_{om}h_{on}\rangle$$
$$-\frac{1}{4}\delta_{kl}\cdot\sum_{m=1}^{3}\sum_{n=1}^{3}\langle h\rangle_{mk}^{-1}\langle h\rangle_{nl}^{-1}\langle\sum_{o=1}^{3}h_{om}h_{on}\rangle +$$
$$\frac{1}{4}\sum_{m=1}^{3}\sum_{n=1}^{3}\sum_{o=1}^{3}\sum_{p=1}^{3}\langle h\rangle_{mi}^{-1}\langle h\rangle_{nj}^{-1}\langle h\rangle_{ok}^{-1}\langle h\rangle_{pl}^{-1} \qquad (4\text{-}14)$$
$$\langle\sum_{q=1}^{3}\sum_{r=1}^{3}h_{qm}h_{qn}h_{ro}h_{rp}\rangle.$$

The corresponding expression for the stress-strain correlation term in the limit of linear elasticity,

$$\eta_{ij}\sigma_{kl} = \frac{1}{2}\left(\sum_{m=1}^{3}\langle h\rangle_{mj}^{-1}\sum_{n=1}^{3}\langle h\rangle_{in}^{T-1}\sum_{o=1}^{3}h_{om}h_{on}-\delta_{ij}\right)\cdot\sigma_{kl}, \qquad (4\text{-}15)$$

can be found in an analogous way,

$$\langle\eta_{ij}\sigma_{kl}\rangle = \frac{1}{2}\sum_{m=1}^{3}\sum_{n=1}^{3}\sum_{o=1}^{3}\langle h\rangle_{mj}^{-1}\langle h\rangle_{in}^{T-1}\langle h_{om}h_{on}\sigma_{kl}\rangle - \frac{1}{2}\delta_{ij}\langle\sigma_{kl}\rangle. \qquad (4\text{-}16)$$

The above equation is correct in the limit of linear elasticity. To account for non-linear behaviour, the theory of finite elasticity needs to be applied. This is

done in the following steps.

Equation (3-34),

$$C_{iklm} = \frac{1}{\langle V \rangle} \langle \eta_{ik} \sum_{\alpha > \beta} \frac{\partial U}{\partial r_{\alpha\beta}} \frac{H_{np} h_{pq}^{-1}(x_{\alpha\beta})_q H_{jt} h_{ts}^{-1}(x_{\alpha\beta})_s}{r_{\alpha\beta}} \rangle \langle \eta_{nj} \eta_{lm} \rangle^{-1}, \quad (3\text{-}34)$$

is slightly rewritten by using the fact that $h_{ik}^{-1} x_k = s_i$ and that $\mathbf{H}$ can be replaced by $\langle \mathbf{h} \rangle$:

$$C_{iklm} = \frac{1}{\langle V \rangle} \langle \eta_{ik} \sum_{\alpha > \beta} \frac{\partial U}{\partial r_{\alpha\beta}} \frac{\langle h \rangle_{np}(s_{\alpha\beta})_p \cdot \langle h \rangle_{jt}(s_{\alpha\beta})_t}{r_{\alpha\beta}} \rangle \langle \eta_{nj} \eta_{lm} \rangle^{-1}. \quad (4\text{-}17)$$

Without summation convention, the first term on the right side is

$$\langle \eta_{ik} \sum_{\alpha > \beta} \frac{\partial U}{\partial r_{\alpha\beta}} \frac{\langle h \rangle_{np}(s_{\alpha\beta})_p \cdot \langle h \rangle_{jt}(s_{\alpha\beta})_t}{r_{\alpha\beta}} \rangle =$$

$$= \langle \eta_{ik} \sum_{\alpha > \beta} \sum_{p=1}^{3} \sum_{t=1}^{3} (\langle h \rangle_{np} \langle h \rangle_{jt} s_{\alpha\beta p} s_{\alpha\beta t}) \frac{\partial U}{\partial r_{\alpha\beta}} \frac{1}{r_{\alpha\beta}} \rangle \quad (4\text{-}18)$$

Using Eq. (4-10) and writing Eq. (4-6) with explicit summations,

$$\eta_{ik} = \frac{1}{2} \sum_{u=1}^{3} \sum_{v=1}^{3} \sum_{w=1}^{3} \langle h \rangle_{iu}^{T-1} h_{uv}^T h_{vw} \langle h \rangle_{wk}^{-1} - \frac{1}{2} \delta_{ik}, \quad (4\text{-}19)$$

the average stress-strain fluctuation term can be written (after reordering the indices) as

$$\langle \eta_{ij} \sum_{\alpha > \beta} \frac{\partial U}{\partial r_{\alpha\beta}} \frac{\langle h \rangle_{km} s_{\alpha\beta m} \cdot \langle h \rangle_{ln} s_{\alpha\beta n}}{r_{\alpha\beta}} \rangle =$$

$$= \frac{1}{2} \sum_{m=1}^{3} \sum_{n=1}^{3} \sum_{o=1}^{3} \sum_{p=1}^{3} \langle h \rangle_{km} \langle h \rangle_{ln} \langle h \rangle_{oi}^{-1} \langle h \rangle_{pj}^{-1}$$

$$\langle \sum_{q=1}^{3} \sum_{\alpha < \beta} h_{qo} h_{qp} s_{\alpha\beta m} s_{\alpha\beta n} \frac{\partial U}{\partial r_{\alpha\beta}} \frac{1}{r_{\alpha\beta}} \rangle - \quad (4\text{-}20)$$

$$- \frac{1}{2} \delta_{ij} \sum_{m=1}^{3} \sum_{n=1}^{3} \sum_{\alpha > \beta} \langle h \rangle_{km} \langle h \rangle_{ln} \langle s_{\alpha\beta m} s_{\alpha\beta n} \frac{\partial U}{\partial r_{\alpha\beta}} \frac{1}{r_{\alpha\beta}} \rangle$$

All terms in Eq. (4-14) and (4-20) together need less than 1.5 kBytes of memory when stored as 64-bit numbers, independent of the number of frames processed. This allows the accurate calculation of the strain-strain and the stress-strain fluctuation term and thus the precise determination of the matrix of

the elastic constants.

4.1.5 Results

4.1.5.1 Influcence of the Acceptance Ratio

As mentioned at the end of chapter 4.1.3.1, the influence of the acceptance probability, which is a function of the maximum allowed change in the cell shape, on the convergence of the elastic constants was investigated. A cell of 32 atoms at $T^* = 0.31$ was used for this purpose. The upper and the lower limit of the acceptance probabilities were set to 5 - 10%, 45 - 50%, and 90 - 95%, respectively. Figure 4.4 shows the relative error of $(C_{11} + C_{22} + C_{33})/3$. The relative error of this figure is defined as

$$\Delta_{rel}(n) = \frac{C(n)}{C(n=10^7)} \qquad (4\text{-}21)$$

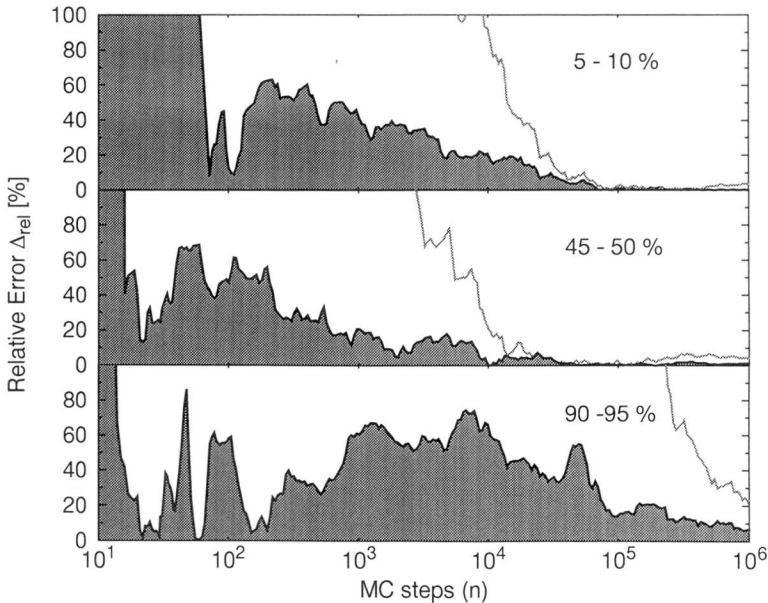with $C(n)$ being $(C_{11}(n) + C_{22}(n) + C_{33}(n))/3$ and n the number of Monte Carlo steps.

Figure 4.4:   Relative difference between actual $(C_{11}+C_{22}+C_{33})/3$ and the same value after 10^7 MC steps. Solid lines delimiting shaded areas were calculated with Eq. (3-34) (stresses and strains), the other lines with Eq. (3-29) (strains alone), $T^* = 0.31$, 32 atoms

After an initial run of 10^6 steps to equilibrate the structure and to find a good starting value for Δh_{max}, the elastic constants were calculated from runs of 10^7 steps assuming finite stresses. It can be clearly seen that there is hardly any difference between simulations with an acceptance rate of 5 - 10% and 45 - 50%, whereas higher acceptance rates clearly deteriorate the speed of convergence. This is mainly due to the smaller and smaller Δh_{max} values (Table 4-6), which reduce the speed with which the system explores its phase space.

Table 4-6: Stationary values of Δh_{max} as a function of the acceptance interval

p_{acc_min}	p_{acc_max}	Δh_{max} [red. units]
0.05	0.10	0.0245
0.45	0.50	0.0096
0.90	0.95	0.0012

For all subsequent simulations, acceptance rates of 12.5 - 17.5% or 45 - 50% were chosen. No influence of the acceptance rates on converged values of the elastic constants could be observed.

4.1.5.2 Elastic Constants at Very Low Temperatures

As shown in Table 4-3, MC simulations of a 108-atom cell were done at $T^* = 0.01$, 0.02, and 0.05. These results are of interest, because at such low
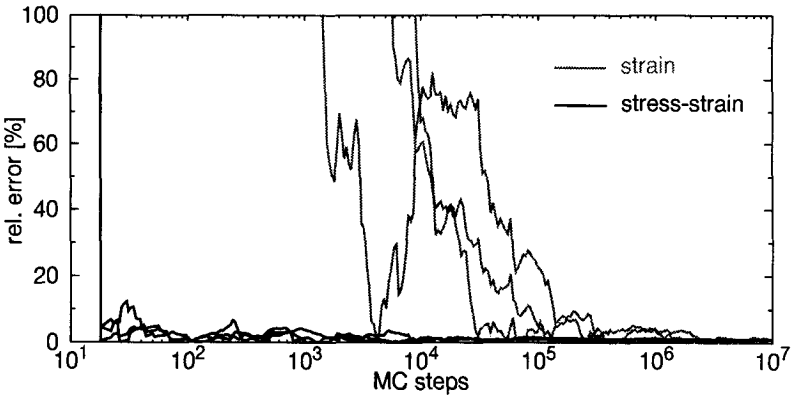
Figure 4.5: Relative error of the averages of the three symmetry equivalent elastic constants at $T^* = 0.01$, 10^7 sampling steps after 10^7 equilibration steps

temperatures, the anharmonic effects are small and the stress-strain correlation should converge very fast. At $T^* = 0.01$, this is indeed the case, as the above figure shows:

After a few steps, the elastic constants computed with the finite stress-strain fluctuation formula are to within a few percent of the final values, which themselves differ by less than a tenth of a percent from the static values.[Gusev96a] The roughly 19 (6 accepted) steps the stress-strain correlation needs to reduce its relative error down to about 10% are necessary to find an average cell shape, from which the strain can be calculated. The same level of accuracy is reached with the strain fluctuation method only after more than 10^5 steps.

The complete matrix of the elastic constants at $T^* = 0.01$ and a table com-

Table 4-7: Elastic constants at $T^* = 0.01$; please note that the values are quite large, since $C_{ik}^* \propto 1/T^*$ (1 reduced unit equals 0.300 MPa), the values in the right column are very well converged (the level of accuracy can be estimated from the off-diagonal elements that should be zero).

$$\frac{1}{N}\langle \eta_{ik}\eta_{lm}\rangle^{-1} \text{ (PR)}$$

$$\begin{bmatrix} 7104. & 3546. & 3551. & -27. & 0. & -7. \\ 3546 & 7174. & 3594. & 61. & 19. & 18. \\ 3551. & 3594. & 7289. & -25. & 16. & 25. \\ -27. & 60. & -25. & 3535. & -3. & -101. \\ 0. & 19. & 16. & -3. & 3623. & 31. \\ -7. & 18. & 25. & -101. & 31. & 3612. \end{bmatrix}$$

$$\frac{V}{NkT}\langle \eta_{ik}t_{nj}\rangle \langle \eta_{nj}\eta_{lm}\rangle^{-1} \text{ (GZS)}$$

$$\begin{bmatrix} 7178. & 3578. & 3577. & 0. & -4. & 2. \\ 3581. & 7180. & 3579. & 4. & -2. & 0. \\ 3579. & 3575. & 7182. & 4. & 1. & 2. \\ -1. & 0. & 2. & 3594. & 0. & -1. \\ -1. & -1. & 2. & 0. & 3595. & 2. \\ 0. & 1. & 0. & 2. & 2. & 3592. \end{bmatrix}$$

paring the symmetry equivalent elastic constants at $T^* = 0.01, 0.02,$ and 0.05 are given in Tables 4-7 and 4-8.

Table 4-8: Reduced symmetry-equivalent elastic constants at $T^* = 0.01, 0.02,$ and 0.05, strain (PR) and stress-strain fluctuation (GZS) formula. The reduced units have to be multiplied by 0.300 ($T^* = 0.01$), 0.598 ($T^* = 0.02$), and 1.487 MPa to obtain SI units

T^*	Method	$\frac{1}{3}(C_{11}+C_{22}+C_{33})$	$\frac{1}{3}(C_{12}+C_{13}+C_{23})$	$\frac{1}{3}(C_{44}+C_{55}+C_{66})$
0.01	(PR)	7189.5 ± 44.1	3563.7 ± 12.5	3589.9 ± 22.5
	(GZS)	7179.8 ± 1.0	3593.8 ± 0.7	3578.0 ± 0.4
0.02	(PR)	3540.4 ± 10.5	1749.8 ± 4.5	1773.3 ± 11.7
	(GZS)	3545.0 ± 2.3	1764.8 ± 0.6	1776.5 ± 0.7
0.05	(PR)	1360.3 ± 2.9	675.7 ± 2.3	688.8 ± 3.2
	(GZS)	1367.1 ± 0.4	675.9 ± 0.1	686.1 ± 0.3

As is obvious from Table 4-8, there is a relation between the elastic constants of a crystal, if its lattice particles occupy centers of symmetry and interact

with central forces. This so-called Cauchy relation[BornHuang54, Quesnel93a] can be expressed as[Gusev96a]

$$\frac{2C_{44}}{(C_{11} - C_{12})} = 2 \qquad C_{12} = C_{44}. \qquad (4\text{-}22)$$

In Fig. 4.6, the ratio $2C_{44}/(C_{11}\text{-}C_{12})$ is plotted as a function of the tempera-
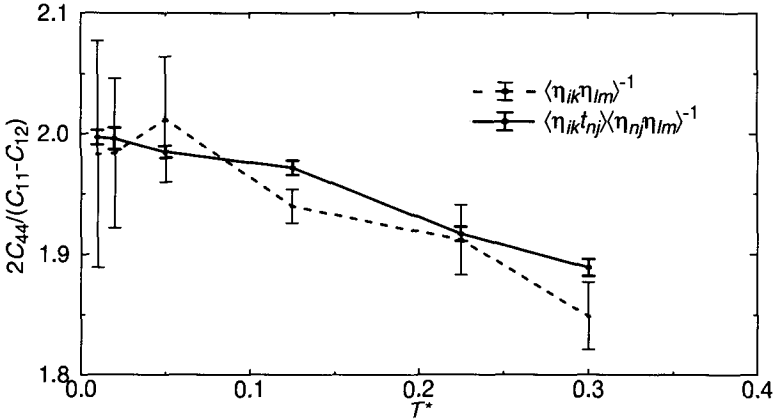

Figure 4.6: Cauchy relation of a 108-atom nearest-neighbour Lennard-Jones solid as a function of the reduced temperature

ture for the strain and the stress-strain fluctuation method. For both methods, this ratio approaches 2.0 at infinitely small temperature, with larger and larger deviations as the temperature rises and anharmonic effects come into play. These effects can be thought of as deflections of the individual atoms from the center of symmetry by thermal fluctuations. It can be further observed that the stress-strain fluctuation approach leads to a smoother form of the temperature dependence of the anisotropy ratio. Its error bars[a] are - especially at low temper-

---

a. The standard deviations dC_{11}, dC_{12} and dC_{44} of the elastic constants C_{11}, C_{12} and C_{44} were calculated from the scattering of the corresponding symmetry-equivalent elastic constants $\{C_{11}, C_{22}, C_{33}\}$, $\{C_{12}, C_{13}, C_{23}\}$, and $\{C_{44}, C_{55}, C_{66}\}$ The total derivative

$$d\alpha = d\left(\frac{2C_{44}}{(C_{11} - C_{12})}\right) = \frac{\partial \alpha}{\partial C_{11}} dC_{11} + \frac{\partial \alpha}{\partial C_{12}} dC_{12} + \frac{\partial \alpha}{\partial C_{44}} dC_{44}$$

$$= \frac{2C_{44}}{(C_{11} - C_{12})^2} dC_{11} + \frac{2C_{44}}{(C_{11} - C_{12})^2} dC_{12} + \frac{2}{C_{11} - C_{12}} dC_{44}$$

of α was used to calculate the error propagation.

atures, but even at $T^* = 0.225$ and 0.3 - smaller, which is a further indication that the stress-strain fluctuation approach takes advantage of the quasi-harmonic form of the effective potential.

4.1.5.3 Elastic Constants at Intermediate Temperatures

In Tables 4-2 and 4-3 on page 87, it can be seen that a particularly large number of simulations with various cell sizes have been performed at $T^* = 0.125$. Before the influence of the cell size on the resulting elastic constants is examined, the difference between working with linear and with finite stress in the stress-strain fluctuation method will be quantified by looking at the 108-atom cell at $T^* = 0.125$, 0.225, and 0.3. After sufficient equilibration ($O(10^8$ steps)), variable-shape MC simulations of 10^8 steps were done. The elastic constants calculated from these runs are listed in Table 4-9.

Table 4-9: Averages of the symmetry equivalent elastic constants calculated with linear and finite stresses, 108-atom nearest-neighbour Lennard-Jones solid. The conversion factors to SI units are given in the first column.

T^*		$\langle \eta_{ij}\sigma_{nj}\rangle\langle \eta_{nj}\eta_{lm}\rangle^{-1}$	$\langle \eta_{ik}t_{nj}\rangle\langle \eta_{nj}\eta_{lm}\rangle^{-1}$
0.125 (3.658 MPa)	C_{11}	495.46 ± 0.14	496.92 ± 0.17
	C_{12}	237.57 ± 0.12	241.03 ± 0.09
	C_{44}	251.41 ± 0.06	250.35 ± 0.12
	$2C_{44}/(C_{11}-C_{12})$	1.950 ± 0.002	1.957 ± 0.003
0.225 (6.431 MPa)	C_{11}	237.65 ± 0.18	239.00 ± 0.20
	C_{12}	109.27 ± 0.15	112.58 ± 0.04
	C_{44}	122.46 ± 0.10	121.32 ± 0.12
	$2C_{44}/(C_{11}-C_{12})$	1.907 ± 0.006	1.919 ± 0.006
0.3 (8.405 MPa)	C_{11}	157.27 ± 0.06	158.30 ± 0.35
	C_{12}	69.62 ± 0.08	72.48 ± 0.12
	C_{44}	82.10 ± 0.06	81.09 ± 0.07
	$2C_{44}/(C_{11}-C_{12})$	1.873 ± 0.004	1.890 ± 0.011

The following tendencies can be observed: The C_{11} and C_{12} values are consistently higher if finite stresses were included, whereas the C_{44} component is somewhat smaller. Thus the ratio $2C_{44}/(C_{11}-C_{12})$ is always closer to the theoretical value of 2. In general, the scattering of the finite stress data is a bit larger, especially at higher temperature. Obviously the switching from linear to finite

stresses brings a measurable although not dramatic effect.

The influence of the size of the simulation cell on the elastic constants (i.e. finite size effect) was investigated by a series of simulations at $T^* = 0.3$. Cells of 32, 108, 256, and 2048 atoms were run for 10^6 to 10^8 steps, depending on the size; i.e. the computing time was roughly the same for all systems. Since the very small 32-atom cell was used as well, all calculations were done with the finite-stress formalism. In Table 4-10, the results of elastic constant calculations

Table 4-10: Comparison of the elastic constants of different cell sizes at $T^* = 0.3$, finite stresses

N [atoms]	MC steps	$\langle C_{11}, C_{22}, C_{33} \rangle^*$	$\langle C_{12}, C_{23}, C_{13} \rangle^*$	$\langle C_{44}, C_{55}, C_{66} \rangle^*$
32	10^8	155.46 ± 0.16	72.05 ± 0.02	80.03 ± 0.12
108	10^8	158.38 ± 0.22	72.57 ± 0.10	81.14 ± 0.07
256	10^7	158.09 ± 0.55	72.48 ± 0.17	80.74 ± 0.05
2048	$2 \cdot 10^6$	159.42 ± 1.98	73.44 ± 1.32	80.81 ± 0.67

using stress-strain correlations are given. There is no clear size dependence, except for the very small 32 atom system, which has somewhat lower values than the rest. A correction proposed by Cowley[Cowley83a] was used for all results presented in this chapter, which normalizes the vibrational contributions by N-1 instead of N. At $T^* = 0.5$, the same conclusions can be drawn, as Table 4-12 shows.

Similar calculations with *linear* stress-strain correlations have been made at $T^* = 0.31$. Table 4-11 gives the values of the various simulations. Again, the

Table 4-11: Comparison of different cell sizes at $T^* = 0.31$, linear stresses

N [atoms]	MC steps	$\langle C_{11}, C_{22}, C_{33} \rangle^*$	$\langle C_{12}, C_{23}, C_{13} \rangle^*$	$\langle C_{44}, C_{55}, C_{66} \rangle^*$
32	10^8	146.74 ± 0.19	65.39 ± 0.19	77.02 ± 0.14
256	10^7	148.45 ± 0.49	63.87 ± 0.27	78.53 ± 0.51
2048	$2 \cdot 10^6$	148.38 ± 1.46	65.16 ± 0.69	77.83 ± 0.46

averages do not differ substantially, but the standard deviations clearly indicate that the smaller the simulation cell is the more precise the elastic constants can be determined. The average values of the finite stress calculations of Table 4-10, however, do suggest that the optimum system size seems to be the 108 atom system, offering the best trade-off between rate of convergence and self stabili-

zation.

Table 4-12: Symmetry equivalent elastic constants at $T^* = 0.5$ for samples of 32, 108, 256, and 2048 atoms, finite stresses, stress-strain fluctuations

N [atoms]	MC steps	$\langle C_{11}, C_{22}, C_{33}\rangle^*$	$\langle C_{12}, C_{23}, C_{13}\rangle^*$	$\langle C_{44}, C_{55}, C_{66}\rangle^*$
32	10^8	54.67 ± 0.18	22.35 ± 0.02	29.65 ± 0.10
108	10^8	60.20 ± 0.22	24.45 ± 0.13	32.04 ± 0.05
256	10^7	62.02 ± 0.22	25.73 ± 0.12	32.36 ± 0.09
2048	$2 \cdot 10^6$	60.13 ± 1.72	23.86 ± 1.03	31.36 ± 0.92

It is therefore advisable to use as small a system as possible while taking into account that a minimum cell size is required to provide mechanical stability against the thermal vibrations. If collective motions contribute significantly to the mechanical spectrum, it must be avoided to have cells or cutoffs that are too small to include these effects. The first limitation (mechanical stability) is of particular importance for crystalline systems, whereas the second one applies mainly to amorphous cells.

4.1.5.4 Elastic Constants at High Temperatures

As listed in Table 4-3, the elastic constants of cells of 32, 108, 256, and 2048 atoms have been determined by simulations carried out at $T^* = 0.5$. This temperature is the upper limit of the existence of literature data and most probably the upper limit for stable Lennard-Jones crystals. The melting temperature of argon is -189.3 °C (= 83.9 K, $T^* = 0.7$). Due to the absence of the long-range attractive force, the melting temperature of the nearest-neighbour Lennard-Jones solid is closer to $T^* = 0.5$[Cowley83a,Rutledge94b]. At this temperature, anharmonic effects become important and reduce the efficiency of the stress-strain fluctuation method. At the same time, the crystal is able to sample its phase space more efficiently. This improves the convergence of the strain-strain fluctuation method. As a consequence, the behaviour of the two methods should become more and more equal as the temperature raises. To quantify this statement, the convergence behaviour of the 32-atom system is shown in Fig. 4.7 and a list of the elastic constants of all simulations is given in Table 4-12.

Two conclusions can be drawn from the above table: First, the average values of the elastic constants increase with increasing cell size from 32 to 256 atoms, indicating that especially the 32- and to some extent the 108-atom cell is too small for the large thermal fluctuations close to the melting point of the structure. Second, the standard deviations are smaller for the smaller cell sizes, con-
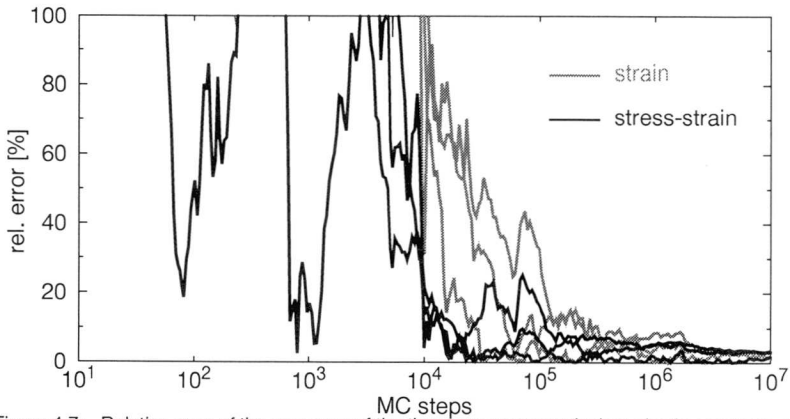
Figure 4.7: Relative error of the averages of the three symmetry equivalent elastic constants at $T^* = 0.5$, 10^8 sampling after 10^6 equilibration steps

firming Cowley's statement[Cowley83a], that 'the modulus, which depends on averages of fluctuations, seems to require a fixed number of configurations *per atom* for a given uncertainty'. The 2048-atom cell in particular has not reasonably converged in roughly the same amount of CPU time.

4.1.5.5 Molecular Dynamics Calculations

Table 4-13 presents the results of various MD and MC calculations, which can be grouped in the following way:

In the first two lines, elastic constants from MC calculations with cutoffs, but without splines are listed. As described in Table 4-4, the cutoff was fixed to a value of 5.35 Å (1.4 in reduced units), a distance just between the first and the second nearest-neighbour shell. The difference between these values and the reference computations is quite small (2 - 4%) but nevertheless significant. The introduction of a cutoff (even at a position where the probability of finding an atom is minimal) already has an effect on the elastic constants, which can not be neglected.

As the following lines in the table show, the use of a spline does not improve the situation - on the contrary, the elastic constants are getting less and less accurate with increasing spline width. But it is of minor importance, whether MC or MD algorithms are used, as long as both are canonical. And with MD, there is neither a clear advantage of the stress-strain fluctuation approach over the strain fluctuations. It is not possible to make more comments on that, since the evaluation of the stresses was done by Discover 94 entirely and there is no exact information how this is done.

Table 4-13: $T\sigma N$-MD and variable-shape MC results with nearest neighbors (nn) or with cutoffs with and without splines; symmetry equivalent elastic constants computed with the strain and the (linear) stress-strain fluctuation method; the shading of the cells is proportional to the difference between the actual value and the reference values listed at the bottom.

Method	Spline	Fluctuations	$\langle C_{11}, C_{22}, C_{33}\rangle^*$	$\langle C_{12}, C_{23}, C_{13}\rangle^*$	$\langle C_{44}, C_{55}, C_{66}\rangle^*$
MC	no	$\langle \eta_{ik}\eta_{lm}\rangle^{-1}$	160.63 ± 1.60	73.02 ± 0.58	84.10 ± 0.39
		$\langle \eta_{ik}\sigma_{nj}\rangle\langle \eta_{nj}\eta_{lm}\rangle^{-1}$	159.49 ± 0.38	71.45 ± 0.27	83.30 ± 0.23
MC	yes (0.4Å)	$\langle \eta_{ik}\eta_{lm}\rangle^{-1}$	173.80 ± 0.97	84.80 ± 0.61	90.50 ± 0.83
		$\langle \eta_{ik}\sigma_{nj}\rangle\langle \eta_{nj}\eta_{lm}\rangle^{-1}$	167.12 ± 0.52	78.23 ± 0.28	86.32 ± 0.23
MD	yes (0.4Å)	$\langle \eta_{ik}\eta_{lm}\rangle^{-1}$	164.86 ± 1.10	76.20 ± 0.42	89.14 ± 0.15
		$\langle \eta_{ik}\sigma_{nj}\rangle\langle \eta_{nj}\eta_{lm}\rangle^{-1}$	176.40 ± 0.62	87.87 ± 0.51	90.10 ± 0.08
	yes (1.2Å)	$\langle \eta_{ik}\eta_{lm}\rangle^{-1}$	182.09 ± 0.26	88.71 ± 0.23	102.18 ± 0.3
		$\langle \eta_{ik}\sigma_{nj}\rangle\langle \eta_{nj}\eta_{lm}\rangle^{-1}$	200.17 ± 0.09	104.78 ± 0.02	104.16 ± 0.04
MC (10^8 steps)	no (nn)	$\langle \eta_{ik}\eta_{lm}\rangle^{-1}$	157.36 ± 0.13	69.87 ± 0.24	81.97 ± 0.16
		$\langle \eta_{ik}\sigma_{nj}\rangle\langle \eta_{nj}\eta_{lm}\rangle^{-1}$	157.27 ± 0.06	69.62 ± 0.08	82.10 ± 0.06
Reference		*Cowley*	157.1 ± 1.0	69.3 ± 0.9	82.2 ± 0.2

4.1.5.6 Hybrid Monte Carlo Simulations

The results of a variable shape (EtN)-MD simulation run with relatively large time-steps at $T^* = 0.3$ are reported and compared with the 'standard' MC simulation in the following table:

Table 4-14: Symmetry equivalent elastic constants resulting from a 25'000 steps HMC run with 50 EtN-MD steps each, 108 atoms

Method	$\langle C_{11}, C_{22}, C_{33}\rangle^*$	$\langle C_{12}, C_{23}, C_{13}\rangle^*$	$\langle C_{44}, C_{55}, C_{66}\rangle^*$
$\langle \eta_{ik}\eta_{lm}\rangle^{-1}$	150.48 ± 2.55	63.30 ± 1.42	82.23 ± 3.03
$\langle \eta_{ik}\sigma_{nj}\rangle\langle \eta_{nj}\eta_{lm}\rangle^{-1}$	182.80 ± 2.49	94.96 ± 1.18	90.47 ± 0.85
MC (10^8 steps)	157.31 ± 0.11	69.74 ± 0.22	82.03 ± 0.13

The above numbers are averages over 25'000 steps, with each step consisting of a short MD simulation of 50 steps (90.36 fs step width, 5.4 Å cutoff, 0.4 Å spline). With this combination of number of steps and stepwidth, the acceptance ratio was 0.564. At the end of each MD trajectory, a modified Boltzmann weight decided whether a step was accepted or not. If yes, the new configuration served - with new velocities - as the starting point of the next simulation.

Otherwise, the old configuration initiated the next MD run. The accuracy is - considering the effort - not spectacularly good, as indicated by the difference between the strain and the stress-strain fluctuations and the scattering between symmetry equivalent elastic constants.

The HMC using a self-written code, which is mentioned at the end of chapter 4.1.3.3 yielded the following results (Table 4-15):

Table 4-15: Symmetry equivalent elastic constants from the finite stress-strain fluctuations, nearest-neighbours, $T^* = 0.3$, hybrid Monte Carlo moves with varying order of deformation and $\textit{EhN}$-MD

	$\langle C_{11}, C_{22}, C_{33} \rangle^*$	$\langle C_{12}, C_{23}, C_{13} \rangle^*$	$\langle C_{44}, C_{55}, C_{66} \rangle^*$
Deformation	156.51 ± 0.19	68.69 ± 0.24	82.25 ± 0.31
Deformation-MD	166.30 ± 0.07	74.99 ± 0.05	86.43 ± 0.04
MD-Deformation	166.63 ± 0.11	75.49 ± 0.08	86.70 ± 0.10

The pure deformation, which was performed to test the code, agreed quite well with the standard values from variable-shape MC. The results of the moves that combined random deformation and $\textit{EhN}$-MD are obviously independent on the sequence of MD and deformation, but both deviate considerably from the pure deformation MC. The reasons for this are not exactly known, since there is a large number of error sources ranging from simple programming errors to methodological deficiencies.

4.1.6 Discussion

4.1.6.1 Estimation of the Precision of the Elastic Constants

The convergence criterion (Eq. (3-37) or (3-38)) provides a useful check of whether a simulation has reached at least a stationary state or whether some relaxations still occur. In this section, the accuracy of selected calculations will be examined more closely in order to quantify the possible uncertainties. In the next section, these values will be compared with those obtained from the literature.

The selected calculations are those with the firmest theoretical basis and the longest trajectories. The canonical variable-shape MC algorithm described in chapter 4.1.3.1 is a simple and well established algorithm and the use of finite stresses allows to rigorously calculate the necessary fluctuation terms. The 108-atom cell is a balanced compromise between computational efficiency and stability, permitting to perform about 10^8 steps. This is enough to completely equilibrate the structure, since the possible relaxations of the simple fcc crystal are

quite limited.

The following figure (Fig. 4.8) shows the convergence of the elastic constants at $T^* = 0.125$. Both the strain and the finite stress-strain fluctuations
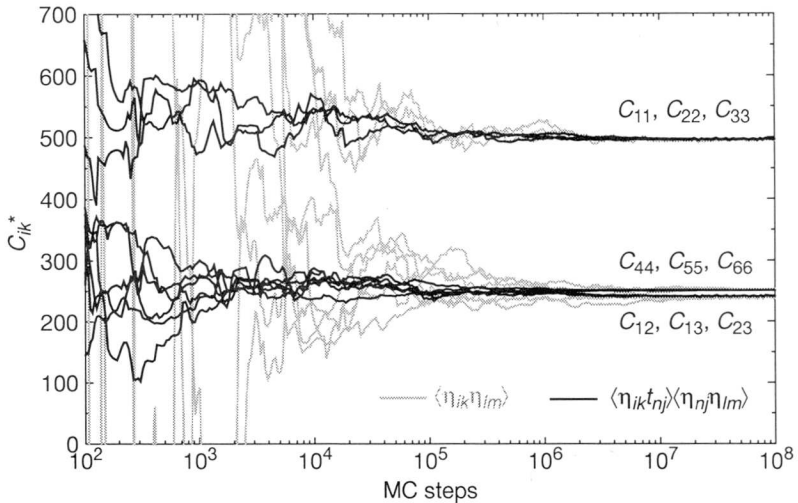

Figure 4.8: The convergence of the nonzero elastic constants of a 108-atom system at $T^* = 0.125$, 10^8 MC steps

deliver elastic constants which have converged very well after 10^8 steps as the figure and Table 4-16 show. The finite stress-strain fluctuations, however, lead to

Table 4-16: Elastic constants at $T^* = 0.125$.

$\dfrac{1}{N}\langle \eta_{ik}\eta_{lm}\rangle^{-1}$	$\dfrac{V}{NkT}\langle \eta_{ik}t_{nj}\rangle\langle \eta_{nj}\eta_{lm}\rangle^{-1}$
$\begin{bmatrix} 496.5 & 238.3 & 237.2 & -1.1 & -0.2 & 0.7 \\ 238.3 & 495.3 & 238.1 & -0.2 & 0.7 & -0.8 \\ 237.2 & 238.1 & 494.7 & 0.2 & 0.3 & 1.1 \\ -1.1 & -0.2 & 0.2 & 252.4 & -0.8 & -1.0 \\ -0.2 & 0.7 & 0.3 & -0.8 & 252.6 & 0.3 \\ 0.7 & -0.8 & 1.1 & -1.0 & 0.3 & 250.7 \end{bmatrix}$	$\begin{bmatrix} 497.1 & 240.9 & 241.2 & 0.1 & 0.2 & -0.3 \\ 241.3 & 496.5 & 240.5 & -0.1 & -0.1 & -0.2 \\ 241.6 & 240.6 & 496.3 & -0.1 & 0.0 & -0.1 \\ 0.2 & 0.0 & -0.1 & 250.4 & -0.1 & -0.2 \\ 0.5 & 0.4 & 0.3 & 0.0 & 250.5 & 0.2 \\ -0.5 & -0.3 & 0.0 & -0.1 & 0.0 & 250.2 \end{bmatrix}$

a significantly faster convergence, as already pointed out.

Several methods can be used now to estimate the precision of the elastic constants:

The first, and maybe most important check is the difference between the

strain and the finite stress-strain results, as expressed in Eq. (3-37). The relevant stress-strain correlation matrix is given below and indicates that the differ-

Table 4-17: The stress-strain correlation matrix at $T^* = 0.125$

$$\frac{1}{kT}\langle \eta_{ik} t_{nj} \rangle$$

0.996	0.003	0.008	0.004	0.001	−0.003
0.006	0.998	0.003	0.000	−0.005	0.002
−0.009	0.001	0.998	−0.001	−0.003	−0.005
0.004	0.000	−0.002	−0.992	0.003	0.003
0.002	−0.001	−0.002	0.003	0.992	0.000
−0.003	0.004	−0.003	0.004	−0.001	0.998

ence between the two methods is in the order of 0.2 - 0.4%. It is therefore not necessary to continue the simulation, since the thermodynamical equilibrium has been approached quite well.

The second, quite obvious way to estimate the reliability of the calculation offer those elements in the matrix of the elastic constants that should be zero due to the symmetry of the problem. In the above example, these elements are -0.07 ± 0.73 reduced units for the strain fluctuations and -0.01 ± 0.23 for the stress-strain fluctuations.

The third indicator, which is related to the above one, is the deviation between symmetry equivalent elastic constants. In the case of the cubic symmetry of the fcc crystal, $\{C_{11},C_{22},C_{33}\}$, $\{C_{12},C_{13},C_{23}\}$, and $\{C_{44},C_{55},C_{66}\}$ form such groups of equivalent elastic constants. The deviation within such a group is in the range of 0.3 - 0.5 reduced units for the strain fluctuations and 0.1 - 0.2 for the stress-strain fluctuations.

The forth possibility to estimate the convergence offer the symmetry of the matrix of the elastic constants or the stress-strain correlation matrix. Using the stress-strain fluctuations, the matrix of the elastic constants is not symmetric, although - as described in chapter 1.3.2 - it should be so. In the above example, the symmetric elements - zero and nonzero - differ by about 0.2 ± 0.15 reduced units.

Putting everything together, a reasonable estimate of the precision of a simulation would be the strain fluctuation formula to yield an error of ± 0.6 and the stress-strain fluctuation formula one of ± 0.2 reduced units. Since this does not contradict the precision indicated by the scattering between the symmetry equivalent elastic constants, these values are presented in the next tables.

The final - and in case of amorphous structures most important - method is the simulation of more than one structure and the comparison of the final results.

This has been done in the case of the 108-atom structures, for which two simulation runs of 10^8 steps have been executed.

Table 4-18: Average elastic constants obtained from two runs of 10^8 MC steps at the temperatures indicated, finite stress-strain fluctuation formula

T^*	Run	$\langle C_{11}, C_{22}, C_{33} \rangle^*$	$\langle C_{12}, C_{23}, C_{13} \rangle^*$	$\langle C_{44}, C_{55}, C_{66} \rangle^*$
0.125	1	496.92 ± 0.17	241.03 ± 0.09	250.35 ± 0.12
	2	496.63 ± 0.21	240.89 ± 0.18	250.35 ± 0.06
0.225	1	239.00 ± 0.20	112.58 ± 0.04	121.32 ± 0.12
	2	238.46 ± 0.17	112.13 ± 0.07	121.36 ± 0.05
0.3	1	158.30 ± 0.35	72.48 ± 0.12	81.09 ± 0.07
	2	158.38 ± 0.22	72.57 ± 0.10	81.14 ± 0.07

4.1.6.2 Static Minimum Energy Calculations

In principle, it is possible to use Eq. (1-52),

$$C^T_{ijkl} = \left(\frac{\partial t_{ij}}{\partial \eta_{kl}} \right) = \rho_0 \left(\frac{\partial^2 A}{\partial \eta_{ij} \partial \eta_{kl}} \right)_T, \qquad (1\text{-}52)$$

to get the elastic constants of a material by performing a series of deformations and minimizations. In practice, however, it is not possible to determine the free energy A directly. Instead of that, it is often assumed that the entropic contributions can be neglected and therefore the potential energy U can be used instead. The validity of this approximation is discussed in Refs [Theodorou86a] and [RutledgeSuter91a].

The 108-atom cell was minimized with a Newton-Raphson algorithm down to a maximum gradient of 10^{-4} kcal·mol^{-1}·Å^{-1}. The cell shape was included into this minimization and then deformed by a specific strain.

Since a general minimization scheme, which was used for crystalline and amorphous polymers, was applied, a detailed description is now given: In order to compute all elements of the matrix of the elastic constants, 25 deformations were carried out for each off-diagonal element (C_{ik}, $i > k$). These finite deformations consisted of all possible combinations of η_i and $\eta_k \in \{-2\eta_0, -\eta_0, 0, \eta_0, 2\eta_0\}$ with η_0 being typically 0.001. After each deformation, the cell's potential energy U_{pot} was again minimized down to 10^{-4} kcal·mol^{-1}·Å^{-1} with the cell parameters held fixed. A function

$$U_{pot}(\eta_i, \eta_k) = a_0 + a_1 \eta_i + a_2 \eta_k + a_3 \eta_i \eta_k + a_4 \eta_i^2 + a_5 \eta_k^2 \qquad (4\text{-}23)$$

was fitted to these 25 minimum values using a singular value decomposition algorithm[Pressetal92] obtained from Netlib[a].

The a_3 value of the above function is directly proportional to C_{ik}, whereas $2a_4$ is proportional to C_{ii} and $2a_5$ to C_{kk}. It was therefore not necessary to compute the diagonal terms of the elasticity matrix explicitly. The goodness of fit was estimated via a χ^2 and a gamma formalism.[Pressetal92] In all cases, the fit was excellent (i.e. no anharmonic effects at such small deformations).

The results of these calculations are given in the next table:

Table 4-19: Elastic constants of a 108 atom Lennard-Jones solid

$$\rho_0 \left(\frac{\partial^2 U_{pot}}{\partial \eta_{ij} \partial \eta_{kl}} \right)_T \text{ [red. units]} \qquad \frac{V}{NkT} \langle \eta_{ik} t_{nj} \rangle \langle \eta_{nj} \eta_{lm} \rangle^{-1}$$

7205.	3602.	3603.	0.0	0.0	0.0		7178.	3578.	3577.	0.	−4.	2.
3602.	7205.	3603.	0.0	0.0	0.0		3581.	7180.	3579.	4.	−2.	0.
3603.	3603.	7205.	0.0	0.0	0.0		3579.	3575.	7182.	4.	1.	2.
0.0	0.0	0.0	3603.	0.0	0.0		−1.	0.	2.	3594.	0.	−1.
0.0	0.0	0.0	0.0	3603.	0.0		−1.	−1.	2.	0.	3595.	2.
0.0	0.0	0.0	0.0	0.0	3603.		0.	1.	0.	2.	2.	3592.

These zero-temperature elastic constants have been converted to reduced units, assuming a low temperature of 1.198 K, and compared with MC values reproduced from Table 4-8. At this low temperature, the fluctuation approach and the static minimum energy results agree perfectly.

4.1.6.3 Comparison with Literature Values

It is not sensible to compare the isothermal elastic constants of the nearest-neighbour Lennard-Jones solid with the experimental (adiabatic) ones of a rare gas solid like argon ($C_{11} \approx 4.1$ GPa, $C_{12} \approx 2.4$ GPa, $C_{44} \approx 2.3$ GPa, extrapolated to T = 0)[Korpiun77], because - as pointed out in chapter 4.1.1 - they differ considerably in their interactions. So only model calculations using the same nearest-neighbour Lennard-Jones solid will be taken as reference. The first calculation of isothermal elastic constants was performed by Squire et al.[Squire69a] in 1968. The authors simulated a 108-atom system with corrections for the finite cutoff applied, which leads to somewhat higher elastic constants than nearest-neighbour interactions alone: C_{11} = 2.84 GPa, C_{12} = 1.61 GPa and C_{44} = 1.69 GPa at T = 40 K. The elastic constants were calculated by using a combination of fluctuation, Born, and kinetic terms obtained from a derivation of the partition function. Cowley[Cowley83a] used the same approach to make very accurate MC simula-

---

a. http://tonic.physics.sunysb.edu/docs/num_meth.html or ftp://ftp.zib-berlin.de/netlib

tions of 10^6 - 10^7 steps at various temperatures. Sprik et al.[Sprik84a] did some HtN-MD of $4 \cdot 10^4$ - 10^5 steps at $T^* \approx 0.31$, but the accuracy of their results is suffering from the shortness of the simulation runs. In 1988, Ray published an comprehensive overview including fluctuation formula for the EhN, ThN, HtN, and TtN ensemble.[Ray88a] Computations of isothermal elastic constants computed in the EhN and ThN ensemble were published previously.[Ray85a] The adiabatic and isothermal elastic constants obtained from theses publications are given in the next table (4-20):

Table 4-20: Overview over elastic constants calculations; Cowley: MC, $2.16 \cdot 10^6$, $T^* = 0.3$, 108 atoms; Sprik et al.: HtN-MD, 10^5 steps, 108 atoms, $T^* = 0.307$, 8.6 fs time step; Ray et al.: ThN-MD, $2 \cdot 10^4$ steps, 500 atoms, $T^* = 0.3$, 10 fs time step

C_{ik}^*		Cowley[Cowley83a]	Sprik et al.[Sprik84a]	Ray et al.[Ray88a]
adiabatic	C_{11}	182.0 ± 0.5	170 ± 9	185.1 ± 1.9
	C_{12}	94.1 ± 0.5	84 ± 8	95.7 ± 1.4
	C_{44}	82.2 ± 0.2	81.7 ± 0.3	81.6 ± 1.6
isothermal	C_{11}	157.1 ± 1.0	-	165.6 ± 4.9
	C_{12}	69.3 ± 0.9	-	76.3 ± 4.5
	C_{44}	82.2 ± 0.2	-	81.6 ± 1.6

Since Cowley's values are most accurate and serve as a reference in Sprik's and Ray's publications, we use the values in the shaded cells for comparison with our own results. Cowley did not only give the elastic constants at $T^* = 0.3$, but also at $T^* = 0.125$ and $T^* = 0.225$ and at higher temperatures.

Comparing these numbers with those from chapter 4.1.6.1, the final Table 4-21 can be established:

4.1.6.4 Conclusions

In the limit of thermodynamic equilibrium, the new stress-strain fluctuation formula (Eq. (3-35)) is *equivalent* to the well-established strain fluctuation formula of Parrinello and Rahman (Eq. (3-29)). Simple systems like the 108-atom nearest-neighbour Lennard-Jones solid allow very long simulations of up to 10^8 MC steps. The absence of complicated intra- and intermolecular interactions leads to a fast equilibration of the structures. It is therefore possible to approach the thermodynamic equilibrium very closely and to check for the validity of the above statement: the theoretical equivalence could be proved practically.

Table 4-21: Comparison of elastic constants results from strain and stress-strain fluctuations at $T^* = 0.125$, 0.225, and 0.3 with results from Ref. [Cowley83a]

T^*	$\overset{*}{C}_{ik}$	Eq. (3-29)	Eq. (3-35)	Cowley
0.125	C_{11}	496.12 ± 0.70	496.77 ± 0.24	494.0 ± 1.1
	C_{12}	238.00 ± 0.35	240.96 ± 0.16	237.8 ± 1.1
	C_{44}	251.36 ± 0.75	250.35 ± 0.09	250.0 ± 0.2
0.225	C_{11}	237.73 ± 0.72	238.73 ± 0.33	237.0 ± 0.8
	C_{12}	109.68 ± 0.58	112.35 ± 0.23	108.2 ± 0.8
	C_{44}	122.27 ± 0.21	121.34 ± 0.09	121.9 ± 0.2
0.3	C_{11}	157.03 ± 0.36	158.34 ± 0.28	157.1 ± 1.0
	C_{12}	69.51 ± 0.19	72.52 ± 0.11	69.3 ± 0.9
	C_{44}	81.84 ± 0.29	81.11 ± 0.07	82.2 ± 0.2

In the case of finite simulation runs, the *convergence* of the elastic constants is markedly improved by the new algorithm, especially at very low temperatures, where sampling of the phase space is slow. Here the elastic constants obtained by the new formula converge orders of magnitude faster. In the limit of zero temperature the results match those from the static minimum energy approach. Even at intermediate or high temperatures close to the melting point, the stress-strain fluctuation method is converging at least as fast as the strain fluctuation formula.

It is possible to use MC, MD, or Hybrid-MC *methods to sample* the configurational phase space of a structure. It is extremely important to do this canonically. For MC, a slight dependence of the rate of convergence, but not of the final results, on the acceptance ratio could be observed. If cutoffs and splines are used, e.g. in the MD simulations, the elastic constants depend strongly on the choice of these parameters.

The *precision* of the elastic constants is extremely high. It is possible to determine them with an accuracy of a few tenths of a percent. In order to achieve this, 10^6 to 10^8 steps are necessary even for a quite small 108-atom system. It seems that a certain number of configurations per atoms is necessary to obtain a given precision. Since it was not possible to observe significant size effects, the smallest stable crystal cell should be used. Delocalized thermal motions are obviously not significantly contributing to the elastic constants, as can also be deduced from Ref. [Cowley83a].

4.2 Polyethylene - Planar Zig-Zag Chains

4.2.1 Introduction

Polyethylene (PE) is a partially crystalline thermoplastic[Franck88], which is used in huge quantities. The mechanical properties - especially the elastic constants - are those of a typical amorphous material (i.e. 1 - 3 GPa[Ward83]). In the last decade, however, a methodology was developed to produce polyethylene with highly oriented chains.[Smith86a]. Commercially available are now filaments with a modulus of more than 100 GPa. Thus the formerly theoretical question of the ultimate modulus of a perfectly oriented PE crystal has become more and more of practical interest. It is very difficult to determine this number by experiment, because the stress that is transferred by the amorphous matrix to the crystallites is not known exactly, but depends on the morphology and the phase boundary. Therefore, the experimental values at room temperature - furthermore depending on the methodology - are scattering widely between 196 and 329 GPa[Nakamae91a,Rutledge94a].

It is not surprising that there were many trials to obtain estimates through theoretical calculations. Some examples will be briefly discussed while comparing the results of the present work with literature values (chapter 4.2.6.1), but it can already be stated that the theoretical results differ even more from each other than the experimental ones, spanning a range from 160 to more than 400 GPa (mostly at $T = 0$ K)[Nakamae91a].

In the following chapter a model of monocrystalline PE will be generated and its elastic constants will be computed using the strain and the linear stress-strain fluctuation approaches.

4.2.2 Description and Cell Generation

Linear polyethylene crystallizes in an orthorhombic unit cell (space group 62: *Pnma*)[XrayTable83] with lattice constants of $a=7.417$ Å, $b = 4.945$ Å, and $c = 2.547$ Å.[Bunn39a] The two 'all-trans' chains in this cell, which is shown in Fig. 4.9, lead to a density of 0.997 g·cm^{-3}, being in agreement with the experimental density of PE crystals, which is 1.007 ± 0.008 g·cm^{-3}[Tadokoro90]. Two different cells were generated with the 'Crystal Cell' package[MSIPolymer1] of 'InsightII':

The small simulation box consisted of $3 \times 4 \times 8$ unit cells which totaled a minimized cell size of $21.651 \times 19.608 \times 20.569$ Å with 1152 atoms. In order to prevent modelling just $C_{16}H_{34}$-chains, so-called *bonds-across-boundaries* were used, which connect one end of the chain in one periodic box with the other end
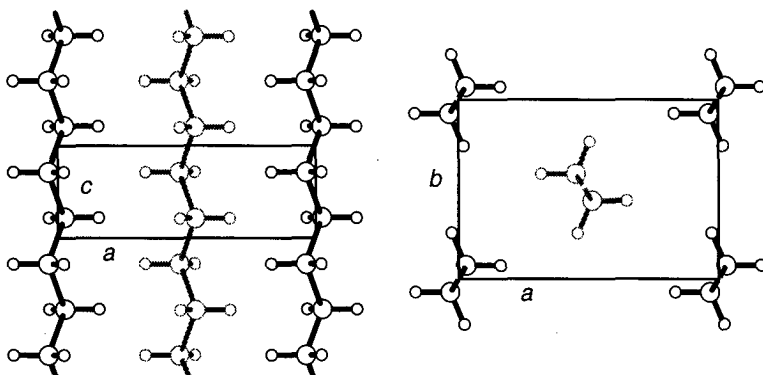
Figure 4.9: Schematic representation of the unit cell of orthorhombic Polyethylene[Bunn39a]

of its own image in a neighboring box. The chains created by this procedure do not have any ends or special points, but they are not infinite with respect to their vibrational behavior. Due to the periodic continuations conditions, collective motions along the chains will be amplified rather than damped.

As will be seen later, the stability of the relatively small cell was rather poor, so a large, thermally more stable cell was generated. This cell comprised $4 \times 6 \times 12$ unit cells and had a minimized size of $28.869 \times 29.412 \times 30.854$ Å. It contained 3456 atoms in 48 chains of 24 CH_2-groups.

The setup of these cells involved the following steps:

- Generation of a helical repeat unit and a crystal asymmetric unit (CAU) according to the 'Crystal Cell User Guide'[MSIPolymer1]

- Conversion of the CAU into a Cartesian coordinate (.car) and molecular data file (.mdf) by the 'hlx2pbc' macro provided by MSI. The number of repeat units in the chain direction was also set by this program. Manual check of the bonds across boundaries in the '.mdf' file.

- Assembly of several such cells in the other two dimensions in order to form an approximately cubic shape.

For the subsequent molecular mechanics and dynamics simulations, the *pcff91* and the *scaled_pcff* forcefields were used. They differ by about 3 % in the σ values of the Lennard-Jones interaction parameters of carbon and hydrogen atoms. This reduction was made, because the densities of hydrocarbon compounds are generally somewhat too low (a more detailed discussion of this problem is given in chapter 4.5.2.2).

4.2.3 Simulation Procedure

4.2.3.1 Small Cell Equilibration

The small crystal cell was equilibrated at 300 K using $T\sigma N$-MD for 230 ps. The *pcff91*-forcefield and a cutoff of 8.5 Å (spline: 0.5 Å) made it necessary to use a tail-correction pressure of 1417 bar. A Parrinello-Rahman pressure control with a cell mass of 20 a.m.u. was used to keep the average pressure at this level. The timestep was set to 0.5 fs, because of the Nosé-Hoover thermostat. The final density (averaged over the last 10 ps) was 0.958 g·cm^{-3}.

In dynamics, it turned out that the size of this cell was too small, as Fig. 4.10 shows:
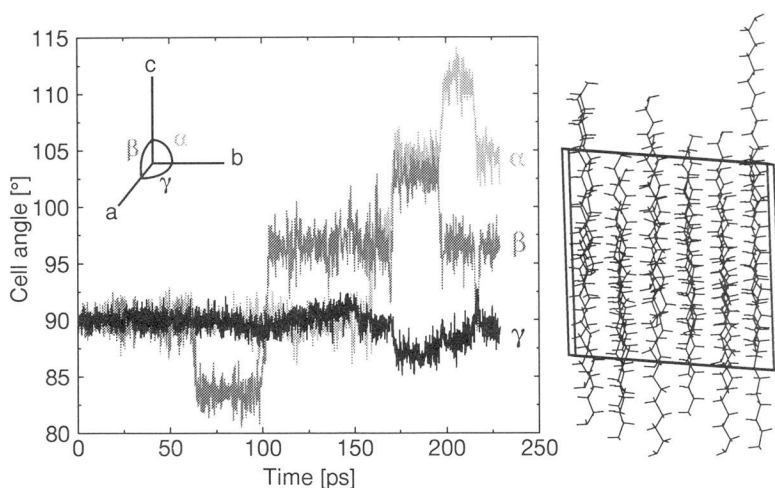
Figure 4.10: The cell angles of the small PE crystal as a function of the MD-time; the cell after 230 ps

The cell angles, especially α and β undergo sudden, sometimes simultaneous, jumps of 6 to 7 degrees. This phenomenon becomes more clear when the final structure is examined: The thermal fluctuations, which are very large for such a small structure (about 5 %), led to a rearrangement of some chains in the structure. These chains were simultaneously shifted by one crystal repeat unit. This process occurred several times during the simulation. A second, closely related process is the diffusion of individual chains along their axes, as a result of the low friction along the chain direction.

There are several possibilities to circumvent the above problem: One is to use the ThN-ensemble where the cell shape is fixed, another - similar - solution

seems to be the increase of the cell mass W (Eq. (2-67)). But this last change does actually not reduce the amplitude but the frequency of the thermal fluctuations. The method chosen in this work is the enlargement of the simulation cell, since this reduces the absolute (and therefore even more the relative) fluctuations of the cell, as described in chapter 3.2.3. The diffusion of the chains along their axes is also hindered, which could not be achieved by switching to the *ThN*-ensemble.

4.2.3.2 Large Cell Equilibration

Generating a large cell, performance and stability have to be balanced to achieve a reasonable compromise. The cell parameters of the large simulation box have been given in chapter 4.2.2. After the generation and an initial minimization, a *TσN*-simulation over 150 ps in 0.5 fs steps was started. The standard cutoff and spline of 8.5 and 0.5 Å and Parrinello-Rahman and Nosé-Hoover control algorithms were applied to keep the temperature at 300 K and the pressure at a net value of 1 bar. The *scaled_pcff* forcefield demanded a somewhat reduced correction pressure of 1281 bars. The cell remained stable during the simulation, as Fig. 4.11 reveals:
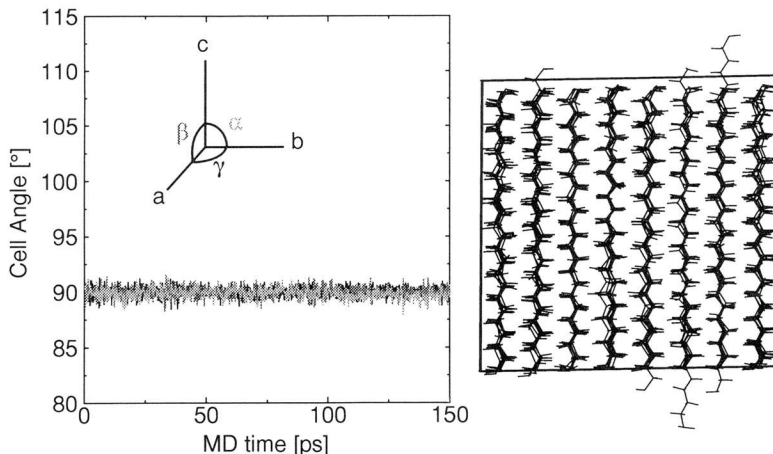

Figure 4.11: The cell angles of the large PE cell as a function of the MD time (with same scale as in Fig. 4.10 for better comparison); the large PE cell after 150 ps

No collective transformations and hardly any chain diffusion could be observed. The average density during this simulation was 0.995 ± 0.008 g·cm^{-3}, which is much closer to the experimental value of 1.007 g·cm^{-3}, justifying the use of the *scaled_pcff* forcefield.

4.2.4 Results

4.2.4.1 Effect of the Cell Mass on the Mechanical Relaxation Spectrum

Despite its deficiencies, the small cell was used for a short investigation of the influence of the cell mass on the spectrum of the mechanical relaxation. The mechanical relaxation spectrum (MRS) is the Fourier transform of the time-auto-correlation function of a mechanically relevant quantity. In the case of PE, the length of the cell vector parallel to the chain direction was used as the relevant degree of freedom.

There are two ways of weighting the amplitudes of the frequencies to obtain the contributions to the total fluctuation (the compliance) of the polymer[Landau86c]. They both use the *fluctuation-dissipation theorem*:

The first one is a classical approximation that holds, if $kT \gg \hbar\omega/2\pi$, which is the case if $\omega/2\pi \ll 6.25 \cdot 10^{12}$ Hz:

$$\langle x^2 \rangle = \frac{2kT}{\pi} \int_0^\infty \frac{\alpha''(\omega)}{\omega} d\omega \qquad (4\text{-}24)$$

$\alpha''(\omega)$ is the imaginary part of the Fourier transform of the fluctuating quantity $x(t)$. So this approximation is obviously not valid for most of the frequencies appearing in our calculations.

According to the above considerations, it would be more appropriate to use the quantum mechanical formula.

$$\langle x^2 \rangle = \frac{\hbar}{2\pi^2} \int_0^\infty \alpha''(\omega) \coth\left(\frac{\hbar}{4\pi} \frac{\omega}{kT} \right) d\omega \qquad (3\text{-}24)$$

The problem with this approach is that the system that produces the fluctuations is a completely classical one.

Besides these transformations, both the classical and the quantum mechanically weighted spectra were numerical integrated in order to estimate the contribution of individual processes to the total compliance.

A set of simulations was performed at 300 K with the familiar $T\sigma N$-MD algorithm and the *scaled_pcff* forcefield. A small box was used to perform 200 ps, with each 0.5 fs step being recorded to the disk for later evaluation. From these $4 \cdot 10^5$ steps, the last 262'144 (2^{18}) were taken for the computation of the time-autocorrelation function of the cell edge length c. The first half of this autocorrelation function was transformed using a fast Fourier (Cooley-Tukey FFT) algorithm and weighted according to Eqs (4-24) and (3-24). The cell masses W were

set to 1, 10, 100 and 1000 a.m.u., respectively.

Figure 4.12 makes the comparison between the classical and the quantum mechanical weighting of the fluctuations of a cell with a pressure control mass $W = 1$. There are relatively large contributions at the low-frequency end of the
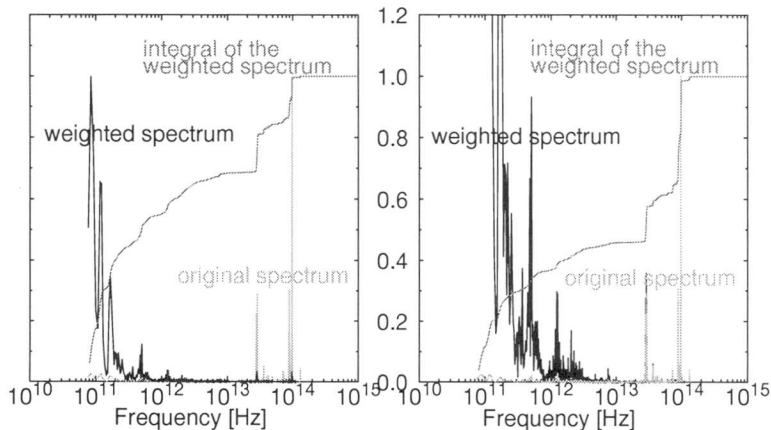

Figure 4.12: Classical and quantum mechanical weighting of the mechanical relaxation spectrum; small PE crystal with $W = 1$

spectrum, where the statistical uncertainty is largest. So this part is not very meaningful. The peaks at $3 \cdot 10^{13}$ and 10^{14} Hz, however, are significant and their contribution to the mechanical relaxation spectrum depends on whether a classical or a quantum mechanical approach is made. The peak at 10^{14} Hz can be attributed to bond length and the one at $3 \cdot 10^{13}$ Hz to bond angle fluctuations.

With heavier cell masses, the peaks shift to lower frequencies and their relative contributions change such that the peak at originally at 10^{14} Hz becomes more and more dominant, as Fig. 4.12 shows. The shift in the frequencies is proportional to the square root of the cell mass. The classical and the quantum mechanical approach yield almost identical curves.

4.2.4.2 Elastic Constants of Orthorhombic PE

As the small crystal cell could not be used for the calculation of the elastic constants, the MD simulation of the large PE cell was taken for this purpose. The elastic constants were determined from the last 100 ps from information stored in 'table' files. In these table files, the cell parameters (a, b, c, α, β, and γ) and the six components of the stress tensor (σ_{xx}, σ_{yy}, σ_{zz}, σ_{yz}, σ_{xz}, and σ_{xy}) have been recorded during the simulation at an interval of 1 fs.
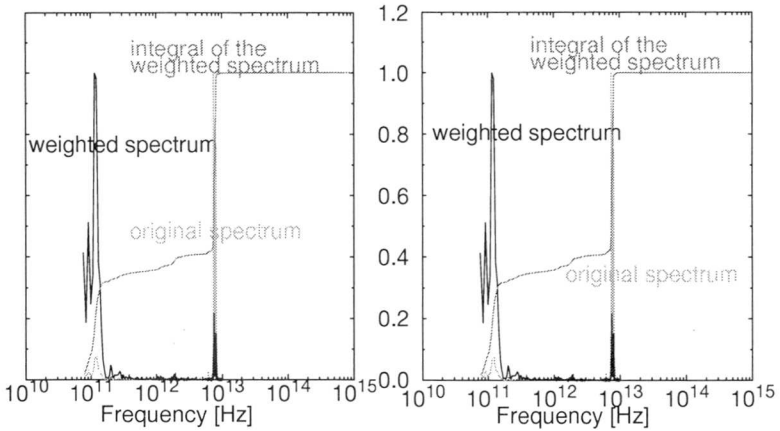
Figure 4.13: Classical and quantum mechanical weighting of the mechanical relaxation spectrum; small PE crystal with $W = 100$

The program 'ElastFluct.f' reads these table files and computes the elastic constants using both the strain and the linear stress-strain fluctuation formula. Besides this, the stress-strain correlation and the eigenvalues of the matrices of the elastic constants are printed. Figure 4.14 displays the convergence of the
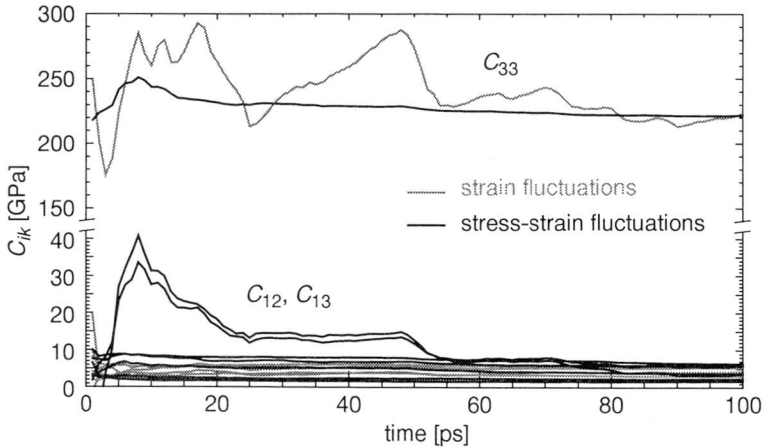

Figure 4.14: Convergence of the elastic constants of PE during the last 200 ps of $T\sigma N$-MD

elastic constants. The final value of the C_{33}-component is almost the same, whereas the convergence of the stress-strain fluctuations is much smoother than

that of the strain fluctuations. In contrast to that, the C_{12} and C_{13} components computed from the stress-strain fluctuations exhibit a strange peak at about 8 ps which seems to be related to instabilities of the C_{33}-values. The precise nature of these spikes is not known.

The temporal evolution of the elements of the stress-strain correlation matrix is plotted in Fig. 4.15. This matrix should converge towards an identity matrix in the limit of thermodynamic equilibrium.
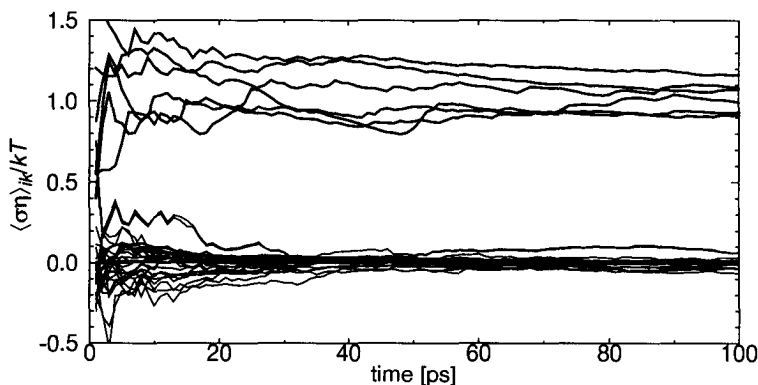

Figure 4.15: Stress-strain correlations as function of the correlation length. The diagonal elements (thick lines) converge slowly towards one, whereas the off-diagonal elements (thin lines) tend to zero.

Finally, the matrices of the elastic constants are listed below:

Table 4-22: Elastic constants averaged over the last 100 ps of a 150 ps *TσN*-MD simulation. Components that should be non-zero according to the symmetry of the crystal (chapter 1.3.4) are bold faced.

$\dfrac{kT}{\langle V\rangle}\langle\eta_{ik}\eta_{lm}\rangle^{-1}$ [GPa]

5.25	**3.11**	**4.29**	0.06	0.02	0.6
3.11	**5.36**	**5.83**	−0.03	−0.06	0.37
4.29	**5.83**	223.29	0.12	0.03	−0.60
0.06	−0.03	0.12	**2.31**	0.17	0.02
0.02	−0.06	0.03	0.17	**1.81**	0.06
0.6	0.37	−0.60	0.02	0.06	**2.14**

$\langle\eta_{ik}\sigma_{nj}\rangle\langle\eta_{nj}\eta_{lm}\rangle^{-1}$ [GPa]

5.81	**3.67**	**3.70**	−0.09	0.02	0.65
3.94	**6.41**	**5.98**	0.04	−0.05	0.49
4.20	**5.73**	221.72	0.13	0.03	−0.62
−0.05	−0.02	0.36	**2.11**	0.10	0.03
0.04	−0.03	−0.02	0.08	**1.67**	0.05
0.64	0.38	−1.51	0.06	0.06	**2.32**

All Eigenvalues of the above matrices are positive, guaranteeing the mechanical stability of the structure.

4.2.4.3 Static Minimum Energy Calculation

The same minimization procedure as in chapter 4.1.6.2 was used to compute the matrix of the elastic constants at 0 K. Using a unit cell and the *scaled_pcff* forcefield, the numbers in Table 4-22 were obtained.

Table 4-23: Elastic constants of PE: static minimum energy (left) and stress-strain fluctuation approach at 300 K (right).

$$\frac{1}{V_0}\left(\frac{\partial^2 U_{pot}}{\partial \eta_{ij}\partial \eta_{kl}}\right)_T \text{ [GPa]}$$

$$\langle \eta_{ik}\sigma_{nj}\rangle \langle \eta_{nj}\eta_{lm}\rangle^{-1} \text{ [GPa]}$$

10.89	5.02	1.81	0.0	0.0	0.0	5.81	3.67	3.70	−0.09	0.02	0.65
5.02	8.19	3.03	0.0	0.0	0.0	3.94	6.41	5.98	0.04	−0.05	0.49
1.81	3.03	251.49	0.0	0.0	0.0	4.20	5.73	221.72	0.13	0.03	−0.62
0.0	0.0	0.0	3.52	0.0	0.0	−0.05	−0.02	0.36	2.11	0.10	0.03
0.0	0.0	0.0	0.0	2.03	0.0	0.04	−0.03	−0.02	0.08	1.67	0.05
0.0	0.0	0.0	0.0	0.0	4.07	0.64	0.38	−1.51	0.06	0.06	2.32

A comparison with the fluctuation results at 300 K shows that the influence of temperature can not be neglected, especially for the off-diagonal elements. The only exception is C_{33}: this value is not very much affected by temperature and does not change by more than 1%, if the strains were chosen to be ten times smaller or the maximum gradient for the minimization was allowed to be ten times larger).

4.2.5 Interlude: Amorphous Polyethylene

4.2.5.1 Structure Generation

PE, as mentioned in the introduction, is a semi-crystalline material and its elastic behaviour depends on both the elastic properties of the crystalline and the amorphous part. To determine the latter, the standard simulation routine for amorphous structures was used:

- To obtain a cubic structure of approx. 25 Å size, a chain of 600 CH_2 groups was generated and terminated with hydrogens at both ends. To avoid problems in the subsequent packing, the chain was randomized (without cutoffs) by 5 ps at 500 K and 3 ps at 300 K.

- Using this chain, 5 simulation cells were generated with 'Amorphous Cell' at 300 K and a density of 0.95 g·cm^{-3}. After minimization (5000 steps down to 0.001 kcal·mol^{-1}·Å^{-1}), the three structures with the lowest energies were used in the following dynamics runs.

- Each of the three structures was first held for 50 ps in a *ThN*-ensemble and then for 25 ps in an *TσN*-ensemble. For the second ensemble, an automatic

van-der-Waals tail correction was used, which yielded an average correction pressure of 1005, 1007, and 998 bars and an reduction of the average density down to 0.83 g·cm^{-3}. This reduction is partly explainable by the use of the *pcff91*-forcefield, which is known to overestimate the van-der-Waals radii and/ or the C-H bondlength.

- The production run for each structure consisted in 1 ns of *TσN*-MD at 300 K with a correction pressure of 1005 bars.

4.2.5.2 Simulation Results

These production runs, however, have been stopped after a few hundred picoseconds, because of cell instabilities:
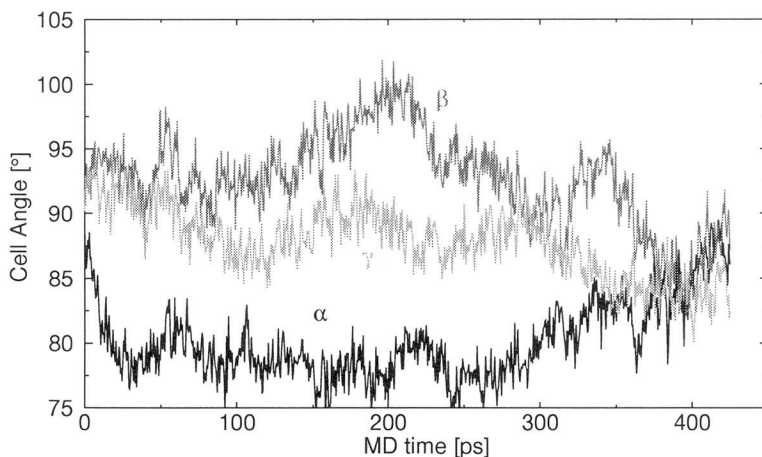
Figure 4.16: Cell angle fluctuations of the first structure of amorphous PE at 300 K.

All simulation cells made large fluctuations in the cell angles, such as those of the first structure shown in Fig. 4.16. The state of the cells could be described as 'melt-like' and the shear moduli would tend to zero for infinitely long trajectories. It was therefore not possible to compute the elastic constants. To do so, larger cells are required and it might be necessary to sample the stress-fluctuations in a *ThN*-ensemble.

4.2.6 Discussion

4.2.6.1 Comparison with Literature Values

It is quite difficult to compare the C_{33} value of about 220 GPa obtained by the fluctuation formula with data from the literature. The first uncertainty is the

convergence of the calculation, which can roughly be estimated by the using the same techniques as in chapter 4.1.6.1. Based on the stress-strain correlations, for example, the uncertainty is found to be in the range of 10 - 15% (Fig. 4.15). The other possible checks (crystal symmetry restrictions, and symmetry of the matrix of the elastic constants) lead to more conservative estimates. It would therefore be desirable to perform a more extended sampling of the phase space by either a longer MD trajectory or a specialized MC algorithm. With the large cell necessary for thermal stability, however, 1 fs of MD takes about 6 CPU seconds on a workstation.

The second - and in this case even larger - uncertainty is the scattering of the experimental and theoretical values. They range from 160 to more than 400 GPa, with the 'observed' values concentrating between 220 and 230 GPa[Nakamae91a] and quantum mechanical and semi-empirical results ranging from 276 to 420 GPa[Herena96a]. It might be interesting to comment on some experimental and theoretical work:

Matrices of the elastic constants have been calculated by Odajima and Maeda[Odajima66a], Anand[Anand67a], Sorensen *et al*[Boyd88a] and many others. Not only the C_{33} element varies from 242 to 341 GPa but also C_{11} is between 4.8 and 14.3 GPa and C_{22} between 2.9 and 12.2 GPa.

Often, it is not clearly indicated at which temperature these values were measured or calculated. Experiments from Barham *et al.*[Barham79a] show a strong dependence of the modulus of PE fibres ranging from 262 GPa (288 GPa, if corrected) at 77 K down to about 140 GPa at room temperature. Part of this reduction seems to originate from morphological changes so only a small part can be attributed to a reduction of the crystal modulus.

A more recent theoretical analysis by Lacks and Rutledge[Rutledge94a] estimates that the zero temperature C_{33} value is 316 GPa and the one at room temperature 290 GPa (C_{11} and C_{22} are both 8.8 GPa). This fits quite well into the extrapolations made by Irvine and Smith[Smith86a], where experimental results are well fitted by assuming an axial modulus of 300 GPa. The value of 349 GPa obtained by Meier[Meier93a] was corrected by himself to 333 GPa for the single chain and 299 GPa for the crystal as a whole (at 0 K)[Meier96a]. The same 299 GPa are also supported in a discussion of quantum mechanical and semiempirical calculations made by Crist and Hereña.[Herena96a] A most recent *ab initio* MD calculation from Hageman *et al.*[Hageman97a] yields an ultimate Young modulus of 334 GPa.

4.2.6.2 Conclusions

It is not the purpose of this work to defend the 220 GPa obtained from the fluctuation approach heavily, because the fluctuations have not fully converged. Furthermore, this number depends largely on the forcefield (in particular on the C-C bond stretching and angle bending parameters). The static minimum energy result of about 250 GPa yields a *temperature dependence* consistent with other results but seems to be too low by about 50 GPa with respect to the zero-temperature values obtained from quantum-mechanical and semi-empirical calculations and extrapolations of experimental results. These (and the necessity to scale van-der-Waals parameters to compensate for long C-H bonds[a]) are strong indications that the *scaled_pcff* force field is not perfectly adequate for the simulation of hydrocarbons.

Irrespective of the force field used, the intermolecular interactions between individual PE chains are very weak, both in crystals and in the amorphous phase. This makes it necessary to use relatively large simulation cells, which in turn reduce the effectiveness of the fluctuation formula, demanding long simulation runs.

Despite this restriction, the fluctuation approaches seem to be capable of reproducing the temperature dependence of the elastic constants. The C_{33} value obtained from the new stress-strain fluctuation method converges considerably faster than the one from the strain fluctuation approach. The combination of the two methods - the stress-strain correlation matrix - allows for a quantitative estimation of the degree of convergence.

a. E. Leontidis, private communication (1997)

4.3 Polypropylene - Helical Chains

4.3.1 Introduction

Similar to polyethylene, polypropylene (PP) is also a technologically important thermoplastic with poorly understood mechanical properties. The experi-
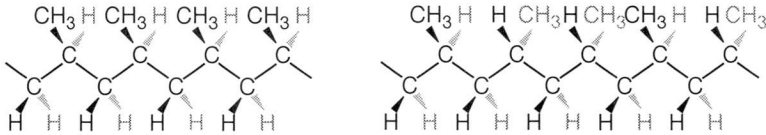
Figure 4.17: Isotactic (left) and atactic (right) polypropylene

mental values of the crystal modulus of isotactic PP (it-PP), for example, range from 18 to 80 GPa.[Hong90a] This quite low value - less than a third of that of PE - has its origin in the lower density of chains (2.9 chains$\cdot$nm^{-2} vs. 5.5 chains$\cdot$nm^{-2}) and in the helical structure of the chains in the crystal. Elongations of the crystal do result not only in bond and angle but also in torsion deformations, which tend to 'unwind' the helix.

4.3.2 Crystal Modifications and Cell Generation

4.3.2.1 Crystal Modifications

There are several crystal modifications of it-PP[Tadokoro90,Corradini83a]: the monoclinic α-form, the most stable one, which was simulated in this work, the hexagonal β- and the trigonal γ-form. Another monoclinic γ-form is reported, too.[Ferro92a] The α-modification was first described by Natta and Corradini[Natta60a]: they reported a monoclinic structure with $a = 6.65 \pm 0.05$ Å, $b = 20.96 \pm 0.15$ Å, $c = 6.5 \pm 0.05$ Å, and $\beta = 99\ 20' \pm 1$.

The detailed structure of the it-PP crystal is quite complicated, since the individual chains form 3/1 helices, which can be either left(L)- or right(R)-handed. In addition to that, the methyl groups, which are directed outwards of the helix, can point up ($\uparrow$) or down ($\downarrow$), resulting in four different possible conformations. The most regular structure is the one shown schematically in Fig. 4.18 c) with the four possible helix conformations distributed on a regular grid. However, it was found[Tadokoro92a] that this 'ordered' crystal lattice only appears after annealing at higher temperature. In 'native' PP crystals, the distribution of left- and right-handed chains is the same, but the methyl groups point up or down randomly (Fig. 4.18 b)). The disordered structure shown in Fig. 4.18 a) and d) and used for most of the following calculations, is therefore
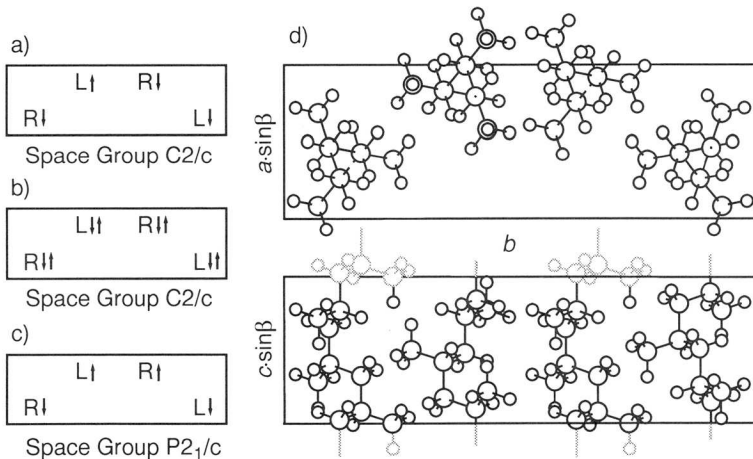
Figure 4.18: The PP crystal cell: a) schematic setup of the PP cell used for the simulations, b) randomly distributed *up* or *down* helices appearing in 'native' α-it-PP. c) ordered α-it-PP structure, d) atomistically detailed unit cell according to a).

stable as well. For comparison, an ordered structure according to Fig. 4.18 c) was built and simulated as well.

4.3.2.2 Structure Generation

A simulation cell containing $3 \times 1 \times 3$ unit cells and $9 \cdot 108 = 972$ atoms was built, using the 'Crystal Cell' module[MSIPolymer1] in the 'Insight' modelling environment. In order to do this, helical repeat units of the four different helix conformations had to be generated and placed into the crystal asymmetric unit (CAU). The values of the fractional positions, the setting angle, and the vertical offset are given in Table 4-24:

Table 4-24: Parameters for setting of the helices for the ordered it-PP α-crystal

Helix		R↓	L↓	L↑	R↑
Fractional coordinates	a	0.0	0.0	0.5	0.5
	b	0.125	0.875	0.375	0.625
Vertical offset [Å]		-2.0	-3.2	1.25	-2.0
Setting angle [°]		-135.0	15	-72.0	72.0

Using periodic continuation conditions, the fractional coordinates and the vertical offset are only meaningful relative to each other. In the structure used for almost all simulations, the last helix in the above table was an R↓ instead of a R↑ helix.

This CAU was converted into a cartesian coordinate file and surrounded by the appropriate number of unit cells, which were merged into one simulation box of approximately cubic shape with a edge length of about 20 Å. As in the case of PE, 'bonds across boundaries' were applied to connect the chain ends of neighbouring cells. The *pcff91* forcefield was able to reproduce the experimental cell shape sufficiently well, as is shown in the next table:

Table 4-25: Cell shape at 300 K (average taken from 530 to 930 ps (20'000 frames) of a *TσN*-MD run, Comparison with corresponding experimental values (from ref. Natta60a)

	a [Å]	*b* [Å]	*c* [Å]	α [°]	β [°]	γ [°]
Simulation	19.70	21.06	19.95	89.5	98.5	89.3
Experiment	19.95	20.96	19.50	90.0	99.3	90.0

4.3.3 Simulation Procedure

4.3.3.1 MD Simulations

The cell generated with the above methodology and setting parameters was first minimized in order to remove the largest energy terms. A short minimization of a few hundred steepest-descent or conjugate gradient steps should always be done after the generation of a structure, because the geometry of the repeat units and groups used to build it is only adapted for a particular force field (*cvff* in the case of the MSI/Discover software) and needs to be changed if another force field is applied.

The elastic constants of it-PP were calculated at three different temperatures, 300 K (25°C), 335 K (60°C), and 375 K (100°C). In the *TσN*-ensemble, the strain-strain and the stress-strain fluctuation formula were used. In addition to these calculations, simulations in the *ThN*-ensemble were started to compute the Born and the stress-fluctuation terms (details are given in the next chapter).

Table 4-26: Overview of the MD simulations performed with it-PP crystals

Temperature	*TσN*	Born-*ThN*	Fluct-*ThN*
300 K (25°C)	1000 ps	50 config.	250 ps
335 K (60°C)	580 ps	50 config.	250 ps
375 K (100°C)	1000 ps	50 config.	250 ps

Table 4-26 lists the MD simulations performed in the two ensembles. The configurations necessary for the Born term were taken at intervals of 20 fs from a 1 ps

ThN simulation. The cell shape used in the ThN-ensemble was the average cell shape of the ToN-simulation.

The temperature was kept constant in all simulations by a Nosé-Hoover thermostat, which in turn limited the stepsize to 0.5 fs. The default coupling constant Q (see chapter 2.5.2.3) and a cell mass $W = 20$ were applied. Regardless of the density, all constant-stress calculations were performed by using a tailcorrection pressure of 1417 bar.

4.3.3.2 Elasticity from Stress Fluctuations in the ThN-Ensemble

Elastic constants can not only be computed from strain fluctuations in the ToN-ensemble but also from stress-fluctuations in the ThN-ensemble.[Ray88a] There are three terms that add up to the elastic constants:

The *Born term*, which is represents the elastic constants at 0 K, is computed similar to the static minimum energy elasticity by deforming an instantaneous frame and measuring the change of the internal stresses at 0 K:

$$C_{ik}^{Born} = \langle \frac{\partial \sigma_i}{\partial \varepsilon_k} \rangle \qquad (4\text{-}25)$$

The *kinetic energy term*, which is the bulk modulus (compressibility) of an ideal gas at the simulation temperature, compensates the neglect of temperature in the Born term:

$$C_{ik}^{Kinetic} = -\frac{NkT}{V}. \qquad (4\text{-}26)$$

The last term - the *stress fluctuation term* - takes into account that the atoms in the crystal do not form a monoatomic Bravais lattice and that there are other deviations from the ideal behaviour:

$$C_{ik}^{Fluctuation} = \frac{V}{kT} \langle \sigma_i \sigma_k \rangle. \qquad (4\text{-}27)$$

The stress σ is the actual stress minus the average stress, since it is assumed that the cell is in a stress-free state (should be checked!).

4.3.4 Results

4.3.4.1 Static Minimum Energy Calculations

The procedure described in chapter 4.1.6.2 was applied to compute the elastic constants using the *pcff91* forcefield. The results of the static minimum energy approach are listed in Table 4-28.

Table 4-27: Static minimum energy elastic constants (left) compared with results from stress-strain fluctuations at 300 K (right).

$\dfrac{1}{V_0}\left(\dfrac{\partial^2 U_{pot}}{\partial \eta_{ij}\partial \eta_{kl}}\right)_T$ [GPa]	$\langle \eta_{ik}\sigma_{nj}\rangle \langle \eta_{nj}\eta_{lm}\rangle^{-1}$ [GPa]
$\begin{bmatrix} 12.11 & 5.80 & 8.43 & 0.0 & -0.41 & 0.0 \\ 5.80 & 10.82 & 4.84 & 0.0 & -0.20 & 0.0 \\ 8.43 & 4.84 & 62.58 & 0.0 & -5.45 & 0.0 \\ 0.0 & 0.0 & 0.0 & 3.12 & 0.0 & 0.20 \\ -0.41 & -0.20 & -5.45 & 0.0 & 6.24 & 0.0 \\ 0.0 & 0.0 & 0.0 & 0.20 & 0.0 & 4.53 \end{bmatrix}$	$\begin{bmatrix} 8.79 & 3.96 & 7.33 & 0.12 & 0.43 & -0.35 \\ 4.00 & 7.24 & 3.83 & 0.24 & -0.62 & 0.04 \\ 7.78 & 4.02 & 58.84 & 0.87 & -7.56 & -0.26 \\ 0.19 & 0.26 & 0.84 & 2.57 & 0.18 & -0.63 \\ -0.40 & -0.70 & -2.98 & 0.13 & 5.26 & -0.48 \\ -0.11 & 0.03 & 0.01 & -0.27 & -0.49 & 2.02 \end{bmatrix}$

4.3.4.2 MD Simulations

The results of the MD simulations are given in the next few tables. The first table (Table 4-28) shows the average of the cell shape taken from the last

Table 4-28: Average it-PP cell parameters, obtained from the last 500 ps of $T\sigma N$-MD

T [K]	$\langle a\rangle$ [Å]	$\langle b\rangle$ [Å]	$\langle c\rangle$ [Å]	$\langle\alpha\rangle$ [°]	$\langle\beta\rangle$ [°]	$\langle\gamma\rangle$ [°]
300	19.700	21.053	19.954	89.52	98.51	89.32
335	19.755	21.173	19.958	89.56	98.52	89.37
375	19.811	21.313	19.962	89.59	98.58	89.38

10^6 MD steps (500 ps). From this information, it is possible to estimate the thermal expansion coefficient in the a-, b-, and c-direction. The corresponding table (4-29) compares the expansion coefficients obtained from the above simulation at 300 K with experimental values and with simulation results from Lacks and Rutledge.[Rutledge95a] The thermal expansion in the a- and b- directions is quite

Table 4-29: Thermal expansion coefficients from Table 4-28, from experiment and from Lacks and Rutledge[Rutledge95a]

[10^{-5} K^{-1}]	this work	experiment	Lacks and Rutledge	
α_a	8.0	6.2	8.2	7.3
α_b	16.2	15	8.7	7.2
α_c	0.57	-1.0, -0.45	-0.84	-0.48

well reproduced, but in the c-direction a small expansion is predicted instead of the observed contraction. The difference between experimental and simulated values is small, allowing minor effects to come into play.

The average normal stresses lower with temperature from ~1300 bars to ~1270 bars, whereas the shear stresses are hardly affected by temperature and remain in the range of 2-4 bars. The average normal stresses differ from the applied correction pressure of 1417 bars by more than 100 bars, due to the finite step size (0.5 fs) of the simulation.

The next three tables, Table 4-30 to 4-33, list the matrices of the elastic

Table 4-30: Elastic constants averaged over the last 500 ps of a 1000 ps $T\sigma N$-MD simulation at 300 K. Non-zero components are bold faced.

$\dfrac{kT}{\langle V \rangle} \langle \eta_{ik}\eta_{lm} \rangle^{-1}$ [GPa]						$\langle \eta_{ik}\sigma_{nj} \rangle \langle \eta_{nj}\eta_{lm} \rangle^{-1}$ [GPa]					
8.33	**3.73**	**7.22**	–0.02	**0.28**	–0.22	**8.79**	**3.96**	**7.33**	0.12	**0.43**	–0.35
3.73	**6.95**	**3.63**	0.22	**–0.73**	0.05	**4.00**	**7.24**	**3.83**	0.24	**–0.62**	0.04
7.22	**3.63**	**54.76**	0.86	**–6.26**	–0.32	**7.78**	**4.02**	**58.84**	0.87	**–7.56**	–0.26
–0.02	0.22	0.86	**2.47**	0.05	**–0.46**	0.19	0.26	0.84	**2.57**	0.18	**–0.63**
0.28	**–0.73**	**–6.26**	0.05	**5.82**	–0.53	**–0.40**	**–0.70**	**–2.98**	0.13	**5.26**	–0.48
–0.22	0.05	–0.32	**–0.46**	–0.53	**2.11**	–0.11	0.03	0.01	**–0.27**	–0.49	**2.02**

constants obtained from strain and stress-strain fluctuations. The convergence of the individual matrix elements (from stress-strain fluctuations) at 300 K is shown in Fig. 4.19. A detailed discussion of these values will follow in
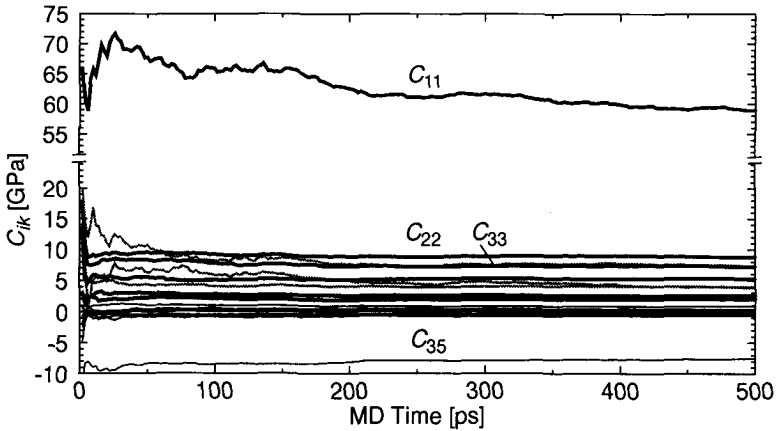
Figure 4.19: Convergence of the elastic constants of it-PP (stress-strain fluctuations, diagonal elements as heavy lines; C_{12}, C_{13}, and C_{23} in heavy grey lines), simulation at $T = 300$ K

chapter 4.3.5. Despite the large negative number found for the C_{35} component, *all eigenvalues of all matrices are positive, guaranteeing mechanical stability.*

Table 4-31: Elastic constants averaged over the last 500 ps of a 580 ps TσN-MD simulation at 335 K. Non-zero components are bold faced.

$$\frac{kT}{\langle V\rangle}\langle\eta_{ik}\eta_{lm}\rangle^{-1}\ [\text{GPa}]$$

$$\begin{bmatrix}
\mathbf{7.93} & 3.62 & \mathbf{7.12} & 0.10 & \mathbf{-0.54} & -0.13 \\
3.62 & \mathbf{6.61} & 3.53 & 0.14 & \mathbf{-0.65} & 0.04 \\
\mathbf{7.12} & 3.53 & \mathbf{55.96} & 0.76 & \mathbf{-6.50} & -0.28 \\
0.10 & 0.14 & 0.76 & \mathbf{2.51} & 0.01 & \mathbf{-0.49} \\
\mathbf{-0.54} & \mathbf{-0.65} & \mathbf{-6.50} & 0.01 & \mathbf{5.44} & -0.41 \\
-0.13 & 0.43 & -0.28 & \mathbf{-0.49} & -0.41 & \mathbf{1.90}
\end{bmatrix}$$

$$\langle\eta_{ik}\sigma_{nj}\rangle\langle\eta_{nj}\eta_{lm}\rangle^{-1}\ [\text{GPa}]$$

$$\begin{bmatrix}
\mathbf{8.23} & 3.75 & \mathbf{7.68} & 0.09 & \mathbf{0.27} & -0.21 \\
3.91 & \mathbf{7.02} & 4.05 & 0.14 & \mathbf{-0.92} & 0.12 \\
7.31 & 3.72 & \mathbf{58.16} & 0.77 & \mathbf{-7.57} & -0.22 \\
0.18 & 0.25 & 0.89 & \mathbf{2.55} & 0.16 & \mathbf{-0.67} \\
-0.58 & -0.70 & -2.68 & 0.11 & \mathbf{5.02} & -0.41 \\
-0.13 & 0.03 & -0.22 & \mathbf{-0.27} & -0.39 & \mathbf{1.87}
\end{bmatrix}$$

Table 4-32: Elastic constants averaged over the last 500 ps of a 1000 ps TσN-MD simulation at 375 K. Non-zero components are bold faced.

$$\frac{kT}{\langle V\rangle}\langle\eta_{ik}\eta_{lm}\rangle^{-1}\ [\text{GPa}]$$

$$\begin{bmatrix}
\mathbf{7.67} & \mathbf{3.24} & \mathbf{7.18} & 0.05 & \mathbf{-0.42} & -0.17 \\
3.24 & \mathbf{6.30} & 3.84 & 0.14 & \mathbf{-0.71} & 0.09 \\
\mathbf{7.18} & 3.84 & \mathbf{56.29} & 0.57 & \mathbf{-6.74} & -0.21 \\
0.05 & 0.14 & 0.57 & \mathbf{2.23} & -0.04 & \mathbf{-0.48} \\
\mathbf{-0.42} & \mathbf{-0.71} & \mathbf{-6.74} & -0.04 & \mathbf{5.39} & -0.33 \\
-0.17 & 0.09 & -0.21 & \mathbf{-0.48} & -0.33 & \mathbf{1.79}
\end{bmatrix}$$

$$\langle\eta_{ik}\sigma_{nj}\rangle\langle\eta_{nj}\eta_{lm}\rangle^{-1}\ [\text{GPa}]$$

$$\begin{bmatrix}
\mathbf{8.12} & 3.53 & \mathbf{7.68} & 0.11 & \mathbf{0.18} & -0.30 \\
3.70 & \mathbf{6.62} & 4.21 & 0.17 & -0.74 & 0.11 \\
7.17 & 3.85 & \mathbf{56.61} & 0.58 & \mathbf{-7.34} & -0.17 \\
0.11 & 0.16 & 0.30 & \mathbf{2.33} & 0.19 & \mathbf{-0.64} \\
-0.43 & -0.67 & -2.59 & 0.04 & \mathbf{4.99} & -0.33 \\
-0.19 & 0.14 & -0.19 & \mathbf{-0.31} & -0.35 & \mathbf{1.71}
\end{bmatrix}$$

The matrix of the elastic constants of the ordered structure of Fig. 4.18 c) is given in Appendix F.

4.3.4.3 Elastic Constants from Constant-Shape MD simulations

Table 4-33 lists selected elements of the matrix of the elastic constants, that were computed in the ThN-ensemble. At 300 K, the Born, the kinetic energy, and the stress fluctuation term as well as the sum of these three contributions were given. At 335 and 375 K, only the sums, i.e. the effective elastic constants, were listed. In general, the results obtained in this ensemble do not seem to be very consistent. The C_{33} and C_{66} values agree quite well with other calculations, but especially C_{44} and C_{55} are much too high, whereas the C_{11} and C_{22} components at 375 K are even negative! The convergence of the stress fluctuations seems to be so slow that an equilibration could not be achieved in the 250 ps of the simulation. It was therefore not possible to verify Ray's statement that the elastic constants converge much faster in the ThN-ensemble than in the TtN-ensemble.[Ray88a]

Table 4-33: Elastic constants from *ThN*-simulations of it-PP at 300 K, 335 K, and 375 K, all values in GPa

	Born	Kinetic	Fluct	300 K	335 K	375 K
C_{11}	221.27	-0.48	-209.63	11.16	13.89	-0.34
C_{22}	230.48	-0.48	-222.14	7.86	9.78	-3.61
C_{33}	248.32	-0.48	-191.43	56.41	57.97	51.09
C_{44}	103.00	0	-79.19	23.81	25.41	19.62
C_{55}	112.55	0	-84.47	28.08	25.89	23.62
C_{66}	97.21	0	-94.27	2.94	1.44	0.92
C_{12}	45.78	0	-40.78	5.00	5.12	1.40
C_{13}	32.70	0	-21.43	11.27	10.91	3.82
C_{23}	23.51	0	-20.04	3.47	4.36	2.81
C_{35}	-3.87	0	1.55	-2.32	2.09	5.91

4.3.5 Discussion

4.3.5.1 Rotation of the Matrix of the Elastic Constants

In contrast to PE, the chains in the it-PP simulation box are not parallel to the x_3-axis of the external frame of reference. In order to be able to estimate the modulus in the fiber direction, it is first necessary to rotate this external coordinate frame until its x_3-axis is aligned with the PP-chains. A procedure was written that performs such a rotation (using Eq. 1-50) by minimizing a penalty function. This function was proportional to the sum of the squares of those elements that should be zero by summetry minus the square of the C_{33} value (i.e. C_{33} was maximized and a monoclinic symmetry was favoured). The resulting matrices are given in the next table (Table 4-35). The experimentally accessible

Table 4-34: Matrices of table 4-30, rotated successively by 1° around the x_1-axis, 8° around the x_2-axis and 3.3° around the x_3-axis

$\dfrac{kT}{\langle V \rangle} \langle \eta_{ik}\eta_{lm} \rangle^{-1}$ [GPa]	$\langle \eta_{ik}\sigma_{nj} \rangle \langle \eta_{nj}\eta_{lm} \rangle^{-1}$ [GPa]
$\begin{bmatrix} 8.91 & 3.47 & 5.97 & 0.14 & 1.46 & -0.31 \\ 3.47 & 6.96 & 3.83 & 0.09 & -0.78 & 0.13 \\ 5.97 & 3.83 & 56.79 & -0.02 & -0.76 & 0.06 \\ 0.14 & 0.09 & -0.02 & 2.61 & 0.34 & -0.42 \\ 1.46 & -0.78 & -0.76 & 0.34 & 4.52 & -0.40 \\ -0.31 & 0.13 & 0.06 & -0.42 & -0.40 & 1.96 \end{bmatrix}$	$\begin{bmatrix} 9.18 & 3.70 & 7.03 & 0.28 & 1.52 & -0.39 \\ 3.78 & 7.25 & 4.03 & 0.14 & -0.68 & 0.12 \\ 6.46 & 4.21 & 60.15 & -0.12 & -1.50 & 0.10 \\ 0.33 & 0.11 & 0.04 & 2.71 & 0.42 & -0.56 \\ 0.68 & -0.73 & 3.07 & 0.31 & 4.41 & -0.35 \\ -0.13 & 0.10 & 0.35 & -0.20 & -0.33 & 1.88 \end{bmatrix}$

modulus, and the linear compressibility along the chain axis, E_3 and β_3, were calculated from the compliance matrix S_{ik} $(=C_{ik}^{-1})$ using[Tadokoro92a]

$$E_3 = \frac{1}{S_{33}} \qquad \text{and} \qquad \beta_3 = S_{31} + S_{23} + S_{33}. \qquad (4\text{-}28)$$

For the strain fluctuations $E_3 = 51.9$ GPa and $\beta_3 = 0.31 \cdot 10^{-2}$ GPa^{-1}, whereas the stress-strain fluctuations yield $E_3 = 56.3$ GPa and $\beta_3 = 0.26 \cdot 10^{-2}$ GPa^{-1}.

4.3.5.2 Comparison with Literature Values

One of the earliest values of Young's modulus in the chain direction is 28 GPa from Miyazawa which was opposed to an observed 32 GPa from Sakurada et al.[Tadokoro90] In the more recent work of Tashiro et al[Tadokoro92a], experimental E_3 values of 35 to 43 GPa - depending on the methodology - and a β_3 of $0.4 \cdot 10^{-2}$ GPa^{-1} are reported. As mentioned in the introduction, Hong et al[Hong90a] quote Young's moduli between 18 and 80 GPa.

Theoretical three-dimensional matrices were computed by Tashiro et al[Tadokoro92a] and by Lacks and Rutledge[Rutledge95a]. In Tadokoro's work, the reference axes are as follows: $x(1)$-axis $= a \cdot \sin\beta$, $y(2)$-axis $= b$, and $z(3)$-axis $= c$. This is identical with the rotated matrices of Table 4-30. Lacks and Rutledge do not specify the relation between external cartesian and crystal coordinate system explicitly, but it is assumed that it is the same. A comparison with these literature values and the numbers obtained in this work is given in Table 4-35. Almost all values fit perfectly in the range spanned by the previous calculations, except for the C_{44} value, which is a bit lower, and the C_{35} value from the stress-strain fluctuations. As was seen in the process of rotating the elasticity matrix, this component is extremely dependent on the orientation (only 1 or 2° would suffice to change the sign without involving considerable changes in the other components).

4.3.5.3 Conclusions

At 300 K, the elastic constants obtained from the strain and the stress-strain fluctuations agree very well with experimental and other theoretical results. Young's modulus in the chain direction (51.9 GPa from the strain and 56.3 GPa from the stress-strain fluctuations) is higher than the experimental values of 35 - 43 GPa. Looking at Fig. 4.19, it can be seen that at least the stress-strain calculation has not yet converged and that a further drop by a few GPa can be anticipated. This would bring the stress-strain value closer to the one obtained from strain fluctuations and reasonably close to the experimental val-

Table 4-35: Comparison between the elastic constants [in GPa] and the linear compressibility in the chain direction [in 10^{-2} GPa^{-1}] obtained in theoretical calculations at 300 K from Tashiro et al[Tadokoro92a], Lacks and Rutledge[Rutledge95a] and the strain and the stress-strain fluctuation formula of this work. Off-diagonal elements in the last column are averages of the two symmetry-equivalent numbers. SLKB* and KDG* denote modifications of force fields by Sorensen, Liau, Kesner, and Boyd and Karasawa, Dasgupta, and Goddard, which are used in Ref. [Rutledge95a].

	Tashiro et al	Lacks & Rutledge		this work	
		SLKB*	KDG*	η_{ik}	t_{ik}, η_{lm}
C_{11}	7.78	9.9	9.1	8.91	9.18
C_{22}	11.55	10.8	8.6	6.96	7.25
C_{33}	42.44	55.1	64.5	56.79	60.15
C_{44}	4.02	4.0	4.3	2.61	2.71
C_{55}	3.10	4.9	4.7	4.52	4.41
C_{66}	2.99	1.7	3.5	1.96	1.88
C_{12}	3.91	3.4	3.6	3.47	3.74
C_{13}	3.72	7.1	7.2	5.97	6.75
C_{23}	3.99	4.4	4.3	3.83	4.12
C_{15}	0.90	< 1	< 1	1.46	1.10
C_{25}	-0.36	< 1	< 1	-0.78	-0.71
C_{35}	-0.57	< 1	< 1	-0.76	0.79
C_{46}	-0.12	< 1	< 1	-0.42	-0.38
E_3	40.1	-	-	51.9	56.3
β_3	0.97	-	-	0.31	0.26

ues. The influence of the temperature on the convergence of the C_{33}^{rot}-component (the modulus along the chain axis, which has been rotated to be parallel to the external x_3-axis) is given in the next figure. The opposing trends (raise with temperature for the values from the strain fluctuations, drop of those from the stress-strain fluctuations) are an effect of the relatively bad convergence at 300 K, which becomes much better at 375 K. It is therefore not appropriate to quantify the decrease of C_{33}^{rot} with temperature. However, it can be stated that it must be relatively small and in the order of the 2.5 - 3.5 GPa/100 K found by Lacks and Rutledge[Rutledge95a].

The thermal expansivity of it-PP is quite well reproduced, with the exception of the small contraction in the chain direction, which must be attributed to

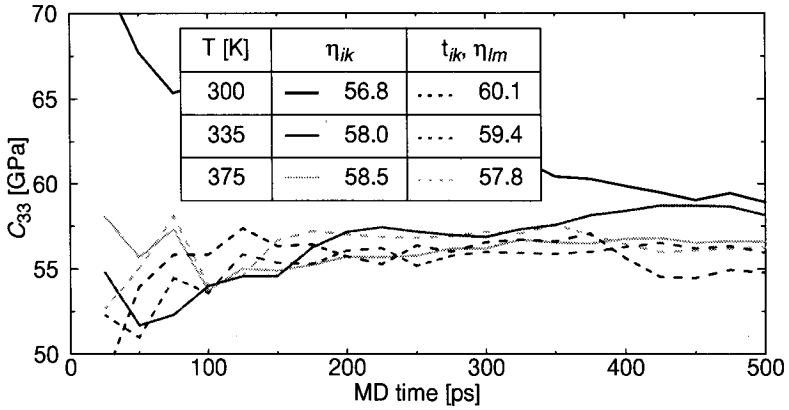| T [K]	η_{ik}	t_{ik}, η_{lm}
300	—— 56.8	.... 60.1
335	—— 58.0	.... 59.4
375	.... 58.5	.... 57.8

Figure 4.20: Convergence of the C_{33}-component of the elasticity matrix at 300, 335, and 375 K; the table gives the temperature dependence of the C_{33}^{rot}-component [in GPa] calculated with strain and stress-strain fluctuations

deficiencies in the *pcff91*-forcefield.

4.4 Cellulose-Iβ - Chains with Hydrogen Bonds

4.4.1 Introduction

Cellulose is the most abundant natural polymer on earth; there exist about $800 \cdot 10^9$ t[Woodwell78a] primarily in the cell walls of higher plants but also in some algae, fungi, protistans, bacteria, and tunicata. The annual production rate of approx. $70 \cdot 10^9$ t exceeds that of synthetic, man-made polymers by a factor of 10^3. In nature, highly crystalline cellulose fibers act as reinforcements in composite materials, like the lignin/cellulose complex in the reticulum of trees. These cellulose composites are responsible for the mechanical stability of the higher plants.[Kraessig92]

In industrial applications, cellulose is mainly used in the form of its derivates in the production of paper and of textile yarns like cotton and viscose. Further applications are wood-like materials made up from wooden filler particles and polymer matrices. Examples are plywoods, resinbonded boards or extrudable panels. In total, cellulose in its various forms constitutes about 50% of the polymer utilized in the industry worldwide.[Maldas93a]

The reinforcing abilities of individual cellulose fibers are becoming of interest in order to increase the elastic moduli of synthetic polymers and rubbers. The experimental results reveal substantial effects even of comparatively small amounts of cellulose whiskers in rubbery materials.[Chanzy95a] To make full use of the capabilities of such systems, it is important to establish a connection between the morphology of a reinforced two-phase matrix-whisker polymer, the elastic behaviour of its constituents, and the overall elastic properties.

With the knowledge of the complete matrix of the elastic constants of the polymer matrix and the reinforcing particles, it is possible to compute the elastic behaviour of the composite system. Assuming isotropy of the rubberous part, its elastic constants can readily be determined by tensile and shear experiments. The elastic constants of the anisotropic, crystalline cellulose whiskers are not accessible through experimental methods as stated in chapter 4.2.1.

It is therefore of theoretical and practical interest to compute the full matrix of the elastic constants of cellulose. The results of the structure generation and the simulation runs will be presented after a short discussion about the various modifications of crystalline cellulose.

4.4.2 Crystal Modifications and Cell Generation

4.4.2.1 Crystal Modifications

Despite repeated efforts in the last 70 years, the crystalline structures of native and of chemically modified cellulose still are disputed. At present, there is evidence for at least four major modifications of crystalline cellulose[Kraessig92]: cellulose-I is the form in which native cellulose appears; after its treatment with strong alkaline solutions or after precipitation from solution in suitable solvents, the cellulose-II modification is observed. Cellulose-III is formed by the decomposition of the reaction product of native cellulose and liquid ammonia, whereas cellulose-IV is obtained by treating regenerated cellulose-II fibers in hot baths under stretch. Although the existence of cellulose-I and cellulose-II is well established - in contrast to the latter two modifications[Atalla74a] - not only the actual arrangement of the chains in the unit cell but also the size and shape of the unit cells still are subject to ongoing research.

Recent studies[Atalla84a, Sugiyama90a,Chanzy91a] give indication that crystals of native cellulose-I are composed of two crystalline phases: a monoclinic, two chain Iβ-phase which is dominant in ramie, cotton and tunicin and a triclinic Iα-phase occurring in *Valonia ventricosa* and bacterial cellulose. The fraction of the Iα-phase depends on the origin of the cellulose and amounts to 65% in *Valonia* samples. This phase, however, is only metastable and can be converted by hydrothermal annealing into the thermodynamically stable Iβ-phase.

While the cell parameters of cellulose-Iα are still under discussion, it is generally accepted that the Iβ-phase is monoclinic and contains two cellulose chains at the twofold screw axes, one at the corner and another one in the center of the unit cell. Unresolved is the question, whether the two chains are parallel or antiparallel. In one of the first proposals, still widely in use, from Meyer, Mark and Misch[Meyer37a], the two chains were in antiparallel position. Later, Gardner and Blackwell[Gardner74a] and Woodcock and Sarko[Woodcock80a] suggested models in which there was a parallel arrangement of the chains. In the present work, the model structure of Woodcock and Sarko was used for the calculation of the elastic constants. The latest reports, however, support an antiparallel alignment of the chains in cellulose-II,[Chanzy95b] which in turn makes an antiparallel setup of the chains in cellulose-Iβ more likely. MD calculations made by Kroon-Batenburg *et al.*[Kroon96a] favour, on the other hand, parallel chains according to the Woodcock/Sarko structure.

The cellulose-I structure suggested by Woodcock and Sarko is monoclinic, with unit cell parameters given in Table 4-36. The arrangement of the cellulose

Table 4-36: Unit cell dimensions and helical setting parameters of Cellulose-Iβ and Cellu-
lose-II

Property		Cellulose-Iβ	Cellulose-II
a [Å]		7.78	8.00
b [Å]		8.20	9.05
c [Å]		10.34	10.38
γ [°]		96.5	116.8
Chain 1	Position/Orientation	[0,0] / 'up'	[0,0] / 'up'
	Setting angle [°]	-42.0	28.0
	Vert. offset [Å]	0.0	0.0
Chain 2	Position/Orientation	$[\frac{1}{2},\frac{1}{2}]$ / 'up'	$[\frac{1}{2},\frac{1}{2}]$ / 'down'
	Setting angle [°]	-42.0	18.0
	Vert. offset [Å]	-2.6	1.0

chains in the cell is shown in Figure 4.21. The various intra- and intermolecular
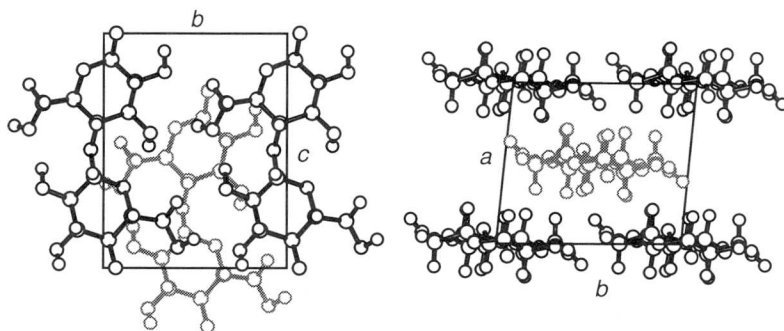
Figure 4.21: Unit cell projections of the parallel-chain structure of cellulose-Iβ. The center chain
is drawn gray-shaded, the corner chains are solid black.

hydrogen bonds are not shown in order not to cluster the picture too much. The
intramolecular hydrogen bonds are depicted in Fig. 4.24, the intermolecular
hydrogen bonds act mainly between neighbouring sheets in the b-direction.

Based on experimental data and the comparison with chemically similar
molecules, Chanzy et al.[Chanzy95b] suggested a crystal structure of cellulose-II
whose unit cell parameters are listed in Table 4-36, too.

4.4.2.2 Structure Generation

The commercial Insight/Discover[MSIDiscover1] program package was used for the setup and minimization of the crystalline simulation cell and for the computation of the molecular dynamics (MD) trajectory. Note: In the Discover simulations, the cartesian coordinate frame was set such that the *a*-edge of the simulation cell was parallel to the x_1-direction and the *b*-edge was in the x_1-x_2-plane. This is in contrast to the orientation of the coordinate frame used in the literature and in this work, in which the chains and thus the *c*-direction are parallel to the x_3-axis and the *b*-axis is in the x_2-x_3-plane (in the case of monoclinic symmetry parallel to the x_2-axis).

After the building and minimization of a chemical repeat unit of cellulose, a short oligomer with a degree of polymerization (DP) = 3 was generated in order to extract the helical repeat unit. Two such helical repeat units were placed in a box of the size of the Woodcock and Sarko crystal cell, one at a corner (0,0) and one in the center $(\frac{1}{2},\frac{1}{2})$ with an offset in the *c*-direction of -2.6 Å. The setting angle for both chains was -42° (cf. Table 4-36). In the refinement process, different force-fields were used to find the most suitable one for cellulose. This refinement procedure consisted in a systematic change of the cell parameters, the setting locations, and the setting angles of the chains followed by an energy minimization to find the most stable crystal conformation.[MSIPolymer1] The *amber, cvff* and *pcff* force-fields were tested, and it turned out that the most sensitive cell parameter was the γ angle. The *amber* force-field gave a correct estimate of 96.5°, but lacked some parameters necessary for dynamic simulations. Of the remaining two force-fields, *cvff* seemed to be more suitable than *pcff* (as Table 4-37 shows) and was thus used for the further computations. In subse-

Table 4-37: Minimum energy cell parameters of cellulose Iβ with *pcff* and *cvff* force field compared with experimental values

	a [Å]	b [Å]	c [Å]	α [°]	β [°]	γ [°]
pcff	7.89	8.38	10.63	93.25	89.05	99.05
cvff	7.77	8.14	10.68	90.73	89.79	97.34
exp.	7.78	8.20	10.34	90	90	96.5

quent dynamics, as the results will show, the γ angle was quite close to the experimental value. The *cvff* is an all-atom force field with flexible bond lengths, bond angles and torsional degrees of freedom.[MSIDiscover1] No Morse bond potentials, no out-of-plane and no cross terms were used. There are no explicit

terms for the hydrogen bonds, but large partial charges invoke similar effects.

To reduce the effects of the small unit cells, a super cell of $2 \times 2 \times 2$ unit cells with periodic boundary conditions was generated. The images of the cellulose chains were connected to their parent chains by 'bonds across boundaries' in order to mimic infinitely long molecules. This super cell contained 672 atoms in 8 chains.

4.4.3 Simulation Procedure

The MD simulation was carried out in the familiar $T\sigma N$-ensemble, where the pressure was controlled by a Parrinello-Rahman manostat and the temperature by a Nosé-Hoover algorithm. The coupling constant W between the internal stress fluctuations and the velocity of the cell shape changes was again set to 20 a.m.u. The fictitious mass Q of the Nosé-Hoover thermostat was chosen as $7.33 \cdot 10^6$ kcal·mol^{-1}·fs^{-2} at 325 K. Again, the dynamic properties, i.e. the temperature fluctuations, depend on Q, whereas static quantities, such as the average temperature, are not influenced by the choice of this variable, but rather by the stepwidth of the simulation.[Nose91a] The smaller the timestep, the closer the average temperature approaches the target temperature. A canonical ensemble of the correct temperature will only be created by using infinitely small timesteps. Having, e.g., 325 K as the target temperature, a timestep of 0.5 fs leads to an average temperature of 318.3 K (cf. chapter 2.5.2.3).

The long-range Lennard-Jones interactions were taken into account by applying an external pressure of 180 MPa (1800 bar). The Coulombic interactions were treated with a conventional splined cutoff (switching from full interactions at 7.5 Å down to no interactions at 8.5 Å) and with Ewald terms that were summed up to an accuracy of 0.0025 kcal·mol^{-1}.

Calculations were performed at 325 K (for the sake of comparison with Ref. [Chanzy95a]), 150, and 400 K, which allows the calculation of the temperature dependence of the density (thermal expansion coefficients) and of the elastic constants of cellulose. Splined cutoffs made it possible to perform $2 \cdot 10^6$ MD steps of 0.5 fs, totalling 1 ns, whereas the computationally more expensive Ewald summation reduced the simulation length to $0.5 \cdot 10^6$ steps or 250 ps. These values correspond to roughly 1 month of CPU time on a workstation per simulation run and are the limit of feasibility.

In addition to the simulation of cellulose-Iβ, the cellulose-II structure of Ref. [Chanzy95b] was generated with the same methodology as described above using the parameters of Table 4-36, chain 2 being antiparallel to chain 1. Just like for cellulose-Iβ, the application of the *cvff* force-field led to the best agree-

ment of the simulation structure with the experimental values. For this structure, a *TσN*-MD simulation was made for $0.5 \cdot 10^6$ steps of 0.5 fs (250 ps). Again, Ewald summation of the coulombic interaction terms was used.

4.4.4 Results

4.4.4.1 Cell Shape and Thermal Expansion

In this subchapter, only results from calculations with Ewald summation of the charged interactions are presented.

An example of the thermal fluctuations of the lengths of the vectors spanning up the cellulose-Iβ simulation cell is given in Figure 4.22. The averages of
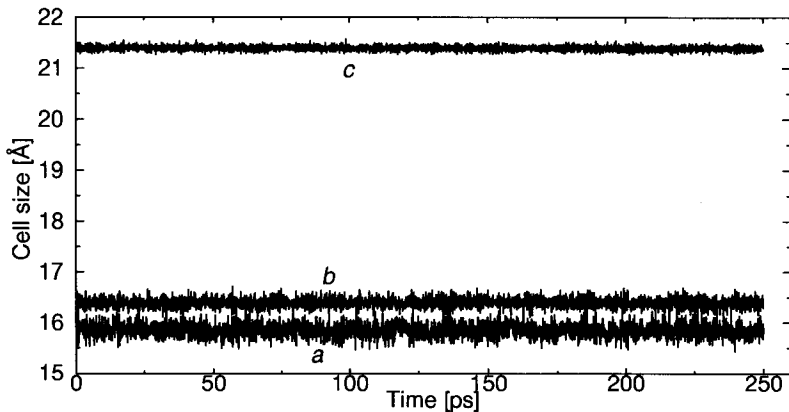

Figure 4.22: Fluctuations of the vector lengths *a*, *b*, and *c* of the cellulose-Iβ simulation cell at 325 K (Ewald summation)

the cell parameters $\{a, b, c, \alpha, \beta, \gamma\}$ taken at any subtrajectory are not significantly different from those of the whole trajectory, indicating that the cell is fluctuating around a quasi-equilibrium point at 150 and at 325 K. At 400 K, however, a transition occurred after approx. 130 ps, in which *b* increased by about 0.4 Å (Fig. 4.26) and the α and γ values by about 2°. The reason for this transition is most probably the small cell size in combination with the elevated temperature, which creates considerable fluctuations. In order to have some indication of the material's behaviour at 400 K, relatively stable parts of the trajectory were taken for further investigation.

In Figure 4.22, visual inspection already allows to estimate the elastic constants in the *c*-direction (along the chains) being higher and in the *a*-direction being lower than in the *b*-direction, because the fluctuations are smaller in the

c-direction and larger in the *a*-direction. This is supported by the apparently higher frequency of the oscillations of the *c*-value than of the *a*-value. So the *c*-direction, which is parallel to the chains, is a 'hard' direction, whereas the *a*-direction, where only weak Lennard-Jones forces act perpendicular to the hydrogen-bonded sheets, is a 'soft' one. These rough estimates will be confirmed by the following standard deviations of the cell parameters and by numerical analysis in chapter 4.4.4.2.

Table 4-38: Summary of simulation cell parameters of minimized cellulose-Iβ, at 150, 325, and 400 K. Averages were taken from $2.5 \cdot 10^5$ frames at 150 and 325 K and from $1.2 \cdot 10^5$ frames at 400 K. The time interval between the frames was 1 fs (2 MD steps)

T [K]	a [Å]	b [Å]	c [Å]	α [°]	β [°]	γ [°]
0	15.53	16.27	21.37	90.2	89.9	97.5
150	15.70 ± 0.08	16.29 ± 0.07	21.38 ± 0.03	90.0 ± 0.4	90.0 ± 0.6	97.5 ± 0.4
325	15.85 ± 0.13	16.40 ± 0.10	21.39 ± 0.05	90.0 ± 0.7	90.0 ± 1.1	97.5 ± 0.8
400	15.96 ± 0.14	16.46 ± 0.10	21.40 ± 0.05	90.0 ± 0.9	89.9 ± 1.3	97.8 ± 1.0

The average values and the standard deviations of the cell parameters at 150, 300 and 400 K are given in Table 4-38. Linear regressions of these parameters show that there is virtually no drift of the cell shape with time, i.e. that there are no significant relaxations in the timescale of the simulation. Only at 400 K, the reduced stability of the cell becomes manifest in higher values of the slope of the regression line (cf. Fig. 4.26).

From Table 4-38, it is possible to compute the matrix of the thermal expansion coefficients. Assuming no change in the cell symmetry (i.e. shape), the thermal expansion coefficients at 325 K can be estimated as $\alpha_1 = 7 \pm 2 \cdot 10^{-5}$, $\alpha_2 = 5 \pm 1 \cdot 10^{-5}$, and $\alpha_3 = 5 \pm 1 \cdot 10^{-6}$ K^{-1}. As with PP, these values are in accord with experimental measurements of the α_1 and α_2 coefficients, but are not able to reproduce the contraction effect along the chains of $-4.5 \cdot 10^{-5}$ K^{-1}[Godovsky92].

The cellulose II structure was not completely stable, as the next figure shows. Especially the *b* and γ values exhibit drifts, that are of the same or a larger magnitude than the thermal fluctuations, making it impossible to evaluate the elastic constants properly.
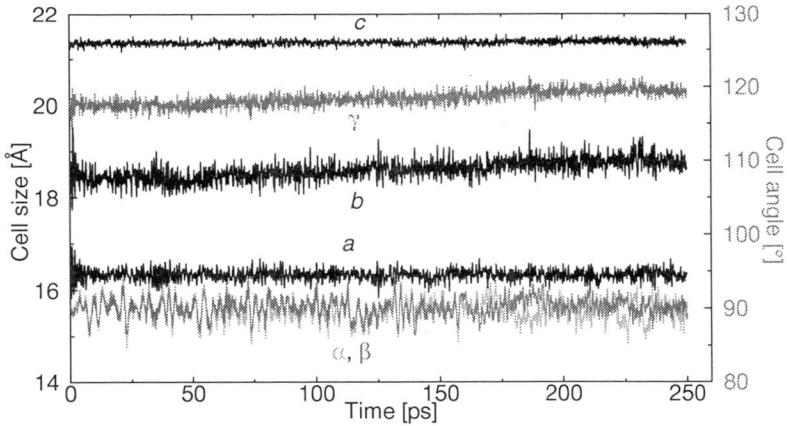
Figure 4.23: cell sizes and angles of Cellulose-II at 325 K (Ewald sum)

4.4.4.2 Elastic Constants

The strain and the stress-strain fluctuation formalisms of Eqs. (3-29) and (3-36) were used to compute the elastic constants of cellulose-Iβ at 150, 325, and 400 K. At first, the results using a splined cutoff and an Ewald summation for the coulombic interactions at 325 K are compared:

The matrices of the elastic constants (in the Discover coordinate system) obtained from interactions with a splined cutoff, given in Table 4-39, differ dra-

Table 4-39: Elastic constants averaged over the last 500 ps of a 1000 ps $T\sigma N$-MD simulation at 325 K, cutoff = 8.5 Å, spline = 1 Å for all non-bonded interactions. Non-zero components are bold faced, gray number signify large deviations from the 'typical' values of hydrogen-bonded sheets (see chapter 4.5.4).

$\dfrac{kT}{\langle V\rangle}\langle\eta_{ik}\eta_{lm}\rangle^{-1}$ [GPa]							$\langle\eta_{ik}\sigma_{nj}\rangle\langle\eta_{nj}\eta_{lm}\rangle^{-1}$ [GPa]					
39.1	**16.5**	19.5	−0.1	−0.1	3.0		44.6	**18.8**	22.3	−0.1	−0.1	3.4
16.5	58.4	**19.2**	−0.1	0.0	**−0.7**		14.5	51.4	**16.9**	−0.1	0.0	**−0.6**
19.5	**19.2**	**193.2**	0.1	0.3	4.3		18.6	**18.2**	**183.9**	0.1	0.3	4.1
−0.1	−0.1	0.1	9.8	−0.4	0.1		−0.1	−0.1	0.1	9.6	−0.3	0.1
−0.1	0.0	0.3	−0.4	9.1	0.0		−0.1	0.0	0.3	−0.4	9.1	0.0
3.0	**−0.9**	4.3	0.1	0.0	6.0		3.1	**−0.7**	4.4	0.1	0.0	6.1

matically from those that used an Ewald summation for the charged interactions (Table 4-41).

The comparison with literature values (chapter 4.4.5.1) shows that the simulations which involve an Ewald summation of the far-reaching coulombic inter-

Table 4-40: Elastic constants averaged over a 250 ps $T\sigma N$-MD simulation at 325 K, cutoff = 8.5 Å, spline = 1 Å, Ewald summation for the coulombic interactions. Non-zero components are bold faced.

$\frac{kT}{\langle V \rangle}\langle \eta_{ik}\eta_{lm}\rangle^{-1}$ [GPa]						$\langle \eta_{ik}\sigma_{nj}\rangle\langle \eta_{nj}\eta_{lm}\rangle^{-1}$ [GPa]					
17.2	**12.9**	**6.8**	–0.1	0.1	**–0.5**	**17.3**	**13.2**	**6.9**	–0.1	0.0	**–0.3**
12.9	**34.3**	**14.7**	0.1	0.0	**–0.5**	**11.9**	**31.6**	**10.7**	0.1	0.0	**–0.6**
6.8	**14.7**	**162.0**	0.1	0.0	**0.9**	**6.4**	**13.5**	**160.8**	0.1	0.0	**0.9**
–0.1	0.1	0.1	**5.0**	**–0.2**	–0.1	0.0	0.2	0.6	**4.9**	**–0.2**	–0.1
0.1	0.0	0.0	**–0.2**	**2.1**	0.0	0.1	0.2	0.0	**0.0**	**2.1**	0.0
–0.5	**–0.5**	**0.9**	–0.1	0.0	**3.8**	**–0.7**	**–1.5**	**1.5**	–0.1	0.0	**3.8**

actions are much more reliable than those from calculations with splined cutoffs. The reason for this can be seen in Figs. 4.24 and 2.5. Figure 4.24 shows a struc-
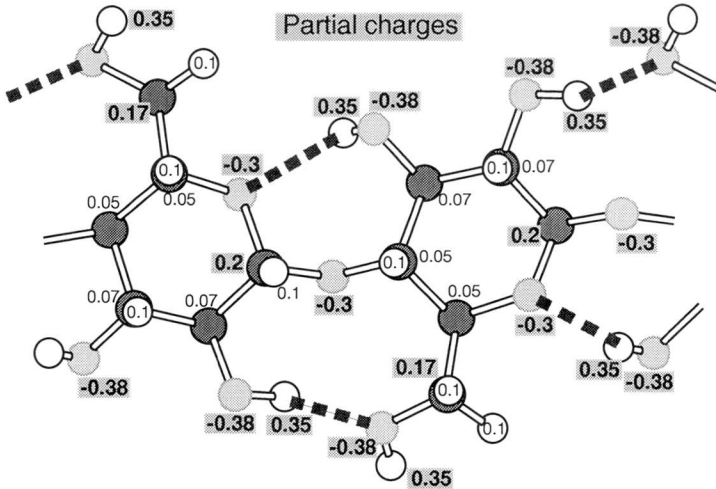
Figure 4.24: Partial charges of a structural repeat unit of cellulose I

tural repeat unit of a cellulose sheet with the corresponding partial charges from the *cvff* forcefield. There is a number of relatively highly charged atoms forming hydrogen bonds, which are indicated by thick broken lines. Figure 2.5 on page 41 plots the Coulombic interactions computed with atom- and group-based cutoffs and with Ewald summation as a function of the cutoff radius or the Ewald summation accuracy. It can be easily seen that the Coulombic interaction energy takes almost arbitrary numbers depending on the cutoff radius. This problem

was less pronounced for the PE and it-PP crystals because the partial charges were much smaller ($O(0.05\text{-}0.15)$) and the neutral groups less extended.

In order to obtain reliable results for the elastic constants of cellulose, the charged interactions *must* be treated using an Ewald summation or an equivalent technique.

The elastic constants at 150 K, computed with Ewald summation, are given in Table 4-42, and the convergence of the C_{11}, C_{22}, and C_{33} component is

Table 4-41: Elastic constants averaged over a 250 ps $T\sigma N$-MD simulation at 150 K, cutoff = 8.5 Å, spline = 1 Å, Ewald summation for the coulombic interactions. Non-zero components are bold faced.

$\dfrac{kT}{\langle V \rangle} \langle \eta_{ik}\eta_{lm} \rangle^{-1}$ [GPa]						$\langle \eta_{ik}\sigma_{nj} \rangle \langle \eta_{nj}\eta_{lm} \rangle^{-1}$ [GPa]					
19.4	**15.2**	**6.8**	0.2	−0.1	**−1.2**	**21.7**	**17.0**	**7.6**	0.2	−0.1	**−1.4**
15.2	**37.0**	**14.3**	−0.4	0.2	**−0.3**	**12.4**	**30.1**	**11.7**	−0.3	0.1	**−0.3**
6.8	**14.3**	**158.3**	0.0	0.1	**0.9**	**6.7**	**14.1**	**156.0**	0.0	0.1	**0.9**
0.2	−0.4	0.0	**7.2**	**−0.4**	0.0	0.1	−0.4	0.0	**6.8**	**−0.4**	0.0
−0.1	0.2	0.1	**−0.4**	**2.1**	−0.2	−0.1	0.2	0.1	**−0.4**	**2.2**	−0.2
−1.2	**−0.3**	**0.9**	0.0	−0.2	**4.4**	**−1.3**	**−0.3**	**0.9**	0.0	−0.2	**4.6**

shown in Fig. 4.25.

Figure 4.25: Convergence of the C_{11}, C_{22}, and C_{33} component of the matrices of the elastic constants of cellulose-Iβ at 150 K

At a temperature of 400 K, the cellulose cell became slightly unstable, as is manifest from Fig. 4.26. Actually, it is not possible to evaluate the elastic constants from this trajectory at all, since the system is not in equilibrium. In order to have an approximate idea of the elasticity matrix, the first and the last 100 ps (from 0 to 100 and from 150 to 250 ps) were used to compute the matrix of the

Figure 4.26: Cell edge vectors of cellulose Iβ at 400 K (Ewald summation, 1800 bar correction pressure

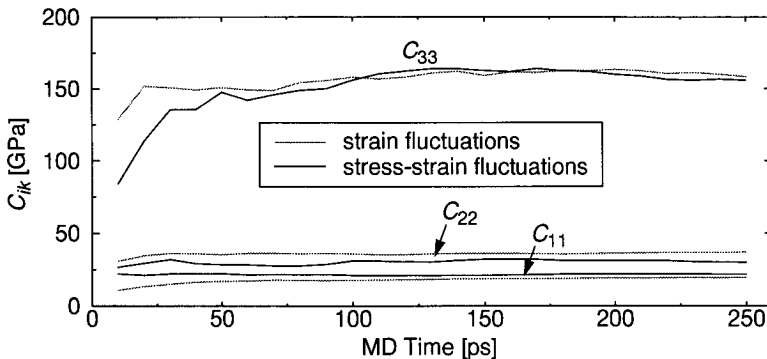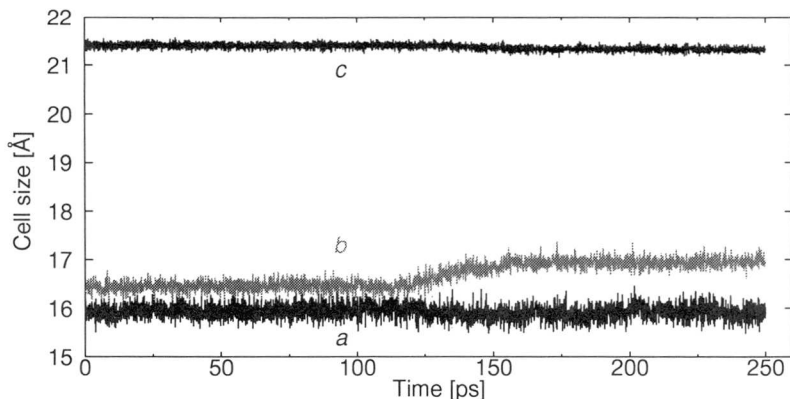elastic constants. The elastic constants of the last 100 ps are also listed in
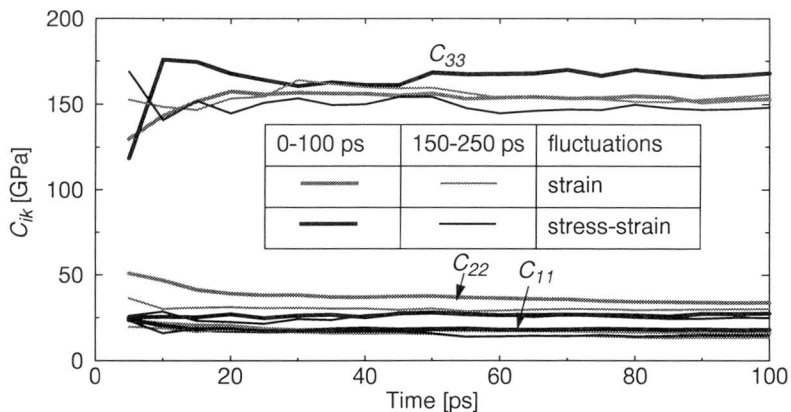
Figure 4.27: Convergence of the C_{11}, C_{22}, and C_{33} components of the matrix of the elastic constants of cellulose-Iβ at 400 K. Averages obtained from two intervals between 0 - 100 and 150 - 250 ps.

Table 4-43. The difference between the two matrices is relatively large, because of the short trajectory used for their evaluation. The diagonal elements of the stress-strain correlation matrix range from 0.94 to 1.02 kT, whereas the off-diagonal elements vary between -0.2 and 0.2 kT.

A short simulation run was started at 450 K to check the thermal stability of the cellulose-Iβ cell. After approximately 70 ps, the structure started 'melting', i.e.

Table 4-42: Elastic constants averaged over the last 100 ps of a 250 ps $T\sigma N$-MD simulation at 400 K, cutoff = 8.5 Å, spline = 1 Å, Ewald summation for the coulombic interactions. Non-zero components are bold faced.

$\frac{kT}{\langle V \rangle} \langle \eta_{ik} \eta_{lm} \rangle^{-1}$ [GPa]						$\langle \eta_{ik} \sigma_{nj} \rangle \langle \eta_{nj} \eta_{lm} \rangle^{-1}$ [GPa]					
13.6	**8.8**	**6.4**	0.1	0.3	**0.3**	**14.8**	**9.6**	**7.0**	0.1	0.3	**0.3**
8.8	**30.1**	**9.2**	–0.7	0.4	**–2.6**	**7.2**	**24.9**	**7.6**	–0.6	0.4	**–2.1**
6.4	**9.2**	**155.6**	–4.1	–1.5	**–1.9**	**6.1**	**8.7**	**148.2**	–3.9	–1.5	**–1.8**
0.1	–0.7	–4.1	**1.2**	**–0.5**	0.2	0.1	–0.6	–3.7	**1.1**	**–0.5**	0.2
0.3	0.4	–1.5	**–0.5**	**2.8**	–0.1	0.3	0.5	–1.7	**–0.6**	**2.9**	–0.1
0.3	**–2.6**	**–1.9**	0.2	–0.1	**2.8**	**0.3**	**–2.6**	**–1.9**	0.2	–0.1	**2.9**

the cell angles preformed large jumps of several degrees. It is therefore quite probable that the instabilities observed at 400 K are due to the large thermal fluctuations of the small cellulose Iβ cell. There is of course no melting of cellulosic materials at this temperature, this is only an effect of the finite-size of the simulation box. 'Infinite' cellulose crystals do not melt, but start decomposing at 480 - 550 K[Brandrup89]

4.4.4.3 Mechanical Relaxation Spectra

To obtain the relaxation spectra of the three cell edges, their time-autocorrelation functions were computed and then Fourier transformed. The resulting spectra are plotted in Fig. 4.28. The contributions to the mechanical loss spec-
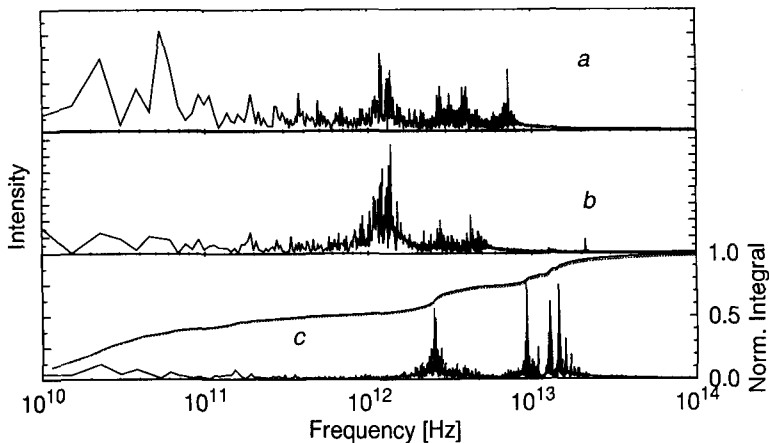

Figure 4.28: Fast-Fourier-transform of the time-autocorrelation function of $a(t)$, $b(t)$, and $c(t)$ of cellulose-Iβ at 325 K. The classical and the quantum mechanical integral of the relaxation spectrum in the c-direction have also been plotted (almost on top of each other)

trum along the chains (c-direction) have been calculated for the classical and the quantum mechanical case using the formulae of chapter 4.2.4.1. There is hardly any difference between the quantum mechanical and the classical integral. In contrast to the corresponding Fourier transforms of polyethylene and polypropylene crystals, there exists a variety of peaks belonging to different processes being responsible for the fluctuations. The long range interactions between the charged groups (hydrogen bonds) couple different fluctuation modes in neighbouring chains. These undirected forces are responsible for the broadening of the peaks.

4.4.4.4 Static Minimum Energy Calculation of the Elastic Constants

According to the methodology presented in chapter 4.1.6.2, the elastic constants at 0 K were evaluated for cellulose-Iβ using the *cvff*-forcefield and an Ewald summation of the Coulombic interactions.

Table 4-43: Elastic constants of cellulose-Iβ: static minimum energy (left) and stress-strain fluctuation approach at 150 K (right, table 4-39).

$$\frac{1}{V_0}\left(\frac{\partial^2 U_{pot}}{\partial\eta_{ij}\partial\eta_{kl}}\right)_T \text{ [GPa]} \qquad \langle\eta_{ik}\sigma_{nj}\rangle\langle\eta_{nj}\eta_{lm}\rangle^{-1} \text{ [GPa]}$$

21.5	15.1	7.2	0.2	−0.5	−0.8		21.7	17.0	7.6	−0.2	−0.1	−1.4
15.1	38.6	14.0	−0.3	−0.2	0.1		12.4	30.1	11.7	−0.3	0.1	−0.3
7.2	14.0	168.6	−1.3	0.1	1.6		6.7	14.1	156.0	0.0	0.1	0.9
0.2	−0.3	−1.3	7.1	−0.5	−0.7		0.1	−0.4	0.0	6.8	−0.4	0.0
−0.5	−0.2	0.1	−0.5	1.8	0.1		−0.1	0.2	0.1	−0.4	2.2	−0.2
−0.8	0.1	1.6	−0.7	0.1	4.5		−1.3	−0.3	0.9	0.0	0.2	4.6

In contrast to the previous calculations (PE and PP), the static minimum energy results of cellulose are subject to a considerable uncertainty. Since several calculations for the diagonal elements are made, their standard deviation can be estimated to be in the range of 0.5 GPa. A similar conclusion can be drawn from those elements that should be zero due to the symmetry of the crystal. The origin of this behaviour is the use of the Ewald summation technique. Although relatively small deformations (± 0.2%, as for PE and PP) were used, the coulombic interactions with their 'infinite' range had a substantial influence in the subsequent minimizations. Application of deformations, that were 10 times smaller (max. 0.02%) did not improve the situation, but led to larger errors due to problems with the precision of the minimization.

4.4.5 Discussion

4.4.5.1 Comparison with Literature Values

There is a number of reports on the elastic constants of cellulose I in the literature, most of them dealing with Young's modulus in the chain direction.[Nishino95a] Most experimental and theoretical E_3 values are between 78 and 180 GPa. Experimental X-ray studies from Nishino *et al.*[Nishino95b] and from Matsuo *et al.*[Matsuo90a] yielded E_3 values of 138 and 120 - 135 GPa. There are theoretical calculations of parts of the matrix of the elastic constants from Gillis[Gillis69a] and of the full matrix from Tashiro and Kobayashi[Tashiro88a] which are given in Table 4-44. Of these two, only Tashiro and Kobayashi's values seem to

Table 4-44: Theoretical matrices of the elastic constants from Gillis and from Tashiro and Kobayashi, all values in GPa

Gillis			Tashiro and Kobayashi					
16.4	0.0	0.7	15.1	1.6	1.2	0	0	4.3
0.0	25.2	0.8	1.6	54.5	−2.5	0	0	−3.2
0.7	0.8	319.2	1.2	−2.5	167.7	0	0	0.5
		0.2	0	0	0	3.5	1.4	0
		0.2	0	0	0	1.4	8.1	0
		2.5	4.3	−3.2	0.5	0	0	4.5

be reasonably close to the experimental findings and the theoretical E_3 estimations.

Comparing Young's moduli in the chain direction of this work (Table 4-45)

Table 4-45: Young's modulus in the chain direction $E_3 = 1/S_{33}$ computed at 150, 325, and 400 K using stress (η) and stress-strain (σ-η) fluctuations

T [K]	η–Fluct. [GPa]	σ-η-Fluct. [GPa]
150	151.4	150.2
325	155.2	150.4
400	133.1	126.1

with the literature values, it can be stated that they are more or less between the experimental and the theoretical results. It is difficult to compare the matrix from Tashiro *et al.* with the present calculations, but considering the fact that there were no temperature effects taken into account, the agreement between the

Young's moduli is quite good. Larger discrepancies occur for the C_{12}, C_{13}, and C_{23} values, where the far reaching undirected Coulombic interactions might enhance the coupling between the orthogonal stress and strain states.

4.4.5.2 Conclusions

The elastic moduli of cellulose along the chain direction - determined by the strain and the stress-strain fluctuations - are in the range of 150 - 155 GPa. This is in reasonable agreement with both experimental and theoretical results.

It is, however, extremely important to treat the Coulombic interactions properly by using e.g. an Ewald summation technique, because the regular structure of the crystal and highly charged atoms deny the use of a cutoff.

These strong Coulombic interactions are also responsible for the excellent elastic properties of cellulose-Iβ. The elastic modulus in the chain direction is not as high as for PE, but in the directions perpendicular to the chains, the elastic moduli are several times higher, due to the intermolecular hydrogen bonds (which are modeled by large partial charges in the *cvff* forcefield). This explains why nature is using such huge quantities of this material in all kinds of structural elements.

4.5 Polyamide-6 - Monoclinic Crystals

4.5.1 Introduction

Excellent mechanical, dynamical and chemical properties like high tensile and impact strength, low coefficient of friction, good hardness and high resistance against organic solvents are the main features of polyamides that make them technologically so important. They are used as engineering materials in bearings, gears, cams etc., for tubes, jackets of electrical wires, casings and for the production of fibers and yarns [Billmeyer84,Franck88].

Polyamide(PA)-6 (R_1-CO[-NH-(CH$_2$)$_5$-CO]$_n$-NH-R_2) is produced within minutes by fast anionic polymerization from waterfree ε-caprolactam. The resulting material is composed of spherulites of crystalline lamellae embedded in an amorphous matrix.[Puffr91] The crystalline parts are not always perfectly ordered - mesomorphous[Puffr67a] - for the degree of crystallinity not only depends on the processing history but also on the method of measurement and varies between 20% and 60%.[Puffr91,Bhat89a] In order to understand the behaviour and the properties of Polyamide-6 and related materials, the semicrystalline morphology of these materials needs to be considered in detail, as performed in a recent investigation[Hsia95a]. In this work, the elastic constants of both amorphous and crystalline domains were determined by fitting the behaviour of a finite-element representation of the morphology to experimental data.

In the present work, the inverse approach is made. Starting from a force field, the elastic properties of amorphous and crystalline PA-6 will be computed, which may serve as an input for a finite-element calculation. This chapter reports the fine-tuning of the *pcff91* force field and the subsequent calculation of the elastic constants of the α-crystal of PA-6.

4.5.2 Crystal Modifications and Cell Generation

4.5.2.1 Crystal Modifications

Polyamide-6 crystals can exist in two major forms: a monoclinic α- and a monoclinic γ-form, although the existence of other structures has also been reported. The two forms usually coexist in the bulk material. The α-phase can be converted to the γ-phase by iodine treatment, and the γ-phase can be converted to the α-phase by phenol treatment and by stretching. The α-phase has been found to be the most stable structure of PA-6 crystals.[Lin92a] A schematic representation of the unit cell is given in Fig. 4.29 and the cell parameters are listed in Table 4-46.

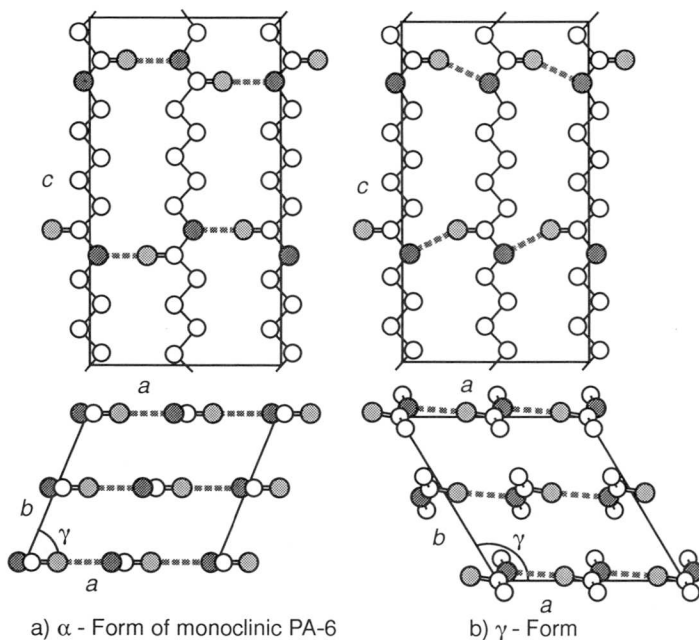a) α - Form of monoclinic PA-6   b) γ - Form

Figure 4.29: Front and top view of: a) α - Form of monoclinic PA-6, b) γ - Form of monoclinic PA-6
(hydrogen atoms are omitted for clarity)

Table 4-46: Experimental cell parameters of α - and γ - PA-6[Tadokoro90]; average of the
last $2 \cdot 10^5$ TσN-MD steps at 300 K in the middle column (scaled force field)

Parameter	α - PA-6	α - PA-6 (MD)	γ - PA-6
a [Å]	9.56	9.64	9.33
b [Å]	8.01	8.03	9.56
c [Å]	17.24	17.38	16.88
α [°]	90	90.0	90
β [°]	90	90.0	90
γ [°]	67.5	69.0	121

4.5.2.2 Structure Generation and Forcefield Modification

At first, it was necessary to redefine the PA-6 repeat unit. The default
repeat unit, provided with the 'Insight' package and the redefined unit are shown
in Fig. 4.30. The grouping of the default repeat unit was adjusted to the *cvff*
forcefield, while the changes inferred by the *scaled_pcff* forcefield made it nec-
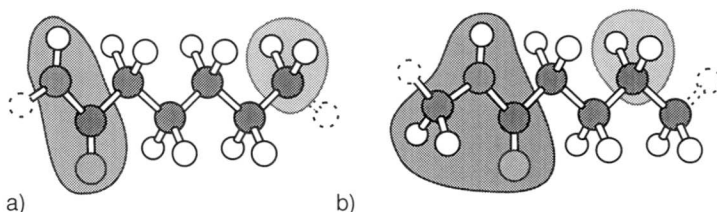
Figure 4.30: Polyamide-6: a) default repeat unit, b) modified repeat unit with neutral groups

essary to extend the amine group to the next CH2-group.

A macrocell of 3×3×2 units cells of α-monoclinic PA-6, containing 36 chains of 4 repeat units (2736 atoms in total) was built using the 'Crystal Cell' tools of the 'Insight' modeling package[MSIPolymer1]. As for all polymer crystals, bonds across boundaries were applied in order to mimic infinite chains. While simulating the cell, it was realized that the density of the crystal was about 2-3 % too low. In order to correct for this, two of the nonbonded parameters of the *pcff* forcefield were reduced by 3 %.The table below shows the difference between

Table 4-47: Changes in the s-parameter of the Lennard-Jones potential of carbon (c) and hydrogen (h) atoms

	σ^c [Å]	σ^h [Å]
pcff	4.0100	2.9950
scaled_pcff	3.8897	2.9052

the *pcff* and the new forcefield, named *scaled_pcff*. After this change, the average density of the crystal cell (1.22 ± 0.01 g·cm^{-3} from the last 100 ps of an *TσN*-MD run) was in perfect agreement with literature values shown in Table 4-48.

Table 4-48: Literature value for the density of crystalline and amorphous PA-6

	ρ_c [g·cm^{-3}]	ρ_a [g·cm^{-3}]
Mean Value[Lewis80a]	1.22 ± 0.01	1.10 ± 0.01

The *scaled_pcff* forcefield was therefore used for all subsequent simulations of Polyamides (PA-6 and PA-12).

Although there are considerable charges in the PA-6 repeat unit, the Coulombic interactions were computed using a cutoff, because the Ewald summation would have slowed down the whole process too much. (A short test run required 47 seconds/step on an Indigo II workstation, i.e. approx. $\frac{1}{2}$ day/ps.) The

results of the simulations of the crystal should be interpreted with this limitation in mind. But since all charged groups are neutral and small - most of them consist of CH_2-groups, and the largest group, HN-CH_2, is less than 3 Å in diameter - the effect should be much smaller than for cellulose. The amorphous cell computations are even less sensitive to the problem of large partial charges because they lack long-range order.

4.5.3 Simulation Procedure

After the setting up of the crystal structure, the cell was minimized down to an energy of -2.902 kcal/(mol·atom), followed by a $T\sigma N$-MD simulation of $3 \cdot 10^5$ steps (150 ps), conducted at 300 K. The long-range Lennard-Jones interactions were taken into account by a correction pressure of 1630 bar. As usual, a Parrinello-Rahman pressure control and a Nosé-Hoover thermostat algorithm were used to keep stress and temperature approximately constant (the effective pressure was 1514 bar and the effective temperature 293 K).

After some initial fluctuations, the simulation cell was stable in dynamics,
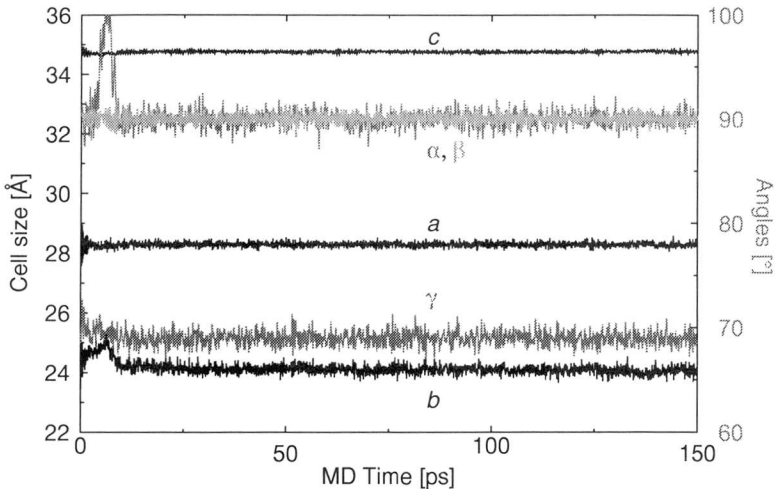

Figure 4.31: Cell parameters of crystalline PA-6 ($T\sigma N$-MD at 300 K)

as can be verified from Fig. 4.31. In the last 100 ps, the cell parameters and the components of the actual stress were stored every fs, totalling 10^5 samples. From these samples, the elastic constants were calculated using Eqs. (3-29) and (3-36). The results of this procedure are reported in the next chapter.

4.5.4 Results

4.5.4.1 Elastic Constants from Fluctuation Approaches

Table 4-49 lists the values of the elastic constants averaged over the last

Table 4-49: Elastic constants of PA-6 averaged over the last 100 ps of a 150 ps $T\sigma N$-MD simulation at 300 K. Non-zero components are bold faced.

$\frac{kT}{\langle V\rangle}\langle\eta_{ik}\eta_{lm}\rangle^{-1}$ [GPa]						$\langle\eta_{ik}\sigma_{nj}\rangle\langle\eta_{nj}\eta_{lm}\rangle^{-1}$ [GPa]					
26.67	**2.75**	**0.36**	0.06	–0.06	**–1.08**	**21.15**	**2.18**	**0.29**	0.04	–0.05	**–0.85**
2.75	**8.13**	**9.79**	0.00	–0.04	**0.33**	**4.30**	**12.73**	**15.34**	0.00	–0.07	**0.51**
0.36	**9.79**	**191.0**	–0.07	0.61	**0.84**	**0.36**	**9.58**	**186.8**	–0.07	0.60	**0.82**
0.06	0.00	–0.07	**1.21**	**–0.32**	–0.01	0.06	0.00	–0.08	**1.37**	**–0.36**	–0.01
–0.06	–0.04	0.61	**–0.32**	**3.31**	0.09	–0.04	–0.03	0.45	**–0.24**	**2.43**	0.07
–1.08	**0.33**	**0.84**	–0.01	0.09	**1.31**	**–0.92**	**0.28**	**0.72**	–0.01	0.08	**1.12**

100 ps of the MD-trajectory and Fig. 4.32 shows the convergence of the diagonal elements of the elasticity matrix with averaging time.
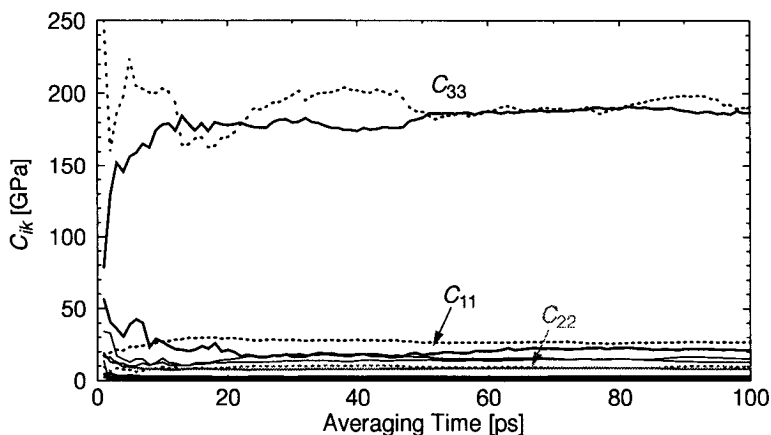

Figure 4.32: Convergence behaviour of the diagonal elements (and C_{12}, C_{13}, and C_{23}) of the elasticity matrix form the strain (dotted lines) and the stress-strain fluctuations (solid lines)

4.5.5 Discussion

4.5.5.1 Relationship Between Structure and Elastic Constants

The calculation of the Eigenvalues of the strain fluctuation matrix of Table 4-49, as shown below, gives three orthogonal directions with largely differ-

Table 4-50: Eigenvalues and Eigenvectors of the elasticity matrix (strain fluctuations)

Eigenvalue [GPa]	Components of the Eigenvector (Voigt notation)					
191.52	0.003	0.053	**0.999**	0.000	0.003	0.004
27.10	**0.990**	0.137	-0.010	0.002	-0.003	-0.040
7.25	-0.135	**0.987**	-0.053	0.001	-0.016	0.071
3.36	0.003	0.013	-0.004	-0.148	**0.988**	0.043
1.23	0.049	-0.065	-0.001	0.101	-0.027	**0.991**
1.17	-0.007	0.008	0.000	**0.984**	0.151	-0.095

ent elastic constants. The highest value is of course along the x_3-(c)-direction, parallel to the chains. Still a relatively high value of 27 GPa can be found along the x_1-(a)-direction. Comparison with Fig. 4.29 shows that this is more or less parallel to the hydrogen bridges between carbonyl and amine groups. The value of 7.25 GPa in the x_2-(b)-direction is typical of Lennard-Jones interactions. Almost identical results can be obtained using the stress-strain fluctuations.

4.5.5.2 Comparison With Literature Values

Again, the available experimental and theoretical data are so widely scattered that hardly any precise conclusions are possible. Experimental results range from 165 to 175 GPa, whereas computational results span a range from 190 to 312 GPa, as the next table summarizes.

Table 4-51: Experimental and theoretical estimations of the ultimate Young's modulus in the chain direction of PA-6

	Reference	E_3 [GPa]	Method
theoretical	Manley et al.[Manley73a]	244 - 263	energy balance
	Tashiro et al.[Tashiro81a]	312	general matrix
experimental	Sakurada et al.[Sakurada70a]	165	X-ray diffraction
	Kaji et al.[Kaji78a]	183	X-ray diffraction
	Lewis et al.[Lewis80a]	164.8	macroscopic & Takayangi model
	Matsuo et al.[Matsuo93a]	173 - 175	X-ray diffraction

The results of this work (179 GPa from the strain-, and 174 GPa from the stress-strain-fluctuations) compare very well with the most recent experimental data from Matsuo et al.[Matsuo93a] They are, however, lower than Young's modulus

obtained from theoretical calculations. No comparison is made here for the whole matrix of the elastic constants, since the only one published in the literature from Tashiro *et al.* has quite an unrealistic C_{33}-value of more than 300 GPa.

Concerning the transverse moduli E_1 and E_2, experimental results of 11.4 - 12 GPa and 7.7 - 9 GPa can be found[Matsuo94a], which - for the E_1 modulus - are considerably lower than the values of this work (19.5 - 23.6 GPa and 7.2 - 11.3 GPa, respectively). The difference of almost a factor 2 can be rationalized by the sensitivity of this value to the partial charges used to model the hydrogen bonds and by the difficulties to properly sum up these coulombic interactions.

4.5.5.3 Conclusions

A reduction of the atom radii of carbon and hydrogen atoms in the *pcff* forcefield was made by 3 % to match the experimental and calculated density of α - PA-6. The crystal cell was large enough to remain stable in dynamics at 300 K, so the elastic constants could be calculated from the strain and the stress-strain fluctuations. Young's modulus in the chain direction was found to be 174 and 179 GPa, which compares well with recent experimental data, but which is lower than most other theoretical calculations. The transverse modulus along the direction of the hydrogen bonds is considerably higher than experimental data. This fact can be explained by the difficulties arising from the modeling of hydrogen bonds with partial charges. The favourable Ewald summation could not be performed on these large cells without slowing down the calculations too much. The transverse modulus perpendicular to the hydrogen bonds is in complete agreement with experimental numbers.

4.6 Polyamide-6 - Amorphous Cells

4.6.1 Introduction

As already pointed out in chapter 4.5.1, polyamide-6 is a semicrystalline material composed of mesomorphous crystalline (30 - 40 %[Kawasaki64a,Inoue76a]) and amorphous parts. The very good mechanical properties do not depend on the morphology only, but also on the amount of water absorbed from the moisture of the air. The equilibrium content of water in the polymer depends on the activity of water in the air (relative humidity)[Puffr67a,Asada63b,Inoue76a], the concentration of NH-CO-groups[Song90a], and the degree of crystallinity. The crystalline phase exhibits insignificant solubility for water molecules, so that the amorphous phase is responsible for the observed effects[Puffr67a,Song90a,Starkweather59a, Kawasaki64a,Prevorsek71b]. These comprise the mechanical relaxations, called γ, β and α, which take place in PA-6 at approx. -120°C, -40°C and +50 to +90°C[Prevorsek71b,Kettle77a, Khanna95a], respectively. The γ relaxation is attributed to the motion of methyl groups and is hardly affected by the presence of water, while the β relaxation, which is caused by water molecules bonded to amide groups via hydrogen bonds, naturally is highly sensitive to the water content and disappears in thoroughly dried nylon. The α relaxation - the glass transition - is assigned to the motion of large chain segments in the range of 15 repeat units.[Prevorsek71b, Boyd59a] There exists a variety of experimental curves for the dependence of the glass transition temperature T_g on the water content: In one measurement, T_g decreases with increasing water content in several stages: A fast drop of T_g is found between 0 and 2 wt% of water, while between 2 and 4 wt% the dependence is less pronounced, followed again by a further reduction at water concentrations higher than 4 wt%.[Kettle77a] In other experiments, however, T_g declines fast with increasing water content up to 3 wt% and then reduces more slowly beyond this level.[Prevorsek71b, Khanna95a,Reimschuessel78a]

From these and other effects like anisotropic swelling of oriented samples[Kaimin73a], sorption isotherms[Hernandez94a] and changes in Raman spectra[Stuart94a], a 3-stage model has been proposed[Puffr67a] (Figure 4.33): At first, water forms a double hydrogen bond between two adjacent carbonyl groups (Site *1* in Figure 4.33). In this step a large amount of energy is released and the molecules are referred to as firmly bound. The second stage is the extension of the already existing hydrogen bonds between carbonyl and amide groups by bridging water molecules, which are classified as loosely bound water (Site *2*). These first 2-3% of absorbed water strongly affect the glass transition due to the change in the interchain distance and the creation of voids in the
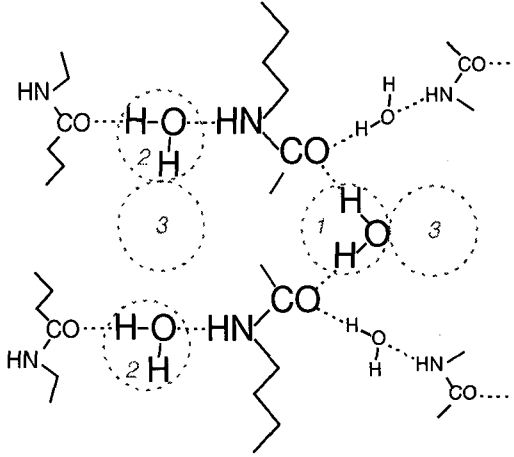
Figure 4.33: Model of adsorption of water in nylon. Site *1*: firmly bound water, *2*: loosely bound water, *3*: sites for capillary condensed water

structure. In the third stage, further water is attached to the already absorbed water molecules and forms clusters in capillary sites (Site *3*).

The effect of relatively large water concentrations (10 wt%, corresponding to 100% relative humidity) on the storage modulus of PA-6 is depicted in Figure 4.34:[Prevorsek71b] The glass transition temperature is reduced by the pres-
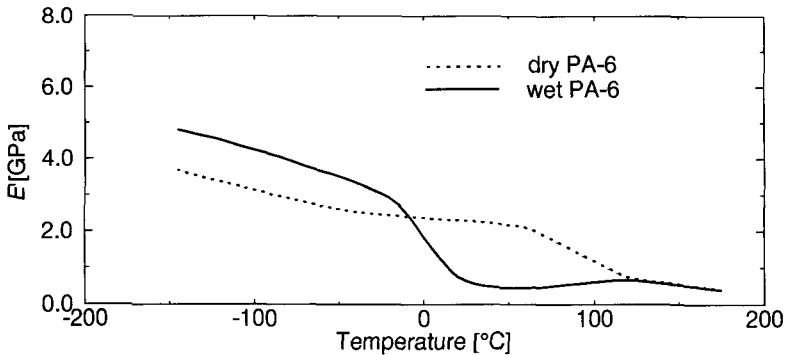

Figure 4.34: Storage Modulus of (semicrystalline) Nylon-6 as a function of temperature. Dotted line: dry PA-6 (0 wt% water), solid line: wet PA-6 (10 wt% water)

ence of water from approx. 80° C close to 0° C. This is a consequence of the increased mobility of the chain segments by the widening of the hydrogen bonds by the bridging water molecules. At temperatures below the transition point, the

plasticizing effect of water is reversed into an antiplasticizing one, which is expressed by the higher modulus of wet PA-6.

In the following work it was investigated whether or not the above described influence of water on the elastic constants could be reproduced by using fluctuation approaches. To do this, several atomistically detailed microstructures of amorphous PA-6 with and without water molecules were generated and minimized. $T\sigma N$-MD simulations of 1000 ps at 150, 300, and 450 K were performed to gather information about the temperature dependence of the mechanical behavior.

4.6.2 Cell Generation

4.6.2.1 Introduction

In contrast to polymer crystals, the conformation of a chain in an amorphous material is not specified and can vary to a large extent. The long relaxation times of dense polymeric systems forbid the generation of an amorphous cell from an ordered system by melting and subsequent equilibration. It is therefore necessary to build a representative chain conformation from the very beginning of the construction process.

This was done by using the 'Amorphous Cell' module in the 'Insight' modelling package.[MSIPolymer1] The method used therein can be briefly described as the stepwise RIS method of Theodorou and Suter[Theodorou85a] , which is loosely based on the the scanning method of Meirovitch[Meirovitch83a,Meirovitch85a]. After placing the first two backbone bonds in a random orientation in the center of an empty cell with periodic continuation conditions, the chain is built up in a bond-by-bond fashion. For each step, a number of random configurations is built with a couple of so-called *lookahead* bonds in order to estimate the partition function of this short segment and to avoid deadlocks. In the building process, either the RIS states and their corresponding weights are used or the minima of the backbone torsion potential define the possible states. If adjacent minima are separated by high barriers (e.g. double bonds), a bond is allowed only the state it was in in the initially - in vacuo - constructed molecule. To increase the flexibility of the chain, a number of substates around each state and a corresponding substate width can be specified. From these lookahead conformations, a dihedral angle ϕ_i is selected with the probability[Flory89]

$$q_i^* = \frac{\exp\left(\frac{-\Delta U_i}{RT}\right)}{\sum\limits_{\{\phi_i\}} \exp\left(-\frac{-\Delta U_i}{RT}\right)}. \tag{4-29}$$

The term ΔU_i stands for the change in the nonbond energy if the entire looka-head were added.

The density of the final structure is determined by the size of the periodic box. For linear polymers without cyclic groups, it is possible to take the experimental density. If polymers with ring structures are used, it is necessary to specify a target density that is 20 to 30 % below the experimental density. Otherwise, almost all structures will be rejected during the building process because of spearing or catenation.

4.6.2.2 Dry and Wet Samples

A single chain of 50 modified (chapter 4.5.2.2) repeat units with 952 atoms - including the two terminating hydrogen atoms - was generated by using the following parameters for the construction:

- Temperature: 300 K
- Density: 1.10 g/cm^3
- Lookahead bonds: 5
- Number of substates: 1
- Substate width   10
- Max. lookahead configurations: 50

If a water-saturated structure was to be generated, there were at first 35 water molecules (corresponding to 10 wt% in the amorphous phase and about 6 wt% in the semicrystalline material) being placed in the empty simulation cell before the chain was grown around them.

There were 3 'dry' and 'wet' structures each built.

4.6.3 Simulation Procedure

4.6.3.1 Equilibration

To remove the largest overlaps, all structures were first minimized by 500 steps of steepest descent routines. The cutoff was set to 8.5 Å with a spline width of 1 Å.

After minimization, 250 ps of *TpN*-MD - i.e. the cell size was allowed to vary, but the cell shape was kept cubic - were conducted at 300 K. Since a Berendsen thermostat was used, it was possible to make steps of 1 fs. The pressure

was set to 1630 bar in order to compensate for the neglect of long-range Lennard-Jones interactions.

This was done because cells that were allowed to fluctuate in shape immediately after minimization were sometimes heavily distorted in the initial period of an MD run. The *TpN*-simulation allowed for the relaxation of the largest internal strains and for the setting of the density.

4.6.3.2 Sampling

The sampling runs of both wet and dry amorphous PA-6 were conducted according to the following scheme:
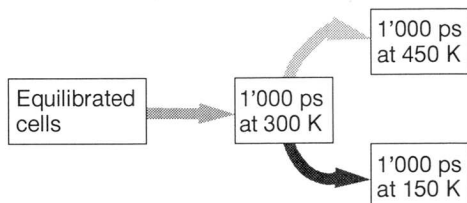
i.e. after sampling the structure for 1 ns ($2 \cdot 10^6$ steps) at approx. 300 K, the temperature was raised to 450 or lowered to 150 K and another $2 \cdot 10^6$ steps were performed at the new temperature. Again, an MD algorithm sampling the *TσN*-ensemble with a Nosé-Hoover thermostat and a Parrinello-Rahman manostat was used. A correction pressure of 1630 bar was applied, irrespective of the exact density.

4.6.4 Results

4.6.4.1 Densities and Thermal Expansion

A good overview over the fluctuations in density and the stability of the simulations is given in Fig. 4.35. At all three temperatures, the density shows no substantial drifts. Furthermore, the increase in the fluctuation width with raising temperature can be well observed. Going from 300 K to higher or lower temperature, the equilibration period of the density seems to be rather short and in the range of 100 ps. If all six (3 'dry' and 3 'wet' structures) were plotted together, the following picture (Fig. 4.36) results: The antiplasticizing effect of water at low temperatures is manifest in an increase of the density, whereas at room temperature, water has no significant influence. At 450 K, the lower density of the 'wet' structures indicates a weakening of the nonbonded interactions by the presence of water molecules - a plastification takes place. Table 4-52 lists the average
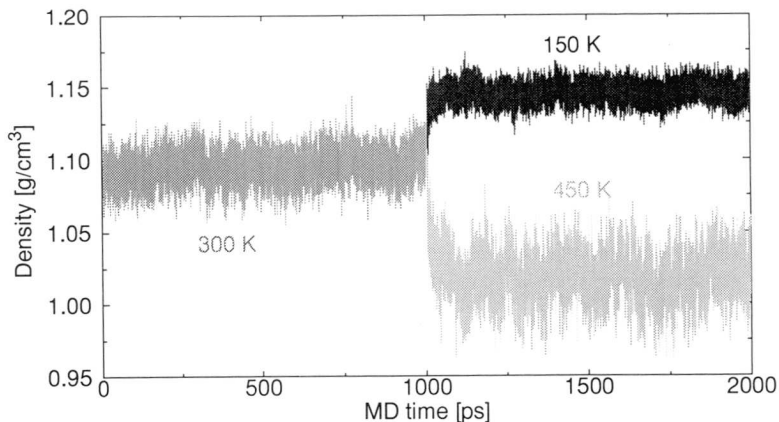
Figure 4.35: Density of structure 1 of wet PA-6 as a function of time and temperature
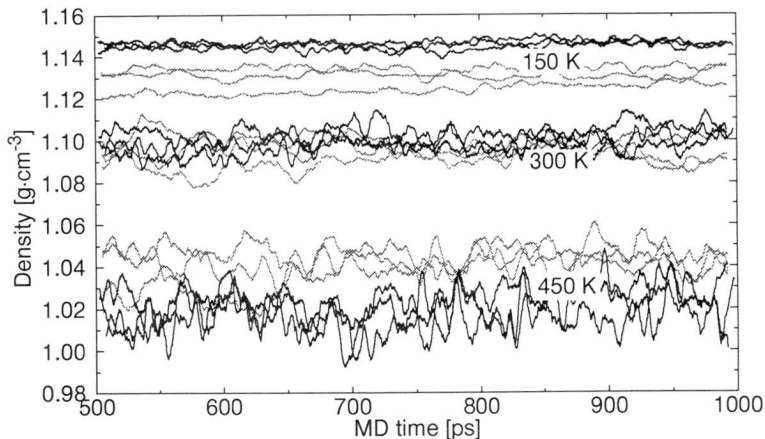

Figure 4.36: Densities of all six structures during the second 500 ps of dynamics; black lines refer to 'wet' structures, whereas gray lines signify 'dry' structures

Table 4-52: Average densities of dry and wet amorphous PA-6 cells

T [K]	$\langle \rho_{dry} \rangle$ [g/cm^3]	$\langle \rho_{wet} \rangle$ [g/cm^3]
150	1.1297 ± 0.0052	1.1455 ± 0.0007
300	1.0950 ± 0.0051	1.0997 ± 0.0027
450	1.0416 ± 0.0040	1.0201 ± 0.0030

densities of dry and wet PA-6 as a function of the temperature. From these val-

ues, the thermal expansion coefficient α (for isotropic materials, the tensor of the thermal expansivity, $\eta_{ik} = \alpha_{ik}\Delta T$, reduces to $\alpha_{ik} = \alpha\delta_{ik}$, where δ_{ik} denotes the familiar Kronecker symbol) can be computed as

$$\alpha = \frac{1}{2}\frac{\left[\frac{V}{V_0}\right]^{\frac{2}{3}} - 1}{\Delta T} = \frac{1}{2}\frac{\left[\frac{\rho_0}{\rho}\right]^{\frac{2}{3}} - 1}{\Delta T}. \qquad (4\text{-}30)$$

The resulting thermal expansion coefficients are summarized below:

Table 4-53: Thermal expansion coefficients of 'dry' and 'wet' PA-6 at two temperature intervals

	Temperature	Thermal expansion
Dry	150 → 300 K	$7.0 \cdot 10^{-5}$ K^{-1}
	300 → 450 K	$11.3 \cdot 10^{-5}$ K^{-1}
Wet	150 → 300 K	$9.3 \cdot 10^{-5}$ K^{-1}
	300 → 450 K	$17.1 \cdot 10^{-5}$ K^{-1}

The values of Table 4-53 agree well with experimental data[Brandrup89] of $\alpha = 7\text{-}10 \cdot 10^{-5}$ K^{-1} at 20° and $10\text{-}14 \cdot 10^{-5}$ K^{-1} at 100°C. The experimental density at 20°C is 1.10 g/cm^3 (compare Tables 4-48 and 4-52).

4.6.4.2 Diffusion of Water

From coordinate files, which were saved every 10 ps, the mean square displacement r^2 of the water molecules of the wet structures could be calculated. The displacement of the center of mass of the water molecules was replaced by the displacement of the oxygen atoms without noticeable loss of precision. Assuming an Einstein diffusion (i.e. random walk mechanism), the diffusion constant D is defined by

$$\langle r^2 \rangle = 6Dt. \qquad (4\text{-}31)$$

Taking the logarithm on both sides yields

$$\log \langle r^2 \rangle = \log (6Dt) = \log (6D) + \log (t) \qquad (4\text{-}32)$$

In a $\log\langle r^2 \rangle$ vs. $\log(t)$ plot, there should be a straight line with a slope of one and an intercept of $\log(6D)$. If the slope is different from one, there is no random walk, but another mechanism (e.g. constraint motion along specific paths, hopping between two neighbouring sites). In Fig. 4.37, the average mean square
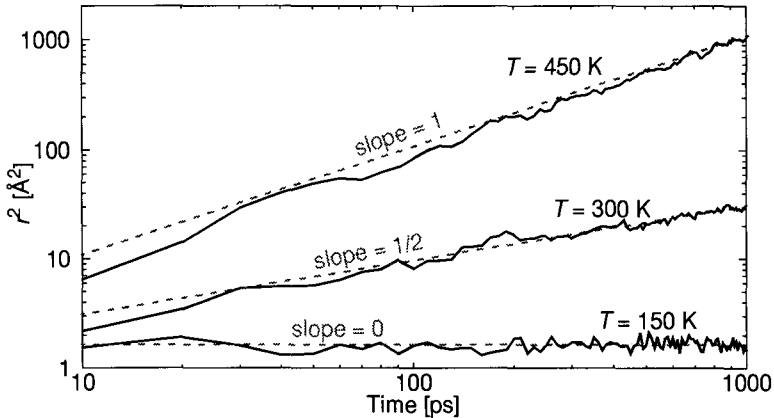
Figure 4.37: Mean square displacement of the water molecules at 150, 300, and 450 K, average over three microstructures, over all water molecules, and over all independent sub-trajectories

displacement of the water molecules in PA-6 has been plotted as a function of time and temperature. The three straight lines with slopes of 1, $\frac{1}{2}$, and 0 are only guidelines for the eyes and do not represent any regression analysis. Only at 450 K, a random walk mechanism can be observed, whereas an anomalous diffusion is manifest at 300 K. At 150 K, the mobility of the water atoms is so low that no diffusion at all can be observed within the simulation time.

It is therefore only meaningful to compute the diffusion constant at 450 K, where the intercept of the straight line at 1000 ps yields a value of $D \approx 1.8 \cdot 10^{-5}$ cm^2/s. There is no experimental data at this temperature available, but an extrapolation from 20°, 60°, and 100°C[Brandrup89] to 177°C results in $D \approx 4.6 \cdot 10^{-5}$ cm^2/s. Since experimental diffusion constants are known to be subject to substantial uncertainties and the extrapolation spans more than 70 K, the calculated value is still plausible.

4.6.4.3 Clustering of Water Molecules

An attempt was made to quantify the distribution of the water molecules in the polyamide microstructures. In a first step, the microstructures were tessellated into Voronoi polyhedra, using a code of Peter Mott[Mott92a].

According to Figure 4.38, two water molecules were considered to belong to the same *cluster*, if any two of their atoms shared a common surface. In a second step, the number and size of the different water clusters in a polyamide structure were determined. Doing this for each coordinate frame, a 'dynamics' of the formation and disintegration of the water clusters could be established. A
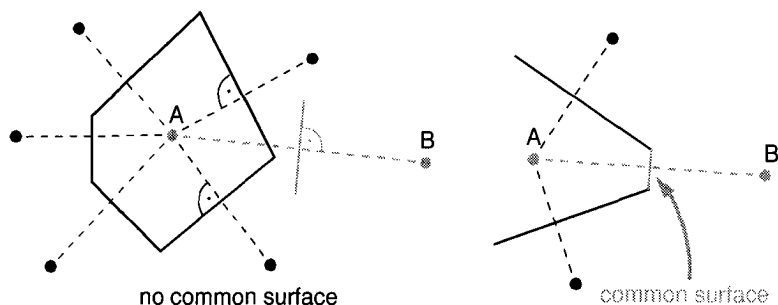
no common surface   common surface

Figure 4.38: Definition of the Voronoi polyhedron, where A and B have no common surface (left), situation, where A and B possess a common surface (right)

short example of this process is given in Table 4-54. At the low temperature of

Table 4-54: Dynamics of the water clusters in structure 2 at 150 K, arrows with numbers indicate the exchange of individual water molecules or the merge of two neighbouring clusters.

Time [ps]	water molecules in cluster				
	# 1	# 2	# 3	# 4	# 5
0-200	20	11	2	1	1
300-400	21	10	2	1	1
500-1000	31	2	1	1	

150 K, the cluster dynamics is rather slow, which allows to track the motion of individual water molecules quite well. At higher temperatures, the temporal resolution of 10 ps is sometimes too long to follow all changes. More detailed analyses at 300 and 450 K can be found in Appendix G-1.

From these tables and from more detailed examinations, the following conclusions can be drawn: It is not possible to observe a significant change in the average size of the clusters with time or with temperature. There seems to be nothing like Ostwald ripening, i.e. a growth of the large clusters at the expense of the small ones. Instead of this, there is a dynamic process of clustering and breaking apart of the water molecules. Some water molecules are quite fixed in the local structure - i.e. they remain isolated for the whole observation period or stay together for quite a while - whereas more mobile water molecules can form large clusters from time to time. These large clusters, however, only have a short lifetime (<10 ps) before they separate into two or more smaller units. This is an indication that the bridges connecting the different parts of the larger clusters are

quite thin, whereas cores of more closely connected water molecules must also exist.(see Fig. 4.39).
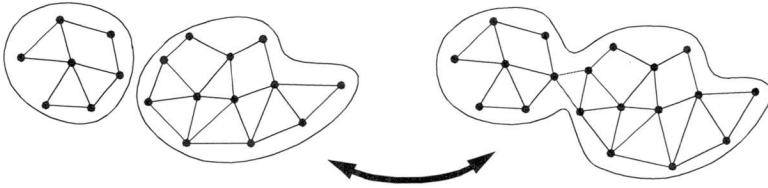

Figure 4.39: Model of the cluster dynamics of water molecules in PA-6

The distribution of the different cluster sizes and the probability of finding a water molecule in a cluster of a given size are plotted in Fig. 4.40. Although the
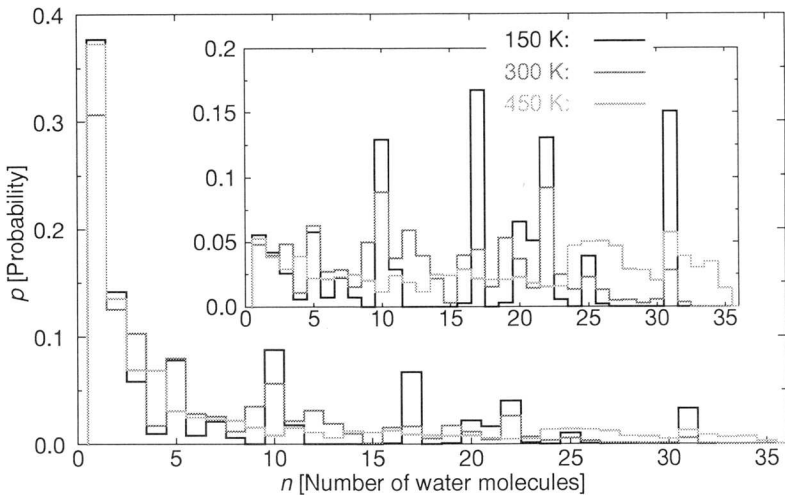

Figure 4.40: Distribution of the cluster sizes in PA-6 at 150, 300, and 450 K (large plot); probability of finding a water molecule in cluster of a given size (small plot)

statistics is not excellent, it can be clearly seen that the increased mobility of the water molecules at elevated temperatures leads to a more or less uniform distribution of the cluster sizes, i.e. there is no preferred cluster size anymore. If the temperature is only 150 K, there are just a few clusters, which hardly change their size. The initial water distribution (from the previous run at 300 K) remains almost frozen for the rest of the simulation.

The exact orientation of the water molecules within the clusters was not studied in detail, but the following picture (Fig. 4.41) might provide an idea:
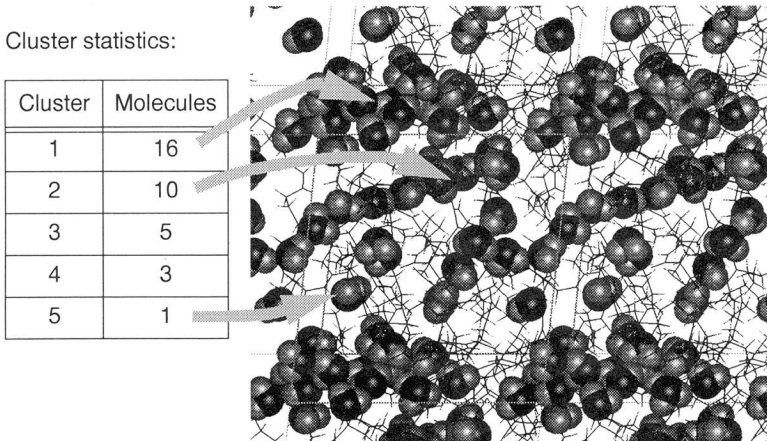
Cluster statistics:

Cluster	Molecules
1	16
2	10
3	5
4	3
5	1

Figure 4.41: Distribution of water in PA-6 (300 K, after 700 ps of $T\sigma N$-MD)

There is no 'ice-like' structure, but there are complexes being formed of partly oriented water molecules, which was also observed in a recent study of Terzis et al.[Terzis97a].

4.6.4.4 Elastic Constants

There were in total 18 trajectories of 1000 ps from which the elastic constants were calculated: 3 microstructures of 'dry' and 'wet' PA-6 at 150, 300, and 450 K. From each trajectory, the first 500 ps were discharged for relaxation processes and only the last 500 ps contributed to the fluctuations from which the elastic constants were calculated. Since the cell parameters a, b, c, α, β, and γ and the stress tensor σ were recorded with an interval of 10 fs, $5 \cdot 10^4$ frames were used for the computation of the elastic constants each. Both the strain fluctuation approach from Parrinello and Rahman, and the Gusev-Zehnder-Suter stress-strain fluctuation approach were applied. Appendix G-2 lists the results of the stress-strain fluctuation approach for all trajectories. From these trajectories, the two Lamé constants λ and μ were fitted to the matrices of the elastic constants such, that the difference to a theoretical matrix of an isotropic material,

$$\begin{bmatrix} \lambda+2\mu & \lambda & \lambda & 0 & 0 & 0 \\ \lambda & \lambda+2\mu & \lambda & 0 & 0 & 0 \\ \lambda & \lambda & \lambda+2\mu & 0 & 0 & 0 \\ 0 & 0 & 0 & \mu & 0 & 0 \\ 0 & 0 & 0 & 0 & \mu & 0 \\ 0 & 0 & 0 & 0 & 0 & \mu \end{bmatrix} \qquad (1\text{-}78)$$

was minimal.

Averaged over the three microstructures, these Lamé constants are summarized in Table 4-55. As could be recognized immediately from the data and

Table 4-55: Lamé constants of amorphous PA-6 as a function of the temperature and the water content

T [K]	'Dry' [GPa]	'Wet' [GPa]
150	$\lambda = 5.60 \pm 0.41$ $\mu = 2.07 \pm 0.21$	$\lambda = 6.40 \pm 0.30$ $\mu = 2.22 \pm 0.19$
300	$\lambda = 4.26 \pm 0.19$ $\mu = 1.05 \pm 0.15$	$\lambda = 4.63 \pm 0.29$ $\mu = 0.81 \pm 0.11$
450	$\lambda = 2.21 \pm 0.10$ $\mu = 0.25 \pm 0.04$	$\lambda = 0.94 \pm 0.10$ $\mu = 0.08 \pm 0.03$

also from Fig. 4.42, there is an stiffening effect of water at low temperatures,
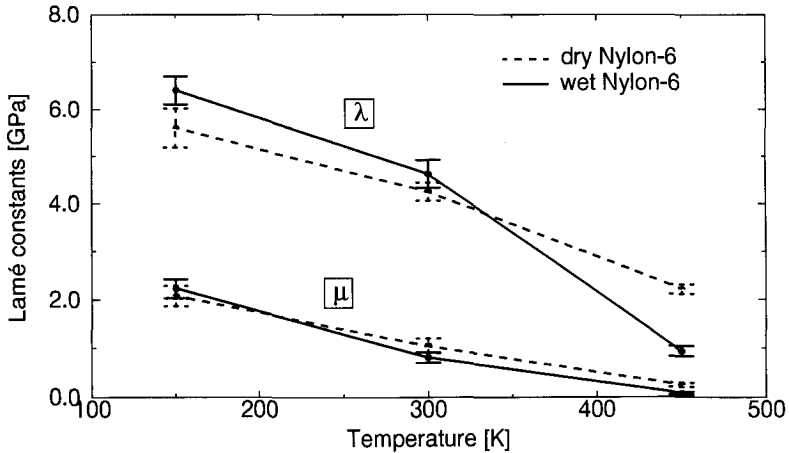

Figure 4.42: The temperature dependence of the Lamé constants of dry and wet PA-6 (average values and standard deviations)

whereas at high temperatures, water acts as a plasticizer. At room temperature, the two effects almost balance, and the influence of water is only small. A comparison with experimental data will be given in the next chapter, where the results obtained from the simulations will be discussed.

4.6.5 Discussion

4.6.5.1 Comparison with Literature Values

For the density, the thermal expansion coefficient, and the water diffusion, experimental values from the 'Polymer Handbook'[Brandrup89] have already been given. The computations all seem to be in reasonable agreement with experimental findings. This is a good validation of the model being used, although the simulation time at 300, and even more at 150 K, is too short to see a regular diffusion of the water molecules. The anomalous diffusion at 300 K is a well-known phenomenon, which occurs also in other systems (rare gases in BPA-PC), as the next plot (Fig. 4.43) shows: At relatively short times, the MD simulation is not
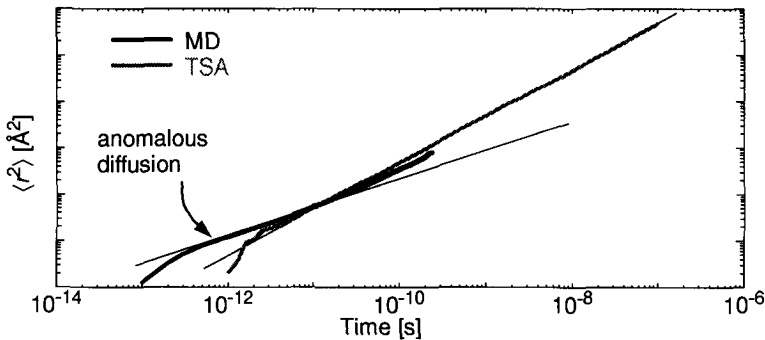

Figure 4.43: Diffusion of He in BPA-PC with MD and a transition state approach (TSA) at 300 K

able to propagate the diffusants far enough in order to establish a normal diffusion behaviour. Since water is considerably larger than helium, the curves in the above plot would be shifted to the right, so that no normal diffusion can be observed within the simulation period. The clustering behaviour of water in PA-6 was examined by Frank et al.[Frank96a] They found that clustering of water molecules starts at 6 wt% and that at 10 wt% on the average 2 - 3 water molecules are present in a cluster. In our simulations, the average number of molecules in a cluster is more than 5. The difference between the two numbers might originate from a different definition of a cluster. Hernandez and Gavara[Hernandez94a] estimated that nearly 90 % of the water molecules in PA-6 are moving freely. Ana-

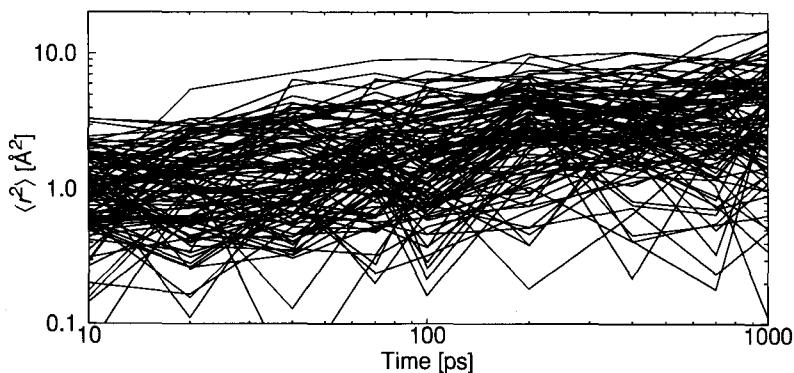lyzing the individual trajectories of water molecules (Fig. 4.44), it was not

Figure 4.44: Squared displacement of all 105 water molecules of the 3 PA-microstructures at 300 K

possible to make this distinction between 'adsorbed' or 'free' water. The 3-stage adsorption model presented in the introduction could therefore not be confirmed in this way.

One of the most important problems is it, to decide, whether the simulation was long enough for the relevant mechanical relaxations to take place. Strictly speaking, it was not, since a complete relaxation of the chain would involve a self-diffusion in the order of the radius of gyration and the water molecules were not able to move sufficiently.

On the other hand, the finite size of the simulation box reduces the relaxation times considerably. (This argument is explained in more detail in chapter 4.8.2). An indication of this mechanism being active is the fast adaptation of the density after the sudden change in temperature after 1 ns. The density relaxed within 100 ps and remained fairly constant afterwards (Fig. 4.35). This in turn allows to determine the thermal expansion coefficient quite well.

The elastic constants - the main concern of this work - compare with experimental data[Prevorsek71b] as follows:

As already mentioned, the general trend is reproduced, i.e. a stiffening effect of water below the glass transition and a plasticizing effect above the glass transition can be observed.

At 150 and also at 300 K, the computed values are consistently higher than the measured ones. This discrepancy (which is much smaller, if other sources of experimental values like Table 4-56 are considered) can be rationalized by the insufficient mobility of the water molecules, as became manifest in the diffusion
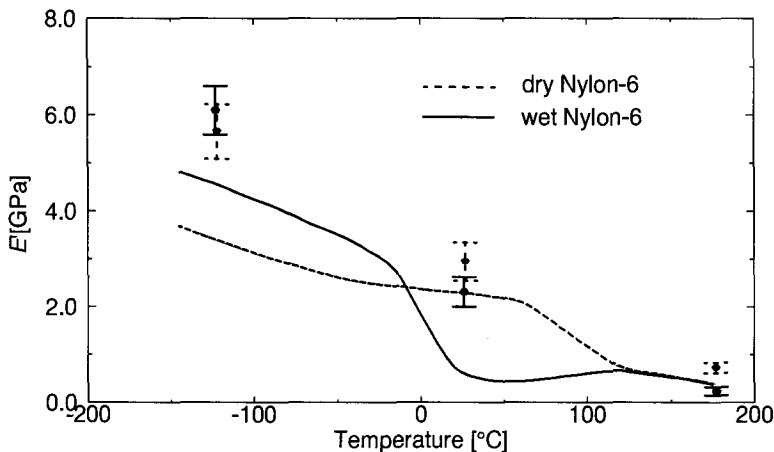
Figure 4.45: Experimental (solid lines) and computed (circles and error bars) storage moduli of
dry and 'wet' (10 wt% water) PA-6

behaviour. They are more or less trapped in the locations they occupied at the
end of the structure generation and are not able to diffuse to 'better' places.
Therefore, the influence of water on the elastic constants is not as marked as in
the experiment. Parallel to that, the polymer chain mobility is not sufficient to
sample the whole phase space within the simulation time. The width of the fluc-
tuations is therefore smaller and the elastic constants higher than in the case of
a fully relaxed polymer. Another reason for the difference is the fact that in a
semicrystalline material with 30 - 40% crystallinity and 10 wt% of water, the
effective water content in the amorphous part is approx. 15 wt%. In our simula-
tion, however, there were only 10 wt% water in the amorphous part.

At the high temperature of 450 K, the mobility of both the water molecules
and the polymer chain is sufficient to explore most of the available phase space.
The elastic constants are therefore quite close to the experimental curves. The
convergence of the two curves at temperatures above 120° C is due to the fact
that, above the boiling point, the water molecules diffuse out of the polyamide. It
can thus be assumed that the calculated elastic constants reflect the plasticizing
effect of water better.

Finally, Table 4-56 compares the values of the Young's and shear moduli of
PA-6 found in the 'Polymer Handbook'[Brandrup89] with computed values. The
experimental results at 100° C are compared with computed values at 450 K,
because - as mentioned in the introduction - there is an α-relaxation at 50 to
90° C, which would make a straight interpolation of the computed data question-

Table 4-56: Young's and shear moduli of semicrystalline experimental[Brandrup89] and amorphous computed PA-6

Modulus	T, state	exp. [MPa]	calc. [MPa]
E	23° C, dry	3000	2940 ± 400
	23° C, moist	1500	2310 ± 310
	100° C, dry	500	720 ± 110
G	23° C, dry	1100	1050 ± 150
	100° C, dry	200	250 ± 40

able. A further problem, which makes a comparison difficult, is that the experimental morphology is semicrystalline, whereas the simulation was performed on a purely amorphous microstructure. Besides these limitations, the simulated data seem to be in better agreement with experiment than Figure 4.45 suggests. The missing details about the experimental setup prevent a straightforward decision about their reliability.

4.6.5.2 Conclusions/Summary

At low temperatures (150 K) there is virtually no diffusion; a limited amount of clustering/unclustering happens. At room temperature, only anomalous diffusion of water could be observed. The clusters rearrange quite quickly (approx. every 30 ps). The classical 3-stage model could not be reproduced. Instead of this, a dynamical model of clusters with mobile peripheral atoms and relatively lasting cores was presented. At 450 K, the diffusion obeys a normal, random walk law and the cluster dynamics is very fast. The calculated diffusion coefficient does not contradict experimental results.

At low temperatures, the antiplasticizing effect of water expresses itself in an increase of the density due to some attractive interactions between water molecules and the polymer matrix (hydrogen bonds). At room temperature, the thermal motion of water more and more balances these attractive forces. Hardly any effect on the density could therefore be seen. At higher temperatures, the mobilization of the water molecules reduces the density of the polyamide matrix.

The dependence of the elastic constants on the temperature and the water content could be reproduced qualitatively, which is somewhat astonishing, since the limited size and the short trajectory prevent the water from taking its equilibrium positions at low and medium temperatures. A large part of the quantitative discrepancy between simulated and experimental elastic modulus might be attributed to this fact.

4.7 Polyamide-12 - Amorphous Cells

4.7.1 Introduction

The physical properties of polyamides, especially the elastic constants, depend on the amount of absorbed water, as pointed out in the previous chapter. In many applications, it would be desirable to reduce this dependency since the relative humidity of the air and therefore the water content and finally the properties of the polymer are subject to climatic changes. A reduction of the concentration of the functional, water absorbing carbonyl and amide groups automatically reduces the number of possible absorption sites and limits thus the equilibrium water content. On the other hand, the hydrogen bridges between carbonyl and amide groups are essential for the outstanding mechanical properties of polyamides. With their concentration reducing, the material approaches the behavior of polyolefines. Polyamide-12 (PA-12) is a compromise between reduced water absorption and enhanced polyolefinic character.

The results of MD runs at various temperatures with 'dry' and 'wet' microstructures are reported and the relation between the concentration of carbonyl and amide groups and the sensitivity of - mainly elastic - properties towards the water content is discussed.

4.7.2 Cell Generation

4.7.2.1 Dry and Wet Samples

A repeat unit of PA-12 was generated according to Figure 4.46. Analogous to PA-6, there were charged groups in the original setup. Simulations with
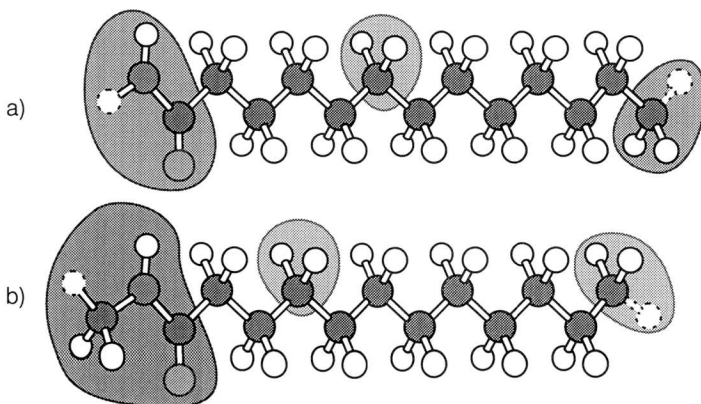

Figure 4.46: Repeat unit of PA-12 with (a) and without (b) charged groups

charged groups according to Fig. 4.46 a) and with neutral groups were carried out. Except where explicitly noted, only the results obtained from neutral charge groups will be presented.

The above repeat units were subject to a short run of 1000 $Th N$-MD steps to modify the torsion angles a bit. This modification away from an all-trans conformation eases the task of the 'Amorphous Cell' construction run.[a]

The degree of polymerization n_{ru} as a function of the cell size l is given by

$$n_{ru} = \frac{\rho[g/cm^3] \cdot l[\text{Å}]^3 \cdot 10^{-30} \cdot N_A}{m_w[g/mol]} \tag{14}$$

which can be shortened to

$$n_{ru} = (l[\text{Å}])^3 \cdot 0.00308247, \tag{15}$$

assuming an experimental density ρ of 1.01 g/cm^3 (for amorphous mouldings[Brandrup89]) and setting the mass of the repeat unit W = 197.32 g/mol. Together with the number of atoms per repeat unit (37 atoms), it can be estimated that 28 repeat units with 980 atoms yield a cell of approx. 21 Å size.

A single chain of the above size was polymerized with random angles between the repeat units. Again, a short $Th N$-MD run was started in order to further randomize the torsional degrees of freedom. Afterwards, an 'Amorphous Cell' construction run was started using the following parameters:

- Temperature: 300 K
- Density: 1.01 g/cm^3
- Number of Substates: 1
- Substate Width   5.0
- Lookahead   5
- Number of Lookahead Configurations: 50
- Bonds per Step: 5

If 'wet' cells were generated, 12 water molecules were placed in the simulation cell before the polyamide chain was grown around them. This number was estimated from water concentrations of 16[Pathmanathan95a] and 25 mol%[Varlet90a] at saturation and a degree of crystallinity of about 30 %[Varlet90a] given in the literature. From these informations, a concentration of 40 mol%, corresponding to 3.7 wt% water in the amorphous phase was chosen, balancing between a statistically sufficient number of water molecules and a realistic water content that allows comparison with experimental findings. The nylon cell contains 28 poly-

---

a. Andrew Tiller, MSI, private commuNcation

mer repeat units to which $0.4 \cdot 28 = 11.2$ water molecules - which were rounded up to 12 - were added.

Of the 5 configurations that were each built, the 3 with the lowest energy after the initial minimization were chosen.

4.7.3 Simulation Procedure

To remove the largest overlaps, all structures were first minimized by 5000 steps of steepest descent and conjugate gradient routines. The cutoff was set to 8.5 Å with a spline width of 0.5 Å.

After minimization, 50 ps of TpN-MD were conducted at 300 K with a Nosé-Hoover thermostat and a stepsize of 0.5 fs. The pressure was set to 1110 bar to compensate for the neglect of long-range Lennard-Jones interactions.

The sampling runs of PA-12 were conducted according to the same scheme as for amorphous PA-6, i.e. after sampling the structure for 1 ns ($2 \cdot 10^6$ steps) at approx. 300 K, the temperature was raised to 450 or lowered to 150 K and another $2 \cdot 10^6$ steps were performed at the new temperature. An MD algorithm sampling the $T\sigma N$-ensemble with a Nosé-Hoover thermostat and a Parrinello-Rahman manostat was used. A constant correction pressure of 1110 bar was applied again. The cell parameters and the stresses were saved to table files every 10 fs and the coordinates and velocities of all atoms were stored every 10 ps for further analysis.

4.7.4 Results

4.7.4.1 Densities and Thermal Expansion

The mechanical relaxation at the three different temperatures (150, 300, and 450 K) of the 'wet' structure no. 2 is given as an overview in Figure 4.47.
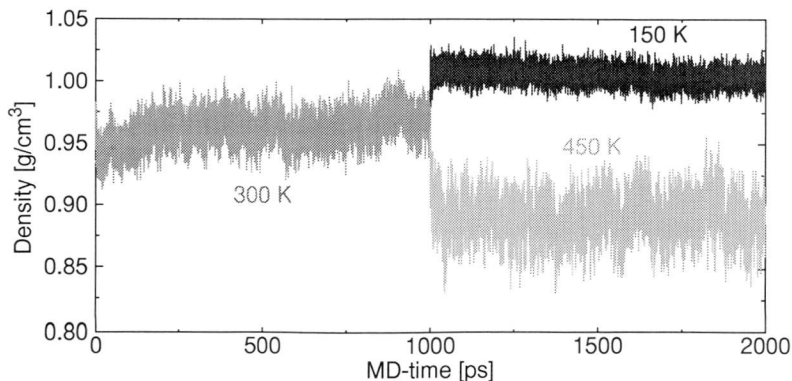

Figure 4.47: Density of structure 2 of wet PA-12 as a function of time and temperature

After an initial densification period of a few hundred picoseconds, the structure reaches a 'quasi-equilibrium'. At 150 K, there is a slight drift to lower densities after an initial raise, whereas at 450 K, the average values of the fluctuations seem to be stable. Taking the second half of each trajectory and averaging over the three microstructures, the densities of Table 4-57 result. The density of

Table 4-57: Average densities of dry and wet amorphous PA-12 cells

T [K]	$\langle \rho_{dry} \rangle$ [g/cm^3]	$\langle \rho_{wet} \rangle$ [g/cm^3]
150	1.0055 ± 0.0112	1.0052 ± 0.0068
300	0.9549 ± 0.0162	0.9574 ± 0.0128
450	0.8904 ± 0.0164	0.8897 ± 0.0166

0.956 g/cm^3 at 300 K is a bit lower than the experimental values of 0.99 g/cm^3[Asada76a] and 1.01 g/cm^3[Varlet90a], but still acceptable. In general, the influence of water on the density is much smaller than it is for PA-6. The thermal expansion coefficient at 300 K is the same for both dry and wet microstructures and has a value of about $14 \cdot 10^{-5}$ K^{-1}, which is in accord with the value of $11 \cdot 10^{-5}$ K^{-1} found in the 'Polymer Handbook'[Brandrup89].

4.7.4.2 Diffusion of Water

The diffusion of the water molecules in the wet microstructures was assessed by the same analysis as in chapter 4.6.4.2. Figure 4.48 shows the
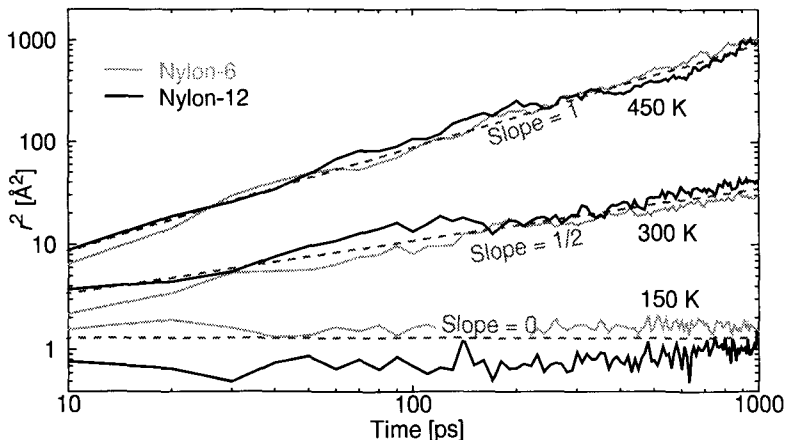

Figure 4.48: Average of the mean square displacement of the water molecules in PA-6 and PA-12, the dashed lines have slopes of exactly 0, $\frac{1}{2}$, and 1 and are not the result of a regression analysis

results of this analysis and makes a comparison with the corresponding values of PA-6. The absence of any diffusion at 150 K and the anomalous diffusion at room temperature found with PA-6 are confirmed with PA-12. In both polymers, the water molecules seem to behave very similarly; the differences can be attributed to the different statistics (a total of 105 water molecules in PA-6 vs. 36 in PA-12). This finding is supported by the very similar diffusion constants cited in the 'Polymer Handbook'[Brandrup89] (55 vs. $85 \cdot 10^{-8}$ cm^2/s at 100° C).

In the next chapter, the influence of water on the elastic constants of PA-12 will be examined.

4.7.4.3 Elastic Constants

The elastic constants of the 18 PA-12 trajectories (3 'dry' and 3 'wet' microstructures at 3 different temperatures) were computed analogous to those of PA-6. I.e. the cell parameters and stresses recorded during the last 500 ps of each trajectory were used to compute the strain and the stress-strain fluctuations. The detailed results of the stress-strain fluctuations are given in Appendix H, whereas the following tables refer to the results obtained from the

Table 4-58: Lamé constants of the three dry and three wet PA-12 microstructures, strain fluctuations only

T [K]	#	Dry PA-12	Wet PA-12
150	1	$\lambda = 3.78 \pm 0.20$ $\mu = 1.44 \pm 0.13$	$\lambda = 4.51 \pm 0.15$ $\mu = 1.38 \pm 0.10$
	2	$\lambda = 4.48 \pm 0.22$ $\mu = 1.68 \pm 0.14$	$\lambda = 4.16 \pm 0.20$ $\mu = 1.31 \pm 0.12$
	3	$\lambda = 4.40 \pm 0.13$ $\mu = 1.72 \pm 0.08$	$\lambda = 4.01 \pm 0.16$ $\mu = 1.25 \pm 0.10$
300	1	$\lambda = 2.47 \pm 0.09$ $\mu = 0.44 \pm 0.06$	$\lambda = 2.88 \pm 0.10$ $\mu = 0.53 \pm 0.06$
	2	$\lambda = 2.68 \pm 0.09$ $\mu = 0.43 \pm 0.06$	$\lambda = 2.78 \pm 0.10$ $\mu = 0.49 \pm 0.06$
	3	$\lambda = 2.85 \pm 0.10$ $\mu = 0.69 \pm 0.06$	$\lambda = 2.64 \pm 0.08$ $\mu = 0.44 \pm 0.05$
450	1	$\lambda = 1.09 \pm 0.03$ $\mu = 0.09 \pm 0.02$	$\lambda = 0.35 \pm 0.03$ $\mu = 0.10 \pm 0.02$
	2	$\lambda = 1.21 \pm 0.02$ $\mu = 0.09 \pm 0.01$	$\lambda = 1.01 \pm 0.05$ $\mu = 0.11 \pm 0.03$
	3	$\lambda = 0.50 \pm 0.03$ $\mu = 0.07 \pm 0.02$	$\lambda = 0.72 \pm 0.04$ $\mu = 0.07 \pm 0.02$

strain fluctuations. Table 4-58 compares the Lamé constants of the individual dry and wet microstructures, whereas Table 4-59 illustrates the substantial influence of the charged groups of atoms on the elastic constants. Similar to cellulose-Iβ,

Table 4-59: Influence of the charged groups on the elastic constants of PA-12, strain fluctuations only, all values in GPa

	T [K]	Neutral groups	Charged groups
Dry	150	$\lambda = 4.22 \pm 0.36$ $\mu = 1.61 \pm 0.17$	$\lambda = 6.42 \pm 0.92$ $\mu = 3.11 \pm 0.67$
	300	$\lambda = 2.67 \pm 0.18$ $\mu = 0.52 \pm 0.13$	$\lambda = 3.73 \pm 0.48$ $\mu = 1.16 \pm 0.25$
	450	$\lambda = 0.93 \pm 0.31$ $\mu = 0.08 \pm 0.02$	$\lambda = 2.59 \pm 0.47$ $\mu = 0.65 \pm 0.15$
Wet	150	$\lambda = 4.23 \pm 0.27$ $\mu = 1.31 \pm 0.12$	$\lambda = 6.06 \pm 0.70$ $\mu = 3.25 \pm 0.34$
	300	$\lambda = 2.77 \pm 0.14$ $\mu = 0.49 \pm 0.07$	$\lambda = 4.05 \pm 0.39$ $\mu = 1.63 \pm 0.37$
	450	$\lambda = 0.69 \pm 0.27$ $\mu = 0.09 \pm 0.03$	$\lambda = 2.06 \pm 0.23$ $\mu = 0.31 \pm 0.08$

where the charged interactions were summed without and with Ewald summation, a mistake in the summation of the Coulombic interaction leads to an overestimation of the elastic constants. The artificial, additional interactions obviously make the simulation cell stiffer.
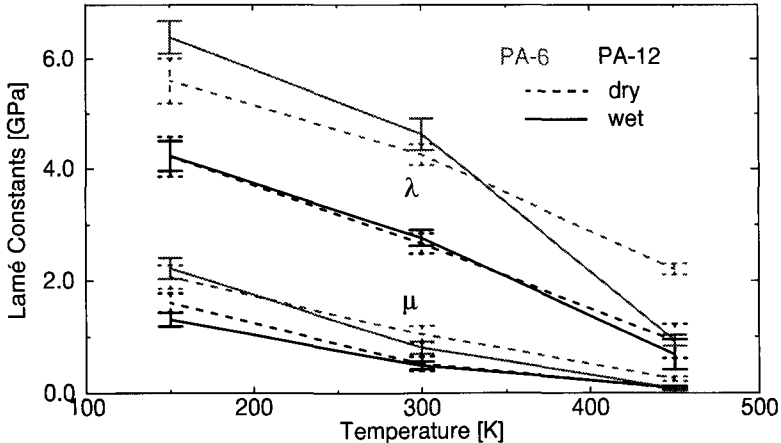

Figure 4.49: Temperature dependence of PA-12 (black) and PA-6 (gray), the dashed lines signify averages over the 'dry' and the solid lines averages over the 'wet' microstructures

In Figure 4.49, the Lamé constants λ and μ of PA-12 are compared with those of PA-6. In contrast to the marked dependence particularly of the first Lamé constant λ of PA-6 on the water content, λ of PA-12 exhibits the antiplastification/plastification transition only in much weaker form. The second Lamé constant μ changes with temperature almost independently of the water content.

4.7.5 Discussion

4.7.5.1 Comparison with Literature Values

Experimental Young's and shear moduli found in the 'Polymer Handbook'[Brandrup89] are compared to calculated ones in Table 4-60. Note that the

Table 4-60: Young's and shear moduli of semicrystalline experimental and amorphous computed PA-12

Modulus	T, state	exp. [MPa]	calc. [MPa]
E	23° C, dry	1400	1470 ± 360
	23° C, moist	1200	1400 ± 190
	100° C, dry	200	230 ± 60
G	23° C, dry	500	520 ± 130
	100° C, dry	100	80 ± 20

computed values that are compared to the dry PA-12 at 100° C are those at 450 K. There was no interpolation of the data between 300 and 450 K, because the α-relaxation is located at about 340 K[Pathmanathan92a]. Keeping the limitations (no direct comparison of experimental data at 100° C, semicrystalline morphology for the experiments versus purely amorphous simulation cell) in mind, the agreement is very good and the effect of the presence of water at 23° C is well reproduced.

4.7.5.2 Conclusions/Summary

The elastic constants of amorphous PA-12 are reproduced by atomistic simulations within the given error bars. These error bars originate from three different sources:

First, the simulation has not yet converged fully and the values are thus subject to a certain scatter. This scatter can be estimated by looking at the stress-strain correlation function (Eq. (3-38)). At 150 and 300 K, the deviation from the identity matrix is in the range of 1 to 3 %, but reaches 4 to 10 % at 450 K. This is also reflected by the temporal behaviour of the elastic constants.

At lower temperatures, they reach much faster more or less stable values than at 450 K.

Second, the individual microstructures exhibit, due to their smallness, a certain degree of anisotropy. This effect is - together with the first one - manifest in Table 4-58, where the uncertainties in the individual Lamé constants originate from a imperfect mapping to the actual matrices of the elastic constants.

The third effect, which is related to the second one, is the question of the *representative volume element*. Materials, which are on a global scale completely amorphous and isotropic, exhibit strong variations of their properties on a local scale. If small boxes are taken out of an amorphous material, they are anisotropic and differ in their average properties. With increasing box size, the anisotropy and the difference in the average properties diminish and disappear, if the representative volume size has been reached. Since the microstructures, that have been used for the simulations, are very small, it was necessary to use several of them to estimate the size of the representative volume element. As could be seen again from Table 4-58, the Lamé constants differ considerably (by about 20 %) between the three simulation boxes. The boxes are therefore smaller than the representative volume element and it was necessary to have a rudimentary statistics by running three of them.

Within the framework of the *scaled_pcff* force field and the MD sampling algorithm, the elastic constants in Table 4-60 reflect in their error bars all three sources of uncertainty mentioned above. The error bars are reasonably small, allowing to make useful statements about the elastic constants of PA-12 at different temperatures and water contents.

As expected, the Lamé constants of dry PA-6 are at all temperatures 30 % higher than those of PA-12. Since this difference vanishes completely for wet PA-6 at 450 K, it can be entirely attributed to the increased density of hydrogen bonds of PA-6 with respect to PA-12. The equilibrium water sorption, which is approximately three times smaller, supports the model of water molecules bridging between two neighbouring amide groups. Geometrical considerations would lead to a fourfold reduction of 'hydrogen bonds', if the density of amide groups is reduced by a factor of two. This explains, why PA-12 in experiments is so much less sensitive to the presence of water. The atomistic model that was used to compute the elastic constants is suitable to include the effects of temperature and water on the elastic constants.

4.8 Polycarbonate - Amorphous Cells

4.8.1 Introduction

Polycarbonate - or more precisely Bisphenol-A-polycarbonate (BPA-PC) - was the first polymer to be simulated in the course of this work in order to obtain its elastic constants. Polycarbonate is a purely amorphous polymer with excellent mechanical properties, especially with a very high fracture toughness, and good optical qualities. It is therefore used in large quantities for the production of CDs, sunglasses, etc.[Franck88] It is of great interest to elucidate the structure-property relationships by atomistic modelling. In the framework of a BMFT-Project with various groups from academia and industry, an attempt was made to compute the elastic constants of BPA-PC using atomistic modelling.

Pioneering work in the field of the atomistic modelling of BPA-PC was done by Hutnik *et al.*, who defined a forcefield for BPA-PC[Hutnik91a], generated amorphous microstructures[Hutnik91b], modelled the chain dynamics[Hutnik91c], and computed the elastic and plastic response of these structures[Hutnik93a]. Their results and methods were used as a basis and starting point for this work.

4.8.2 Cell Generation

The high density of 1.2 g/cm^3 and the high concentration of rings impose a challenge on the building of amorphous structures. It is not trivial to generate good microstructures of BPA-PC:

Modifying a method of Theodorou and Suter[Theodorou85a], Hutnik *et al.*[Hutnik91b] used a model with fixed bond length and bond angles to build a dense structure according to the RIS scheme. The building process was quite complicated and involved many steps in which the interaction potentials were slowly increased to their full strength.

It was not possible to use a similar method from within the 'Amorphous Cell' module of 'InsightII', since on the one hand it was not possible to define RIS weights for rings, and on the other hand, the method described in chapter 4.6.2.1 was not able to generate structures at full density, because always a spearing or catenation occurred and the algorithm stopped. The highest density at which it became possible to produce some structures was 0.6 g/cm^3.

However, it was decided to follow a different path and to build the chains at the lowest possible initial density of 0.01 g/cm^3. Before that, the repeat unit of PBA-PC (Fig. 4.50) was constructed and a chain of 69 repeat units (2285 atoms, including two terminating CH$_3$-groups) was 'polymerized'. Due to the symmetry
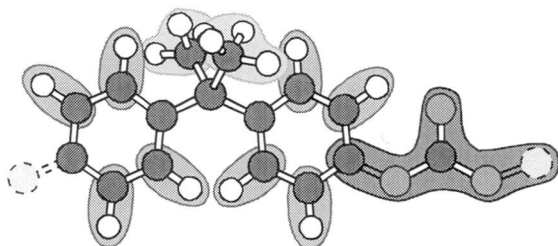
Figure 4.50: Repeat unit of BPA-PC; the filled areas represent the neutral groups in the *pcff91* force field

of the BPA-PC repeat unit, the actual degree of polymerization was 138. The *pcff91* force field was chosen to represent the energetic interactions, as it contained terms specially optimized for some polymers, among them polycarbonate. Three such chains were each grown in the usual stepwise fashion in a cubic cell of 138.6 Å size. After a short minimization of 50 steepest descent and 500 conjugate gradient steps to remove initial overlaps, a *TpN*-MD simulation of 25'000 steps of 1 fs was run to densify each cell. The compression was accelerated by applying a pressure of 1600 bar. This pressure corresponds to the tail correction pressure of BPA-PC at the experimental density of 1.2 g/cm^3 [Hutnik91b] for the cutoff of 8.25 Å.

The densification process is shown in Figure 4.51. The densification was
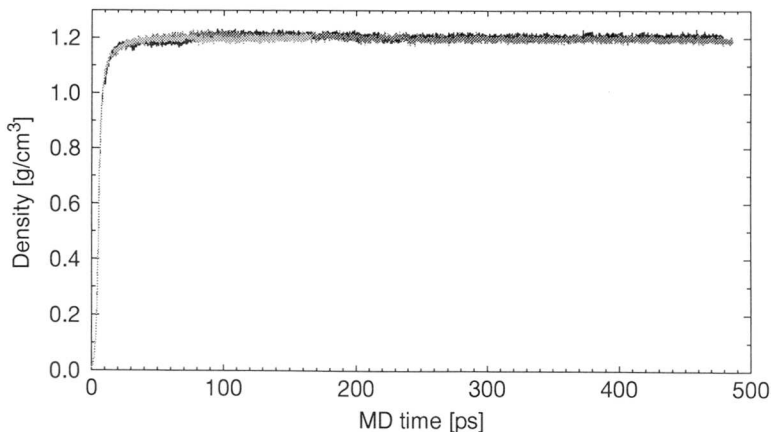

Figure 4.51: Density of the three BPA-PC microstructures as a function of time

very fast: after the first 25 ps, the densities of the three cells lay between 1.172 and 1.178 g/cm^3. This was sufficiently high to switch to a *TσN*-MD simulation

with a Nosé-Hoover thermostat and a Parrinello-Rahman pressure control. (If the simulations had been carried out from the beginning in a variable shape ensemble, very large deviations from a cubic shape would have occurred.) The duration of the $T\sigma N$ simulations, the average densities during the last 50 ps of

Table 4-61: Total MD-simulation time at 300 K, densities averaged over the last 50 ps, and final cell edge lengths of BPA-PC

Cell #	$T\sigma N$-MD [ps]	$\langle \rho \rangle$ [g/cm3]	a [Å]	b [Å]	c [Å]
1	450	1.205 ± 0.007	29.06	28.20	29.63
2	260	1.202 ± 0.007	28.01	29.95	28.72
3	460	1.194 ± 0.007	30.00	27.30	29.85

the MD simulation, and the final cell edge lengths are listed in Table 4-61. As it can already be seen, there is virtually no difference between the calculated densities and the experimental value of 1.2 g/cm^3.

The very fast densification can be explained by the concept of *diffusion of 'free volume'* out of the cube. If a real body is getting more dense, 'free volume' (holes, cavities, and faults) is diffusing out of it, a process that takes place as well in a simulation box. In a random walk diffusion process, the time required to move a distance r away from the origin is given by Eq. (4-31), i.e. the time is proportional to the square of the distance. Comparing a macroscopic body of 1 cm and a simulation box of 20 Å size, the diffusion distances differ by a factor of $5 \cdot 10^6$ and the diffusion times by $2.5 \cdot 10^{13}$, reducing the corresponding processes from minutes in the real body to picoseconds in the simulation box. This allows for a densification in a reasonable computer time.

The structures, nevertheless, are not 'good' representations of amorphous polycarbonates, since the individual chains were considerably compacted during the densification process. Their average end-to-end distance was only 32 and the radius of gyration only 16 Å, compared to RIS values of a chain of the same length, which are 135 and 56 Å. These findings were confirmed by a solubility parameter (square-root of the cohesive energy density) of only 14.5 (J/cm^3)$^{\frac{1}{2}}$, that opposed experimental findings[Hutnik91b] of 20.1 to 20.3 (J/cm^3)$^{\frac{1}{2}}$.

'Good' structures with reasonable end-to-end distances, radii of gyration, and cohesive energy densities were obtained from BAYER, where they had been generated in process involving several stages of minimization and MD simulation.[Batoulis93a] It was therefore possible to estimate the influence of the molecular geometry on the elastic constants of BPA-PC.

4.8.3 Simulation Procedure

4.8.3.1 Torsion angle distribution

The distribution of the torsion angles of the carbonate group (Fig. 4.52) was
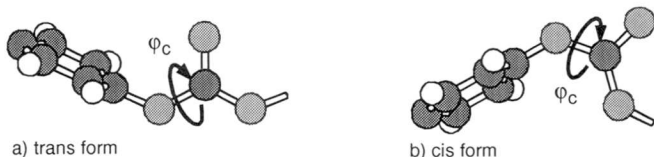

a) trans form   b) cis form

Figure 4.52: Trans (left) and cis (right) conformation of carbonate group. $\varphi_c = 0°$ defines the trans state and $\varphi_c = \pm180°$ the cis-state

computed for simulation cells 1 and 3, since they were equilibrated best. For comparison, 15 small 18.44 Å-cubes from Hutnik and 2 larger 29.74 Å boxes from MSI were also included into the calculations.

4.8.3.2 Static Minimum Energy Elastic Constants

The static minimum energy elastic constants were computed by a random deformation process. First, the polycarbonate structure was minimized down to a gradient of 0.01 kcal/(mol·Å). From thorough minimizations, it was found that this gradient guaranteed that the energy should not lower more than 0.001 kcal/mol if the minimization was continued to a gradient of 10^{-5} kcal/(mol·Å). The cell was then subject to a total of 21 random deformations, with the elements of the strain matrix being limited to ± 0.05 %. The deformed cells were again minimized with their shape and size held fixed. The 21 unknown elastic constants could be calculated from 21 Equations of the form

$$\Delta U_{pot} = \sum_{i=1}^{6} \sum_{k>i}^{6} C_{ik} \varepsilon_i \varepsilon_k \qquad (4\text{-}33)$$

by using linear algebra methods.

4.8.3.3 Fluctuation Approaches for the Elastic Constants

After the unsatisfactory results of the static minimum energy approach, which will be described in chapter 4.8.4.2, it became apparent that the thermal effects on the cell size and shape can not be neglected. Andrei Gusev independently derived a formula, that turned out to be identical to the strain fluctuation approach of Parrinello & Rahman. Applying this formula to very short $T\sigma N$-MD

runs of only10 ps yielded much better results than the static calculations, as can be seen in chapter 4.8.4.3.

However, the elastic constants obtained from this method were strongly dependent on the length of the simulation run. More extended simulations with detailed recording of the cell parameters and the pressure (in 1 fs steps) were performed after the initial densification, which lasted 160 ps and has been included into the total simulation time of Table 4-61. There were thus two runs of more than 250 and one run of 100 ps at 300 K. In order to check for the influence of temperature, the three structures were simulated in the $T\sigma N$-ensemble for 100 ps at 100 K. The starting structure was the one after 160 ps.

To improve the convergence, the idea came up to use the information of the actual pressure that had been printed out in the '.ext' files. The first trial was the computation of the bulk modulus from the slope of the Δp-$\Delta V/\langle V\rangle$-plot (Fig. 4.57). As will be reported later, this trial delivered encouraging results, and a method was searched for to include the information of the full stress tensor to compute the whole matrix of the elastic constants.

The result of this effort was the familiar stress-strain fluctuation formula (Eq. (3-36)), which was applied to an already mentioned structure from BAYER, in order to compare the efficiency of the two fluctuation approaches and the influence of the generation process on the elastic constants. It was first necessary to equilibrate this structure by a minimization and a short (12 ps) TpN-MD run. After that, an MD simulation of 200 ps in the $T\sigma N$-ensemble was performed. The last 10^5 frames (recorded during the last 100 ps) contained the information necessary to evaluate the elastic constants using the strain and the stress-strain fluctuation approaches.

4.8.4 Results

4.8.4.1 Torsion Angle Distribution

The distribution of the torsion angles of the carbonate group of BPA-PC microstructures that were generated with a variety of methods is shown in Figure 4.53. The fraction of *cis* angles (i.e. torsion angles between -90 and 90°) is virtually independent of the generation procedure - which included RIS and torsional potential builders with initial densities between 0.01 and 1.2 g/cm3 and combined minimization and dynamics equilibration - and lies between 25 and 30 %. This result is in marked contrast to recent C^{13}-NMR investigations of Tomaselli *et al.*[Tomaselli97a], which yield a *cis*-fraction of at most 10 %, but most probably less than 5 %.
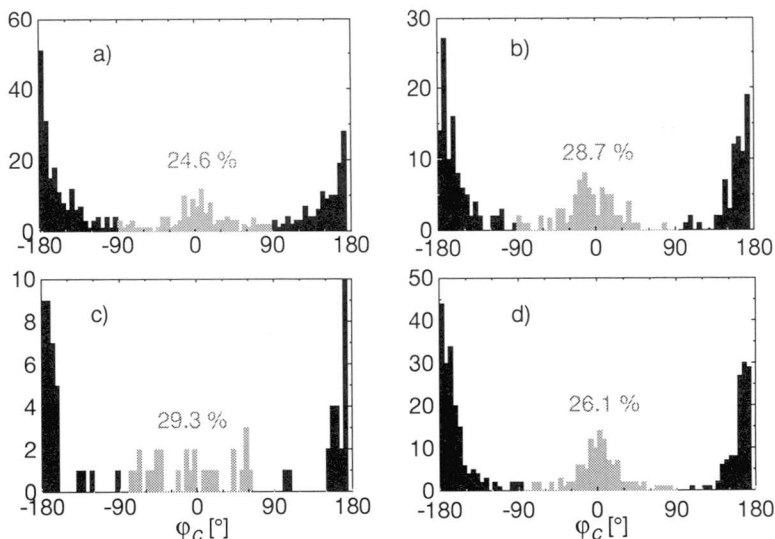
Figure 4.53: Distribution of torsion angles φ_c and the percentage of *cis* angles (gray) of the carbonate group: a) 15 structures of 18 Å from Hutnik et al.[Hutnik91b], b) 2 structures of 29 Å from this work, c) 2 structures of 20 Å from BAYER, d) 3 structures of 29.74 Å from BIOSYM

This experimental finding is also in accord with the forcefield parameters of Hutnik *et al.*[Hutnik91a] and of the *pcff91* forcefield. These forcefields both have values of $\Delta E = E_{cis} - E_{trans}$ of 1.7 and even 3.45 kcal/mol (from diphenylcarbonate using a density functional starting geometry and a subsequent minimization down to 10^{-5} kcal/(mol·Å)), which lead to *cis*-fractions,

$$[cis] = \frac{2\gamma}{1 + \gamma},$$
(4-34)

with $\gamma = \exp\left(\frac{\Delta E}{kT}\right)$, of 5 % or much less.

An MD simulation run on a polycarbonate chain of 5 repeat units was prepared to record the distribution of the torsion angles in dynamics to see whether MD might be responsible for the high fraction of cis-conformations. The vacuum simulation with a timestep of 1 fs and velocity rescaling to keep the temperature at 300 K lasted 25000 ps, during which a total of 5000 torsion angles were recorded: after 50ps roughly 30 % of the carbonyl groups were in a *cis* conformation and the distribution of the torsion angles remained stationary with the torsion angles changing between *cis* and *trans* every few picoseconds.

This result was not highly conclusive, since the polycarbonate chain was

simulated *in vacuo*. Trials were therefore made to simulate a solution of BPA-PC in a theta solvent (in this case chloroform), but the cell became so large that equilibration was not possible within a reasonable time.

4.8.4.2 Static Minimum Energy Approach

After 160 ps of dynamics, the static minimum energy elastic constants of the first and the second PC structure were computed according to chapter 4.8.3.2. As in dynamics, the nonbonded interactions were computed groupwise with a cutoff of 8.5 Å and a spline of 0.5 Å.The resulting matrices of the elastic constants and their Eigenvalues are given in Table 4-62. As can be

Table 4-62: Static minimum energy elastic constants, Lamé constants, and Eigenvalues [all in GPa] of the first (left) and the second (right) BPA-PC structure.

$\dfrac{1}{V_0}\left(\dfrac{\partial^2 U_{pot}}{\partial \eta_{ij}\partial \eta_{kl}}\right)_T$ [GPa]						$\dfrac{1}{V_0}\left(\dfrac{\partial^2 U_{pot}}{\partial \eta_{ij}\partial \eta_{kl}}\right)_T$ [GPa]					
8.45	9.15	11.78	0.60	0.30	0.14	8.06	6.37	8.89	−1.05	0.04	−0.70
9.15	8.44	9.44	0.21	0.99	−0.22	6.37	5.16	8.06	0.12	0.53	−1.16
11.78	9.44	8.91	0.52	0.62	−0.35	8.89	8.06	8.73	−1.75	1.33	−0.28
0.60	0.21	0.52	1.42	−0.18	0.12	−1.05	0.12	−1.75	2.29	0.65	0.61
0.30	0.99	0.62	−0.18	2.00	0.47	0.04	0.53	1.33	0.65	2.54	−0.44
0.14	−0.22	−0.35	0.12	0.47	1.84	−0.70	−1.16	−0.28	0.61	−0.44	2.21

Lamé constants	Eigenvalues $\lambda_{6\times6}$	Lamé constants	Eigenvalues $\lambda_{6\times6}$
$\lambda = 9.28 \pm 0.537$	28.97, 2.44, 1.77	$\lambda = 6.92 \pm 0.694$	23.38, 3.27, 2.57
$\mu = 0.08 \pm 0.340$	1.18, -0.16, -0.31	$\mu = 0.63 \pm 0.439$	1.77, 0.07, -2.10

seen immediately, there is a large difference between the actual matrices of the elastic constants and the one of a perfectly anisotropic material (Eq. (1-78) on page 25). Some Eigenvalues are even negative, indicating problems with the minimization algorithm. The Lamé constants are far away from the experimental values of $\lambda = 4.27 - 5.55$ GPa and $\mu = 0.8 - 1.1$ GPa[Hutnik93a].

Besides the technical problem to find the absolutely lowest point in a global minimum, a short $T\sigma N$-MD simulation of the first PC structure sheds light on the principal problem. During 1 ps, the actual MD frame was dumped out every 100 fs and then minimized - including the cell parameters - down to a maximal gradient of 10^{-5} kcal/(mol·Å). The final energies and cell parameters are listed in Table 4-63: the all-atom *pcff91* forcefield with bond and angle deformation terms leads to a high-dimensional energy hypersurface, where the minima are separated only by low energy barriers. A great number of such minima is accessible

Table 4-63: Energies and cell parameters of minimized MD frames of BPA-PC

Time [ps]	E_{min} [kcal/mol]	Cell parameters					
		a [Å]	b [Å]	c [Å]	α [°]	β [°]	γ [°]
0	-3914.30623	29.51	28.30	28.99	92.07	92.29	89.16
0.1	-3914.38439	29.56	28.28	28.96	91.88	92.33	89.06
0.2	-3914.30623	29.51	28.30	28.99	92.07	92.29	89.16
0.3	-3914.38439	29.56	28.28	28.96	91.88	92.33	89.06
0.4	-3914.15936	29.29	28.46	29.11	92.40	91.53	88.87
...	...	...	...	...	...	...	...
1	-3913.97935	29.34	28.39	29.06	92.37	91.46	89.31

for a molecule at finite temperature, since the energy barriers between them are of the same size as the kinetic energy. A picture (Fig. 4.54) might illustrates this:

Figure 4.54: Model of a two-dimensional cut through the energy hypersurface of an amorphous material

The determination of the curvature of a single minimum is in this case of no use in the determination of the elastic constants, which are determined by the size of the accessible phase space at a given temperature. Since this volume is increasing with temperature, the elastic constants of amorphous materials will always reduce if the temperature is rising.

4.8.4.3 Fluctuation Approaches

The strain fluctuation formula yielded very satisfactory results, as can be seen from Table 4-65 and Figure 4.55. Table 4-65 shows the results of the strain fluctuation formula averaging over the last 250 ps of $T\sigma N$-MD of the first and the third microstructure. The Lamé constants computed from such matrices are shown in Fig. 4.55 as a function of the averaging time. They reduce with increasing simulation time, as larger and larger volumes of the phase space are being

Table 4-64: Matrices of the elastic constants of the first (left) and the third (right) BPA-PC structure, strain fluctuation formula, averaging time: 250 ps (200 - 450 ps), 300 K

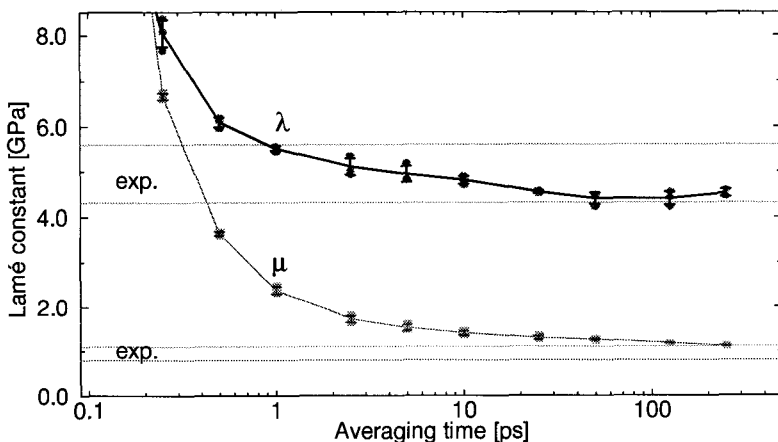| $\dfrac{k\,T}{\langle V\rangle}\langle \eta_{ik}\eta_{lm}\rangle^{-1}$ [GPa]						$\dfrac{k\,T}{\langle V\rangle}\langle \eta_{ik}\eta_{lm}\rangle^{-1}$ [GPa]					
6.96	3.93	4.63	0.17	–0.05	0.13	8.74	4.56	4.33	–0.34	0.57	–0.18
3.93	6.90	4.67	0.27	–0.16	0.36	4.56	5.94	4.41	–0.13	0.37	0.01
4.63	4.67	6.19	0.14	–0.02	0.06	4.33	4.41	6.38	0.18	–0.18	–0.27
0.17	0.27	0.14	1.17	0.15	–0.07	–0.34	–0.13	0.18	0.95	–0.04	–0.11
–0.05	–0.16	–0.02	0.15	0.90	0.06	0.57	0.37	–0.18	–0.04	0.58	–0.35
0.13	0.36	0.06	–0.07	0.06	1.09	–0.18	0.01	–0.27	–0.11	–0.35	0.88

Figure 4.55: Convergence of the Lamé constants of BPA-PC at 300 K, dotted lines mark the range of the experimental results.

visited by the model structure. Within a time accessible by MD and present computers, λ converges in the range of the experimental results, whereas μ still seems to further reduce. This is in accord with observations made with other polymeric systems: the normal components of the elastic constants always converge significantly faster than the shear components.

The results of three MD simulations at 100 K, where the strain fluctuations were averaged over the last 50 ps of the 100 ps runs are in good agreement with experimental data from BAYER as can be seen in Figure 4.56.

The search for a method which would improve the convergence behaviour lead to the following computer experiment: As already mentioned, the information about the actual pressure was used to compute the bulk modulus K by transforming Eq. (1-82) to

$$\Delta p = -K \cdot \frac{\Delta V}{V}. \qquad\qquad ((1\text{-}82))$$

$$\frac{kT}{\langle V \rangle}\langle \eta_{ik}\eta_{lm}\rangle^{-1} \text{ [GPa]}$$

8.04	4.43	5.79	0.19	−0.37	0.27
4.43	9.74	6.21	0.30	0.38	0.48
5.79	6.21	9.02	−0.06	0.03	0.51
0.19	0.30	−0.06	2.05	0.09	−0.09
−0.37	0.38	0.03	0.09	1.87	0.04
0.27	0.48	0.51	−0.09	0.04	0.80

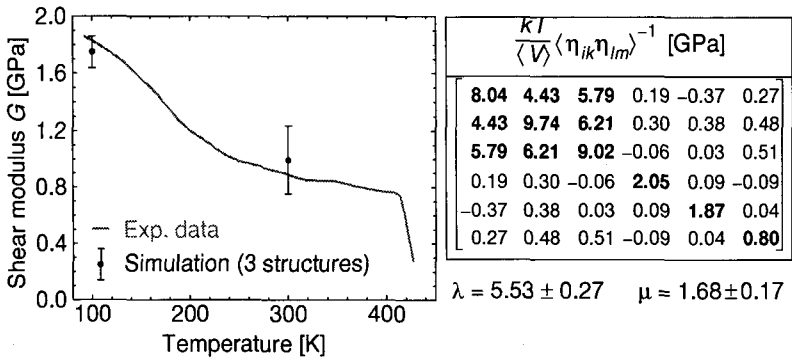$\lambda = 5.53 \pm 0.27 \qquad \mu = 1.68 \pm 0.17$

Figure 4.56: Shear modulus of BPA-PC as a function of the temperature (left, solid line: unpublished experimental values from BAYER, circles and error bars: results from the last 50 ps of 100 ps simulations at 100 and 300 K, averaged over three microstructures) and matrix of the elastic constants of the first microstructure (right)

The bulk modulus could now be obtained from a linear regression of a Δp vs. $\Delta V/\langle V \rangle$ plot.

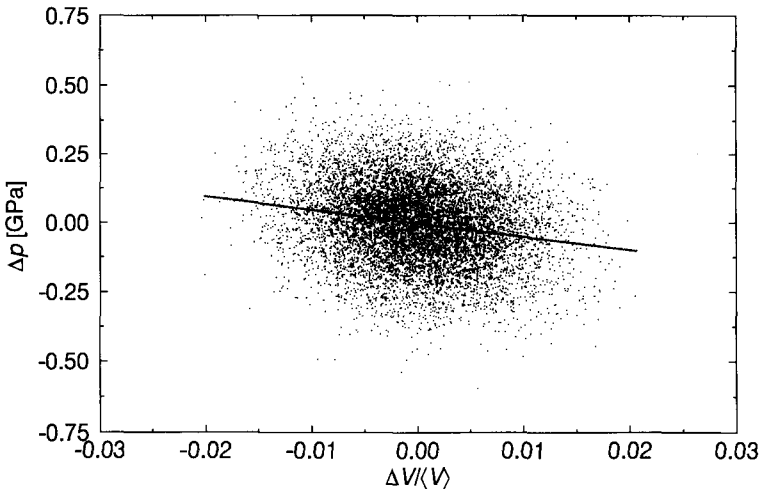Figure 4.57 shows such a plot with MD data of the first structure. The linear

Figure 4.57: Δp-$\Delta V/\langle V \rangle$-plot of the first structure of BPA-PC, 104 points in regular intervals between 170 - 370 ps after beginning of the densification, subtraction of the average pressure of 1523 bar, straight line: regression analysis

regression of the point cloud yielded an intercept of 1523 ± 5 bar, which was subtracted from the above plot, because its origin is the correction pressure of

1600 bar (reduced somewhat by the finite stepsize of the MD integration). The slope $(= -K)$ is -4.954 ± 0.095 GPa, being just at the lower margin of the experimental range[Hutnik93a] of 5.0 - 6.1 GPa.

The resulting elastic matrices from the second half of a 200 ps $T\sigma N$-MD simulation of the BAYER structure mentioned at the end of chapter 4.8.3.3 are displayed in Table 4-66. There are no fundamental differences between these

Table 4-65: Matrices of the elastic constants of the BPA-PC structure from BAYER, strain (left) and stress-strain (right) fluctuation formula, 100 ps averaging time

$\frac{kT}{\langle V \rangle}\langle\eta_{ik}\eta_{lm}\rangle^{-1}$ [GPa]						$\langle\eta_{ik}\sigma_{nj}\rangle\langle\eta_{nj}\eta_{lm}\rangle^{-1}$ [GPa]					
6.81	4.24	5.46	-0.22	0.51	-0.08	6.64	4.17	5.32	-0.24	0.54	-0.11
4.24	7.34	4.67	-0.35	0.49	-0.56	4.13	7.23	4.52	-0.33	0.48	-0.48
5.46	4.67	7.75	-1.35	0.16	-0.24	5.53	4.69	7.94	-1.36	0.10	-0.29
-0.22	-0.35	-1.35	1.15	-0.09	-0.02	-0.20	-0.26	-1.28	1.11	-0.06	-0.07
0.51	0.49	0.16	0.09	0.77	0.13	0.44	0.42	0.16	-0.11	0.76	0.14
-0.08	-0.56	-0.24	-0.02	0.13	1.30	-0.03	-0.60	-0.27	0.01	0.13	1.29
$\lambda = 4.85 \pm 0.25$			$\mu = 1.20 \pm 0.16$			$\lambda = 4.75 \pm 0.26$			$\mu = 1.22 \pm 0.17$		

matrices and those of Table 4-65.

4.8.5 Discussion and Conclusions

The comparison with experimental density, radius of gyration, cohesive energy density, and Lamé constants was made at the appropriate place in the presentation of the results. The three structures that were 'condensed from the gas phase' reached a stable density after about 100 ps. The agreement between the simulated and the experimental density was almost perfect, in contrast to the end-to-end distances and the radii of gyration. Due to the affine compression, the microstructures were several times too compact compared to the corresponding RIS values. The elastic constants obtained from strain (and stress-strain) fluctuations, however, were not significantly influenced by this, as a comparison with a more carefully produced structure from BAYER revealed. It was even possible to grasp the influence of temperature on the elastic constants by performing $T\sigma N$-MD simulations at 100 and 300 K. The results again agreed well with experimental data.

It can be concluded that the global 'shape' of a molecule in an amorphous body is of no influence to the elastic constants. The method of generating and equilibrating amorphous microstructures needn't be capable of relaxing the molecule on large scales. It is more important that the 'local' polymer structure is well equilibrated to obtain reasonable elastic constants.

Static minimum energy evaluations of the elastic constants, performed by Hutnik et al.[Hutnik93a], yielded values that were in general too high ($\lambda = 5.35 \pm 1.15$, $\mu = 2.06 \pm 0.65$). Although the generalized coordinates of Hutnik's model reduce the dimensionality of the phase space considerably, the same explanation of the observed deviations as in the present work is evident. It is therefore not possible to obtain physically meaningful elastic constants from static minimum energy calculations, since the local curvature of the energy hypersurface is not directly related to the curvature of the thermally accessible phase space volume.

5 Conclusions

5.1 Summary

It could be shown that the elastic constants of polymeric systems could be determined with the Parrinello-Rahman strain and the novel stress-strain fluctuation formula. These fluctuation methods have been applied for the first time to the field of polymer science. Crystalline monocrystals of polyethylene, polypropylene, cellulose-Iβ, and polyamide-6 and amorphous microstructures of polyamide-6, polyamide-12, and polycarbonate have been simulated using the Parrinello-Rahman Nosé-Hoover molecular dynamics. In all cases, the simulated elastic constants were in good agreement with experimental values.

The statistical nature of the fluctuation formula implies a dependence of the results on the length of a simulation run. Due to the establishment of the second fluctuation formula, it became possible to quantify the degree of convergence of a simulation. This convergence criterion allows to make estimates of the precision of the elastic constants.

The accuracy of the elastic constants is determined by a number of factors: Maybe the most important one was not subject of this work: Although the generation of forcefields made considerable progress in the recent years, the representation of a quantum mechanical by classical interactions still remains - besides the generation of amorphous microstructures - the most disputable point in the methodology. The other factors like the system size, the sampling method, and the duration of the simulation can be controlled sufficiently well. It has been shown for nearest-neighbour Lennard-Jones solids that the system size and the sampling method hardly influence the final elastic constants. Of course, they influence the convergence behaviour, which in turn determines the necessary simulation (and CPU) time.

Attempts have been made to improve the convergence by switching to other ensembles, but no significant improvements could be achieved. It might be concluded, that the sampling efficiency of polymeric systems does not significantly change going from one ensemble to the other. While, e.g., the elastic constants obtained from stress-strain fluctuations of the Lennard-Jones solid converged significantly faster at low temperatures, no such effect could be observed for polymeric systems.

It could also be shown, that the elastic constants of amorphous polymers do not depend on the global conformation of the chain. It is therefore not necessary to completely equilibrate a microstructure by long simulation runs or to gen-

erate very good starting structures, as long as the local conformation is in agreement with experimental values.

But it turned out that the fluctuation distributions, which are proportional to the elastic constants, strongly depend on the canonicity of the sampling algorithm. Non-canonical integrators significantly change the results, as does a wrong treatment of the long-range Coulombic interactions by charged atom groups or unsuitable summation methods.

Elastic constants are equilibrium properties and it is not meaningful to compute them for systems that undergo a relaxation process. The simulation system must therefore be at least in a quasi-equilibrium, without noticeable changes or drifts in the relevant cell parameters and stress.

Besides these caveats, the fluctuation methods provide robust simulation algorithms, which can reproduce the influence of temperature and the effects of small molecules on the elastic constants of amorphous and crystalline polymers. There are already simulations of polymers with short fiber reinforcements reported in the literature.[Wendling95a] The canonical constant-stress, constant-temperature molecular dynamics sampling method mainly used for this work, also allows - with caution - to derive dynamical information like relaxation spectra and diffusion constants.

5.2 Outlook

At present, the simulation runs necessary to obtain good statistics for the fluctuations are rather long ($O(10^5$ - 10^6) steps for 20 - 30 Å cells) and require days or weeks of CPU time on an average workstation. But the performance of computers doubles every 18 months[Widmann96a], so this problem will be less important in the future. As it has now become possible to compute the elastic constants of purely amorphous and purely crystalline polymers with reasonable accuracy, it is the next logical step, to attack semicrystalline polymers. Although a variety of models[Takayanagi64a,Ouali91a] exists, that link the microscopic with the macroscopic properties of a compound material, a new mesoscopic model was developed, which allows to simulate the effect of the shape and the distribution of the inclusions (crystallites) on the mechanical properties.[Gusev97a,Gusev97b] This approach tessellates a cell containing the amorphous matrix, the crystalline reinforcing particles and the interface between them into small discrete elements. With the knowledge of the complete matrix of the elastic constants of the matrix and the reinforcing particles, it will be possible to compute the elastic behaviour of a polymeric system as a whole.

6 Appendices

Appendix A: Coordinate Transformations

A-1: Direction Cosines

Consider two right-handed, orthogonal coordinate systems with the same origin, but different relative orientation (Fig. A.1).
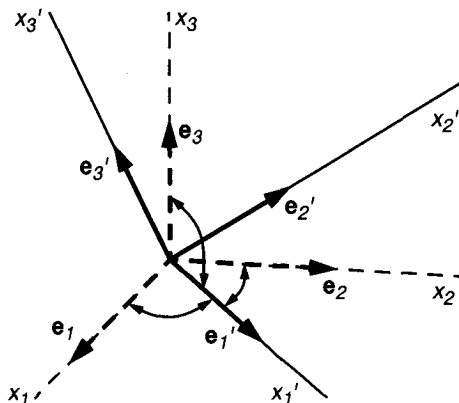

Figure A.1: Direction cosines between e_1' in the transformed coordinate system $\{e_1', e_2', e_3'\}$ and the reference coordinate system $\{e_1, e_2, e_3\}$

In order to determine the matrix that transforms one system into the other, the direction cosines between the axes of the reference and the transformed coordinate system are calculated.[Goldstein80] In Fig. A.1, the direction cosinus between a unit vector e_i' of the transformed system and a unit vector e_j of the system of reference is

$$a_{ij} = \cos (e_i', e_j) = e_i' \cdot e_j . \tag{A-1}$$

The vector e_i' can be expressed in terms of e_1, e_2, e_3 by the relation

$$e_i' = (e_i' \cdot e_1) e_1 + (e_i' \cdot e_2) e_2 + (e_i' \cdot e_3) e_3$$

or   (A-2)

$$e_i' = a_{i1} e_1 + a_{i2} e_2 + a_{i3} e_3 ,$$

leading to the transformation matrix **A**, which, operating on the components of a vector **r** in the reference coordinate system, yields the components of the vector **r'** in the transformed system:

$$\mathbf{r'} = \begin{bmatrix} a_{11} & a_{12} & a_{13} \\ a_{21} & a_{22} & a_{23} \\ a_{31} & a_{32} & a_{33} \end{bmatrix} \mathbf{r} = \mathbf{Ar}. \tag{A-3}$$

The transformation matrix from the primed system to the unprimed system is given by the inverse of the transformation matrix

$$\mathbf{r} = \mathbf{A}^{-1}\mathbf{r'} = \mathbf{A}^{-1}\mathbf{Ar} = \mathbf{r}. \tag{A-4}$$

The nine components of the transformation matrix $\mathbf{A}$ are not independent, since a coordinate system with arbitrary orientation, but fixed origin, has just three degrees of freedom. The connections between the direction cosines arise from the fact, that the basis vectors in both coordinate systems are orthogonal to each other and have unit magnitude. These six conditions can be expressed formally as

$$a_{ij}a_{ik} = \delta_{jk} \qquad j,k = 1,2,3, \tag{A-5}$$

where δ_{jk} represents the Kronecker symbol and the summation convention over repeated indices is used.

A-2: Transformation of the Matrix of the Elastic Constants

Given the transformation matrix $\mathbf{A}$, with elements a_{ij} (Eq. (A-3)), that connects a unprimed reference and a primed, transformed coordinate system. The fourth-rank tensor C_{ijkl} transforms according to

$$C'_{ijkl} = a_{im}a_{jn}a_{ko}a_{lp}C_{mnop}, \tag{1-50}$$

while the 6×6-matrix C_{mn} of the elastic constants transforms like[Lekhnitskii81]

$$C'_{op} = C_{mn}q_{om}q_{pn}, \tag{A-6}$$

with

$$q_{ij} = \begin{bmatrix} a_{11}^2 & a_{12}^2 & a_{13}^2 & 2a_{12}a_{13} & 2a_{13}a_{11} & 2a_{12}a_{11} \\ a_{21}^2 & a_{11}^2 & a_{23}^2 & 2a_{23}a_{22} & 2a_{23}a_{21} & 2a_{22}a_{21} \\ a_{31}^2 & a_{32}^2 & a_{11}^2 & 2a_{33}a_{32} & 2a_{33}a_{31} & 2a_{32}a_{31} \\ a_{31}a_{21} & a_{32}a_{22} & a_{33}a_{23} & a_{33}a_{22}+a_{32}a_{23} & a_{33}a_{21}+a_{31}a_{23} & a_{31}a_{22}+a_{32}a_{21} \\ a_{31}a_{11} & a_{32}a_{12} & a_{33}a_{13} & a_{33}a_{12}+a_{32}a_{13} & a_{33}a_{11}+a_{31}a_{13} & a_{31}a_{12}+a_{32}a_{11} \\ a_{21}a_{11} & a_{12}a_{22} & a_{13}a_{23} & a_{13}a_{22}+a_{12}a_{23} & a_{13}a_{21}+a_{11}a_{23} & a_{11}a_{22}+a_{12}a_{21} \end{bmatrix} \tag{A-7}$$

To transform the compliance matrix, again Eq. (A-6) is used, but with a slightly different q-matrix, where the elements at the intersections of column 1, 2, and 3 with row 4, 5, and 6 are multiplied with a factor of 2, whereas the elements at the intersection of column 4, 5 and 6 with row 1, 2, and 3 are divided by a factor of 2.

A-3: The Eigenvalues and Eigenvectors of a 4th rank tensor

The basic formalism of the eigenvalues and eigenvectors of a 4th rank tensor $\mathbf{A}$ is given by the equation

$$A_{ijkl}x_{kl} = \lambda x_{ij} = \lambda \delta_{ik}\delta_{jl}x_{kl} \tag{A-8}$$

The introduction of the Kronecker-deltas is necessary to perform the suffix substitution. The following set of equations needs to be solved:

$$(A_{ijkl} - \lambda \delta_{ik}\delta_{jl})x_{kl} = 0 \tag{A-9}$$

i.e. eigenmatrices x_{kl} are deformations (ε_{kl}) where the resulting stress (σ_{ij}) is proportional to the applied strain, if A_{ijkl} is the elasticity tensor C_{ijkl}. The proportionality factor λ is the eigenvalue belonging to this system.

The above equations are also valid, if the Voigt notation is used, with one major difference: Assuming, that the eigenstresses are the same ($\sigma_{ij} \equiv \sigma_i$), the eigenstrains will become

$$\lambda_{3x3x3x3}\varepsilon_{kl} \equiv \lambda_{6x6}e_k \tag{A-10}$$

The ε_{kl} transform to e_k according to Eq. (1-55) ($\varepsilon_{kl} \equiv e_k$, if $k = l$, and $\varepsilon_{kl} \equiv \frac{1}{2}e_k$, if $k \neq l$), which results in

$$\lambda_{3x3x3x3}\frac{1}{2}e_k \equiv \lambda_{6x6}e_k$$
$$\lambda_{3x3x3x3} = 2\lambda_{6x6} \tag{A-11}$$

I.e. the eigenvalues obtained from the full 3x3x3x3 tensor of the elastic constants differ by a factor of 2 from those obtained from the Voigt representation of the matrix of elastic constants, if the indices k and l are different. This is the case for the Voigt numbers 4, 5 and 6.

A-4: General Transformation Matrix

If the reference or the transformed coordinate system are not orthogonal or if the unit vectors in the two systems are not of the same length, the transformation matrix from the reference to the transformed coordinate system can be constructed by expressing the unit vectors of the transformed system in terms of the

reference system. In n dimensions, there are n such basis vectors $(\mathbf{a}_1, \mathbf{a}_2, ... \mathbf{a}_n)$, which form the columns of a transformation matrix $\mathbf{A}$,

$$\mathbf{A} = \begin{bmatrix} \mathbf{a}_1 & \mathbf{a}_2 & ... & \mathbf{a}_n \end{bmatrix} . \tag{A-12}$$

This transformation matrix is identical with the one defined by Eq. (A-3) if both *coordinate systems are orthogonal and have basis vectors of the same length.* Otherwise, it is important to distinguish between co- and contravariant components of the transformation matrix.[Renton87, Budiansky74]

A-5: Metric Tensor

The scalar products of the basis vectors $(\mathbf{a}_1, \mathbf{a}_2, \mathbf{a}_3)$ of a *3*-dimensional coordinate system form the metric tensor $\mathbf{g}$ by[Sands82]

$$g_{ik} = \mathbf{a}_i \cdot \mathbf{a}_k \tag{A-13}$$

or, in matrix notation

$$\mathbf{g} = \mathbf{h}^\mathsf{T} \mathbf{h} , \tag{A-14}$$

where $\mathbf{h}$ is tensor containing the base vectors as it's columns,

$$\mathbf{h} = \begin{bmatrix} \mathbf{a}_1 & \mathbf{a}_2 & \mathbf{a}_3 \end{bmatrix} . \tag{A-15}$$

In Eqs (A-12) and (A-15), different symbols were used for the matrix containing the basis vectors of a coordinate system in its colums. The transformation matrix $\mathbf{A}$ connects two arbitrary coordinate systems and is not linked with any physical quantity. It therefore forms a matrix. The tensor $\mathbf{h}$ is used in this work to describe the shape of a crystallographic unit cell or a simulation cell and transforms itself according to Eq. (1-12) and thus forms a tensor.

A-6: Jacobian Matrix

Given the function

$$\mathbf{y} = \mathbf{y}(\mathbf{x}) , \tag{A-16}$$

a matrix

$$J_{ij} = \frac{\partial y_i}{\partial x_j} \tag{A-17}$$

can be defined[Bronstein91], which is called the *Jacobian matrix* of the function $\mathbf{y}$. For the above (Appendix A-1) transformation

$$\mathbf{y} = \mathbf{A}(\mathbf{x}), \tag{A-18}$$

the Jacobian $\mathbf{J}$ connects the basis vectors[Renton87] of the two coordinate systems by

$$e'_i = J_{ij}e_j \qquad \text{and} \qquad e_i = J_{ij}^{-1}e'_j. \tag{A-19}$$

For a canonical transformation, the determinant of the Jacobian[Goldstein80]

$$\det(\mathbf{J}) = \frac{V}{V_0} = \pm 1, \tag{A-20}$$

indicating that the volume of the unit cell (in phase space) remains constant upon the transformation.

A-7: Euler Angles

A coordinate system $\{x,y,z\}$ is rotated in a first step by an angle ϕ around its z-Axis (Fig. A.2a) forming the new coordinates $\{\xi,\eta,z\}$. [Goldstein80] Then these
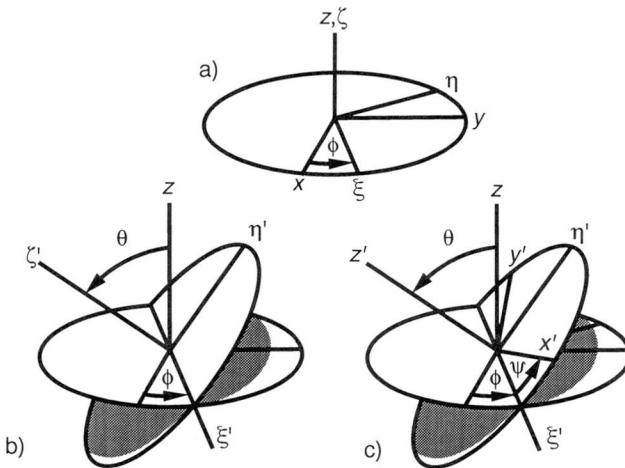

Figure A.2: The rotations defining the Euler angles

new coordinates are rotated around the ξ-axis by an angle θ (Fig. A.2b). The resulting coordinate system $\{\xi',\eta',\zeta'\}$ is again rotated around it's new ζ'-axis by the angle y to its final state $\{x',y',z'\}$ (Fig. A.2c). All rotations are performed counterclockwise!

The transformation matrices of the three rotations are given by

$$Z(\phi) = \begin{bmatrix} \cos\phi & \sin\phi & 0 \\ -\sin\phi & \cos\phi & 0 \\ 0 & 0 & 1 \end{bmatrix}, \tag{A-21}$$

$$X(\theta) = \begin{bmatrix} 1 & 0 & 0 \\ 0 & \cos\theta & \sin\theta \\ 0 & -\sin\theta & \cos\theta \end{bmatrix}, \tag{A-22}$$

and

$$Z(\psi) = \begin{bmatrix} \cos\psi & \sin\psi & 0 \\ -\sin\psi & \cos\psi & 0 \\ 0 & 0 & 1 \end{bmatrix}. \tag{A-23}$$

These three operations are applied in sequence and the product matrix **A** then follows as

$$A =$$

$$= \begin{bmatrix} \cos\psi\cos\phi - \cos\theta\sin\phi\sin\psi & \cos\psi\sin\phi - \cos\theta\cos\phi\sin\psi & \sin\psi\sin\theta \\ -\sin\psi\cos\phi - \cos\theta\sin\phi\cos\psi & -\sin\psi\sin\phi - \cos\theta\cos\phi\cos\psi & \cos\psi\sin\theta \\ \sin\theta\sin\phi & -\sin\theta\cos\phi & \cos\theta \end{bmatrix} \tag{A-24}$$

The inverse transformation from $\{x',y',z'\}$ to $\{x,y,z\}$ is given immediately by the transposed matrix A^T

$$A^{-1} = A^T =$$

$$= \begin{bmatrix} \cos\psi\cos\phi - \cos\theta\sin\phi\sin\psi & -\sin\psi\cos\phi - \cos\theta\sin\phi\cos\psi & \sin\theta\sin\phi \\ \cos\psi\sin\phi - \cos\theta\cos\phi\sin\psi & -\sin\psi\sin\phi - \cos\theta\cos\phi\cos\psi & -\sin\theta\cos\phi \\ \sin\psi\sin\theta & \cos\psi\sin\theta & \cos\theta \end{bmatrix} \tag{A-25}$$

For generalized coordinate MD algorithms however, the use of Euler angles can lead to singularities in the dynamics. To avoid these problems, so-called quaternions[Evans77a,Evans77b] or modified Euler angles can be used.

Appendix B: Finite Elasticity and Cell Shape Tensor

B-1: Finite Strain From Cell Shape Tensor

The finite strain between a reference cell shape tensor **H** and an actual shape tensor **h** can be derived as follows:

Consider a reference cell **H** containing a connecting vector **R** and a

deformed cell **h** containing the transformed connecting vector **r** (Fig. 1.4). The relation between $\mathbf{R}=[X_1,X_2,X_3]^\mathsf{T}$ and $\mathbf{r}=[x_1,x_2,x_3]^\mathsf{T}$ can be written as

$$
\begin{array}{ll}
s_i = H_{ij}^{-1}X_j & \qquad s_i = h_{ij}^{-1}x_j \\
x_i = h_{ij}s_j = h_{ij}H_{jk}^{-1}X_k & \qquad X_i = H_{ij}s_j = H_{ij}h_{jk}^{-1}x_k
\end{array}
\tag{B-1}
$$

So the translation vector **u** is given by

$$
u_i = r_i - R_i = x_i - X_i = h_{ij}H_{jk}^{-1}X_k - X_i. \tag{B-2}
$$

To obtain the finite strain according to Eq. (1-29), the following derivation must be made,

$$
\frac{\partial u_i}{\partial X_j} = h_{ik}H_{kl}^{-1}\frac{\partial X_l}{\partial X_j} - \frac{\partial X_i}{\partial X_j} = h_{ik}\langle h\rangle_{kl}^{-1}\delta_{lj} - \delta_{ij}
$$
$$
= h_{ik}H_{kj}^{-1} - \delta_{ij}, \tag{B-3}
$$

using for the second equation the properties of an orthogonal cartesian coordinate frame and for the third the fact, that multiplication with a Kronecker delta exchanges the indices of a matrix. The product of the gradients of the translation vector is

$$
\frac{\partial u_k}{\partial X_i} \cdot \frac{\partial u_k}{\partial X_j} = \left(h_{kl}H_{li}^{-1} - \delta_{ki} \right) \cdot \left(h_{km}H_{mj}^{-1} - \delta_{kj} \right)
$$
$$
= h_{kl}H_{li}^{-1}h_{km}H_{mj}^{-1} - h_{km}H_{mj}^{-1}\delta_{ki} - h_{kl}H_{li}^{-1}\delta_{kj} + \delta_{ki}\delta_{kj} \tag{B-4}
$$
$$
= h_{kl}H_{li}^{-1}h_{km}H_{mj}^{-1} - h_{im}H_{mj}^{-1} - h_{jl}H_{li}^{-1} + \delta_{ij}.
$$

Combining Eqs (1-29),(B-3), and (B-4), it is found that

$$
\eta_{ij} = \frac{1}{2}\left[\frac{\partial u_i}{\partial X_j} + \frac{\partial u_j}{\partial X_i} + \frac{\partial u_k}{\partial X_i}\frac{\partial u_k}{\partial X_j} \right]
$$
$$
= \frac{1}{2}\left[h_{ik}H_{kj}^{-1} - \delta_{ij} + h_{jl}H_{li}^{-1} - \delta_{ji} + h_{km}H_{mi}^{-1}h_{kn}H_{nj}^{-1} - h_{in}H_{nj}^{-1} - h_{jm}H_{mi}^{-1} + \delta_{ij} \right] \tag{B-5}
$$
$$
= \frac{1}{2}\left[h_{km}H_{mi}^{-1}h_{kn}H_{nj}^{-1} - \delta_{ij} \right],
$$

which, after transposing (=interchanging the indices), using the fact that the inverse of a transpose equals the transpose of the inverse, and rearranging some matrices, results in Eq. (1-36),

$$\eta_{ij} = \frac{1}{2}\left[H_{il}^{T-1}h_{lk}^{T}h_{km}H_{mj}^{-1} - \delta_{ij}\right]. \tag{1-36}$$

According to Eq. (A-14), $h_{lk}^{T}h_{km}$ forms the metric tensor component g_{lm} of the deformed cell, allowing to write Eq. (1-36) as$^{\text{ParrinelloRahman81a, similar: Squire69a}}$

$$\eta_{ij} = \frac{1}{2}\left[H_{il}^{T-1}g_{lm}H_{mj}^{-1} - \delta_{ij}\right]. \tag{B-6}$$

B-2: Finite Stress (Thermodynamic Tension) from Cell Shape Tensor

Equation (1-40),

$$t_{st} = J\sigma_{ij}\frac{\partial X_s}{\partial x_i}\frac{\partial X_t}{\partial x_j} \quad \text{or} \quad \sigma_{ij} = \frac{1}{J}\frac{\partial x_i}{\partial X_s}\frac{\partial x_j}{\partial X_t}t_{st}, \tag{1-40}$$

expresses the relation between the actual stress σ on the deformed cell and the thermodynamic tension t referring to the undeformed cell. Using Eq. (B-1), one easily finds that

$$\frac{\partial X_s}{\partial x_i} = \frac{\partial H_{so}h_{op}^{-1}x_p}{\partial x_i} = H_{so}h_{op}^{-1}\delta_{ip} \quad \text{and} \quad \frac{\partial X_t}{\partial x_j} = \frac{\partial H_{tq}h_{qr}^{-1}x_r}{\partial x_j} = H_{tq}h_{qr}^{-1}\delta_{jr} \tag{B-7}$$

leading to

$$\begin{aligned} J\sigma_{ij}\frac{\partial X_s}{\partial x_i}\frac{\partial X_t}{\partial x_j} &= J\sigma_{ij}H_{so}h_{op}^{-1}\delta_{ip}H_{tq}h_{qr}^{-1}\delta_{jr} \\ &= J\sigma_{pr}H_{so}h_{op}^{-1}H_{tq}h_{qr}^{-1} \\ &= JH_{so}h_{op}^{-1}\sigma_{pr}h_{rq}^{-1}H_{qt} \end{aligned} \tag{B-8}$$

which, in matrix notation, is equivalent to Eq. (1-41). The actual stresses as a function of the thermodynamic tensions can be found in an analogous manner.

B-3: Symmetry of the Thermodynamic Stress Tensor

The thermodynamic tension tensor $\mathbf{t}$ is linked to the instantaneous stress tensor σ by

$$\mathbf{t} = J\mathbf{H}\mathbf{h}^{-1}\sigma\mathbf{h}^{T-1}\mathbf{H}^{T}, \tag{1-41}$$

where σ is a symmetric tensor, $\mathbf{H}$ and $\mathbf{h}$ are general tensors and J is a scalar. The transpose of Eq. (1-41) can be written as

$$\mathbf{t}^T = \left(\mathcal{J}\mathbf{H}\mathbf{h}^{-1}\sigma\mathbf{h}^{T-1}\mathbf{H}^T\right)^T = \mathcal{J}\mathbf{H}^{T^T}\mathbf{h}^{T-1^T}\sigma^T\mathbf{h}^{-1^T}\mathbf{H}^T, \tag{B-9}$$

since

$$(\mathbf{AB})^T = \mathbf{B}^T\mathbf{A}^T \qquad \Leftrightarrow \qquad (\mathbf{ABC})^T = \mathbf{C}^T\mathbf{B}^T\mathbf{A}^T. \tag{B-10}$$

Using the fact, that $\sigma^T = \sigma$ and that the inverse of the transpose of a matrix equals the transpose of the inverse, Eq. (B-9) can be transformed to the familiar

$$\mathbf{t}^T = \mathcal{J}\mathbf{H}\mathbf{h}^{-1}\sigma\mathbf{h}^{T-1}\mathbf{H}^T = \mathbf{t} \tag{B-11}$$

proving that *the tensor of the thermodynamic tensions is indeed symmetric.*

Appendix C: Random Number Generators

A good overview over a great variety of random number generators can be found in 'Numerical Recipies'.[Pressetal92] A discussion of the linear congruential and the Lagged Fibonacci random number generator is also given in Ref. [Widmann96a]

C-1: Multiplicative Congruential Algorithm

The multiplicative congruential random number generation used in this work is based on the 'minimal standard' proposed by Park and Miller[ParkMiller88a], which generates a sequence of integer random numbers by

$$\eta_{n+1} = a\eta_n \bmod m \tag{C-1}$$

with $a = 7^5 = 16807$ and $m = 2^{31}-1 = 2147483647$.

To prevent overflows on a 32 bit computer, Schrage's method is used and Eq. (C-1) is written as

$$\eta_{n+1} = \begin{array}{ll} a(\eta_n \bmod q) - r(\eta_n/q) & \text{if} \geq 0 \\ a(\eta_n \bmod q) - r(\eta_n/q) + m & \text{if} < 0 \end{array} \tag{C-2}$$

with

$$\begin{array}{l} q = m/a = 127773 \\ r = m \bmod a = 2836 \end{array} . \tag{C-3}$$

Since this minimal standard (ran0 in 'Numerical Recipies'[Pressetal92]) does not pass all statistical tests extremely well and successive numbers differ by at most a factor of 16807 - which leads to problems if extremely small numbers are generated - a modification (ran1 in 'Numerical Recipies') was actually used.

Besides some safeguards that prevent initialization with $\eta_1 = 0$ and the return of endpoint values, a Bays-Durham shuffling was used to further randomize the output. This algorithm produces about 10^8 ($\approx$ m/20) random numbers that pass all statistical test. The listing below is a TCL version, that was used by DIS-COVER to produce random numbers for a Hybrid Monte Carlo simulation:

```
set randomSeed 222222
set idum -567
set ia 16807
set im 2147483647
set am [expr 1.0 / $im ]
set iq 127773
set ir 2836
set ntab 32
set ndiv [expr 1 + (($im -1) / $ntab) ]
set eps 1.2e-7
set rnmx [expr 1.0 - $eps ]
set iy 0
for {set i [expr $ntab + 7]} {$i >= 0} {incr i -1} {
  set iv($i) 0
  }
#
proc random {} {
  global ia im am iq ir ntab ndiv eps rnmx idum
  global iy iv
  if {($idum <= 0) || (!$iy)} {
    if {(-$idum) < 1} then {$idum = 1} else {$idum = -$idum}
    for {set j [expr $ntab + 7]} {$j >= 0} {incr j -1} {
      set k [expr $idum/$iq]
      $idum = $ia * ($idum - $k * $iq) - $ir * $k
      if {$idum < 0} { $idum = $idum + $im}
      if {$j < $ntab} {set iv($j) $idum}
      }
    set iy $iv(0)
    }
  set k [expr $idum/$iq]
  $idum = $ia * ($idum - $k * $iq) - $ir * $k
  if {$idum < 0} {$idum = $idum + $im}
  set j [expr $iy / $ndiv ]
  set iy $iv($j)
  set iv($j) $idum
  if {($am * $iy) > $rnmx} then { return $rnmx} \
    else { return [ expr $am * $iy ]}
  }
```

C-2: Lagged Fibonacci Algorithm

The second algorithm that was used in this work is a highly portable and vectorizable code that uses lagged Fibonacci series.[Petersen93a] The basic math of the code is quite simple,

$$t = \eta_{n-r} + \eta_{n-s}$$
$$\eta_n = t - \text{float}(\text{int}(t))$$

(C-4)

but permits - with $r = 273$ and $s = 607$ - to calculate reasonably good random numbers with extremely long periods $(2^{48} \cdot (2^{607}-1))$.

The code from Petersen[Petersen93a] is fully vectorizable, fast and portable to all machines used in this work (SGI Indigo and Crimson, IBM RS6000/560 and DEC Alpha) and was therefore used in all Monte Carlo simulations. It is, however, not as well characterized as the multiplicative congruential algorithm, but seems to be reasonably random (Marsaglia plots in 2D and 3D reveal no patterns). Normally, Monte Carlo simulations are not erroneous due to a 'bad' random number generator, but because of systematic errors due to finite relaxation times in finite lattices.[Stauffer96a]

Appendix D: Phase Space Volume Preservation of Integrators

D-1: Introduction

The integration can be viewed as a transformation in phase-space that transforms old coordinates x and velocities v

$$(x, v) \rightarrow (x', v') \tag{D-1}$$

to new coordinates x' and velocities v'. According to Eq. (A-17), the Jacobian of this transformation is

$$\begin{bmatrix} \dfrac{\partial x'}{\partial x} & \dfrac{\partial v'}{\partial x} \\ \dfrac{\partial x'}{\partial v} & \dfrac{\partial v'}{\partial v} \end{bmatrix}. \tag{D-2}$$

For the integration algorithm to be canonical, it must be volume-preserving in the phase space, i.e. its Jacobi-determinate must be 1 (Eq. (A-20)).

D-2: The Velocity Verlet Algorithm

The Velocity-Verlet algorithm is defined by[Swope82a]

$$x' = x + \Delta t v + \frac{1}{2} \Delta t^2 \frac{f(x)}{m}$$

$$v' = v + \frac{1}{2}\frac{\Delta t}{m}[f(x) + f(x')] = v + \frac{1}{2}\frac{\Delta t}{m}\left[f(x) + f\left(x + \Delta t v + \frac{1}{2}\Delta t^2 \frac{f(x)}{m} \right) \right] \tag{D-3}$$

The differentiations of Eq. (D-2), performed on the next few lines,

$$\frac{dx'}{dx} = 1 + \frac{1}{2}\frac{\Delta t^2}{m}\frac{df}{dx}\bigg|_x$$

$$\frac{dx'}{dv} = \Delta t$$

$$\frac{dv'}{dx} = \frac{1}{2}\frac{\Delta t}{m}\left[\frac{df}{dx}\bigg|_x + \frac{df}{dx}\bigg|_{x'} \cdot \left(1 + \frac{1}{2}\frac{\Delta t^2}{m}\frac{df}{dx}\right)\right]$$

$$\frac{dv'}{dv} = 1 + \frac{1}{2}\frac{\Delta t}{m}\frac{df}{dx}\bigg|_{x'} \cdot \Delta t$$

(D-4)

result in the following determinate of the Jacobian:

$$\frac{dx'}{dx} \cdot \frac{dv'}{dv} - \frac{dx'}{dv} \cdot \frac{dv'}{dx} = 1 + \frac{1}{2}\frac{\Delta t^2}{m}\frac{df}{dx}\bigg|_x + \frac{1}{2}\frac{\Delta t^2}{m}\frac{df}{dx}\bigg|_{x'} + \frac{1}{4}\frac{\Delta t^4}{m}\frac{df}{dx}\bigg|_x\frac{df}{dx}\bigg|_{x'}$$

$$-\frac{1}{2}\frac{\Delta t^2}{m}\frac{df}{dx}\bigg|_x - \frac{1}{2}\frac{\Delta t^2}{m}\frac{df}{dx}\bigg|_{x'} - \frac{1}{4}\frac{\Delta t^4}{m}\frac{df}{dx}\bigg|_x\frac{df}{dx}\bigg|_{x'} = 1$$

(D-5)

It can thus be shown analytically that the velocity Verlet integrator is in principle capable of delivering canonical trajectories.

D-3: The ABM4 and Runge-Kutta Integrators

ABM4 (Adams-Bashforth-Moulton forth order) is a predictor-corrector method[AllenTildesley89], which requires two energy evaluations per timestep. The method itself is not self-starting - the first three steps are generated by the Runge-Kutta method.[MSIDiscover1] First, the predictor step is carried out as

$$\mathbf{r}_p(t+\Delta t) = \mathbf{r}(t) + \frac{\Delta t}{24}(55\mathbf{v}(t) - 59\mathbf{v}(t-\Delta t) + 37\mathbf{v}(t-2\Delta t) - 9\mathbf{v}(t-3\Delta t))$$

$$\mathbf{v}_p(t+\Delta t) = \mathbf{v}(t) + \frac{\Delta t}{24}(55\mathbf{a}(t) - 59\mathbf{a}(t-\Delta t) + 37\mathbf{a}(t-2\Delta t) - 9\mathbf{a}(t-3\Delta t))$$

(D-6)

Using $\mathbf{r}_p$ and $\mathbf{v}_p$, $\mathbf{v}(t+\Delta t)$ and $\mathbf{a}(t+\Delta t)$ are calculated, which involves a force evaluation. With these values, the corrector is carried out as

$$\mathbf{r}_c(t+\Delta t) = \mathbf{r}(t) + \frac{\Delta t}{24}(9\mathbf{v}(t+\Delta t) + 19\mathbf{v}(t) - 5\mathbf{v}(t-\Delta t) + \mathbf{v}(t-2\Delta t))$$

$$\mathbf{v}_c(t+\Delta t) = \mathbf{v}(t) + \frac{\Delta t}{24}(9\mathbf{a}(t+\Delta t) + 19\mathbf{a}(t) - 5\mathbf{a}(t-\Delta t) + \mathbf{a}(t-2\Delta t))$$

(D-7)

The corrected $\mathbf{r}_c$ and $\mathbf{v}_c$ are used to compute $\mathbf{v}(t+\Delta t)$ and $\mathbf{a}(t+\Delta t)$, requiring another energy evaluation.

It does not seem to be possible to proof the area-preservation for the ABM4 algorithm analytically, for there is a whole history of variables that determine the

actual step. It is therefore necessary to establish a simple model system and to perform the integration of the trajectories and the check for the conservation of the phase space volume numerically.

D-4: The Model System

Serge Santos coded a predictor-corrector method with a Runge-Kutta start-up sequence and made the comparison of its behaviour to the velocity-Verlet and the Leapfrog algorithm. The program computes seven trajectories with each method for a number of particles: one trajectory with the initial set of coordinates and velocities and six trajectories with small deviations in one of the space and velocity components. The volume of the phase space at the beginning and at the end is compared. If the volume remains constant, this can be viewed as a demonstration of the area-preservation (not a proof, of course).

A new spherical potential was used with the following form:

$$E = \frac{\varepsilon}{\sigma}\left(\frac{n}{n-1}\right)^{n-1} \cdot \left(\frac{r}{n\sigma}\right)^{n-1} \cdot (r - n\sigma) , \tag{D-8}$$

where σ and ε are interaction parameters and n is a number proportional to the steepness of the potential.
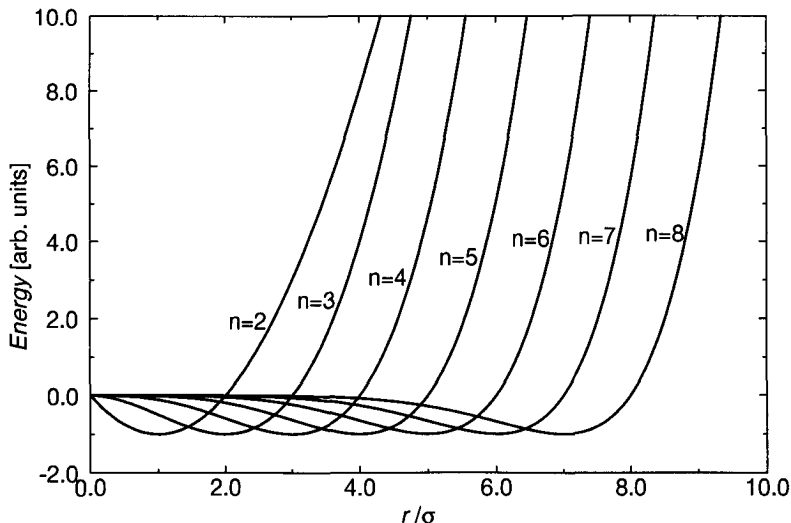

Figure D.1: Plots of the model potential for $n = 2,3,...,8$. At $r = 0$, the energy is zero and reaches a minimum of $-\varepsilon$ at $r = (n-1)\sigma$. The energy is zero again at $r = n\sigma$ and raises then proportional to r^n.

Particles were inserted randomly at places where the potential energy was

negative. The velocity of the particles was also chosen randomly from the Boltz-
mann distribution of a given temperature. A small box in phase space around the
atoms was transformed and the volume of this box was measured at the begin-
ning and at the end. To be precise, the ratio of the final and initial volumes is
obtained by an extrapolation of the box volume to infinitely small values in sev-
eral steps.

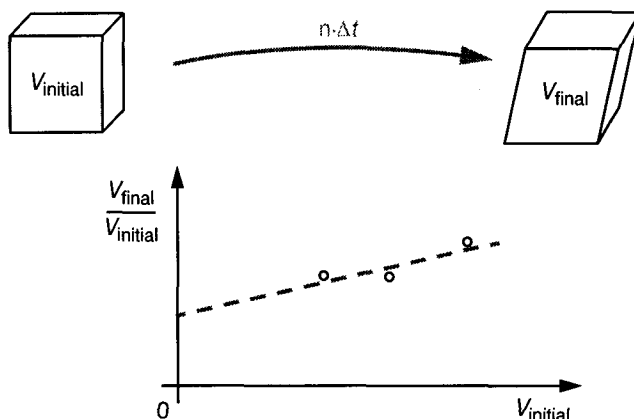If an algorithm is area-preserving, the ratio of the initial and the final volume

Figure D.2:　Extrapolation of the ratio $V_{final}/V_{initial}$ to infinitesimally small V_{inital}

is exactly 1.0.

D-5:　The Results

As Table D-1 shows, only the Velocity Verlet algorithm is canonical (which
can be proved analytically, too). The other two algorithms show bigger or smaller
deviations from canonicity.

The Runge-Kutta and the ABM4 algorithm show the same results after one
step, because the ABM4 integrator is started by a Runge-Kutta sequence. On
the average, the Leapfrog algorithm behaves similar to velocity Verlet. This is not
surprising, since the two methods - differing in the details of implementation - are
algebraically equivalent.[Frenkel96a]

This failure to sample the phase space canonically can have a drastic influ-
ence on the results, as the following data exhibits:

At BAYER, $T\sigma N$ simulations of 100 ps (in steps of 0.5 fs) without equilibration
were performed on several BPA-PC cubes of 20 Å. The equilibration was
skipped because the generation of the cubes involved multiple stages of minimi-

Table D-1: The conservation of the phase-space volume by different integration schemes.
Parameters:1 MD step, $T = 300$ K, $\sigma = 3.94$ Å, $n = 5$, $|\Delta x| = 0.5$ Å,
$|\Delta v| = 0.5$ Å/fs, decrement factor = 0.8, # of decrements = 3

Particle #	V_{final}/V_{init}		
	Vel.verlet	ABM4 = Runge-Kutta	Leapfrog
1	1.00000 ± 0.0	0.29871 ± 0.00019	0.82373 ± 0.06229
2	1.00000 ± 0.0	1.00180 ± 0.00001	1.00382 ± 0.00006
3	1.00000 ± 0.0	0.75618 ± 0.00322	0.99186 ± 0.08841
4	1.00000 ± 0.0	0.27641 ± 0.00001	1.01526 ± 0.00116
5	1.00000 ± 0.0	0.68185 ± 0.00001	0.99405 ± 0.00181
6	1.00000 ± 0.0	0.28967 ± 0.04553	0.98855 ± 0.04987
7	1.00000 ± 0.0	0.71601 ± 0.00006	1.04379 ± 0.00821
8	1.00000 ± 0.0	0.92880 ± 0.00007	1.02598 ± 0.00119
9	1.00000 ± 0.0	0.88946 ± 0.00011	0.95504 ± 0.00241
10	1.00000 ± 0.0	0.40716 ± 0.00001	1.05048 ± 0.00668

zation and MD simulations. While the other parameters were held constant, two different integrators, the ABM4 and the velocity variant of the Verlet algorithm were used. The elastic constants were calculated from the Parrinello-Rahman strain fluctuation approach. The next table shows, that they proved to be very sensitive to the choice of the integrator:

Table D-2: The elastic constants of BPA-PC (strain fluctuations)

Method	λ [GPa]	μ [GPa]	ρ [g/cm^3]
ABM4	8 - 10	3 - 3.5	1.205
Velocity-Verlet	4.2 - 4.8	0.8 - 1.2	1.185
Experiment	4.2 - 5.7	0.8 - 1.1	1.20

As can be clearly seen, correct values for the elastic constants can only be obtained if the phase space is sampled correctly.

Appendix E: Reduced Units

If a system consists of identical particles which interact only with a simple Lennard-Jones potential, its behaviour is completely specified by a few parameters like the particle mass m_a, the distance of zero interaction energy σ, and the depth of the potential ε. It is convenient to define the fundamental quantities of mass, distance and energy in terms of these parameters in order to obtain results that are independent of the particular choice of m_a, σ, and ε. The physical quantities convert as follows:

mass	$m^* = m/m_a$	a)	
distance	$r^* = r/\sigma$	b)	
energy	$E^* = E/\varepsilon$	c)	
temperature	$T^* = kT/\varepsilon$	d)	
density	$\rho^* = \rho\sigma^3$	e)	(E-1)
pressure	$p^* = p\sigma^3/\varepsilon$	f)	
time	$t^* = \left(\varepsilon/m\sigma^2\right)^{1/2}t$	g)	
force	$\mathbf{f}^* = \mathbf{f}\sigma/\varepsilon$	h)	
elastic constants	$C_{ij}^* = C_{ij}V/NkT$	i)	

and so on.

Using reduced units, the functional form of the Lennard-Jones *m-n* potential (Eq. (2-8)) and the expression of the forces simplify to

$$U^* = 4\left[\frac{1}{r^{*m}} - \frac{1}{r^{*n}}\right] \tag{E-2}$$

and

$$f_{\alpha\beta k}^* = 24\left(\frac{x_k}{r^{*n+2}_{\alpha\beta}} - 2\frac{x_k}{r^{m+2}_{\alpha\beta}}\right) \tag{E-3}$$

which greatly increases the computational efficiency.[AllenTildesley89]

For MD simulations of Lennard-Jones systems, it is necessary to obtain the distribution of the initial velocities and the equations of motion in reduced units. Expressing the velocities in reduced units,

$$v^* = \left(\frac{m}{\varepsilon}\right)^{\frac{1}{2}}v \qquad \Leftrightarrow \qquad v = \left(\frac{\varepsilon}{m}\right)^{\frac{1}{2}}v^*, \tag{E-4}$$

allows to write the distribution of initial velocities as

$$p^*(v_i^*)\,dv^* = \left(\frac{1}{2\pi\varepsilon T^*}\right)^{\frac{1}{2}}\exp\left(\frac{-v_i^{*2}}{2T^*}\right)\sqrt{\varepsilon}\,dv^*$$

$$= \left(\frac{1}{2\pi T^*}\right)^{\frac{1}{2}}\exp\left(\frac{-v_i^{*2}}{2T^*}\right)dv^* \qquad\qquad (E\text{-}5)$$

which is identical to a gaussian distribution with a mean value of 0 and a second moment of $\sqrt{T^*}$. The velocity-Verlet integrator (Eq. (2-77)) is written in reduced units as

$$\mathbf{r}^*(t^*+\delta t^*) = \mathbf{r}^*(t^*) + \delta t^*\mathbf{v}^*(t^*) + \frac{1}{2}\delta t^{*2}\mathbf{a}^*(t^*)$$

$$\mathbf{v}^*(t^*+\delta t^*) = \mathbf{v}^*(t^*) + \frac{1}{2}\delta t^*\,[\mathbf{a}^*(t^*) + \mathbf{a}^*(t^*+\delta t^*)] \qquad (E\text{-}6)$$

with the acceleration

$$\mathbf{a}^* = \left(\frac{\sigma m}{\varepsilon}\right)\mathbf{a} \qquad \Leftrightarrow \qquad \mathbf{a} = \frac{\mathbf{v}}{t} = \left(\frac{\varepsilon}{\sigma m}\right)\mathbf{a}^* . \qquad (E\text{-}7)$$

Appendix F: Elastic constants of 'ordered' it-PP

A $\mathit{Tt}N$-MD simulation of 1000 ps ($2\cdot10^6$ steps) has been performed with a completely ordered it-PP structure. The averages of the strain and the stress-strain fluctuations of the last 500 ps have been used to calculate the matrix of the elastic constants:

Table F-1: Elastic constants averaged over the last 500 ps of a 1000 ps $\mathit{Tt}N$-MD simulation at 300 K. Non-zero components are bold faced.

$\dfrac{kT}{\langle V\rangle}\langle\eta_{ik}\eta_{lm}\rangle^{-1}$						$\langle\eta_{ik}\sigma_{nj}\rangle\langle\eta_{nj}\eta_{lm}\rangle^{-1}$					
8.25	**3.43**	**7.02**	0.02	−0.17	−0.03	**9.05**	**3.79**	**7.57**	−0.01	**0.52**	−0.04
3.43	**7.19**	**3.36**	−0.09	−0.30	0.02	**3.94**	**8.01**	**4.66**	−0.03	−0.32	0.05
7.02	**3.36**	**56.00**	0.03	−5.92	0.02	**7.48**	**3.68**	**59.57**	0.03	−7.04	0.04
0.02	−0.09	0.03	**2.43**	−0.03	−0.19	−0.06	−0.07	−0.38	**2.62**	0.08	−0.35
0.17	−0.30	−5.92	−0.03	**5.20**	−0.04	−0.22	−0.27	−2.42	−0.03	**5.18**	−0.05
−0.03	0.02	0.02	−0.19	−0.04	**2.33**	−0.05	0.11	0.42	**0.02**	−0.16	**2.58**

The difference to the matrix of the disordered structure (Table 4-30) is not significant, although the components, which should be zero due to the crystal symmetry, are in general smaller.

Appendix G: Cluster Dynamics and Elastic Constants of PA-6

G-1: Cluster Dynamics of Water in Amorphous PA-6

This appendix lists in tabular form the water cluster sizes of three amorphous PA-6 microstructures with 35 water molecules at 150, 300, and 450 K.

Table G-1: 150 K, Structure 1

Time [ps]	molecules in cluster								
	# 1	# 2	# 3	# 4	# 5	# 6	# 7	# 8	rest
0-1000	17	5	2	10	1				

Table G-2: 150 K, Structure 2

Time [ps]	molecules in cluster								
	# 1	# 2	# 3	# 4	# 5	# 6	# 7	# 8	rest
0-200	20	11	2	1	1				
300-400	21	10	2	1	1				
500-1000	31	2	1	1					

Table G-3: 150 K, Structure 3

Time [ps]	molecules in cluster								
	# 1	# 2	# 3	# 4	# 5	# 6	# 7	# 8	rest
0	3	22	8	1	1				
100	3	23	2	4	1	1	1		
200	3	22	3	5	1	1			
300	3	6	3	4	1	16	1	1	
400	25	7	1	1	1				
500	25	6	1	1	1	1			
600	25	5	1	1	1	2			
700	3	22	5	1	1	2	1		
800	3	22	6	1	1	1	1		
900	25	8	1	1					
1000	3	22	7	1	1	1			

Table G-4: 300 K, Structure 1

Time [ps]	molecules in cluster								
	# 1	# 2	# 3	# 4	# 5	# 6	# 7	# 8	rest
0	17	10	7	1					
100	21	10	1	2	1				
200	11	3	11	9	1				
300	10	9	5	9	1	1			

Table G-4: 300 K, Structure 1

	#1	#2	#3	#4	#5	#6	#7	#8	rest
400	10	3	5	9	7	1			
500	9	3	12	10	1				
600, 700	16	3	5	10	1				
800	19	5	10	1					
900	10	5	2	10	7	1			
1000	17	5	2	10	1				

Table G-5: 300 K, Structure 2

| | molecules in cluster | | | | | | | | |
Time [ps]	#1	#2	#3	#4	#5	#6	#7	#8	rest
0	2	4	10	1	13	1	3	1	
100	3	22	3	1	3	1	2		
200	17	3	10	2	1	2			
300	18	11	1	2	1	2			
400	6	14	12	2	1				
500	6	13	12	2	1	1			
600	8	13	11	2	1	1			
700	19	12	2	1	1				
800	20	12	2	1					
900	19	11	2	1	1	1			

Table G-6: 300 K, Structure 3

| | molecules in cluster | | | | | | | | |
Time [ps]	#1	#2	#3	#4	#5	#6	#7	#8	rest
0	5	12	6	2	9	1			
100	3	22	2	4	1	2	1		
200	5	24	3	2	1				
300,400	2	22	9	1	1				
500	2	23	3	5	1	1			
600	3	23	3	5	1				
700	3	22	3	4	1	1	1		
800	3	23	3	5	1				
1000	3	22	8	1	1				

Table G-7: 450 K, Structure 1

| | molecules in cluster | | | | | | | | |
Time [ps]	#1	#2	#3	#4	#5	#6	#7	#8	rest
0	17	5	2	10	1				
100	26	6	2	1					
200	7	7	9	4	1	4	1	2	

Table G-7: 450 K, Structure 1

300	25	6	1	1	1	1			
400	4	15	1	8	3	2	2		
500	3	24	3	3	2				
600	25	3	1	4	1	1			
700	32	1	2						
800	6	24	1	2	1	1			
900	30	1	1	2	1				
1000	29	2	1	3					

Table G-8: 450 K, Structure 2

	molecules in cluster								
Time [ps]	# 1	# 2	# 3	# 4	# 5	# 6	# 7	# 8	rest
0	20	11	2	1	1				
100	19	16							
200	1	32	1	1					
300	16	16	2	1					
400	1	31	1	1	1				
500	32	1	1	1					
600	2	24	7	2					
700	19	9	2	3	1	1			
800	8	10	8	1	1	1	1	2	1,2
900	31	4							
1000	29	4	1	1					

Table G-9: 450 K, Structure 3

	molecules in cluster								
Time [ps]	# 1	# 2	# 3	# 4	# 5	# 6	# 7	# 8	rest
0	3	22	8	1	1				
100	35								
200	28	2	2	3					
300	21	2	5	2	1	1	1	2	
400	31	4							
500	25	3	1	2	4				
600	31	2	1	1					
700	6	12	5	3	6	1	1	1	
800	12	27	4	2					
900	24	4	1	6					
1000	31	1	2	1					

G-2: Elastic Constants of 'Dry' and 'Wet' PA-6

In the next eight tables, the elastic constants of PA-6 are listed for the dry and wet microstructures at 0, 150, 300, and 450 K. The elastic constants were obtained from the stress-strain fluctuations of the last 500 ps of the 1000 ps πN-MD runs.

Table G-10: Static minimum energy elastic constants of 'dry' and 'wet' PA-6

Dry, 0 K, Structure 1	Wet, 0 K, Structure 1	Wet, 0 K, Structure 3
$\begin{bmatrix} 13.5 & 6.1 & 5.9 & -0.4 & 0.0 & 0.0 \\ 6.1 & 14.3 & 6.6 & -0.2 & -0.2 & 0.4 \\ 5.9 & 6.6 & 10.7 & 0.1 & -0.2 & 0.0 \\ -0.4 & -0.2 & 0.1 & 3.4 & -0.3 & -0.2 \\ 0.0 & -0.2 & -0.2 & -0.3 & 2.8 & 0.0 \\ 0.0 & 0.4 & 0.0 & -0.2 & 0.0 & 3.1 \end{bmatrix}$	$\begin{bmatrix} 13.6 & 6.8 & 6.3 & -0.6 & 0.5 & 0.9 \\ 6.8 & 13.7 & 6.1 & -1.4 & -0.4 & -1.0 \\ 6.3 & 6.1 & 14.9 & -0.6 & -0.4 & -0.1 \\ -0.6 & -1.4 & -0.6 & 3.3 & 0.6 & 0.2 \\ 0.5 & -0.4 & -0.4 & 0.6 & 3.5 & -0.3 \\ 0.9 & -1.0 & -0.1 & 0.2 & -0.3 & 3.4 \end{bmatrix}$	$\begin{bmatrix} 13.9 & 6.6 & 6.7 & 0.3 & 0.2 & 0.3 \\ 6.6 & 13.5 & 6.3 & 0.5 & 0.2 & 0.0 \\ 6.7 & 6.3 & 13.5 & 0.3 & -0.2 & -0.3 \\ 0.3 & 0.5 & 0.3 & 2.8 & -0.1 & -0.1 \\ 0.2 & 0.2 & -0.2 & -0.1 & 3.3 & -0.1 \\ 0.3 & 0.0 & -0.3 & -0.1 & -0.1 & 3.5 \end{bmatrix}$
$\lambda = 6.28 \pm 0.34, \mu = 3.23 \pm 0.22$	$\lambda = 5.81 \pm 0.26, \mu = 2.06 \pm 0.16$	$\lambda = 5.27 \pm 0.29, \mu = 2.05 \pm 0.18$

Table G-11: Elastic constants of 'dry' PA-6 at 150 K, stress-strain fluctuation approach

Dry, 150 K, Structure 1	Dry, 150 K, Structure 2	Dry, 150 K, Structure 3
$\begin{bmatrix} 8.4 & 5.2 & 4.2 & -0.3 & 0.6 & -0.2 \\ 6.0 & 12.9 & 6.8 & 0.3 & 0.2 & 0.4 \\ 4.9 & 6.8 & 8.7 & -0.3 & 0.4 & 0.0 \\ -0.4 & 0.3 & -0.3 & 2.4 & -0.3 & 0.0 \\ 0.6 & 0.2 & 0.3 & -0.3 & 1.6 & 0.0 \\ -0.3 & 0.4 & 0.0 & 0.0 & 0.0 & 1.8 \end{bmatrix}$	$\begin{bmatrix} 8.5 & 6.1 & 6.1 & 0.4 & -0.3 & 0.1 \\ 7.2 & 11.5 & 6.4 & -0.1 & 0.0 & 0.1 \\ 5.5 & 4.7 & 9.1 & 0.0 & 0.6 & 0.0 \\ 0.5 & -0.1 & 0.0 & 2.1 & -0.3 & -0.2 \\ -0.3 & 0.0 & 0.6 & -0.2 & 2.9 & -0.1 \\ 0.1 & 0.1 & 0.0 & -0.2 & -0.1 & 2.4 \end{bmatrix}$	$\begin{bmatrix} 11.9 & 6.3 & 5.2 & -0.1 & 0.3 & -0.7 \\ 6.3 & 9.4 & 5.0 & -0.1 & -0.6 & 0.0 \\ 4.5 & 4.3 & 8.3 & -0.3 & -0.3 & -0.2 \\ -0.1 & -0.1 & 0.3 & 1.6 & 0.1 & -0.3 \\ 0.3 & -0.5 & -0.4 & 0.2 & 1.7 & 0.0 \\ -0.6 & 0.0 & -0.2 & -0.3 & 0.0 & 1.7 \end{bmatrix}$
$\lambda = 5.71 \pm 0.42, \mu = 2.10 \pm 0.26$	$\lambda = 5.81 \pm 0.26, \mu = 2.06 \pm 0.16$	$\lambda = 5.27 \pm 0.29, \mu = 2.05 \pm 0.18$

Table G-12: Elastic constants of 'wet' PA-6 at 150 K, stress-strain fluctuation approach

Wet, 150 K, Structure 1	Wet, 150 K, Structure 2	Wet, 150 K, Structure 3
$\begin{bmatrix} 8.6 & 4.6 & 5.0 & 0.0 & -0.7 & 0.6 \\ 7.1 & 12.5 & 8.2 & -0.2 & -0.0 & 0.3 \\ 5.6 & 6.0 & 10.6 & 0.3 & -0.1 & 0.0 \\ 0.0 & -0.2 & 0.4 & 2.2 & 0.0 & 0.3 \\ -0.7 & -0.0 & -0.1 & 0.0 & 2.0 & 0.3 \\ 0.8 & 0.2 & 0.1 & 0.3 & 0.3 & 1.5 \end{bmatrix}$	$\begin{bmatrix} 12.2 & 6.5 & 7.1 & -0.1 & 0.2 & 0.4 \\ 6.4 & 10.7 & 5.8 & 0.4 & -0.3 & 0.6 \\ 7.2 & 6.1 & 10.1 & -0.5 & 0.3 & -0.3 \\ -0.1 & 0.4 & 0.5 & 2.2 & -0.2 & 0.5 \\ 0.2 & -0.3 & 0.3 & -0.2 & 2.0 & -0.5 \\ 0.5 & 0.6 & -0.3 & 0.5 & -0.5 & 1.8 \end{bmatrix}$	$\begin{bmatrix} 11.6 & 6.4 & 6.1 & -0.0 & -0.3 & 0.2 \\ 7.1 & 13.1 & 7.9 & 0.3 & -0.3 & 0.0 \\ 5.0 & 5.9 & 9.6 & 0.2 & -0.0 & -0.4 \\ -0.0 & 0.3 & 0.2 & 1.9 & -0.1 & -0.3 \\ -0.2 & -0.2 & 0.0 & -0.1 & 2.2 & -0.2 \\ 0.2 & 0.0 & -0.5 & -0.4 & -0.3 & 2.4 \end{bmatrix}$
$\lambda = 6.15 \pm 0.24, \mu = 2.14 \pm 0.15$	$\lambda = 6.63 \pm 0.28, \mu = 2.13 \pm 0.18$	$\lambda = 6.41 \pm 0.15, \mu = 2.38 \pm 0.09$

Table G-13: Elastic constants of 'dry' PA-6 at 300 K, stress-strain fluctuation approach

Dry, 300 K, Structure 1	Dry, 300 K, Structure 2	Dry, 300 K, Structure 3
5.9 4.1 4.2 -0.1 0.3 -0.5 4.6 6.7 4.4 -0.2 -0.2 -0.2 4.7 4.4 6.4 -0.2 0.0 -0.1 -0.2 -0.2 -0.2 1.1 0.0 -0.1 0.3 -0.2 0.0 0.0 1.2 0.1 -0.6 -0.2 -0.1 -0.1 0.1 0.8	5.3 5.1 4.7 0.0 0.1 0.1 5.8 8.8 4.9 0.1 0.3 0.2 4.2 3.8 5.7 -0.1 0.5 0.3 0.0 0.1 -0.1 1.2 -0.2 -0.2 0.1 0.2 0.5 -0.2 1.1 0.0 0.1 0.2 0.4 -0.2 0.0 1.6	7.7 4.9 4.1 0.2 0.3 -0.4 4.4 6.7 4.3 0.3 -0.1 0.0 3.4 3.9 5.7 -0.2 -0.2 -0.4 0.2 0.3 -0.2 0.8 0.1 -0.5 0.2 -0.1 -0.2 0.1 1.0 -0.1 -0.4 0.0 -0.4 -0.5 -0.1 1.4
$\lambda = 4.35 \pm 0.11$, $\mu = 0.99 \pm 0.07$	$\lambda = 4.27 \pm 0.24$, $\mu = 0.97 \pm 0.15$	$\lambda = 4.17 \pm 0.15$, $\mu = 1.19 \pm 0.09$

Table G-14: Elastic constants of 'wet' PA-6 at 300 K, stress-strain fluctuation approach

Wet, 300 K, Structure 1	Wet, 300 K, Structure 2	Wet, 300 K, Structure 3
5.7 4.2 4.2 0.1 -0.2 0.1 5.2 7.4 5.2 0.3 -0.1 0.2 4.3 4.2 6.0 -0.1 -0.2 0.3 0.1 0.3 -0.1 0.9 0.0 0.1 -0.2 -0.1 -0.2 0.0 0.5 0.2 0.1 0.1 0.4 0.1 0.2 0.3	6.9 4.3 5.0 -0.2 -0.1 0.2 4.1 5.4 4.0 -0.1 -0.2 0.2 5.2 4.2 5.9 -0.1 0.2 -0.1 -0.2 -0.1 -0.1 0.8 -0.2 0.1 -0.1 -0.2 0.2 -0.2 0.9 -0.2 0.2 0.2 -0.1 0.1 -0.2 0.5	7.2 5.0 5.3 0.1 -0.3 0.6 4.8 7.3 5.0 -0.1 -0.0 0.5 4.6 4.5 6.4 -0.1 -0.1 -0.1 0.1 -0.1 -0.1 0.7 0.1 0.0 -0.3 -0.0 -0.1 0.1 0.7 0.2 0.6 0.5 -0.1 0.0 0.2 0.6
$\lambda = 4.53 \pm 0.11$, $\mu = 0.78 \pm 0.07$	$\lambda = 4.37 \pm 0.16$, $\mu = 0.75 \pm 0.10$	$\lambda = 4.98 \pm 0.13$, $\mu = 0.91 \pm 0.08$

Table G-15: Elastic constants of 'wet' PA-6 at 450 K, stress-strain fluctuation approach

Dry, 450 K, Structure 1	Dry, 450 K, Structure 2	Dry, 450 K, Structure 3
2.0 1.5 1.6 0.2 -0.2 0.0 2.6 3.5 3.0 0.1 -0.2 0.0 1.9 2.1 2.3 -0.1 0.0 0.1 0.3 0.1 0.2 0.3 0.0 -0.1 -0.2 -0.1 0.0 0.0 0.2 0.0 0.0 0.0 0.1 -0.1 0.1 0.2	2.3 1.9 1.7 -0.2 -0.1 0.2 3.5 4.0 3.3 -0.1 -0.1 0.0 1.6 1.7 2.1 -0.1 -0.1 0.1 -0.2 -0.1 -0.1 0.2 0.2 0.0 -0.1 -0.0 -0.1 -0.1 0.3 0.0 0.2 0.0 0.1 0.0 0.0 0.3	3.2 2.4 2.6 0.1 -0.1 -0.2 2.9 3.6 3.0 0.2 0.1 0.1 2.4 2.3 2.8 0.1 0.1 0.1 0.1 0.1 0.1 0.3 0.0 -0.1 -0.1 0.1 0.1 0.0 0.2 -0.1 -0.2 0.1 0.1 -0.1 -0.1 0.4
$\lambda = 2.14 \pm 0.07$, $\mu = 0.23 \pm 0.04$	$\lambda = 2.17 \pm 0.06$, $\mu = 0.26 \pm 0.04$	$\lambda = 2.32 \pm 0.05$, $\mu = 0.27 \pm 0.03$

Table G-16: Elastic constants of 'wet' PA-6 at 450 K, stress-strain fluctuation approach

Wet, 450 K, Structure 1	Wet, 450 K, Structure 2	Wet, 450 K, Structure 3
1.5 1.2 1.1 -0.0 -0.1 0.0 1.0 1.2 1.0 -0.1 -0.1 -0.0 0.6 0.6 0.8 -0.0 -0.0 -0.0 -0.0 -0.1 -0.0 0.0 0.0 -0.0 -0.1 -0.1 -0.0 0.0 0.1 0.0 0.0 -0.0 -0.1 -0.0 0.0 0.2	1.7 1.4 1.3 0.0 0.1 0.3 1.3 1.3 1.3 -0.0 0.1 0.2 0.7 0.6 0.7 -0.0 0.1 0.1 0.0 -0.0 -0.0 0.0 0.0 0.0 0.1 0.0 0.1 0.0 0.1 0.0 0.3 0.2 0.2 0.0 0.0 0.2	1.7 1.4 1.7 -0.1 0.1 -0.1 0.7 0.8 0.8 0.0 0.0 -0.1 0.6 0.5 0.7 -0.0 0.0 -0.1 -0.0 0.0 -0.0 0.1 0.0 0.0 0.1 0.0 0.0 0.0 0.1 -0.1 -0.1 -0.1 -0.1 0.0 -0.1 0.1
$\lambda = 0.85 \pm 0.02$, $\mu = 0.10 \pm 0.01$	$\lambda = 1.06 \pm 0.05$, $\mu = 0.07 \pm 0.03$	$\lambda = 0.92 \pm 0.04$, $\mu = 0.07 \pm 0.02$

Appendix H: Elastic Constants of PA-12

In the next eight tables, the elastic constants of PA-6 are listed for the dry and wet microstructures at 0, 150, 300, and 450 K. Except the static minimum energy approach, all matrices were calculated from the fluctuations of the stresses and strains in the last 500 ps of the 1000 ps $7tN$-MD simulation.

Table H-1: Elastic constants of 'dry' PA-12 at 150 K, stress-strain fluctuation approach

Dry, 150 K, Structure 1	Dry, 150 K, Structure 2	Dry, 150 K, Structure 3
$\begin{bmatrix} 7.7 & 4.3 & 3.9 & 0.1 & -0.5 & -0.2 \\ 4.3 & 6.6 & 3.2 & 0.3 & -0.2 & -0.5 \\ 4.0 & 3.4 & 6.5 & 0.4 & -0.4 & -0.2 \\ 0.1 & 0.4 & 0.3 & 1.4 & -0.1 & -0.1 \\ -0.5 & -0.2 & -0.2 & -0.1 & 1.5 & 0.1 \\ -0.3 & 0.5 & -0.2 & 0.0 & 0.1 & 1.0 \end{bmatrix}$	$\begin{bmatrix} 4.7 & 5.4 & 6.5 & -1.4 & -0.8 & -0.2 \\ 5.2 & 7.7 & 5.2 & 0.6 & -1.0 & -1.9 \\ 6.9 & 4.0 & 4.5 & 0.7 & 1.1 & 1.1 \\ -1.1 & 0.6 & 0.0 & 0.5 & 0.2 & 0.6 \\ -0.9 & -0.6 & 1.0 & 0.3 & 1.3 & -0.5 \\ 0.7 & -1.5 & 0.7 & -1.3 & -0.7 & 0.1 \end{bmatrix}$	$\begin{bmatrix} 7.5 & 4.6 & 4.6 & 0.0 & 0.2 & 0.3 \\ 4.5 & 7.6 & 4.3 & 0.1 & 0.4 & -0.1 \\ 4.5 & 4.2 & 8.2 & 0.1 & 0.2 & -0.1 \\ 0.0 & 0.2 & 0.1 & 1.4 & -0.2 & -0.3 \\ -0.4 & 0.3 & 0.8 & -0.1 & 1.7 & -0.1 \\ 0.0 & 0.1 & -0.3 & 0.0 & -0.1 & 1.9 \end{bmatrix}$
$\lambda = 3.89 \pm 0.20, \mu = 1.49 \pm 0.13$	$\lambda = 5.46 \pm 0.54, \mu = 0.19 \pm 0.34$	$\lambda = 4.51 \pm 0.12, \mu = 1.66 \pm 0.08$

Table H-2: Elastic constants of 'wet' PA-12 at 150 K, stress-strain fluctuation approach

Wet, 150 K, Structure 1	Wet, 150 K, Structure 2	Wet, 150 K, Structure 3
$\begin{bmatrix} 7.4 & 3.9 & 4.5 & -0.2 & 0.1 & 0.4 \\ 3.9 & 7.2 & 4.4 & 0.0 & -0.4 & -0.8 \\ 4.5 & 4.4 & 7.0 & -0.7 & -0.3 & -0.1 \\ 0.0 & -0.3 & -0.1 & 1.3 & 0.0 & 0.0 \\ -0.1 & -0.4 & -0.1 & 0.1 & 1.3 & -0.4 \\ 0.1 & -0.7 & -0.2 & 0.0 & -0.1 & 1.0 \end{bmatrix}$	$\begin{bmatrix} 6.6 & 4.0 & 4.1 & 0.2 & -0.3 & -0.6 \\ 3.9 & 5.9 & 4.0 & -0.8 & -0.3 & 0.2 \\ 4.3 & 3.9 & 7.8 & -0.5 & 0.4 & 0.1 \\ 0.3 & -0.4 & 0.2 & 1.4 & 0.0 & 0.1 \\ 0.0 & -0.3 & -0.2 & -0.3 & 1.2 & -0.1 \\ 0.0 & -0.2 & 0.1 & 0.0 & -0.1 & 0.9 \end{bmatrix}$	$\begin{bmatrix} 7.3 & 4.2 & 4.1 & -0.1 & 0.4 & 0.2 \\ 4.2 & 6.4 & 3.4 & 0.0 & -0.2 & 0.1 \\ 4.0 & 3.4 & 6.0 & -0.1 & -0.4 & 0.1 \\ 0.0 & -0.1 & 0.0 & 1.1 & 0.0 & -0.3 \\ -0.3 & -0.3 & -0.1 & -0.1 & 1.4 & -0.3 \\ 0.2 & 0.1 & 0.0 & -0.2 & -0.2 & 0.7 \end{bmatrix}$
$\lambda = 4.38 \pm 0.18, \mu = 1.38 \pm 0.12$	$\lambda = 4.10 \pm 0.23, \mu = 1.33 \pm 0.15$	$\lambda = 4.00 \pm 0.18, \mu = 1.24 \pm 0.11$

Table H-3: Elastic constants of 'dry' PA-12 at 300 K, stress-strain fluctuation approach

Dry, 300 K, Structure 1	Dry, 300 K, Structure 2	Dry, 300 K, Structure 3
$\begin{bmatrix} 3.6 & 2.6 & 2.6 & -0.2 & 0.1 & -0.3 \\ 2.7 & 3.1 & 2.3 & 0.0 & 0.3 & -0.3 \\ 2.6 & 2.2 & 3.3 & -0.2 & -0.1 & -0.1 \\ -0.2 & 0.0 & -0.2 & 0.4 & 0.0 & 0.0 \\ 0.1 & 0.3 & -0.1 & 0.0 & 0.5 & 0.1 \\ -0.3 & -0.2 & -0.1 & 0.0 & 0.1 & 0.5 \end{bmatrix}$	$\begin{bmatrix} 3.3 & 2.6 & 2.8 & 0.2 & 0.3 & 0.3 \\ 2.5 & 3.4 & 2.8 & -0.2 & 0.0 & 0.1 \\ 2.7 & 2.9 & 3.7 & 0.3 & 0.0 & 0.2 \\ 0.1 & -0.1 & 0.2 & 0.4 & 0.0 & 0.1 \\ 0.2 & 0.1 & 0.2 & 0.0 & 0.7 & 0.1 \\ 0.3 & 0.2 & 0.2 & 0.1 & 0.0 & 0.3 \end{bmatrix}$	$\begin{bmatrix} 4.4 & 2.9 & 3.1 & 0.0 & 0.3 & -0.1 \\ 2.9 & 4.3 & 2.5 & 0.1 & 0.2 & -0.1 \\ 3.0 & 2.5 & 4.4 & 0.0 & 0.2 & -0.2 \\ 0.0 & 0.0 & 0.1 & 0.7 & 0.2 & 0.1 \\ 0.2 & 0.1 & 0.3 & 0.2 & 0.6 & -0.2 \\ -0.1 & -0.1 & -0.3 & 0.2 & -0.2 & 0.4 \end{bmatrix}$
$\lambda = 2.48 \pm 0.09, \mu = 0.44 \pm 0.05$	$\lambda = 2.68 \pm 0.10, \mu = 0.43 \pm 0.06$	$\lambda = 2.87 \pm 0.10, \mu = 0.67 \pm 0.06$

Table H-4: Elastic constants of 'wet' PA-12 at 300 K, stress-strain fluctuation approach

Wet, 300 K, Structure 1	Wet, 300 K, Structure 2	Wet, 300 K, Structure 3
$\begin{bmatrix} 4.2 & 2.9 & 3.0 & -0.1 & 0.2 & 0.0 \\ 3.0 & 3.5 & 2.6 & 0.1 & -0.1 & -0.2 \\ 3.2 & 2.7 & 4.3 & -0.5 & -0.1 & -0.2 \\ -0.1 & -0.1 & -0.2 & 0.5 & 0.1 & 0.0 \\ 0.1 & -0.1 & 0.1 & 0.1 & 0.5 & -0.1 \\ 0.0 & -0.2 & -0.3 & 0.1 & 0.0 & 0.6 \end{bmatrix}$	$\begin{bmatrix} 3.8 & 2.8 & 3.1 & 0.1 & -0.2 & 0.0 \\ 2.8 & 3.4 & 2.6 & 0.1 & -0.2 & 0.6 \\ 3.0 & 2.7 & 3.8 & 0.2 & 0.1 & -0.1 \\ 0.1 & 0.2 & 0.1 & 0.7 & 0.2 & 0.1 \\ 0.0 & -0.2 & -0.1 & 0.0 & 0.5 & 0.2 \\ 0.2 & 0.3 & -0.1 & -0.1 & 0.1 & 0.6 \end{bmatrix}$	$\begin{bmatrix} 4.0 & 2.7 & 2.9 & -0.1 & 0.1 & 0.0 \\ 2.5 & 3.6 & 2.4 & -0.1 & 0.0 & 0.0 \\ 2.8 & 2.4 & 3.1 & -0.1 & 0.0 & -0.2 \\ -0.1 & -0.1 & 0.0 & 0.4 & 0.1 & 0.0 \\ 0.0 & 0.0 & 0.2 & 0.1 & 0.3 & -0.1 \\ 0.0 & 0.0 & -0.2 & 0.1 & -0.1 & 0.4 \end{bmatrix}$
$\lambda = 2.87 \pm 0.11,\ \mu = 0.56 \pm 0.07$	$\lambda = 2.75 \pm 0.11,\ \mu = 0.49 \pm 0.07$	$\lambda = 2.70 \pm 0.10,\ \mu = 0.42 \pm 0.06$

Table H-5: Elastic constants of 'wet' PA-12 at 450 K, stress-strain fluctuation approach

Dry, 450 K, Structure 1	Dry, 450 K, Structure 2	Dry, 450 K, Structure 3
$\begin{bmatrix} 1.3 & 1.1 & 1.1 & 0.0 & 0.0 & 0.0 \\ 1.1 & 1.2 & 1.1 & 0.0 & 0.1 & 0.1 \\ 1.2 & 1.2 & 1.3 & 0.0 & 0.1 & 0.0 \\ 0.0 & -0.1 & 0.0 & 0.1 & 0.0 & 0.0 \\ 0.1 & 0.1 & 0.0 & 0.0 & 0.1 & 0.0 \\ 0.0 & 0.0 & 0.0 & 0.0 & 0.0 & 0.1 \end{bmatrix}$	$\begin{bmatrix} 1.6 & 1.4 & 1.4 & 0.0 & 0.1 & 0.0 \\ 1.2 & 1.3 & 1.2 & 0.0 & 0.0 & 0.0 \\ 1.1 & 1.1 & 1.2 & 0.0 & 0.0 & 0.1 \\ 0.0 & 0.0 & 0.0 & -0.1 & 0.0 & 0.0 \\ 0.0 & 0.0 & 0.0 & 0.0 & 0.0 & 0.0 \\ -0.1 & 0.1 & 0.1 & 0.0 & 0.0 & 0.1 \end{bmatrix}$	$\begin{bmatrix} 0.8 & 0.6 & 0.5 & 0.0 & 0.1 & 0.1 \\ 0.6 & 0.7 & 0.5 & 0.0 & 0.0 & 0.0 \\ 0.5 & 0.5 & 0.5 & 0.0 & 0.0 & 0.1 \\ 0.0 & 0.0 & 0.0 & 0.0 & 0.0 & 0.0 \\ 0.0 & 0.0 & 0.0 & 0.0 & 0.1 & 0.0 \\ 0.0 & 0.0 & 0.0 & 0.0 & 0.0 & 0.1 \end{bmatrix}$
$\lambda = 1.10 \pm 0.02,\ \mu = 0.09 \pm 0.01$	$\lambda = 1.34 \pm 0.05,\ \mu = 0.01 \pm 0.03$	$\lambda = 0.54 \pm 0.03,\ \mu = 0.07 \pm 0.02$

Table H-6: Elastic constants of 'wet' PA-12 at 450 K, stress-strain fluctuation approach

Wet, 450 K, Structure 1	Wet, 450 K, Structure 2	Wet, 450 K, Structure 3
$\begin{bmatrix} 0.6 & 0.4 & 0.3 & 0.0 & 0.0 & 0.0 \\ 0.5 & 0.8 & 0.4 & 0.1 & 0.0 & -0.1 \\ 0.3 & 0.3 & 0.5 & 0.0 & 0.0 & -0.1 \\ 0.0 & 0.0 & 0.0 & 0.0 & 0.0 & 0.0 \\ 0.0 & 0.0 & 0.0 & 0.0 & 0.1 & 0.0 \\ -0.1 & 0.0 & -0.1 & 0.0 & 0.0 & 0.1 \end{bmatrix}$	$\begin{bmatrix} 1.1 & 1.1 & 1.0 & 0.0 & -0.2 & -0.1 \\ 1.0 & 1.5 & 1.2 & 0.0 & -0.1 & 0.0 \\ 0.9 & 1.2 & 1.3 & 0.1 & 0.1 & -0.1 \\ 0.0 & 0.1 & 0.0 & 0.1 & 0.0 & 0.0 \\ -0.1 & -0.1 & -0.1 & -0.1 & 0.1 & 0.0 \\ 0.0 & -0.1 & -0.1 & -0.1 & 0.0 & 0.1 \end{bmatrix}$	$\begin{bmatrix} 0.9 & 0.7 & 0.8 & 0.1 & 0.1 & 0.0 \\ 0.7 & 0.8 & 0.8 & 0.0 & 0.1 & -0.1 \\ 0.8 & 0.8 & 1.1 & 0.0 & 0.0 & 0.1 \\ 0.0 & 0.0 & 0.0 & 0.0 & 0.0 & 0.0 \\ 0.1 & 0.1 & 0.1 & 0.0 & 0.1 & 0.0 \\ 0.0 & 0.0 & -0.1 & 0.0 & 0.0 & 0.1 \end{bmatrix}$
$\lambda = 0.38 \pm 0.04,\ \mu = 0.11 \pm 0.03$	$\lambda = 1.10 \pm 0.05,\ \mu = 0.10 \pm 0.03$	$\lambda = 0.79 \pm 0.04,\ \mu = 0.07 \pm 0.03$

7 References

[Acton90] F. S. Acton, *Numerical Methods That Work*, The Mathematical Association of America, Washington D.C. (1990)

[AllenTildesley89] M. P. Allen and D. J. Tildesley, *Computer Simulation of Liquids*, Clarendon Press, Oxford (1989)

[Allinger89a] N. L. Allinger, Y. H. Yuh and J.-H. Lii, *Molecular Mechanics. The MM3 Force Field for Hydrocarbons*, J. Am. Chem. Soc. **111**(23), 8551-8566 (1989)

[Anand67a] J. N. Anand, *Molecular Forces and Elastic Constants of Polyethylene Single Crystals*, J. Macromol. Sci. Phys. **B1**(3), 445-458 (1967)

[Andersen80a] H. C. Andersen, *Molecular Dynamics Simulations at Constant Pressure and/or Temperature*, J. Chem. Phys. **72**(4), 2384-2393 (1980)

[Asada63a] T. Asada and S. Onogi, *The Diffusion Coefficient for the Nylon 6 and Water System*, J. Coll. Sci. **18**, 784-792 (1963)

[Asada76a] T. Asada, K. Inoue, and S. Onogi, *Diffusion in the Nylon 12 and Water System*, Polymer Journal **8** (1), 21-29 (1976)

[Atalla74a] R. H. Atalla, Appl. Polym. Sci. Symp. **28**, 659-669 (1974)

[Atalla84a] D. L. VanderHart and R. H. Atalla, *Studies of Microstructure in Native Celluloses Using Solid-State 13C-NMR*, Macromolecules **17**, 1465-1472 (1984)

[Barber92] J. R. Barber, *Elasticity*, Kluver Academic, Dordrecht, Solid Mechanics and Its Applications **12** (1992)

[Barham79a] P. J. Barham and A. Keller, *The Achievement of High-Modulus Polyethylene Fibers and the Modulus of Polyethylene Crystals*, J. Poly. Sci.: Polym. Let. Ed. **17**, 591-593 (1979)

[Barker76] J. A. Barker, *Interatomic Potentials for Inert Gases from Experimental Data*, in: M. L. Klein and J. A. Venables, *Rare Gas Solids* **1**(4), 213-264, Academic Press, London (1976)

[BellZucker76] R. J. Bell and I. J. Zucker, *Long-Range Forces*, in: M. L. Klein and J. A. Venables, *Rare Gas Solids* **1**(2), 123-175, Academic Press, London (1976)

[Berendsen84a] H. J. C. Berendsen, J. P. M. Postma, W. F. van Gunsteren, A. DiNola and J. R. Haak, Molecular Dynamics with Coupling to an External Bath, J. Chem. Phys. **81**(8), 3684-3690 (1984)

[Berk70a] H. L. Berk and K. V. Roberts, *The Water-Bag Model*, Methods in Computational Physics **9**, 87-134 (1970)

[Bhagavantam66] S. Bhagavantam, Crystal Symmetry and Physical Properties, Academic Press, London and New York (1966)

Bhat89a N. V. Bhat and D. S. Kelkar, The Effect of Heat Setting on the Elastic and Viscoelastic Properties of Nylon-6 Films, J. Polym. Sci. C **16**, 375-388 (1989)

Billmeyer84 F. W. Billmeyer, Textbook of Polymer Science, Chapter 15, Wiley-Interscience Publication,New York (1984)

Binder92a K. Binder, *The Monte Carlo Method in Condensed Matter Physics*, Springer Verlag, Berlin, Topics in Applied Physics **71** (1992)

Binder92b K. Binder and D. W. Heermann, *Monte Carlo Simulation in Statistical Physics*, 2nd edition, Springer Verlag, Berlin, Solid State Sciences **80** (1992)

BornHuang54 M. Born and K. Huang, *Dynamical Theory of Crystal Lattices*, Clarendon, Oxford (1954)

Boyd59a R. H. Boyd, Dielectric Loss in 66 Nylon (Polyhexamethylene Adipamide), J. Chem. Phys. **30**, 1276-1283 (1959)

Boyd88a R. A. Sorensen, W. B. Liau, L. Kesner, and R. H. Boyd, Prediction of Polymer Crystal Structure and Properties. Polyethylene and Poly(oxymethylene), Macromolecules **21**(1), 200-208 (1988)

Brandrup89 J. Brandrup and E. H. Immergut, Polymer Handbook, 3rd edition, John Wiley & Sons, New York (1989)

Bronstein91 I. N. Bronstein and K. A. Semendjajew, *Taschenbuch der Mathematik*, G. Grosche, V. Ziegler and D. Ziegler (editors), B. G. Teubner Verlagsgesellschaft, Stuttgart (1991)

Brown91a D. Brown and J. H. R. Clarke, *Molecular Dynamics Simulation of an Amorphous Polymer under Tension. 1. Phenomenology*, Macromolecules **24**(8), 2075-2082 (1991)

Bulgac90a A. Bulgac and D. Kusnezov, *Canonical Ensemble Averages from Pseudomicrocanonical Dynamics*, Phys. Rev. A **42**(8), 5045-5048 (1990)

Budiansky74 B. Budiansky, *Tensors*, in: C. E. Pearson, *Handbook of Applied Mathematics* (4), 179-225, Van Nostrand Reinhold, New York (1974)

Bunn39a C. W. Bunn, *The Crystal Structure of Long-Chain Normal Paraffin Hydrocarbons. The Shape of the CH2-Group*, Trans. Farad. Soc. **34**, 482-491 (1939)

CaginRay88a T. Cagin and J. R. Ray, *Third-order Elastic Constants from Molecular Dynamics: Theory and Example Calculation*, Phys. Rev. B **38**(12), 7940-7946 (1988)

Car95a R. Car, *Molecular Dynamics from First Principles*, in: K. Binder and G. Ciccotti, *Monte Carlo and Molecular Dynamics of Condensed Matter Systems* **49**, 605-634, Italian Physcal Society, Bologna (1995)

Chanzy91a J. Sugiyama, J. Persson, and H. Chanzy, *Combined Infrared and Electron Diffraction Study of the Polymorphism of Native Celluloses*, Macromolecules **24**, 2461-2466 (1991)

Chanzy95a V. Favier, H. Chanzy, and J. Y. Cavaille, *Polymer Nanocomposites Reinforced by Cellulose Whiskers*, Macromolecules **28**(18), 6365-6367 (1995)

Chanzy95b S. Raymond, A. Kvick, and H. Chanzy, *The Structure of Cellulose II: A Revisit*, Macromolecules **28**(24), 8422-8425 (1995)

Ciarlet88 P. G. Ciarlet, *Mathematical Elasticity 1: Three-Dimensional Elasticity*, North-Holland, Amsterdam, Studies in Mathematics and Its Applications **20**

Corradini83a P. Corradini, V. Petraccone, and B. Pirozzi, *The Role of Intermolecular Interactions in Determining the Mode of Packing of Crystalline Polymers*, European Polymer Journal **19**(4), 299-304 (1983)

Cowley83a E. R. Cowley, *Some Monte Carlo Calculations for the Lennard-Jones Solid*, Phys. Rev. B **28**(6), 3160-3163 (1983)

Duane87a S. Duane, A. D. Kennedy, B. J. Pendelton and D. Roweth, *Hybrid Monte Carlo*, Phys. Let. B **195**(2), 216-222 (1987)

EasonOgden90 G. Eason and R. W. Ogden, *Elasticity - Mathematical Methods and Applications*, Ellis Horwood, Chichester (1990)

Elias84 H.-G. Elias, *Macromolecules 1: Structure and Properties*, 2nd edition, Plenum Press, New York (1984)

Evans77a D. J. Evans and S. Murad, *Singularity Free Algorithm for Molecular Dynamics Simulation of Rigid Polyatomics*, Mol. Phys. **34**(2), 327-331 (1977)

Evans77b D. J. Evans, *On the Representation of Orientation Space*, Mol. Phys. **34**(2), 317-325 (1977)

Evans85a D. J. Evans and B. L. Holian, *The Nose-Hoover Thermostat*, J. Chem. Phys. **83**(8), 4069-4074 (1985)

Fay92a P. J. Fay and J. R. Ray, *Monte Carlo Simulations in the Isoenthalpic-isotension-isobaric Ensemble*, Phys. Rev. A **46**(8), 4645-4649 (1992)

Ferro92a D. R. Ferro, S. Brueckner, S. V. Meille, and M. Ragazzi, *Energy Calculations for Isotactic Polypropylene: A Comparison Between Models of the α and γ Crystalline Structures*, Macromolecules **25**(20), 5231-5235 (1992)

Flory89 P. J. Flory, *Statistical Mechanics of Chain Molecules*, Hanser Publishers, Munich (1989)

Forrest94a B. M. Forrest and U. W. Suter, *Generalized Coordinate Hybrid Monte Carlo*, Molecular Physics **82**(2), 393-410 (1994)

Franck88 A. Franck and K. Biederbick, *Kunststoff-Kompendium*, 2nd edition, Vogel Verlag, Wuerzburg (1988)

Frank96a B. Frank, P. Fruebing, and P. Pissis, *Water Sorption and Thermally Stimulated Depolarization Currents in Nylon-6*, J. Polym. Sci. B: Poly. Phys. **34**, 1853-1860 (1996)

Frenkel96 D. Frenkel and B. Smit, *Understanding Molecular Simulation: From Algorithms to Applications*, Academic Press, San Diego (1996)

Friedman85 H. L. Friedman, *A Course in Statistical Mechanics*, Prentice Hall ,Englewood Cliffs, New Jersey (1985)

Ganster94 J. Ganster, H.-P. Fink, J. Fraatz, and M. Nywlt, *Relation Between Structure and Elastic Constants of Man-Made Cellulosic Fibers: I. A Two Phase Anisotropic Model With Contiguity Parameter*, Acta Polym. **45**, 312-318 (1994)

Gardner74a K. H. Gardner and J. Blackwell, *The Structure of Native Cellulose*, Biopolymers **13**, 1975-2001 (1974)

Gillis69a P. P. Gillis, *Effect of Hydrogen Bonds on the Axial Stiffness of Crystalline Native Cellulose*, J. Polym. Sci. A-2 **7**, 783-794 (1969)

Godovsky92 Y. K. Godovsky, *Thermophysical Properties of Polymers*, Springer Verlag, Berlin (1992)

Goldstein80 H. Goldstein, *Classical Mechanics*, 2nd edition, Addison-Wesley, Reading, Massachusetts (1980

Gould94 P. L. Gould, *Introduction to Linear Elasticity*, 2nd edition, Springer Verlag, New York (1994)

GrabenRay93 H. W. Graben and J. R. Ray, *Eight Physical Systems of Thermodynamics, Statistical Mechanics, and Computer Simulation*, Mol. Phys. **80**(5), 1183-1193 (1993)

Guarnieri94a F. Guranieri and W. C. Still, *A Rapidly Convergent Simulation Method: Mixed Monte Carlo/Stochastic Dynamics*, J. Comp. Chem. **15**(11), 1302-1310 (1994)

Gurtin72 M. E. Gurtin, *The Linear Theory of Elasticity*, in: C. Truesdell, *Mechanics of Solids II*, Springer Verlag, Berlin, Encyclopedia of Physics VIa/2 (1972)

Gusev96a A. A. Gusev, M. M. Zehnder and U. W. Suter, *Fluctuation Formula for Elastic Constants*, Phys. Rev. B **54**(1), 1-4 (1996)

Gusev97a A. A. Gusev, *Representative Volume Element Size for Elastic Composites: A Numerical Study*, J. Mech. Phys. Sol. **45**(9), 1449-1459 (1997)

Gusev97b A. A. Gusev, *Predicting Transverse Failure Strain of Unidirectional Composites*, in preparation

Hageman97a J. C. L. Hageman, R. J. Meier, M. Heinemann, and R. A. de Groot, *Young Modulus of Crystalline Polyethylene from ab Initio Molecular Dynamics*, Macromolecules **30**(19), 5953-5957 (1997)

Hagler94a A. T. Hagler and C. S. Ewig, *On the Use of Quantum Energy Surfacess in the Derivation of Molecular Force Fields*, Comp. Phys. Comm. **84**, 131-155 (1994)

HaglerHwang94a M.-J. Hwang, T. P. Stockfisch and A. T. Hagler, *Derivation of Class II Force Fields. 2. Derivation and Characterization of a Class II Force Field, CFF93, for the Alkyl Functional Group and Alkane Molecules*, J. Am. Chem. Soc. **114**, 2515-2525 (1994)

HaglerMaple94a J. R. Maple, M.-J. Hwang, T. P. Stockfisch, U. Dinur, M. Waldman, C. S. Ewig and A. T. Hagler, *Derivation of Class II Force Fields. I. Methodology and Quantum Force Field for the Alkyl Functional and Alkane Molecules*, J. Comp. Chem. **15**(2), 162-182 (1994)

HaglerMaple94b J. R. Maple, M.-J. Hwang, T. P. Stockfisch and A. T. Hagler, *Derivation of Class II Force Fields. 3. Characterization of a Quantum Force Field for Alkanes*, Israel Journal of Chemistry **34**, 195-231 (1994)

HaglerSun94a H. Sun, S. J. Mumby, J. R. Maple and A. T. Hagler, *An ab Initio CFF93 All-Atom Force Field for Polycarbonates*, J. Am. Chem. Soc. **116**(7), 2978-2987 (1994)

HaglerWaldman93a M. Waldman and A. T. Hagler, *New Combining Rules for Rare Gas van der Waals Parameters*, J. Comp. Chem. **14**(9), 1077-1084 (1993)

Hansen86 J.-P. Hansen and I. R. McDonald, *Theory of Simple Liquids*, 2nd edition, Academic Press, London (1986)

Herena96a B. Crist and P. G. Herena, *Molecular Orbital Studies of Polyethylene Deformation*, J. Polym. Sci. B: Polym. Phys. **34**(3), 449-457 (1996)

Hernandez94a R. J. Hernandez and R. Gavara, *Sorption and Transport of Water in Nylon-6 Films*, J. Polym. Sci. B: Polym. Phys. **32**, 2367-2374 (1994)

Heyes81a D. M. Heyes, *Electrostatic Potentials and Fields in Infinite Point Charge Lattices*, J. Chem. Phys. **74**(3), 1924-1929 (1981)

Hong90a S. Y. Hong and M. Kertesz, *Theoretical Evaluation of Young's Moduli of Polymers*, Phys. Rev. B **41**(16), 11368-11378 (1990)

Hoover85a W. G. Hoover, *Canonical Dynamics: Equilibrium Phase-Space Distributions*, Phys. Rev. A **31**(5), 1695-1697 (1985)

Horton76 G. K. Horton, *Rare Gas Solids - A Century of Excitement and Progress*, in: M. L. Klein and J. A. Venables, *Rare Gas Solids* **1**(1), 1-121, Academic Press, London (1976)

Hsia95a K. J. Hsia, Y.-B. Xin, and L. Lin, *Numerical Simulation of Semi-crystalline Nylon 6: Elastic Constants of Crystalline and Amorphous Parts*, J. Mater. Sci. **29**, 1601-1611 (1995)

Huang87 K. Huang, *Statistical Mechanics*, 2nd edition, John Wiley & Sons, New York (1987)

Hutnik91a M. Hutnik, A. S. Argon and U. W. Suter, *Conformational Characteristics of the Polycarbonate of 4,4'-Isopropylidenediphenol*, Macromolecules **24**(22), 5956-5961 (1991)

Hutnik91b M. Hutnik, F. T. Gentile, P. J. Ludovice, U. W. Suter and A. S. Argon, *An Atomistic Model of the Amorphous Glassy Polycarbonate of 4,4'-Isopropylidenediphenol*, Macromolecules **24**(22), 5962-5969 (1991)

Hutnik91c M. Hutnik, A. S. Argon and U. W. Suter, *Quasi-Static Modeling of Chain Dynamics in the Amorphous Glassy Polycarbonate of 4,4'-Isopropylidenediphenol*, Macromolecules **24**(22), 5970-5979 (1991)

Inoue76a K. Inoue and S. Hoshino, *Swelling of Nylon 6 Film Due to Water Sorption*, J. Polym. Sci.: Polym. Phys. Ed. **14**, 1513-1526 (1976)

Kaimin73a I. F. Kaimin, A. P. Apinis, and A. Y. Galvanovskii, *The Effect of the Moisture Content on the Transition Temperatures of Polycaproamide*, Polym. Sci. U.S.S.R. **17**, 46-51 (1973)

Kaji78a K. Kaji and I. Sakurada, *Determination of the Elastic Modulus of Polyamide Crystals Along the Chain Axis by X-Ray Diffraction, 1 (The α-Form of Nylon-6)*, Makromol. Chem. **179**(1), 209-217 (1978)

Kaplan86 I. G. Kaplan, *Theory of Molecular Interactions*, S. Fraga and M. Klobukowski (editors), Elsevier ,Amsterdam (1986)

Karasava89a N. Karasawa and W. A. Goddard III, *Acceleration of Convergence for Lattice Sums*, J. Phys. Chem. **93**(21), 7320-7327 (1989)

Kawasaki64a K. Kawasaki and Y. Sekita, *Sorption and Diffusion of Water Vapor by Nylon 6*, Journal of Polymer Science: Part A **2**, 2437-2443 (1964)

KellyGroves70 A. Kelly and G. W. Groves, *Crystallography and Crystal Defects*, Longman, London (1970)

Kettle77a G. J. Kettle, *Variation of the Glass Transition Temperature of Nylon-6 with Changing Water Content*, Polymer **18**, 742-743 (1977)

Khanna95a Y. P. Khanna, W. P. Kuhn, and W. J. Sichina, *Reliable Measurements of the Nylon 6 Glass Transition Made Possible by the New Dynamic DSC*, Macromolecules **28**, 2644-2646 (1995)

Korpiun77 P. Korpiun and E. Luescher, in: M. L. Klein and J. A. Venables, *Rare Gas Solids* **2**(12), 743-822, Academic Press, London (1977)

Kraessig92 H. A. Kraessig, *Cellulose: Structure, Accessibility, and Reactivity*, Gordon and Breach Science Publishers, Switzerland (1992)

Kroon96a L. M. J. Kroon-Batenburg, B. Bouma, and J. Kroon, *Stability of Cellulose Structures Studied by MD Simulations. Could Mercerized Cellulose II Be Parallel?*, Macromolecules **29**(17), 5695-5699 (1996)

Kubo66a R. Kubo, *The Fluctuation-Dissipation Theorem*, Rep. Prog. Phys. **29**, 255-284 (1966)

Landau86a L. D. Landau and E. M. Lifshitz, *Theory of Elasticity*, 3rd edition, Pergamon Press, Oxford, *Course of Theoretical Physics* 7 (1986)

Landau86b L. D. Landau and E. M. Lifshitz, *Mechanics*, 3rd edition, Pergamon Press, Oxford, Course of Theoretical Physics 1 (1986)

Landau86c L. D. Landau and E. M. Lifshitz, *Statistical Physics, Part 1*, 3rd edition, Pergamon Press, Oxford, Course of Theoretical Physics 5 (1986)

Leach96 A. R. Leach, *Molecular Modelling; Principles and Applications*, Addison Wesley Longman, Essex (1996)

Lebowitz67a J. L. Lebowitz, J. K. Percus and L. Verlet, *Ensemble Dependence of Fluctuations with Application to Machine Computations*, Phys. Rev. **153**(1), 250-254 (1967)

Lee80a C. Y. Lee and H. L. Scott, *The Surface Tension of Water: A Monte Carlo Calculation Using an Umbrella Sampling Algorithm*, J. Chem. Phys. **73**(9), 4591-4596 (1980)

Leeuw80 S. W. de Leeuw, J. W. Perram and E. R. Smith, *Simulation of Electrostatic Systems in Periodic Boundary Conditions. I. Lattice Sums and Dielectric Constants*, Proc. Royal Soc. London **A 373**, 27 - 56 (1980)

Lekhnitskii81 S. G. Lekhnitskii, *Theory of Elasticity of an Anisotropic Body*, Mir, Moscow (1981)

Leontidis94a E. Leontidis, J. J. de Pablo, M. Laso, and U. W. Suter, *A Critical Evaluation of Novel Algorithms for the Off-Lattice Monte Carlo Simulation of Condensed Polymer Phases*, Adv. Polym. Sci. **116**, 285-318 (1994)

Lewis80a E. L. V. Lewis and I. M. Ward, *Anisotropic Mechanical Properties of Drawn Nylon 6 I. The α-Phase*, J. Macromol. Sci. - Phys. **B18**(1), 1-46 (1980)

Lill92a J. V. Lill and J. Q. Broughton, *Nonlinear Molecular Dynamics and Monte Carlo Algorithms*, Phys. Rev. B **46**(18), 12068-12071 (1992)

Lill93a J. V. Lill and J. Q. Broughton, *Atomistic Simulations Incorporating Nonlinear Elasticity: Slow-stress Relaxation and Symmetry Breaking*, Phys. Rev. B **49**(17), 11619-11633 (1993)

Lin92a L. Lin and A. S. Argon, *Deformation Resistance in Oriented Nylon 6*, Macromolecules **25**(15), 4011-4024 (1992)

Lovett89 D. R. Lovett, *Tensor Properties of Crystals*, Adam Hilger, Bristol (1989)

Ludovice93a C. Qian and P. J. Ludovic, *Stress/Strain Analysis of Polymeric Materials by Molecular Dynamics Simulations*, Macromol. Chem. Macromol. Symp. **65**, 123-132 (1993)

Lyons58a W. J. Lyons, *Theoretical Values of the Dynamic Stretch Moduli of Fiber-Forming Polymers*, Journal of Applied Physics **29**(10), 1429-1433 (1958)

MSIDiscover1 *Discover 2.9.8/96.0/4.0.0 Forcefield Simulations User Guide, Part 1*, Molecular Simulations MSI, San Diego (1996)

MSIPolymer1 *Polymer 3.0.0 User Guide, Part 1*, Biosym/MSI, San Diego (1996)

Maeda81a K. Maeda and S. Takeuchi, *Atomistic Process of Plastic Deformation in a Model Amorphous Metal*, Philos. Mag. A **44**(3), 643-656 (1981)

MaitlandRigby81 G. C. Maitland, M. Rigby, E. B. Smith and W. A. Wakeham, *Intermolecular Forces - Their Origin and Determination*, Clarendon Press, Oxford (1981)

Maldas93a D. Maldas and B. V. Kokta, *Current Trends in the Utilization of Cellulosic Materials in the Polymer Industry*, Trends in Polymer Science **1**(6), 174-178 (1993)

Malvern69 L. E. Malvern, *Introduction to the Mechanics of a Continuous Medium*, Prentice-Hall, Englewood Cliffs (1969)

Manley73a T. R. Manley and C. G. Martin, *The Elastic Modulus of Nylons*, Polymer **14**, 632-638 (1973)

Martyna94a G. J. Martyna, D. J. Tobias and M. L. Klein, *Constant Pressure Molecular Dynamics Algorithms*, Journal of Chemical Physics **101**(5), 4177-4189 (1994)

Matsuo90a M. Matsuo, C. Sawatari, Y. Iwai, and F. Ozaki, *Effect of Orientation Distribution and Crystallinity on the Measurement by X-ray Diffraction of the Crystal Lattice Moduli of Cellulose I and II*, Macromolecules **23**(13), 3266-3275 (1990)

Matsuo93a M. Matsuo, R. Sato, and Y. Shimizu, *Effect of Molecular Orientation Distribution and Crystallinity on the Measurement of the Crystal Lattice Modulus of Nylon 6 by X-ray Diffraction*, Colloid and Polymer Science **271**, 11-21 (1993)

Matsuo94a M. Matsuo, Y. Shimizu, Y. Harashina, and T. Ogita, *General Analysis of the Measurements of the Lateral Crystal Lattice Moduli of Semicrystalline Polymers by X-ray Diffraction and the Application to Nylon 6*, Colloid and Polymer Science **272**(9), 1056-1067 (1994)

McQuarrie76 D. A. McQuarrie, *Statistical Mechanics*, Harper Collins, New York (1976)

Mehlig87a B. Mehlig, D. W. Heermann and B. M. Forrest, *Hybrid Monte Carlo Method for Condensed-Matter Systems*, Phys. Rev. B **45**(2), 679-685 (1987)

Meier93a R. J. Meier, *Regarding the Ultimate Young's Modulus of a Single Polyethylene Chain*, Macromolecules **26**(16), 4376-4378 (1993)

Meier96a R. J. Meier, *First Principles calculation of the Modulus of PE*, lecture at the Monte-Verita conference on Structural and Dynamic Modelling of Mechanical Behavior of Solids (Sept. 1996)

Meirovitch83a H. Meirovitch, *Computer Simulation of Self-avoiding Walks: Testing the Scanning Method*, J. Chem. Phys. **79**(1), 502-508 (1983)

Meirovitch85a H. Meirovitch, *Computer Simulation Technique for Calculating the Entropy of Polymer Chains, Based on the Scanning Method with a Mean-Field Parameter*, Macromolecules **18**(3), 569-573 (1985)

Metropolis49 N. Metropolis and S. Ulam, *The Monte Carlo Method*, J. Am. Stat. Assoc. **44**(247), 335-341 (1949)

Metropolis53 N. Metropolis, A. W. Rosenbluth, M. N. Rosenbluth, A. H. Teller and E. Teller, *Equation of State Calculations by Fast Computing Machines*, J. Chem. Phys. **12**(6), 1087-1092 (1953)

Meyer36a K. H. Meyer and W. Lotmar, *Sur l'elasticite de la cellulose*, Helv. Chim. Acta **19**, 68-86 (1936)

Meyer37a K. H. Meyer, *Über den Bau des krystallisierten Anteils der Cellulose, V. Mitteil.*, Berichte der Bunsengesellschaft **70B**(2), 266-274 (1937)

Mott92a P. H. Mott, A. S. Argon, and U. W. Suter, *The Atomic Strain Tensor*, J. Comp. Phys. **101**(1), 140-150 (1992)

Münster69 A. Münster, *Statistical Thermodynamics*, Springer, Berlin (1969)

Murrell76 J. N. Murrell, *Short and Intermediate Range Forces*, in: M. L. Klein and J. A. Venables, *Rare Gas Solids* **1**(3), 177-211, Academic Press, London (1976)

Nakamae91a K. Nakamae, T. Nishino and H. Ohkubo, *Elastic Modulus of Crystalline Regions of Polyethylene with Different Microstructures: Experimental Proof of Homogeneous Stress Distribution*, J. Macromol. Sci. - Phys. B **30**(1), 1-23 (1991)

Natta60a G. Natta and P. Corradini, *Structure and Properties of Isotactic Polypropylene*, Nuovo Cimento, Supplemento X **15**(1), 40-51 (1960)

Nilsson86a L. Nilsson and M. Karplus, *Empirical Energy Functions for Energy Minimization and Dynamics of Nucleic Acids*, J. Comp. Chem. **7**(5), 591-616 (1986)

Nishino95a T. Nishino, K. Takano, K. Nakamae, K. Sitaka, S. Itakura, J. Azuma, and K. Okamura, *Elastic Modulus of the Crystalline Regions of Cellulose Triesters*, J. Polym. Sci. B: Polym. Phys. **33**, 611-618 (1995)

Nishino95b T. Nishino, K. Takano, and K. Nakamae, *Elastic Modulus of the Crystalline Regions of Cellulose Polymorphs*, J. Polym. Sci. B: Polym. Phys. **33**, 1647-1651 (1995)

Nose84a S. Nose, *A Molecular Dynamics Method for Simulations in the Canonical Ensemble*, Mol. Phys. **52**(2), 255-268 (1984)

Nose84b S. Nose, *A Unified Formulation of the Constant Temperature Molecular Dynamics Methods*, J. Chem. Phys. **81**(1), 511-519 (1984)

Nose91a S. Nose, *Constant Temperature Molecular Dynamics Methods*, Progress of Theoretical Physics Supplement **103**, 1-46 (1991)

Nye85 J. F. Nye, *Physical Properties of Crystals*, 2nd edition, Oxford University Press, Oxford (1985)

Odajima66a A. Odajima and T. Maeda, *Calculation of the Elastic Constants and the Lattice Energy of the Polyethylene Crystal*, J. Polym. Sci. C **15**, 55-74 (1966)

Otten89 R. H. J. M. Otten and L. P. van Ginneken, *The Annealing Algorithm*, Kluwer Academic Publishers, Boston (1989)

Ouali91a N. Ouali, J. Y. Cavaille, and J. Perez , Plast. Rubber Comp. Process. Appl. **16**, 55- (1991)

Panagiatopoulos87 A. Z. Panagiatopoulos, *Direct Determination of Phase Coexistance Properties of Fluids by Monte Carlo Simulation in a New Ensemble*, Mol. Phys. **61**(4), 813-826 (1987)

Pant95a P. V. K. Pant and D. N. Theodorou, *Variable Connectivity Method for the Atomistic Monte Carlo Simulation of Polydisperse Polymer Melts*, Macromolecules **28**, 7224-7234 (1995)

ParkMiller88a S. K. Park and K. W. Miller, *Random Number Generators: Good Ones Are Hard to Find*, Computing Practices **31**(10), 1192-1201 (1988)

ParrinelloRahman81a M. Parrinello and A. Rahman, *Polymorphic Transitions in Single Crystals: A New Molecular Dynamics Method*, J. Appl. Phys. **52**(12), 7182-7190 (1981)

ParrinelloRahman82a M. Parrinello and A. Rahman, *Strain Fluctuations and Elastic Constants*, J. Chem. Phys. **76**(5), 2662-2666 (1983)

Pathmanathan92a K. Pathmanathan, J.-Y. Cavaillé, and G. P. Johari, *The Dielectric Properties of Dry and Water-Saturated Nylon-12*, J. Polym. Sci. B: Polym. Phys. **30**, 341-348 (1992)

Pathmanathan95a K. Pathmanathan and G. P. Johari, *High Temperature Dielectric Relaxation in Nylon 12 and the Effects of Annealing and Absorbed Water*, J. Chem. Soc., Farad. Trans. **91**(2), 337-341 (1995)

Pathria72 R. K. Pathria, *Statistical Mechanics*, Pergamon Press, Oxford, International Series in Natural Philosophy **45** (1972)

Petersen93a W. P. Petersen, *Lagged Fibonacci Series Random Number Generators for the SX-3*, CrossCuts **2**(2), 9-11 (1993)

Pressetal92 W. H. Press, S. A. Teukolsky, W. T. Vetterling and B. P. Flannery, *Numerical Recipies in C - The Art of Scientific Computing*, 2nd edition, Cambridge Univerity Press, Cambridge (1992)

Prevorsek71a D. C. Prevorsek, *Structure of Semicrystalline Fibers From Interpretation of Anelastic Effects*, J. Polym. Sci. C **32**, 343-375 (1971)

Prevorsek71b D. C. Prevorsek, R. H. Butler, and H. K. Reimschüssel, *Mechanical Relaxations in Polyamides*, J. Polym. Sci. A-2 **9**, 867-886 (1971)

Puffr67a R. Puffr and J. Sebenda, *On the Structure and Properties of Polyamides. XXVII. The Mechanism of Water Sorption in Polyamides*, J. Polym. Sci. C **16**, 79-93 (1967)

Puffr91 R. Puffr and V. Kubanek, *Lactam-Based Polyamides*, **1**(5): *Polymerization, Structure, and Properties*, CRC Press, Boca Raton (1991)

Rahman64a A. Rahman, *Correlations in Motion of Atoms in Liquid Argon*, Physical Review **136**(2A), A405-A411 (1964)

Rapold93a R. F. Rapold, *Atomistic Simulation of the Structure and Ring Motion of Dense Amorphous Polystyrene*, Institute of Polymers, ETH Zurich (1993)

Ratajczak80a H. Ratajczak and W. J. Orville-Thomas, *On Some Problems of Molecular Interactions*, 1-20, John Wiley & Sons, Chichester, Molecular Interactions **1** (1980)

Ray84a J. R. Ray and A. Rahman, *Statistical Ensembles and Molecular Dynamics Studies of Anisotropic Solids*, J. Chem. Phys. **80**(9), 4423-4428 (1984)

Ray85a J. R. Ray, M. C. Moody and A. Rahman, *Molecular Dynamics Calculation of Elastic Constants for a Crystalline System in Equilibrium*, Phys. Rev. B **32**(2), 733-735 (1985)

Ray86a J. R. Ray, M. C. Moody, and A. Rahman, *Calculation of Elastic Constants Using Isothermal Molecular Dynamics*, Phys. Rev. B **33**(2), 895-899 (1986)

Ray88a J. R. Ray, *Elastic Constants and Statistical Ensembles in Molecular Dynamics*, Computer Physics Reports **8**, 109-152 (1988)

ReedGubbins73 T. M. Reed and K. E. Gubbins, Applied Statistical Mechanics - Thermodynamic and Transport Properties of Fluids, McGraw-Hill, New York (1973)

Reichl80a L. E. Reich, A Modern Course in Statistical Physic, University of Texas Press, Austin (1980)

Reimschuessel78a H. K. Reimschüssel, *Relationships on the Effect of Water on Glass Transition Temperature and Young's Modulus of Nylon 6*, J. Polym. Sci.: Poly. Chem. Ed. **16**, 1229-1236 (1978)

Renton87 J. D. Renton, *Applied Elasticity: Matrix and Tensor Analysis of Elastic Continua*, Ellis Horwood, Chichester (1987)

Rutledge94a D. J. Lacks and G. C. Rutledge, *Simulation of the Temperature Dependence of Mechanical Properties of Polyethylene*, J. Phys. Chem. **98**(4), 1222-1231 (1994)

Rutledge94b D. J. Lacks and G. C. Rutledge, *Evaluation of the Accuracy of Consistent Quasi-Harmonic Simulations by Comparison with Exact Monte Carlo Results*, J. Chem. Phys. **101**(11) , 9961- (1994)

Rutledge95a D. J. Lacks and G. C. Rutledge, *Temperature Dependence of Structural and Mechanical Properties of Isotactic Polypropylene*, Macromolecules **28**(4), 1115-1120 (1995)

RutledgeSuter91a G. C. Rutledge and U. W. Suter, *Calculation of Mechanical Properties of Poly(p-phenylene terephtalamide) by Atomistic Modelling*, Polymer **32**(12), 2179 - 2189 (1991)

Sakurada70a I. Sakurada and K. Kaji, *Relation Between the Polymer Conformation and the Elastic Modulus of the Crystalline Region of Polymer*, J. Polym. Sci.: Part C **31**, 57-76 (1970)

Sands82 D. E. Sands, *Vectors and Tensors in Crystallography*, Addison-Wesley, Reading (1982)

Shiro71a Y. Shiro and T. Miyazawa, *A General Matrix Method for Treating Elastic Constants of Molecular Crystals; Application to Orthorhombic Polyethylene*, Bull. Chem. Soc. Japan **44**, 2371-2378 (1971)

Shuvalov88 L. A. Shuvalov, *Modern Crystallography IV: Physical Properties of Crystals*, Springer Verlag, Berlin, Solid State Science **37** (1988)

Smith86a P. A. Irvine and P. Smith, *Development of the Axial Young's Modulus with Draw Ratio of Flexible-Chain Polymers*, Macromolecules **19**(1), 240-242 (1986)

Sneddon58 I. N. Sneddon, *The Classical Theory of Elasticity*, in: S. Fluegge, *Encylopedia of Physics*, **VI**: *Elasticity and Plasticity* 1, 1-126, Springer Verlag, Berlin (1958)

Song90a J. Song and G. W. Ehrenstein, *Einfluss der Wasseraufnahme auf die Eigenschaften von Polyamid*, Kunststoffe **80**, 722-726 (1990)

Sprik84a M. Sprik, R. W. Impey and M. L. Klein, *Second-Order Elastic Constants for the Lennard-Jones Solid*, Phys. Rev. B **29**(8), 4368-4374 (1984)

Squire69a D. R. Squire, A. C. Holt and W. G. Hoover, *Isothermal Elastic Constants for Argon. Theory and Monte Carlo Calculations*, Physica **42**, 388-397 (1969)

Srolovitz83a D. Srolovitz, V. Vitek, and T. Egami, *An Atomistic Study of Deformation of Amorphous Metals*, Acta Metall. **31**, 335-352 (1983)

Starkweather59a H. W. Starkweather Jr., *The Sorption of Water by Nylons*, J. Appl. Poly. Sci. **2**, 129-133 (1959)

Stauffer96a D. Stauffer, *Random Number Generation* 1, 1-8, Springer Verlag, Berlin (1996)

Stone96 A. J. Stone, *The Theory of Intermolecular Forces*, Clarendon Press, Oxford, International Series of Monographs on Chemistry **32** (1996)

Stuart94a B. H. Stuart, *A Fourier Transform Raman Study of Water Sorption by Nylon 6*, Polymer Bulletin **33**, 681-686 (1994)

Sugiyama90a J. Sugiyama, T. Okano, H. Yamamoto, and F. Horii, *Transformation of Valonia Cellulose Crystals by an Alkaline Hydrothermal Treatment*, Macromolecules **23**, 3196-3198 (1990)

Swope82a W. C. Swope, H. C. Andersen, P. H. Berens and K. R. Wilson, *A Computer Simulation Method for the Calculation of Equilibrium Constants for the Formation of Physical Cluster of Molecules: Application to Small Water Clusters*, J. Chem. Phys. **76**(1), 637-649 (1982)

Tadokoro84a H. Tadokoro, *Structure and Properties of Cyrstalline Polymers*, Polymer **25**, 147-164 (1984)

Tadokoro90 H. Tadokoro, *Structure of Crystalline Polymers*, R. E. Krieger, Malabar (1990)

Tadokoro92a K. Tashiro, M. Kobayashi, and H. Tadokoro, *Vibrational Spectra and Theoretical Three-Dimensional Elastic Constants of Isotactic Polypropylene Crystal: An Important Role of Anharmonic Vibrations*, Polymer Journal **24**(9), 899-916 (1992)

Takayanagi64a M. Takayanagi, S. Uemura, and S. Minami, J. Polym. Sci. C **5**, 113- (1964)

Tashiro78a K. Tashiro, M. Kobayashi, and H. Tadokoro, *Calculation of Three-Dimensional Elastic Constants of Polymer Crystals. 1. Method of Calculation*, Macromolecules **11**(5), 908-913 (1978)

Tashiro81a K. Tashiro and H. Tadokoro, *Calculation of Three-Dimensional Elastic Constants of Polymer Crystals. 3. α and γ Forms of Nylon 6*, Macromolecules 14(3), 781-785 (1981)

Tashiro88a K. Tashiro and M. Kobayashi, *Theoretical Evaluation of the Three-Dimensional Elastic Constants of Cellulose Crystalline Phases I and II: A Role of Hydrogen Bondings*, Polym. Prepr. **37**(5-10), 3017 (E615) (1988)

Terzis97a A. F. Terzis, P. T. Snee, and E. T. Samulski, *Orientational Order of Water Confined in Anisotropic Cavities*, Chem. Phys. Let. **264**(5), 481-486 (1997)

Theodorou85a D. N. Theodorou and U. W. Suter, *Detailed Molecular Structure of a Vinyl Polymer Glass*, Macromolecules **18**(7), 1467-1478 (1985)

Theodorou86a D. N. Theodorou and U. W. Suter, *Atomistic Modeling of Mechanical Properties of Polymeric Glasses*, Macromolecules **19**(1), 139-154 (1986)

Thurston64 R.N. Thurston, *Wave Propagation in Fluids and Normal Solids*, in: W. P. Mason, *Physical Acoustics: Principle and Methods* I-A(1), 1-110, Academic Press, New York (1964)

Ting96 T. C. T. Ting, Anisotropic Elasticity, Oxford University Press, New York (1996)

Tomaselli97a M. Tomaselli, M. M. Zehnder, P. Robyr, C. Grob-Pisano, R. R. Ernst, and U. W. Suter, *Local Conformations of the Glassy Polycarbonate of 2,2-Bis(4-hydroxyphenyl)propane (Bisphenol-A)*, Macromolecules **30**(12), 3579-3583 (1997)

Treloar60a L. R. G. Treloar, *Calculations of Elastic Moduli of Polymer Crystals: I. Polyethylene and Nylon 66*, Polymer **1**, 95-103 (1960)

VanGunsteren90a W. F. van Gunsteren and H. J. C. Berendsen, *Computer Simulation of Molecular Dynamics: Methodology, Applications and Perspectives in Chemistry*, Angew. Chem., Intern. Ed. Engl. **29**, 992-1023 (1990)

vanKrevelen80 D. W. van Krevelen and P. J. Hoftyzer, *Properties of Polymers. Their estimation and correlation with chemical structure*, 2nd edition, Elsevier, Amsterdam (1980)

Varlet90a J. Varlet, J. Y. Cavaille, and J. Perez, *Dynamic Mechanical Spectrometry of Nylon-12*, J. Polym. Sci. B: Polym. Phys. **28**, 2691-2705 (1990)

Verlet67a L. Verlet, *Computer 'Experiments' on Classical Fluids. I. Thermodynamical Properties of Lennard-Jones Molecules*, Phys. Rev. **159**(1), 98-103 (1967)

Ward83 I. M. Ward, *Mechanical Properties of Solid Polymers*, 2nd edition, John Wiley & Sons, Chichester (1983)

WeinerKollman86a S. J. Weiner, P. A. Kollman, D. T. Nguyen and D. A. Case, *An All Atom Force Field for Simulations of Proteins and Nucleic Acids*, J. Comp. Chem. **7**(2), 230-252 (1986)

Wendling95a J. Wendling, *Inter- und intramolekulare Modifizierung der Flexibilitaet von Polymersystemen: Simulation und Experimente*, Diss. Philipps-Universität (1995), Görich & Weiershäuser, Marburg

Widmann96a A. H. Widmann, *Parallelization in Monte Carlo Simulations of Atomistically Detailed Polymers*, Diss. ETH No. 11355., Inst. f. Polymere, ETH Zurich(1996)

Wobser70a G. Wobser and S. Blasenbrey, *Struktur- und Konformationsberechnung in Polymeren, II. Idealkristall und Defektzustand (Buendelmodell) von Polyäthylen*, Kolloid-Z. u. Z. Polymere **241**, 985-993 (1970)

Woodcock71a L. V. Woodcock, *Isothermal Molecular Dynamics Calculations for Liquid Salts*, Chemical Physics Letters **10**(3), 257-261 (1971)

Woodcock80a C. Woodcock and A. Sarko, *Packing Analysis of Carbohyrates and Polysaccharides. 11. Molecular and Crystal Structure of Native Ramie Cellulose*, Macromolecules **13**(5), 1183-1187 (1980)

Woodwell78a G. M. Woodwell, R. H. Whittaker, W. A. Reiners, G. E. Likens, C. C. Delwiche and D. B. Botkin, *The Biota and the World Carbon Budget*, Science **199**(1), 141-146 (1978)

Wooster73 W. A. Wooster ,Tensors and Group Theory for the Physical Properties of Crystals, Clarendon Press, Oxford (1973)

XrayTable83 T. Hahn (editor), *International Tables for Crystallography*, Kluwer Academic, Dordrecht, **A**: Space-Group Symmetry (1983)

Acknowledgement

It is not possible to thank everybody who has contributed to this work in due words and the following list is therefore neither complete nor weighted - except for the first two names:

Prof. Ulrich W. Suter and *Dr. Andrei A. Gusev* initiated and promoted the present thesis with parental guidance, generous support, and continual scientific advice. Their help and encouragement proved to be invaluable. The german expression 'Doktorväter' describes well what they were to me.

Prof. Wilfred F. van Gunsteren was so kind as to co-examine my doctoral thesis. The vicinity of his group offered many possibilties for fruitful exchange of ideas.

Manuel Laso, Bruce Forrest, and *Minos Leontidis* shared their profound experience in the field of atomistic modelling with me.

Albert Widmann gave me countless tips on how to deal with UNIX and how to improve the readability of my FORTRAN programs.

Serge Santos helped me with statistical mechanics in general and the canonicity of integrators in particular and carefully checked my forcefield code.

*Gitta Nick*s work on the solubility of water in nylons provided many stimulating discussions and allowed for the exchange of simulation data

Marcel Utz enlightened me more than once when I got lost in mathematics and statistical physics.

Michael Geke, Jürgen Wendling, Marco Tomaselli, Roland Rapold, and *Ulla Tromsdorff* discussed many aspects of molecular modelling with me.

Numerous people in the groups of Prof. Binder, Prof. Kremer, Dr. Heermann and at BAYER, BIOSYM/MSI, EMS, and in Jülich inspired and encouraged me throughout my thesis.

Last, but not least, I would like to thank the *members of the group of Prof. Suter,* the office, and the information services who all offered me their help and friendship. They made my time at the institute most interesting and colorful.

Curriculum Vitae

Personal data

Name	Marcel Zehnder
Birthdate	16th June 1966
Birthplace	Olten, Switzerland
Citizenship	Willisau-Land LU, Switzerland
Parents	Hubert Zehnder (1938 - 1997)
	Brigitte Zehnder-Schuler (*1941)
Present adress	Fluhmattstr. 21, 6004 Lucerne
Hobbies	Computers, Mountaineering

Education

1973 - 1978	Primary school in Olten
1978 - 1986	Gymnasium B in Olten and Lucerne
1986 - 1992	Undergraduate studies in materials science at the Federal Institute of Technology, Zürich
	Diploma thesis *Modelling of the Sorption of Water in Glassy Polymers* with Prof. U. W. Suter under the guidance of Dr. A. Gusev
1993 - 1997	Postgraduate studies in the research group of Prof. U. W. Suter

Professional and Teaching Experience

1987 - 1991	Assistance at the Institute of Forming Technology (programming and teaching activities)
1989 - 1997	Softwaredevelopment for Vibrotest AG in Buchrain
1993 - 1997	Assistance at the Institute of Polymers (Installation of UNIX software and supervision of exercises)